The Deep Space Network Progress Report 42-42

September and October 1977

National Aeronautics and
Space Administration

Jet Propulsion Laboratory
California Institute of Technology
Pasadena, California 91103

The Deep Space Network Progress Report 42-42

September and October 1977

Subject: Erratum

The article "Estimated Displacements for the VLBI Reference Point of the
DSS 14 Antenna" appears on pages 218-223 of The Deep Space Network Progress
Report 42-41, July and August 1977, published on October 15, 1977 by the Jet
Propulsion Laboratory. Please note that Equation 26 of this article, on page 222,
should read as follows:

$$D_A = 0.305 [\,|t - 18.5| + 6\,], \text{ in millimeters}$$

Very truly yours,
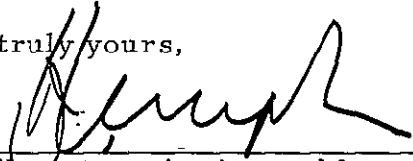
John Kempton, Assistant Manager
Documentation Section

December 15, 1977

Preface

Beginning with Volume XX, the Deep Space Network Progress Report changed from the Technical Report 32- series to the Progress Report 42- series The volume number continues the sequence of the preceding issues Thus, Progress Report 42-20 is the twentieth volume of the Deep Space Network series, and is an uninterrupted follow-on to Technical Report 32-1526, Volume XIX

This report presents DSN progress in flight project support, tracking and data acquisition (TDA) research and technology, network engineering, hardware and software implementation, and operations Each issue presents material in some, but not all, of the following categories in the order indicated.

Description of the DSN

Mission Support
 Ongoing Planetary/Interplanetary Flight Projects
 Advanced Flight Projects

Radio Astronomy

Special Projects

Supporting Research and Technology
 Tracking and Ground-Based Navigation
 Communications—Spacecraft/Ground
 Station Control and Operations Technology
 Network Control and Data Processing

Network and Facility Engineering and Implementation
 Network
 Network Operations Control Center
 Ground Communications
 Deep Space Stations
 Quality Assurance

Operations
 Network Operations
 Network Operations Control Center
 Ground Communications
 Deep Space Stations

Program Planning
 TDA Planning

In each issue, the part entitled "Description of the DSN" describes the functions and facilities of the DSN and may report the current configuration of one of the five DSN systems (Tracking, Telemetry, Command, Monitor & Control, and Test & Training)

The work described in this report series is either performed or managed by the Tracking and Data Acquisition organization of JPL for NASA

Contents

DESCRIPTION OF THE DSN

MISSION SUPPORT

Ongoing Planetary/Interplanetary Flight Projects

SUPPORTING RESEARCH AND TECHNOLOGY

Tracking and Ground-Based Navigation

Communications — Spacecraft/Ground

Station Control and Operations Technology

Network Control and Data Processing

NETWORK AND FACILITY ENGINEERING
AND IMPLEMENTATION

Network

Ground Communications

Deep Space Stations

PROGRAM PLANNING

TDA Planning

Network Functions and Facilities

N A Renzetti

Office of Tracking and Data Acquisition

The objectives, functions, and organization of the Deep Space Network are summarized, deep space station, ground communication, and network operations control capabilities are described

The Deep Space Network (DSN), established by the National Aeronautics and Space Administration (NASA) Office of Tracking and Data Acquisition under the system management and technical direction of the Jet Propulsion Laboratory (JPL), is designed for two-way communications with unmanned spacecraft traveling approximately 16,000 km (10,000 miles) from Earth to the farthest planets of our solar system. It has provided tracking and data acquisition support for the following NASA deep space exploration projects Ranger, Surveyor, Mariner Venus 1962, Mariner Mars 1964, Mariner Venus 1967, Mariner Mars 1969, Mariner Mars 1971, and Mariner Venus Mercury 1973, for which JPL has been responsible for the project management, the development of the spacecraft, and the conduct of mission operations, Lunar Orbiter, for which the Langley Research Center carried out the project management, spacecraft development, and conduct of mission operations, Pioneer, for which Ames Research Center carried out the project management, spacecraft development, and conduct of mission operations, and Apollo, for which the Lyndon B. Johnson Space Center was the project center and

the Deep Space Network supplemented the Manned Space Flight Network (MSFN), which was managed by the Goddard Space Flight Center (GSFC) It is providing tracking and data acquisition support for Helios, a joint U.S /West German project, and Viking, for which Langley Research Center provides the project management, the Lander spacecraft, and conducts mission operations, and for which JPL also provides the Orbiter spacecraft

The Deep Space Network is one of two NASA networks The other, the Spaceflight Tracking and Data Network, is under the system management and technical direction of the Goddard Space Flight Center. Its function is to support manned and unmanned Earth-orbiting satellites. The Deep Space Network supports lunar, planetary, and interplanetary flight projects

From its inception, NASA has had the objective of conducting scientific investigations .throughout the solar sys-

tem. It was recognized that in order to meet this objective, significant supporting research and advanced technology development must be conducted in order to provide deep space telecommunications for science data return in a cost effective manner Therefore, the Network is continually evolved to keep pace with the state of the art of telecommunications and data handling It was also recognized early that close coordination would be needed between the requirements of the flight projects for data return and the capabilities needed in the Network This close collaboration was effected by the appointment of a Tracking and Data Systems Manager as part of the flight project team from the initiation of the project to the end of the mission. By this process, requirements were identified early enough to provide funding and implementation in time for use by the flight project in its flight phase

As of July 1972, NASA undertook a change in the interface between the Network and the flight projects Prior to that time, since 1 January 1964, in addition to consisting of the Deep Space Stations and the Ground Communications Facility, the Network had also included the mission control and computing facilities and provided the equipment in the mission support areas for the-conduct of mission operations The latter facilities were housed in a building at JPL known as the Space Flight Operations Facility (SFOF) The interface change was to accommodate a hardware interface between the support of the network operations control functions and those of the mission control and computing functions This resulted in the flight projects assuming the cognizance of the large general-purpose digital computers which were used for both network processing and mission data processing They also assumed cognizance of all of the equipment in the flight operations facility for display and communications necessary for the conduct of mission operations The Network then undertook the development of hardware and computer software necessary to do its network operations control and monitor functions in separate computers This activity has been known as the Network Control System Implementation Project A characteristic of the new interface is that the Network provides direct data flow to and from the stations; namely, metric data, science and engineering telemetry, and such network monitor data as are useful to the flight project This is done via appropriate ground communication equipment to mission operations centers, wherever they may be.

The principal deliverables to the users of the Network are carried out by data system configurations as follows

- The DSN Tracking System generates radio metric data, i e., angles, one- and two-way doppler and range, and transmits raw data to Mission Control

- The DSN Telemetry System receives, decodes, records, and retransmits engineering and scientific data generated in the spacecraft to Mission Control.

- The DSN Command System accepts coded signals from Mission Control via the Ground Communications Facility and transmits them to the spacecraft in order to initiate spacecraft functions in flight

The data system configurations supporting testing, training, and network operations control functions are as follows.

- The DSN Monitor and Control System instruments, transmits, records, and displays those parameters of the DSN necessary to verify configuration and validate the Network It provides operational direction and configuration control of the Network, and provides primary interface with flight project Mission Control personnel

- The DSN Test and Training System generates and controls simulated data to support development, test, training and fault isolation within the DSN It participates in mission simulation with flight projects

The capabilities needed to carry out the above functions have evolved in three technical areas

(1) The Deep Space Stations, which are distributed around Earth and which, prior to 1964, formed part of the Deep Space Instrumentation Facility The technology involved in equipping these stations is strongly related to the state of the art of telecommunications and flight-ground design considerations, and is almost completely multimission in character.

(2) The Ground Communications Facility provides the capability required for the transmission, reception, and monitoring of Earth-based, point-to-point communications between the stations and the Network Operations Control Center at JPL, Pasadena, and to the mission operations centers, wherever they may be Four communications disciplines are provided tele-type, voice, high-speed, and wideband The Ground Communications Facility uses the capabilities provided by common carriers throughout the world, engineered into an integrated system by Goddard Space Flight Center, and controlled from the communications Center located in the Space Flight Operations Facility (Building 230) at JPL

(3) The Network Operations Control Center is the functional entity for centralized operational control of the Network and interfaces with the users It has two separable functional elements, namely, Network Operations Control and Network Data Processing The functions of the Network Operations Control are:

- Control and coordination of Network support to meet commitments to Network users

- Utilization of the Network data processing computing capability to generate all standards and limits required for Network operations

- Utilization of Network data processing computing capability to analyze and validate the performance of all Network systems

The personnel who carry out the above functions are located in the Space Flight Operations Facility, where mission operations functions are carried out by certain flight projects Network personnel are directed by an Operations Control Chief The functions of the Network Data Processing are

- Processing of data used by Network Operations Control for control and analysis of the Network

- Display in the Network Operations Control Area of data processed in the Network Data Processing Area.

- Interface with communications circuits for input to and output from the Network Data Processing Area.

- Data logging and production of the intermediate data records

The personnel who carry out these functions are located approximately 200 meters from the Space Flight Operations Facility. The equipment consists of minicomputers for real-time data system monitoring, two XDS Sigma 5s, display, magnetic tape recorders, and appropriate interface equipment with the ground data communications

DSN Telemetry System, Mark III-77

E C Gatz
TDA Engineering

This article provides a description of the DSN Telemetry System, Mark III-77, which is now being used to support multiple deep space missions Telemetry functions performed by the Deep Space Stations, Ground Communications Facility, and the Network Operations Control Center are defined Recent improvements to the system and planned upgrades are described

I. Introduction

The Deep Space Network Telemetry System is implemented by means of incremental additions and modifications to provide multiple-mission support to a variety of planetary and interplanetary flight projects The current system, designated Mark III-77, provides support for

(1) Pioneers 6 through 9

(2) Pioneers 10 and 11

(3) Helios A and B

(4) Viking

(5) Voyager 1 and 2

(6) Pioneer Venus

This Mark III-77 configuration is derived from the Mark III-75 configuration (Ref 1), which supported Viking, Helios, and Pioneer projects

II. System Definition

The DSN Telemetry System provides the capability to acquire, process, decode, and distribute deep space probe telemetry data Telemetry data are defined as consisting of science and engineering information modulated on radio signals transmitted from the spacecraft.

The DSN Telemetry System, Mark III-77, performs three main functions

(1) Telemetry data acquisition

(2) Telemetry data conditioning and transmission.

(3) Telemetry System validation

Telemetry data acquisition consists of those functions necessary to extract the telemetry information modulated on the downlink carrier(s) of the spacecraft. Telemetry data conditioning and transmission consist of those functions necessary to decode, format, record, and transmit the data to users Telemetry System validation consists of those functions

4

necessary to validate the performance of the Network in the acquisition, conditioning, and transmission of telemetry data Verification of correct system performance is made and corrective action is taken when such performance does not meet specifications.

III. Key Characteristics

The key characteristics of the DSN Telemetry System, Mark III-77, consist of

(1) High rate X-band telemetry capability at both a 34-m and a 64-m subnet.

(2) Maximum likelihood decoding of short-constraint-length convolutional codes at all Deep Space Stations

(3) Replacement of the Telemetry and Command Processor with a dedicated processor for telemetry, the Telemetry Processor Assembly (TPA)

(4) Centralized monitoring and control of the DSN Telemetry System by the Network Operations Control Center (NOCC)

(5) Real-time reporting of DSN Telemetry System status through the DSN Monitor and Control System

(6) Low-loss on-site recording at selected DSS of pre-detection analog records with non-real-time playback

(7) Production of a digital telemetry Original Data Record (ODR) at each DSS with playback via local manual control or in automatic response to recall requests

(8) Simultaneous reception and recording of five carriers at selected DSS

(9) Replacement of the Data Decoder Assembly (DDA) and incorporation of its functions into the TPA

(10) Increased high-speed data (HSD) line rate to 7200 bps, and wideband capability up to 230 kbps (selected DSS)

(11) Stand-alone fault detection and self-test capability

(12) Generation of a telemetry Intermediate Data Record (IDR), a time-merged record of all received data

IV. Functional Description

A simplified block diagram of the system is shown in Fig 1

Standards and limits messages (predicts) are initially generated at the NOCC for high-speed data line (HSDL) transmission to the DSS for the purpose of selecting the proper data modes and configurations Such messages consist of predicted signal levels, tolerances, data mode, and system configuration information

At the Deep Space Station, the received spacecraft signal is amplified by the Antenna Microwave Subsystem (UWV) The RF carrier is tracked by the Receiver-Exciter Subsystem (RCV) and the sidebands are routed to the Subcarrier Demodulator Assembly (SDA). The subcarrier is regenerated by the SDA and the data are demodulated. The resulting data stream is passed to the Symbol Synchronizer Assembly (SSA) Coded data are decoded, either in special decoder assemblies or by software in the Telemetry Processor Assembly (TPA), depending on code type and data rate All data are formatted for high-speed or wideband data line transmission by the TPA

An Original Data Record (ODR) of the decoded data is then written by either the TPA for high rate data, or the Communications Monitor and Formatter Assembly (CMF) for low rate data. The data are passed to the high-speed or wideband buffer, depending upon the data rate

The data are then transmitted to the Mission Control and Computing Center (MCCC) or Remote Mission Operations Centers (RMOC), and in parallel to the NOCC. At the NOCC, a limited amount of decommutation of telemetry data is performed to analyze system performance and to obtain certain spacecraft parameters useful in controlling the Network The NOCC also receives and displays DSN Telemetry System parameters

A log tape containing all data received at the NOCC, either in real-time or by recall, is generated by the Network Log Processor (NLP) This log is the Network Data Log (NDL) The Data Records Assembly provides for the recall of data from the station ODRs and for merging the recalled data with data on the NDL It also provides for the generation of the IDR

A special configuration at DSS 14 and DSS 43 for the Pioneer Venus 78 entry mission allows simultaneous reception of five carriers and processing of four carriers in real-time For backup purposes, four open-loop receivers are used with bandpass filters and an analog recorder This combination allows for recording a wideband spectrum around the anticipated carrier frequencies of the four atmospheric probes In non-real-time, these data can be played back and converted up to

S-band for reception and processing by conventional receiver-SDA-SSA-TPA telemetry equipment

DSN Telemetry System performance is validated by the NOCC Telemetry Subsystem Real Time Monitor (RTM) processor in response to the controls and standards and limits applied from DSN Operations personnel in the Network Operations Control Area (NOCA). Telemetry System alarms, status, and data are transmitted from the NOCC Telemetry RTM to the NOCC Display Subsystem DSN Telemetry System alarms and status are also transmitted to the DSN Monitor and Control System and are included in the Network Performance Record (NPR) A DSN Telemetry System Performance Record (SPR), containing status and alarms, is maintained for non-real-time analysis. The SPR also contains a list of all telemetry data gaps. This list is used by the Data Records Assembly to compose recall requests from the station ODRs.

The DSN Test and Training System is used to provide simulated DSN Telemetry System data for the checkout of the system and for the training of DSN personnel

V. System Configurations

The current configurations of equipment comprising the DSN Telemetry System are shown in Fig 2

A. DSS Functions and Modifications

1 RF carrier reception and power measurement Receiver and low-noise maser amplifiers are provided at each DSS, with full backup capability At the 64-meter DSSs, both S- and X-band capability is provided Starting in 1978, it is planned to augment one 26-meter subnetwork (DSS 12, 42, and 61) to 34-meter diameter and to add X-band receiving capability.

The receivers are calibrated with test transmitters, and the Automatic Gain Control (AGC) is monitored to provide a measure of received signal level Starting in 1978, precision signal power measurement equipment will be added to each DSS to provide continuous output of received carrier signal power and also system noise temperature

2 Subcarrier demodulation. At 64-meter DSSs, demodulators are provided for two subcarriers per carrier. Only a single subcarrier is envisioned at the 26-meter DSSs, although a second can be accommodated by using the backup equipment.

3. Symbol synchronization. Symbol synchronizers are available for each telemetry stream, operating from 8 to 250,000 symbols per second The symbol synchronizers are operated automatically under software control from the Telemetry Processing Assembly (TPA)

4 Decoding Channel decoding is provided for biorthogonal block codes and for convolutional codes of either long or short constraint length·

(1) *Block Codes* 32, 6 biorthogonal codes are handled by the Block Decoding Assembly (BDA) equipment at 64-meter DSS at data rates up to 16,000 bits per second At other DSS the block decoding is performed by TPA software, limited to a maximum output rate of 2000 bps

(2) *Convolutional Codes — Long Constraint* These codes are sequentially decoded by the Faro algorithm, using TPA software (Ref. 2) Output rates up to 4000 bps can be handled

(3) *Convolutional Codes — Short Constraint* These codes are decoded by maximum-likelihood convolutional decoding equipment (MCD) at each DSS (Ref. 3). Output rates up to 250,000 bps can be handled by this equipment.

5. Data handling and formatting. Two new processors combine to perform these functions, the Telemetry Processing Assembly (TPA) and Communications Monitor and Formatter Assembly (CMF) As indicated in Fig 2 , these assemblies are provided with backups The functions performed by these assemblies for all received telemetry data are as follows

(1) Format the data into standard communications data blocks

(2) Interlace partial status data into the data blocks Partial status includes lock indicators, configuration codes, signal-level, and signal-to-noise ratios.

(3) Generation of Original Data Records (ODR).

(4) Output data blocks on high-speed and wideband circuits as appropriate The CMF handles high-speed interface, the TPA handles the wideband. A temporary ODR (TODR) is maintained on disc to insure that the transfer of data between TPA and CMF is accomplished without loss of data

(5) ODR replay

B. GCF Functions and Modifications

1 Data Transmission GCF high-speed circuits have been upgraded to 7200-bps rate Wideband circuits run at several rates depending on the DSS involved (Ref 4) Error detection is provided on all data blocks

2 Data Records. All telemetry data blocks transmitted to flight projects are also logged on tape in the Central Communications Terminal at JPL. Provision is made also to recall missing data from the station ODRs and to merge the recalled data blocks with those extracted from the central log. This merged record can be supplied to flight projects and is called the Intermediate Data Record (IDR). The details of Telemetry Data Records are described in Ref 5.

C. NOCC Functions and Modifications

The function of the NOCC for Telemetry is to validate the performance of the DSN Specifically, the following functions are performed for every active Deep Space Station and telemetry stream

(1) Monitor the Telemetry System configuration and generate alarms when the configuration departs from that planned

(2) Detect status and anomalies and generate displays and alarms.

  (a) Time tag errors.

  (b) Frame sync status

  (c) DSS lock indicators, signal-to-noise ratios, and signal level

(d) Missing or defective data.

(e) Channel decoder performance.

(3) Decommutate each telemetry stream, at least to the major frame level Analysts in the Network Operations Control Area have the capability to select for display up to four measurements or data fields from each stream.

(4) Generate a gap list for each stream. This is used in recalling data from the DSS (Ref 5).

D. Planned Improvements

This article describes the current configuration of the DSN Telemetry System as of October 1977 Improvements to this system are already being designed, including:

(1) Augmenting of one subnet of 26-meter DSSs (one each at Spain, Australia, and Goldstone, California), to 34-meter diameter and to include X-band operation

(2) Capability to combine the receiver baseband outputs from two or more DSSs at one location to provide an effective increase in signal-to-noise ratio by "arraying" the antennas. This capability will be used to enhance the Voyager project Saturn encounter

(3) Precision signal power and system noise temperature measurement capability.

References

1 Gatz, E C., "DSN Telemetry System, 1973-76," in *The Deep Space Network Progress Report 42-23,* pp 5-9, Jet Propulsion Laboratory, Pasadena, Calif , Oct 15, 1974

2 Wilcher, J. H., "A New Sequential Decoder for the DSN Telemetry Subsystem," in *The Deep Space Network Progress Report 42-34,* pp 84-87, Jet Propulsion Laboratory, Pasadena, Calif , Aug 15, 1976

3 Alberda, M. E , "Implementation of a Maximum Likelihood Convolutional Decoder," in *The Deep Space Network Progress Report 42-37,* pp 176-183, Jet Propulsion Laboratory, Pasadena, Calif , Feb 15, 1967

4 Glenn, M S , "DSN Ground Communications Facility," in *The Deep Space Network Progress Report 42-36,* pp 4-12, Jet Propulsion Laboratory, Pasadena, Calif., Dec 15, 1972

5 Gatz, E C , "DSN Telemetry System Data Records," in *The Deep Space Network Progress Report 42-33,* pp 4-7, Jet Propulsion Laboratory, Pasadena, Calif., June 15, 1976

DSS — GCF — NOCC

WIDEBAND — NCCC AND REMOTE PROJECT INTERFACE

HIGH SPEED — NETWORK OPERATIONS CONTROL AREA DISPLAYS AND I/O

ANTENNA MICROWAVE SUBSYSTEM

ANTENNA MECHANICAL SUBSYSTEM

RECEIVER-EXCITER SUBSYSTEM
RECEIVER ASSEMBLIES
SUBCARRIER DEMODULATOR ASSEMBLIES

DSS TELEMETRY SUBSYSTEM
SYMBOL SYNCHRONIZER ASSEMBLIES
DECODER ASSEMBLIES
TELEMETRY PROCESSOR ASSEMBLY
HIGH-RATE ODR

GCF HIGH-SPEED DATA AND WIDEBAND SUBSYSTEMS
HIGH-RATE TELEMETRY DATA & PARTIAL STATUS
STATION WIDEBAND DATA ASSEMBLY
CENTRAL WIDEBAND DATA ASSEMBLY
COMM MONITOR & FORMATTER ASSEMBLY
STATION HIGH-SPEED DATA ASSEMBLIES
CENTRAL HIGH-SPEED DATA ASSEMBLY
NETWORK LOG PROCESSOR ASSEMBLY
ERROR DETECTION & CORRECTION ASSEMBLY
HIGH-SPEED SWITCH ASSEMBLY
ODR
NETWORK DATA LOG
DATA RECORD ASSEMBLY
TELEMETRY IDR

NETWORK DATA PROCESSING TERMINAL
NC DISPLAY SUBSYSTEM

NETWORK DATA PROCESSING AREA
NDPA COMM PROCESSOR
NC TELEMETRY SUBSYSTEM
NC SUPPORT SUBSYSTEM
SYSTEM PERFORMANCE RECORD

CONTROL FROM DSS MONITOR & CONTROL SUBSYSTEM

NOISE TEMP SIGNAL LEVEL & STATUS

LOW-RATE TELEMETRY DATA & PARTIAL STATUS

NONREAL-TIME PLAYBACK

PRE-POST DETECTION RECORDING SUBSYSTEM

DSS MONITOR & CONTROL SUBSYSTEM

FREQUENCY & TIMING SUBSYSTEM

STATUS   PREDICTS   TIMING

CONTROL & PARTIAL STATUS

PREDICTS

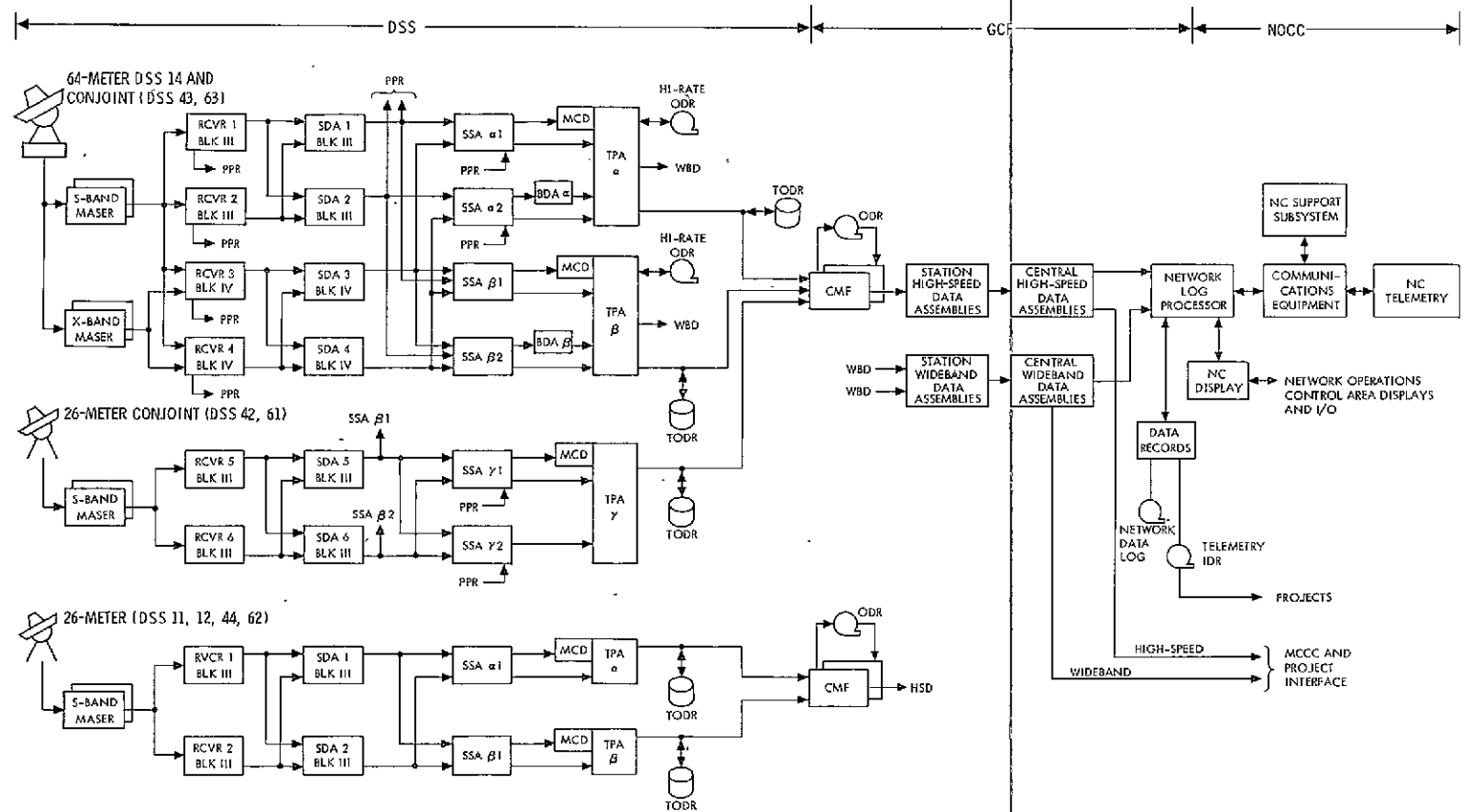Fig. 1   DSN Telemetry System, Mark III-77, functional block diagram

9

Fig. 2 DSN Telemetry System, Mark III-77 configuration

PRECEDING PAGE BLANK NOT FILMED

Voyager Flight Project — DSN Telecommunications Compatibility Test Program

A. I Bryan and R P Kemp

TDA Engineering

B D Madsen

Telecommunications Systems Section

The Voyager Flight Project — DSN Telecommunications Compatibility Test Program consisted of three phases Subsystem Design, System Design and System Verification Tests, which were performed at JPL and at the U.S Air Force Eastern Test Range and Kennedy Space Center Complexes Subsystem Design Tests were performed during mid 1976 System Design Tests were performed during late 1976 and early 1977 System Verification Tests were performed during the spring and summer of 1977 This article describes the System Design Tests and test results that provided the basis for establishment of telecommunications design between the DSN and the Voyager Flight Project

I. Introduction

This report summarizes the DSN—Voyager Flight Project Telecommunications Compatibility Test Program, covering the period from May 1976 through August 1977 This test program followed the standard three-phase plan of establishing telecommunications compatibility as specified in the DSN Standard Practice Document, Deep Space Network — Flight Project Interface Compatibility Test Design Handbook, and in the Mariner Jupiter/Saturn 1977 DSN-Spacecraft Compatibility Test Plan.

The plan specified that telecommunications design compatibility would be established at the subsystem and system levels and conclude with a final verification at Cape Canaveral, Florida. prior to launch In addition, the DSN and flight project equipment, software configurations, requirements and test objectives in all phases were specified

Procedures for conducting the tests as well as test design criteria and test parameters for the ground station hardware and software were prepared by Network personnel Spacecraft telecommunications design performance criteria and test parameters to establish flight project nominal and threshold telecommunications conditions were provided by the Voyager Telecommunications group. The test criteria were included as part of the test procedures to provide real-time assessment of performance All test procedures were jointly approved by the DSN and flight project representatives

II. Types of Tests

The test program included tests between two DSN stations (CTA 21 and MIL 71) and three Voyager Project spacecraft (VGR 77-1, VGR 77-2 and VGR 77-3). Tests between the DSN and VGR 77-1 (designated the Proof Test Model)

included only phases I and II of the total test program and were conducted only at CTA 21. Tests between the DSN and VGR 77-2 and VGR 77-3 (designated Flight Models) included phases II and III of the total test program and were conducted at both CTA 21 and MIL 71.

III. Objectives

The objectives of the test program were to demonstrate, in the major areas of radio frequency acquisition and tracking, command, telemetry and radio metric data (ranging), compatibility between the spacecraft telecommunications subsystems and the Network, to establish system design compatibility between the spacecraft and the Network, and to verify continued interface integrity and maintenance of compatibility during prelaunch activities

IV. DSN — Subsystem and System Compatibility Tests

The results of the DSN-Subsystem Compatibility Testing, Phase I, are documented in Ref 1, the results of the DSN-System Compatibility Testing, Phase II, are documented in Refs 2 and 3

V. DSN — System Verification Tests

The DSN—System Verification Tests, Phase III, began in May 1977 Results of the May 25 tests conducted on VGR 77-2 are documented in Ref. 3 The balance of the testing with VGR 77-2 was conducted on July 14 and 15, 1977 Tests with VGR 77-3 were conducted on June 14 and 22, July 29, and August 1, 1977.

A. Voyager 77-2, May 25, 1977

1. Test objectives The objective of this phase of testing was to verify telecommunications compatibility between the DSN and the Voyager 77-2 spacecraft for both S- and X-band operation. The test criteria and parameters simulated direct communications between a Voyager spacecraft and a Deep Space Station (DSS) for S-band operation only

Selected standard tests were performed for verifying telecommunications radio frequency, telemetry and radio metric (ranging) for the X-band mode of operation

2. Test conditions The Voyager spacecraft was located at the Spacecraft Assembly and Encapsulation Facility No 1,

Kennedy Space Center, Florida The Radio Frequency Subsystem was configured as follows:

S-band

Receiver 1, Channel 18 (2114.676697 MHz)

Receiver 2, Channel 18 (2114 676697 MHz)

Auxiliary oscillator, Channel 18 (2296.481481 MHz)

Exciter chain 1, equipped with a Watkins-Johnson flight-rated traveling wave tube (TWT) amplifier.

Exciter chain 2, equipped with a Ford Aerospace flight-rated solid-state amplifier.

X-band

Exciters chain 1 and chain 2, equipped with Watkins-Johnson flight-rated traveling wave tube (TWT) amplifiers.

The DSN, as represented by MIL 71, Kennedy Space Center, Florida, was configured to simulate a Voyager flight project-committed 64-meter antenna station. The ground hardware included both Block III and Block IV receiver-exciter subsystems and the Mark III data subsystems (MDS) for telemetry, command and radio metric data

The S- and X-band RF links between MIL 71 and SAEF-1 were open air links which had previously been calibrated for amplitude stability. The DSN software provided at MIL 71 was the operational 64-meter antenna station software for the MDS

3. Test results. Table I, DSN (MIL 71) — Voyager 77-2 (SAEF 1) Spacecraft Telecommunications Compatibility Test Summary, provides a listing of test configurations, test criteria, parameters and results. Refer to Figs 1 and 2 for DSN and spacecraft RFS mode configurations Significant test results and comments are discussed below

(1) Radio Frequency Acquisition and Tracking All objectives of these tests were met with no problems noted Testing consisted of threshold-testing the downlink for both one- and two-way X-band operation.

(2) Telemetry. These tests were supported using the 64-meter DSS operational telemetry software The telemetry rates of 115 2 kbps, 44.8 kbps, 7.2 kbps and 40 bps were tested during this series of tests and operation was satisfactory

(3) Radio Metric A special test was performed to ascertain ranging delay as a function of uplink frequency sweep Initial test conditions were as follows

Uplink signal level, −100 0 dBm.

Spacecraft receiver at best lock frequency (2114.676672 MHz)

Ranging acquisition performed for simultaneous S- and X-band operation.

A negative sweep ramp was initiated at 100.0 Hz/sec toward a limit of −60 0 kHz The DRVID values for S- and X-band were averaged over 30-second intervals and printed out on the MDA terminet typewriter During the course of the sweep ramp, the S-band DRVID printouts observed varied only two range units. The X-band DRVID printouts observed varied by three range units It is concluded from this test that no noticeable change in ranging delay can be determined as a function of uplink frequency offset.

B. Voyager 77-3, June 14 and 22, 1977

1 Test Objectives The objective of this phase of testing was to verify telecommunications compatibility between the DSN and the Voyager 77-3 spacecraft The test criteria and parameters simulated direct communications between a Voyager spacecraft and a Deep Space Station for S-band operation only X-band operation was not attempted because of the excess RF losses over the MIL 71 − Building AO link

2 Test Conditions The Voyager spacecraft was located at Building AO, Cape Canaveral Air Force Station, Florida The radio frequency subsystem was configured as follows

S-band

Receiver 1, Channel 14 (2113 312500 MHz)

Receiver 2, Channel 14 (2113 312500 MHz)

Ultrastable oscillator (USO), Channel 18 (2296 481481 MHz)

Exciter chain 1, equipped with a Watkins-Johnson flight-rated traveling wave tube amplifier

Exciter chain 2, equipped with a Ford Aerospace flight-rated solid-state amplifier

The DSN, as represented by MIL 71, Kennedy Space Center, Florida, was configured to simulate a Voyager flight

project-committed 64-meter antenna station The ground hardware included both Block III and Block IV receiver-exciter subsystems and the Mark III data subsystems (MDS) for telemetry, command and radio metric data.

The S-band RF links between MIL 71 and Building AO were open air links which had previously been calibrated for amplitude stability The DSN software provided at MIL 71 was the operational 64-meter antenna station software for the MDS

3. Test Results. During the compatibility test on June 14, while reconfiguring the spacecraft RFS from exciter chain 1 active to exciter chain 2 active, a failure occurred The solid-state amplifier (TWT 2) of exciter chain 2 was determined to be at fault and was sent to the manufacturer for resolution of the failure The problem was found to be a malfunctioning relay in the solid-state amplifier (SSA) The relay circuit was redesigned and repaired, and the SSA was reinstalled in the VGR 77-3 spacecraft to enable continuation of compatibility testing on June 22.

Table II, DSN (MIL 71) − Voyager 77-3 (Bldg AO) Spacecraft Telecommunications Compatibility Test Summary, provides a listing of test configurations, test criteria, parameters and results Refer to Figs. 1 and 2 for DSN and spacecraft RFS mode configurations Significant test results and comments are discussed below

(1) Radio Frequency Acquisition and Tracking All objectives of these tests were met with no problems noted Testing consisted of threshold testing the uplink and the downlink for both one-way and two-way operation.

(2) Telemetry These tests were supported using the 64-meter DSS telemetry software Telemetry rates of 80, 1200, 1280, and 7200 bps were tested and operation was satisfactory. In addition, the remaining open item of wide band data and original data recording with the 64-meter DSS software was successfully demonstrated during a MEIVT 14 test between CTA 21 and MCCC on June 29, 1977, for data rates up through 115 2 kbps using SCA-generated data

(3) Command. Command testing was performed at nominal uplink signal levels and at signal levels below expected project mission conditions Two separate, nontimed commands (2N X-band ranging channel ON and 2 NR X-band ranging channel OFF) were transmitted by MIL 71 and successfully executed by the spacecraft The software used for these tests was the operational version

C. Voyager 77-3, July 29 and August 1, 1977

1. **Test Objectives.** The objective of this phase of testing was to verify telecommunications compatibility between the DSN and the Voyager 77-3 spacecraft for both S- and X-band operation The test criteria and parameters simulated direct communications between a Voyager spacecraft and a Deep Space Station for both S- and X-band operation.

2. **Test Conditions.** The Voyager spacecraft was located at the Spacecraft Assembly and Encapsulation Facility No 2, Kennedy Space Center, Florida The Radio Frequency Subsystem was configured as follows

S-band

    Receiver 1, Channel 14 (2113.312512 MHz)

    Receiver 2, Channel 14 (2113 312512 MHz)

    Auxiliary oscillator, Channel 14 (2295 000000 MHz)

    Exciter chain 1, equipped with a Watkins-Johnson flight-rated traveling wave tube amplifier

    Exciter chain 2, equipped with a Ford Aerospace flight-rated solid-state amplifier

X-band

    Exciters chain 1 and chain 2, equipped with Watkins-Johnson flight-rated traveling wave tube amplifiers

The DSN, as represented by MIL 71, Kennedy Space Center, Florida, was configured to simulate a Voyager flight project-committed 64-meter antenna station. The ground hardware included both Block III and Block IV receiver-exciter subsystems and the Mark III data subsystems (MDS) for telemetry, command and radio metric data

The S- and X-band RF links between MIL 71 and SAEF 2 were open air links which had previously been calibrated for amplitude stability The DSN software provided at MIL 71 was the operational 64-meter antenna station software for the MDS

3 **Test Results.** Table III, DSN (MIL 71) — Voyager 77-3 (SAEF 2) Spacecraft Telecommunications Compatibility Test Summary, provides a listing of test configurations, test criteria, parameters and results Refer to Figs 1 and 2 for DSN and

spacecraft RFS mode configurations Significant test results and comments are discussed below

(1) Radio Frequency This set of tests consisted of threshold testing the X-band downlink in the one-way modes of operation for the two spacecraft exciter and power amplifier string configurations These tests were successfully completed and met the criteria specified. RF carrier residual phase jitter measurements were not completed during this phase of testing because of a hardware problem in the Block IV receiver. Preflight activities of the spacecraft did not permit enough time to correct the receiver problem without impacting the schedule However, based on other observations, e.g., downlink threshold measurements, both one-way and two-way, the residual carrier phase jitter appears to be well within specified tolerances as no degradation of the thresholds was observed

(2) Telemetry These tests were supported using the 64-meter DSS operational telemetry software Telemetry rates of 115 2 kbps, 44.8 kbps and 7.2 kbps were tested during this series of tests and operation was satisfactory.

(3) Radio Metric (Ranging) Ranging delay calibration measurements were performed with the spacecraft in three radio mode configurations. These tests were supported utilizing the operational ranging software All-results were well within specified limits

VI. Conclusions

The DSN—Voyager Project Telecommunications Compatibility Test Program was successfully completed on schedule and was culminated by the successful launches of Voyager 2 on August 20, 1977 and Voyager 1 on September 5, 1977

The importance of a formal compatibility test program is clearly demonstrated by the problems uncovered, verified and resolved during the DSN—Voyager testing Major problem areas discovered, tested, and resolved during the test program were

(1) The DSN must provide an uplink carrier power margin of 35 dB in the spacecraft transponder tracking loop in order to provide simultaneous X-band telemetry and doppler without degradation

(2) Uplink carrier suppression for command modulation of −0 5 dB was selected in order to assure acceptable operation of the Spacecraft Modulation—Demodulation Subsystem

(3) Uplink carrier suppression for ranging modulation of −3.0 dB was selected in order to assure acceptable operation of downlink X-band telemetry

(4) Verification of proper Block III SDA operation with 80 deg modulation index in order to optimize Voyager high-rate telemetry

(5) Verification that the DSN can support the simultaneous channel 14 and channel 18 downlink frequency support requirements of the mission

Had these problems remained undetected and unresolved prior to launch, serious operational problems to the Network with the spacecraft in flight would have resulted

References

1 Bryan, A 'I., and Madsen, B D , "DSN Mariner Jupiter-Saturn 1977 Prototype Radio Frequency Subsystem Compatibility Status and Test Report," *The Deep Space Network Progress Report 42-35*, pp 4-10, Jet Propulsion Laboratory, Pasadena, Calif, Oct. 15, 1976

2 Bryan, A I , et al , "Summary Report and Status of the Deep Space Network—Mariner Jupiter/Saturn 1977 Flight Project Telecommunications Compatibility," *The Deep Space Network Progress Report 42-38*, pp 16-37, Jet Propulsion Laboratory, Pasadena, Calif., Apr. 15, 1977

3 Bryan, A I , et al , "Summary Report and Status of the Deep Space Network—Voyager Flight Project Telecommunications Compatibility," *The Deep Space Network Progress Report 42-40*, pp 21-40, Jet Propulsion Laboratory, Pasadena, Calif, Aug 15, 1977

Table 1. DSN(MIL 71) — Voyager 77-2 (SAEF 1) Spacecraft Telecommunications Compatibility Test Summary

Test date	Test title	Test no	DSN mode	S/C RFS mode	Test conditions	Criteria	Performance	Time, min
7/15/77	DL Threshold One Way	RF-1-2	000500	5403-10	X-band DL frequency 8420 454145 MHz 30 Hz 2 BLo	−145 0 ±1 0 dBm	−144.7 dBm	15
7/14/77	DL Threshold One Way	RF-1-3	000500	6730-16 (Spacecraft Two-Way with SE)	X-band DL frequency 8420 426350 MHz 30 Hz 2 BLo	−145 0 ±1 0 dBm	−145 0 dBm	38
7/15/77	DL Threshold Two Way	RF-1-4	002500	5413-10	X-band DL frequency 8420 432470 MHz 30 Hz 2 BLo	−145 0 ±1 0 dBm	−144 5 dBm	14
7/14/77	DL Threshold Two Way	RF-1-5	002500	6730-16	X-band DL frequency 8420 432215 MHz 30 Hz 2 BLo	−145 0 ±1 0 dBm	−144 3 dBm	23
7/16/77	Transmitter Phase Jitter	RF-5-1	$000\frac{3}{4}00$	5403-10	S-band DL frequency 2296 483140 MHz (one-way)	≤3 0 deg rms	1 18 deg rms	65
			$000\frac{5}{6}00$		X-band DL frequency 8420 453380 MHz (one-way)	≤11 0 deg rms	4 87 deg rms	
					S-band UL frequency 2114 676672 MHz			
			$002\frac{3}{4}00$	5413-10	S-band DL frequency 2296.481440 MHz (two-way)	≤2 3 deg rms	1 74 deg rms	
			$002\frac{5}{6}00$		X-band DL frequency 8420 432215 MHz (two-way)	≤8 4 deg rms	4 97 deg rms	
7/15/77	Transmitter Phase Jitter	RF-5-4	$000\frac{3}{4}00$	7624-16	S-band DL frequency. (one-way) 2296 479488 MHz	≤3 0 deg rms	2 03 deg rms	107
			$000\frac{5}{6}00$		X-band DL frequency (one-way) 8420 424990 MHz	≤11 0 deg rms	6 30 deg rms	
			$002\frac{3}{4}00$	7634-16	S-band UL frequency 2114.676672 MHz			
					S-band DL frequency (two-way) 2296 481408 MHz	≤2 3 deg rms	2 07 deg rms	
			$002\frac{5}{6}00$		X-band DL frequency (two-way) 8420 432215 MHz	≤8 4 deg rms	6.00 deg rms	

Table 1 (contd)

Test date	Test title	Test no	DSN mode	S/C RFS mode	Test conditions	Criteria	Performance	Time, min
7/14/77	Telemetry Performance Verification Test	TM-2-1	002511	7634-16	X-band DL signal level −116 0 dBm	Ability to process	MCD SNR 6.33 dB	35
					TLM bit rate 115 2 kpbs coded		SSA 1 SNR 3 75 dB	
					STb/No = 8 0 dB			
					Subcarrier frequency 360 kHz			
					S-band DL signal level −150 0 dBm		SSA 2 SNR 6.15 dB	
					TLM bit rate 40 bps UNC			
					STb/No = 5.0 dB			
					Subcarrier frequency 22 5 kHz			
7/14/77	Telemetry Performance Verification Test	TM-2-4	002511	7634-16	X-band DL signal level −120 5 dBm	Ability to process	MCD SNR 8 39 dB	16
					TLM bit rate 44 8 kbps coded		SSA SNR 5 25 dB	
					STb/No = 8 0 dB			
					Subcarrier frequency 360 0 kHz			
7/14/77	Telemetry Performance Verification Test	TM-2-6	002511	7634-16	X-band DL signal level −128 5 dBm	Ability to process	MCD SNR 8 74 dB	10
					TLM bit rate 7 2 kbps coded		SSA SNR 5 53 dB	
					STb/No = 8 0 dB			
					Subcarrier frequency 360 0 kHz			
7/15/77	Range Delay Calibration Verification Test	RM-2-A	$102\frac{5}{4}00$	5413-10	S-band UL frequency 2114 676672 MHz	≤1000 ns		14
					S-band DL frequency 2296 481580 MHz			
					S-band DL signal level −100 0 dBm			
					X-band DL frequency 8420 432130 MHz			
					X-band DL signal level −100 0 dBm			

Table 1 (contd)

Test date	Test title	Test no	DSN mode	S/C RFS mode	Test conditions	Criteria	Performance	Time, min
7/15/77	Range Delay Calibration Verification Test (contd)				Spacecraft VCO temp 37 82°C			
					UL signal level −100 0 dBm		S delay: 690 13 ns	
							X delay 617 09 ns	
7/15/77	Range Delay Calibration Verification Test	RM-2-B	$102\frac{5}{4}00$	7413-12	S-band UL frequency 2114 676672 MHz	<1000 ns		
					S-band DL frequency 2296 481440 MHz			
					S-band DL signal level: −100 0 dBm			
					X-band DL frequency 8420 432045 MHz			
					X-band DL signal level −100 0 dBm			
					Spacecraft VCO Temp 27 82°C			
					UL signal level −100 0 dBm		S delay 694 39 ns	
							X delay 619 08 ns	
7/15/77	Range Delay Calibration Verification Test	RF-2-C	$102\frac{5}{4}00$	7633-16	S-band UL frequency 2114 676672 MHz	<1000 ns		
					S-band DL frequency 2296 481440 MHz			
					S-band DL signal level −100 0 dBm			
					X-band DL frequency 8420 432045 MHz			
					X-band DL signal level −100 0 dBm			
					Spacecraft VCO Temp 27 82°C			
					UL signal level −100 0 dBm		S delay 691 3 ns	
							X delay 630 9 ns	

Table 1 (contd)

Test date	Test title	Test no	DSN mode	S/C RFS mode	Test conditions	Criteria	Performance	Time, min
7/15/77	Range Delay Calibration Versus Static Phase Error Test	RM-3-1	$102\frac{5}{4}00$	5413-10	S-band UL signal level −100 0 dBm S-band DL signal level −100 0 dBm X-band DL signal level −100 0 dBm	Observe change in range delay as a function of UL frequency ramp from 0 Hz offset to −60 0 kHz offset	S-band DRVID changed 2 RU X-band DRVID changed 3 RU	21

Table 2   DSN(MIL 71) — Voyager 77-3 (Bldg. AO) Spacecraft Telecommunications Compatibility Test Summary

Test date	Test title	Test no	DSN mode	S/C RFS mode	Test conditions	Criteria	Performance	Time, min
6/14/77	DL Threshold One Way	RF-1-2	000300	4500-14	S-band DL frequency 2296 481100 MHz 10 Hz 2 BLo	−158 0 ±1 0 dBm	−157 2 dBm	15
6/22/77	DL Threshold One Way .	RF-1-3	000300	7722-16	S-band DL frequency 2296 481080 MHz 10 Hz 2 BLo	−158.0 ±1 0 dBm	−158 3 dBm	18
6/14/77	DL Threshold Two Way	RF-1-4	002300	4510-16	S-band DL frequency 2295.000040 MHz 10 Hz 2 BLo	−158 0 ±1 0 dBm	−157 2 dBm	13
6/22/77	DL Threshold Two Way	RF-1-5	002300	6772-16	S-band DL frequency 2295 000004 MHz 10 Hz 2 BLo	−158 0 ±1 0 dBm	−159 0 dBm	14
6/14/77	UL Receiver Threshold	RF-2-1	002300	4510-16	S-band UL frequency 2113 312512 MHz	≤−152 0 dBm	−154 5 dBm	17
6/22/77	UL Receiver Threshold	RF-2-2	002300	6732-16	S-band UL frequency 2113 312512 MHz	≤−152 0 dBm	−155 5 dBm	9
6/14/77	UL Receiver Threshold	RF-2-3	002300	4550-16	S-band UL frequency 2113 312512 MHz	≤−152 0 dBm	−154 7 dBm	17
6/23/77	UL Receiver Threshold	RF-2-4	002300	6772-17	S-band UL frequency 2113 312512 MHz	≤−152 0 dBm	−155 2 dBm	12
6/14/77	Command Processing	CM-1-1	112300	4550-16	S-band frequency 2113 312512 MHz UL carrier suppression −5 0 dB Subcarrier offset 0 0 Hz @ −144 dBm, P_T +0 2 Hz @ −144 dBm, P_T −0 2 Hz @ −144 dBm, P_T	Proper subcarrier and bit sync' acquisition	OK OK OK	23

Table 2 (contd)

Test date	Test title	Test no	DSN mode	S/C RFS mode	Test conditions	Criteria	Performance	Time, min
6/22/77	Command Processing	CM-1-2	112300	6772-16	S-band UL frequency 2113 312512 MHz	Proper subcarrier and bit sync acquisition		42
					UL carrier suppression −5 0 dB	Verification of command execution		
					Subcarrier offset			
					0 0 Hz @−144 dBm, P_T		OK	
					+0 2 Hz @−144 dBm, P_T		OK	
					−0 2 Hz @−144 dBm, P_T		OK	
6/22/77	Telemetry Spectrum Analysis and Modulation Index	TM-1-4	002311	6732-16	S-band UL frequency. 2113 312512 MHz	No unexpected radiation components within 40 dB of carrier	None observed	6
					S-band DL frequency 2295 000004 MHz			
					TLM bit rate 7 2 kbps			
					Subcarrier frequency 360 kHz			
6/22/77	Telemetry Spectrum Analysis and Modulation Index	TM-1-10	002311	6732-16	S-band UL frequency 2113 312512 MHz	No unexpected radiation components within 40 dB of carrier	None observed	9
					S-band DL frequency 2295 000004			
					TLM bit rate 1200 bps			
					Subcarrier frequency 22 5 kHz			
6/22/77	Telemetry Performance Verification Test	TM-2-10	002311	6732-16	S-band DL signal level −141 0 dBm	Ability to process	MCD SNR 3 726 dB	8
					TLM bit rate 1200 bps coded		SSA SNR 1 36 dB	
					STb/No = 5 0 dB			
					Subcarrier frequency 22 5 kHz			
6/22/77	Telemetry Performance Verification Test	TM-2-13	002311	6732-16	S-band DL signal level −131 0 dBm	Ability to process	MCD SNR 9 947 dB Run 1 9 288 dB Run 2	50
					TLM bit rate 7 2 kbps coded		SSA SNR 6 3 dB Run 1 5 35 dB Run 2	
					STb/No = 8 0 dB			
					Subcarrier frequency 360 kHz Run 2 22 5 kHz Run 1			

Table 2 (contd)

Test date	Test title	Test no	DSN mode	S/C RFS mode	Test conditions	Criteria	Performance	Time, min
6/22/77	Telemetry Performance Verification Test	TM-2-14	002311	7732-16	S-band DL signal level −141 0 dBm	Ability to process	MCD SNR 3 633 dB	16
					TLM bit rate 1280 bps coded		SSA SNR 1.488 dB	
					STb/No = 5 0 dB			
					Subcarrier frequency 22 5 kHz			
6/22/77	Telemetry Performance Verification Test	TM-2-15	002311	7732-16	S-band DL signal level −146 3 dBm	Ability to process	MCD SNR 3 610 dB	25
					TLM bit rate 80 bps coded		SSA SNR 1.235 dB	
					STb/No = 6 0 dB			
					Subcarrier frequency 22 5 kHz			
7/29/77	DL Threshold One Way	RF-1-2	000500	4400-11	X-band DL frequency 8415 000375 MHz 30 Hz 2 BLo	−145 0 ±1 0 dBm	−144 7 dBm	14
7/29/77	DL Threshold One Way	RF-1-3	000500	6623-16	X-band DL frequency 8414.998250 MHz 30 Hz 2 BLo	−145 0 ±1 0 dBm	−146 3 dBm	12
7/29/77	DL Threshold Two Way	RF-1-4	002500	4410-11	X-band DL frequency 8415 000290 MHz 30 Hz 2 BLo	−145 0 ±1 0 dBm	−145 0 dBm	10
7/30/77	DL Threshold Two Way	RF-1-5	002500	6633-16	X-band DL frequency 8415 000205 MHz 30 Hz 2 BLo	−145 0 ±1 0 dBm	−147 0 dBm	10
8/1/77	Telemetry Performance Verification Test	TM-2-1	002511	6670-17	X-band DL signal level −116 0 dBm	Ability to process	MCD SNR 9 391 dB	19
					TLM bit rate 115 2 kbps coded		SSA 1 SNR· 5.0 dB	
					STb/No = 8 0 dB			
					Subcarrier frequency. 360 kHz			

Table 3. DSN(MIL 71) — Voyager 77-3 (SAEF 2) Spacecraft Telecommunications Compatibility Test Summary

Test date	Test title	Test no	DSN mode	S/C RFS mode	Test conditions	Criteria	Performance	Time, min
8/1/77	Telemetry Performance Verification Test	TM-2-4	002511	6670-17	X-band DL signal level −120 5 dBm	Ability to process	MCD SNR 8 702 dB	30
					TLM bit rate 44 8 kbps coded		SSA SNR 5 1 dB	
					STb/No = 8 0 dB Subcarrier frequency 360 kHz			
8/1/77	Telemetry Performance Verification Test	TM-2-6	002511	6670-17	X-band DL signal level −128 5 dBm	Ability to process	MCD SNR· 9.356 dB	25
					TLM bit rate 7.2 kbps coded		SSA SNR 5 79 dB	
					STb/No = 8 0 dB			
					Subcarrier frequency 360 0 kHz			
7/30/77	Range Delay Calibration Verification Test	RM-2-A	$102\frac{5}{4}00$	4413-11	S-band UL frequency 2113 312512 MHz	⩽1000 ns		45
					S-band DL frequency 2295 000040 MHz			
					S-band DL signal level −100 0 dBm			
					X-band DL frequency 8415.000290 MHz			
					X-band DL signal level −100 0 dBm			
					Spacecraft VCO Temp 27 66°C			
					UL signal level −100 0 dBm		S delay 645 2 ns	
							X delay 632 2 ns	
7/30/77	Range Delay Calibration Verification Test	RM-2-B	$102\frac{5}{4}00$	6413-11	S-band UL frequency 2113 312512 MHz	⩽1000 ns		
					S-band DL frequency 2295 000040 MHz			
					S-band DL signal level −100 0 dBm			

Table 3 (contd)

Test date	Test title	Test no	DSN mode	S/C RFS mode	Test conditions	Criteria	Performance	Time, min
7/30/77	Range Delay Calibration Verification Test (contd)				X-band DL frequency 8415 000290 MHz			
					X-band DL signal level −100 0 dBm			
					Spacecraft VCO Temp 27 66°C			20
					UL signal level' −100 0 dBm		S delay 645.2 ns	
							X delay 638 2 ns	
7/30/77	Range Delay Calibration Verification Test	RM-2-C	$102\frac{5}{4}00$	6633-16	S-band UL frequency 2113 312512 MHz	⩽1000 ns		
					S-band DL frequency 2295 000040 MHz			
				———	S-band DL signal level −100 0 dBm			
					X-band DL frequency 8415 000290 MHz			
					X-band DL signal level −100 0 dBm			
					Spacecraft VCO Temp 26 4°C			
					UL signal level −100 0 dBm		S delay 632 2 ns	18
							X delay 615 5 ns	

Table 4 Definition of terms for Tables 1, 2, and 3

|	
BER	bit error rate
Bit rate	clock frequency of the telemetry bit information*
bps	bits per second
CPA	Command Processor Assembly
CMF	Communications Monitor and Formatting Assembly
CTA 21	The Deep Space Network Ground Station Compatibility Test Area at JPL
dB	decibel
dBm	decibel referenced to one milliwatt
DL	RF downlink signal
DSN mode	The Deep Space Network Ground Station operational configuration
FDS	Spacecraft Flight Data Subsystem
MCD	Maximum Likelihood Convolutional Decoder
MDA	Metric Data Assembly
MDS	Spacecraft Modulation/Demodulation Subsystem
MDS	The DSN-MARK III Data Subsystems Implementation Project
No	Noise spectral density
P_c	power in RF carrier
P_T	power total
PRA	Planetary Ranging Assembly
PFR	Problem/Failure Report
RDA	Ranging Demodulator Assembly
RF	radio frequency
RFS	Spacecraft Radio Frequency Subsystem
RU	range unit
SAF	Spacecraft Assembly Facility (JPL Building 179)
S/C RFS Mode	The Spacecraft Radio Frequency Subsystem operational configuration
SCA	Simulation Conversion Assembly
SDA	Subcarrier Demodulator Assembly
SE	Spacecraft Ground Support Equipment
SER	symbol error rate
SNR	signal-to-noise ratio
SPS	symbols per second
SSA	Symbol Synchronizer Assembly
SSF	Space Simulator Facility (JPL Building 150)
STb/No	signal-to-noise spectral density ratio
SYMBOL RATE	clock frequency of the telemetry symbol information
TBD	to be determined
TBS	to be supplied
TDL	Telemetry Development Laboratory
TLM	telemetry
TPA	Telemetry Processor Assembly
TWT	travelling wave tube amplifier
UL	RF uplink signal
Uplink Doppler	ramp rate of uplink RF carrier frequency
Uplink Offset	uplink RF carrier frequency displacement relative to the spacecraft receiver rest frequency
USO	ultrastable oscillator
VCO	voltage-controlled oscillator

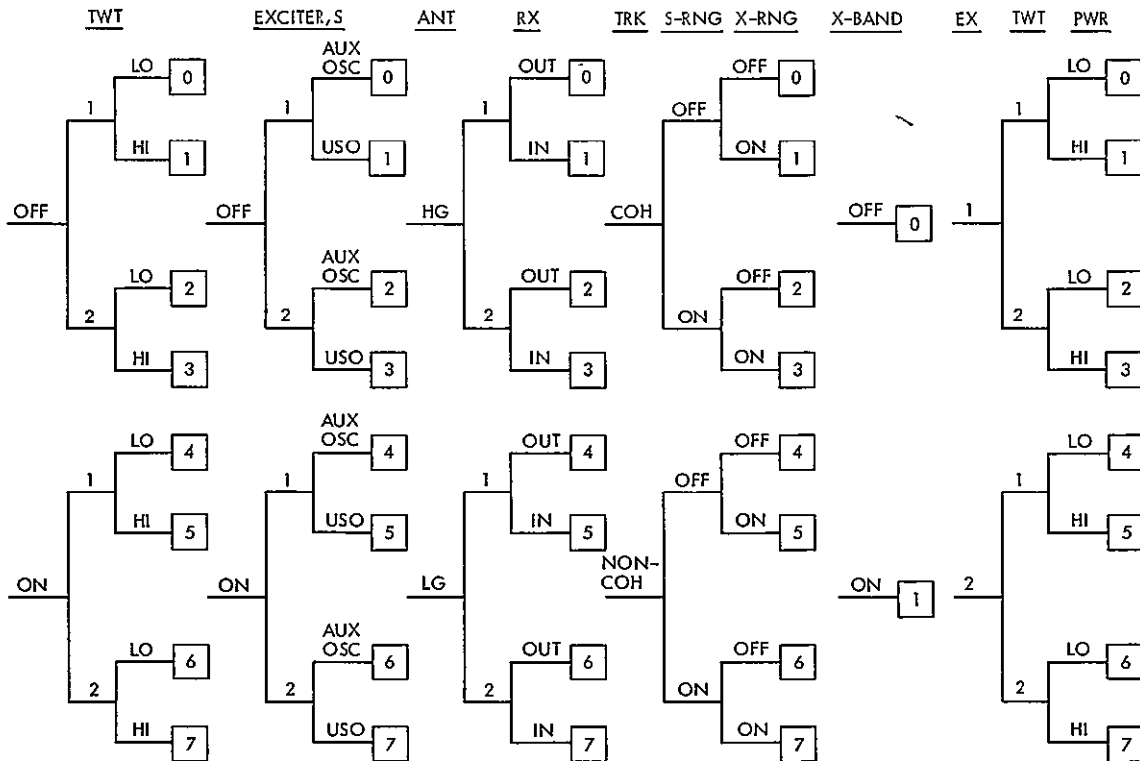**Fig 1. DSN modes**

0 = OFF
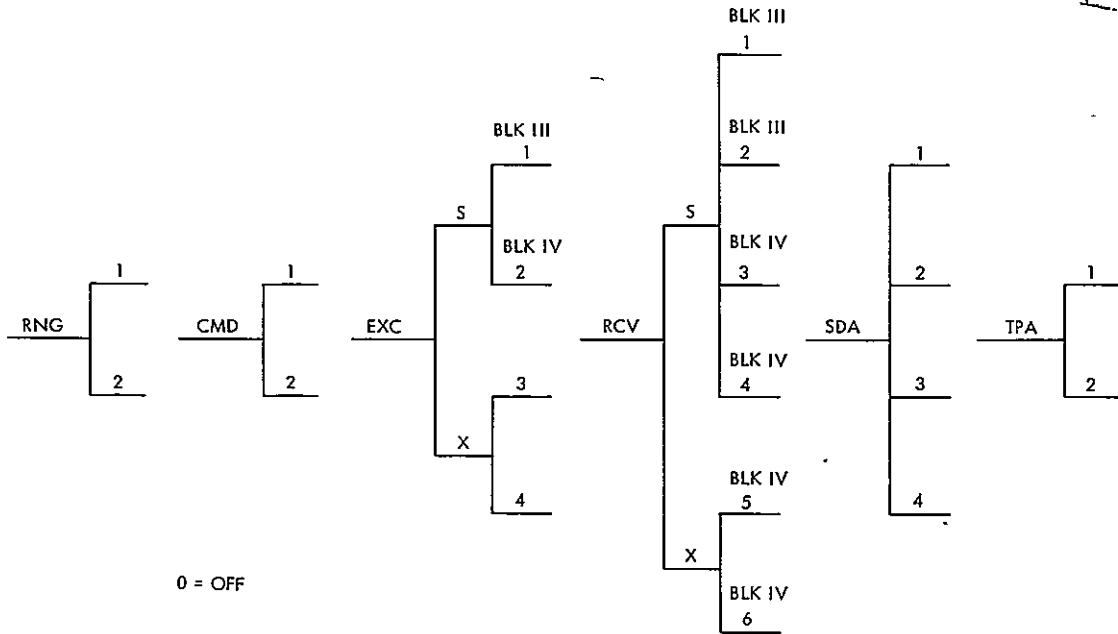
Fig. 2. Voyager operational RFS modes

P4

N78-24165

Viking Extended Mission Support

T W Howe
Deep Space Network Operations

This report covers the period from 1 July through 31 August 1977 and includes the remainder of post DSN Mark III Data Subsystem Implementation Project Viking-related testing at DSS 14 It also includes reports on the Viking DSN Discrepancy Reporting System, Viking command support, tracking support, and periodic tests conducted with the Viking spacecraft

I. Viking Operations

A. Status

As of 21 August 1977, all four Viking spacecraft continued to perform as planned. The Orbiters' X-band transmitter and relay subsystems were on continuously, with relays being performed routinely All Orbiter subsystems continued to perform well, and no performance trends could be established during this reporting period

Lander 1's sampler scoop successfully rolled a Mars rock, and a subrock soil sample was taken The scoop was also used to scratch a rock in an attempt to obtain rock chips for chemical analysis The temperatures at the Lander 2 location started an upward trend, accompanied by lower pressures Lander 2 continues in a dormant state, with no direct links taking place

The first dual-subcarrier high-rate data for 26-meter stations were processed by DSS 11 on August 16 Due to some confusion regarding the 2 kb/s receive capability and the lack of one Symbol Synchronizer Assembly at the station, three

and a half hours of data were lost Following the turnaround from VO-2 to VO-1, commands were sent to replay the recorded data One third of the original data were recovered

B. Maneuvers

(1) There were no scheduled Mars Orbit Trim (MOT) maneuvers during this reporting period The last Viking Orbiter 1 maneuver (MOT-16) took place on 1 July 1977 and changed the orbit period to 24 hours, so that earth occultations occurred during the DSS 14/DSS 43 overlap period The last Viking Orbiter 2 trim maneuver (MOT-10) took place on 18 April 1977

(2) Nonpropulsive maneuvers continued at a rate of two or three per week per Orbiter during the reporting period The maneuvers make it possible to take orbital science data At the present time the 26-meter subnets are unable to obtain telemetry during these maneuvers since the received signal level is about −170 dBm on the low-gain antenna (LGA) By the end of November 1977, the LGA link should improve by 5 dB and make it possible for the 26-meter stations to receive roll-only telemetry

C. Radio Science

Radio science experimentation continued during July and August Earth occultations by Viking Orbiter 1 were supported by DSS 14 and 43 Some difficulties in obtaining post-occultation downlink lock were experienced due to the close proximity of occultation and periapsis

D. Spacecraft Tests

(1) VO-1 High-Gain Antenna Calibration This test was conducted on 15 July 1977 during the DSS 43 view period, using X-band CONSCAN for more accurate DSS antenna pointing During the test it was noted that the signal level had changed by 1 5 dB even though the start and end pointing angles were supposedly equal This same phenomenon occurred during a previous Orbiter 2 high-gain antenna (HGA) calibration over DSS 43

(2) CDU "SNORE" Tests. Routine Command Detector Unit (CDU) signal-to-noise ratio estimator (SNORE) tests were accomplished using DSS 61 on 4 and 25 August (VO-1) and 5 and 23 August (VO-2).

(3) Viking Orbiter 1 Threshold Test. This test was conducted on 3 August 1977 to check on VO-1 uplink signal level residuals and CDU "SNORE" degradations observed previously. It was supported by DSSs 12 and 14, with DSS 12 providing the uplink and DSS 14 providing the downlink.

During the first test, the Planetary Ranging Assembly (PRA) was used to suppress the uplink carrier in 1-dB steps The spacecraft Command Detector Unit was observed to go out of lock at an uplink signal level of -150.8 dBm, which was the same out-of-lock level seen during the previous test

The Radio Frequency Subsystem dropped lock at $-152\ 8$ dBm, which was within 1 dB of the previous test.

The second test again used the PRA range modulation to suppress the uplink carrier, but a step attenuator was placed in the line between the output of the PRA and the input to the exciter This step attenuator was then used to change the modulation in 1-dB steps. Due to the fact that the step attenuator had not been calibrated, the results of this run are questionable

These tests indicated that there has been little, if any, shift in the threshold of the CDU or RFS during the flight of VO-1.

II. Network Support

Table 1 lists the Viking Extended Mission (VEM) tracking support for 1977 through this reporting period It should be noted that in spite of the fact that stations have been removed from tracking support for the DSN Mark III Data Subsystem (MDS) Implementation Project reconfiguration, the total number of tracking passes and hours has remained constant during 1977.

Table 2 identifies the total number of commands transmitted by the DSN for the Viking Project during 1977. August was a record month for command activity during 1977, with DSS 61 sending more than half the total

Table 3 gives the DSN VEM Discrepancy Report status for 1977

III. Mark III Data Subsystem Testing and Status

As indicated in the last report of this series, the MDS implementation had been completed at DSSs 12, 14, 44, and 62 DSSs 12, 44, and 62 were fully trained and tested, while the testing at DSS 14 was just getting underway

A. DSS 14 Test Status

(1) Ground Data System Tests — July 1977. Ground Data System (GDS) tests are tests designed to test the end-to-end configuration of the Deep Space Network and Mission Control Center systems This test was unsuccessful. The test began one hour and twenty minutes late due to various problems The test was delayed again at the one hour and nine minute mark due to a command problem in the Mission Control Center The remainder of the time was spent in unsuccessful attempts to lock on lander block coded data at 1 kb/s data rate

A GDS retest was conducted on July 12 and was considered to be a success, although it got off to a slow start because of problems establishing and validating the Mission Control Center to DSN long loop simulation interface All items of the test sequence of events were completed, with the exception of the temporary ODR demonstration, and the non-real-time data replay of the test

(2) Operations Verification Tests (OVTs) — July 1977 This was the third and last OVT for DSS 14 OVTs serve the dual purpose of providing operational training

for Network personnel and demonstrating the operational proficiency of Network personnel in the use of operational procedures, interfaces, and equipment. The test was successful even though not all sequence items were completed Not enough time remained to exercise the conversion of analog recorded data to digital form, or the data replay and recall capabilities.

(3) Demonstration Passes. Demonstration passes are conducted during the first month following completion of the MDS Reconfiguration Demonstration passes permit the stations to provide support to flight projects without having completed the full test and training plan.

The first demonstration pass for DSS 14 was conducted on July 8 and was successful. A second demonstration pass on July 9 had several problems but was considered successful Further demonstration passes were conducted on July 15, 27, and August 3 and 5 Following the last demonstration pass, DSS 14 was placed under Viking configuration control.

B. DSS 42/43 MDS Implementation Status

DSSs 42/43 were released from tracking support on 15 July 1977 and began their two and a half months of implementation and system performance testing The two months of test and training are scheduled to begin on 1 October 1977.

Table 1. VEM tracking support 1977

DSS	Jan	Feb	Mar	Apr.	May	Jun.	Jul.	Aug	Sept	Oct.	Nov	Dec
	Tracks / Hrs											
11	23 / 135	22 / 142	10 / 100	17 / 118	38 / 228	40 / 289	44 / 322	42 / 343				
12	4 / 11	1 / 6	—	24 / 176	17 / 119	1 / 4	1 / 1	1 / 7				
14	52 / 341	59 / 392	50 / 368	20 / 176	—	—	10 / 46	16 / 126				
42	21 / 247	25 / 226	58 / 453	17 / 138	17 / 162	14 / 112	10 / 69	—				
43	68 / 721	62 / 627	—	63 / 603	60 / 521	57 / 486	31 / 238	—				
44	—	—	7 / 7	1 / 4	—	—	16 / 99	26 / 166				
61	35 / 261	29 / 227	12 / 72	40 / 317	54 / 461	51 / 475	37 / 337	35 / 322				
62	—	2 / 7	4 / 22	9 / 55	3 / 14	2 / 7	—	—				
63	38 / 327	28 / 202	66 / 525	15 / 78	23 / 186	15 / 136	40 / 399	64 / 590				
Total	241 / 2043	228 / 1830	207 / 1547	206 / 1665	212 / 1691	180 / 1509	189 / 1511	184 / 1554				

Note   Number of tracks represent the summation of all Viking spacecraft tracked   Track time, in hours, represents scheduled station support

Table 2. Number of commands transmitted in Viking Extended Mission during 1977

DSS	Jan	Feb.	Mar	Apr	May	Jun.	Jul	Aug	Sept	Oct.	Nov	Dec
11	1521	1394	1027	117	811	0	1	795				
12	0	0	0	1314	721	0	0	0				
14	769	1404	1206	274			74	108				
42	2072	953	1778	8	1886	1619						
43	919	2523	0	2094	1447	972	1190					
44	0	0	2	1				5				
61	605	1116	1328	1925	1922	3838	4257	5589				
62	0	0	1	1991		496						
63	795	472	2039	381	675	383	2579	2318				
Total	6681	7862	7381	6180	7465	7308	8101	8815				

Table 3 DSN VEM Discrepancy Reports

DSS	Jan 0^a / C^b	Feb	Mar.	Apr	May	Jun.	Jul	Aug	Sept	Oct	Nov	Dec
11	4 / 0	3 / 4	4 / 6	1 / 3	2 / 3	2 / 6	2 / 7	1 / 7				
12	4 / 0	0 / 0	0 / 0	5 / 2	7 / 5	0 / 7	0 / 0	0 / 0				
14	14 / 2	11 / 19	4 / 33	3 / 9	2 / 2	0 / 2	6 / 2	4 / 18				
42	0 / 1	2 / 3	0 / 7	0 / 2	0 / 0	0 / 0	0 / 0	0 / 0				
43	10 / 13	11 / 10	0 / 12	9 / 11	8 / 17	2 / 14	1 / 6	0 / 1				
44	0 / 0	0 / 0	0 / 2	0 / 1	0 / 0	0 / 0	1 / 0	1 / 4				
61	1 / 9	1 / 6	0 / 3	0 / 1	1 / 2	0 / 6	1 / 4	0 / 7				
62	0 / 0	0 / 8	1 / 2	2 / 1	0 / 2	0 / 1	0 / 0	0 / 0				
63	1 / 4	7 / 3	1 / 18	0 / 6	4 / 4	3 / 12	4 / 4	9 / 17				
Others^c	4 / 3	3 / 9	2 / 10	4 / 7	7 / 12	10 / 13	8 / 16	5 / 9				
Total	38 / 32	38 / 62	12 / 93	24 / 43	31 / 47	17 / 61	23 / 39	20 / 63				

^{a} Number remaining open at end of month

^{b} Number closed during month

^{c} DSN, NDPA, NOCA, GCF

33

N78-24166

Helios Mission Support

P S. Goodwin
TDA Mission Support

G. M Rockwell
Deep Space Network Operations

This article reports on activities of the Network Operations organization in support of the Helios Project from 15 August 1977 through 15 October 1977

I. Introduction

This article is the eighteenth in a continuing series of reports that discuss Deep Space Network support of Helios Mission Operations Included in this article is information on the Mark III Data Subsystem (MDS) update at the conjoint Deep Space Station 42/43 complex (Canberra, Australia), an update on Radio Science Activities (Ref 1), and other mission-oriented activities

II. Mission Operations and Status

The Helios-1 spacecraft continued in a normal manner during this period, while it reached a major milestone of its journey On September 4, 1977, the Helios-1 spacecraft entered its 1000th day — exceeding its guaranteed 18-month life by more than a year Helios-1 is now in its sixth orbit around the Sun and still going strong despite numerous anomalies At present the spacecraft is nearing its sixth perihelion, which will occur on October 21, 1977 The perihelion phase will run from October 9, 1977, through November 2, 1977 This period of high scientific interest will be covered in the next article of this series

Helios-2 has also continued in a normal manner during this period with no major occurrences As in the case of Helios-1, Helios-2 is also nearing a perihelion phase. This period will run from October 14, 1977, through November 7, 1977, with its fourth perihelion occurring on October 26, 1977 On October 4, 1977, from 2220 GMT until 0030 GMT, DSS-14 (Goldstone, California) was unable to acquire sync on the data from Helios-2. At a Sun-Earth-probe (SEP) angle of 0 89 degrees, the spacecraft entered the blackout region The spacecraft was put in its read-in mode· DATA MODE 4, format 3, and 8 bits per second (b/s) coded While in this configuration, the spacecraft will store data without any further commanding until October 12, 1977, and then will change to real-time transmission The next tracking pass is scheduled for October 8, 1977, over DSS 63 (Spain) from 0930 GMT to 1300 GMT at an SEP angle of 1 0 degree Good solid data lock is again expected at an SEP angle of 3 5 degrees, which will occur on October 12, 1977

The relationship between the SEP angles of both Helios spacecraft is shown in Fig 1 This figure shows clearly the close alignment of the two spacecraft during this period

Overall coverage of both Helios-1 and Helios-2 is listed in Table 1

III. Special Activities

A. DSN Mark III Data Subsystem (MDS) Support of Helios

As reported in the last article (Ref. 1), the conjoint complex DSS 42/43 (Canberra, Australia) was taken down for MDS implementation on July 15, 1977 The complex was brought up on September 26, 1977, to begin its MDS test and training phase The first Helios demonstration track was on October 2, 1977, and was very successful. Other demonstration tracks are scheduled during this period and will be reported in the next article of this series The Helios configuration for DSS 42/43 is shown in Fig 2. This will be the same for DSS 61/63 (Spain), which begins MDS implementation on October 16, 1977

B. Support of On-Board and Ground Experiments

As indicated before (Ref. 1), this perihelion period is of extreme interest to the science experimenters. The activities occurring during this period of October to December 1977 are shown in Fig 3 Of these, the unique periods are the radial and spiral lineups and the Special Traveling Interplanetary Phenomena (STIP) period IV. The latter involves alignment of Helios-2 (1/4 AU in front of Earth). Voyagers 1 and 2 (1/2 AU behind Earth — down the tail), and Pioneer 9 (in front of Earth) Also, certain Earth satellites will be involved, such as ISEE-A and -B, GEOS, and IMPs H and J, and will be acquiring data along with the IMS Magnetometer Network and the European Ground Arrays This presents a unique opportunity for interplanetary and terrestrial magnetospheric measurements Hopefully, results of the above-planned activities will be available for the next article.

Data collection for Experiment 12 (Faraday Rotation) and the Solar Wind Experiment is also underway during this perihelion period. For Experiment 12, polarimetry and Meteorological Monitor Assembly (MMA) data collection is involved as it was earlier this year during Helios-2 superior conjunction (Ref. 2) The results of these experiments will be covered in the next article of this series.

References

1 Goodwin, P S., Burke, E S., Rockwell, G M., "Helios Mission Support," in *The Deep Space Network Progress Report 42-41*, pp 39–42, Jet Propulsion Laboratory, Pasadena, California, August 15, 1977.

2 Goodwin, P S , Burke, E.S , Rockwell, G M , "Helios Mission Support," in *The Deep Space Network Progress Report 42-40*, pp 52–56, Jet Propulsion Laboratory, Pasadena, California, June 15, 1977

Table 1. Helios tracking coverage

	Spacecraft	Station Type	Number of Tracks	Tracking time (Hours, Mins)
August	Helios-1	26-meter	30	233 24
		64-meter	0	0 00
	Helios-2	26-meter	0	0 00
		64-meter	26	99 54
September	Helios-1	26-meter	39	225 16
		64-meter	0	0 00
	Helios-2	26-meter	0	0 00
		64-meter	30	94 18
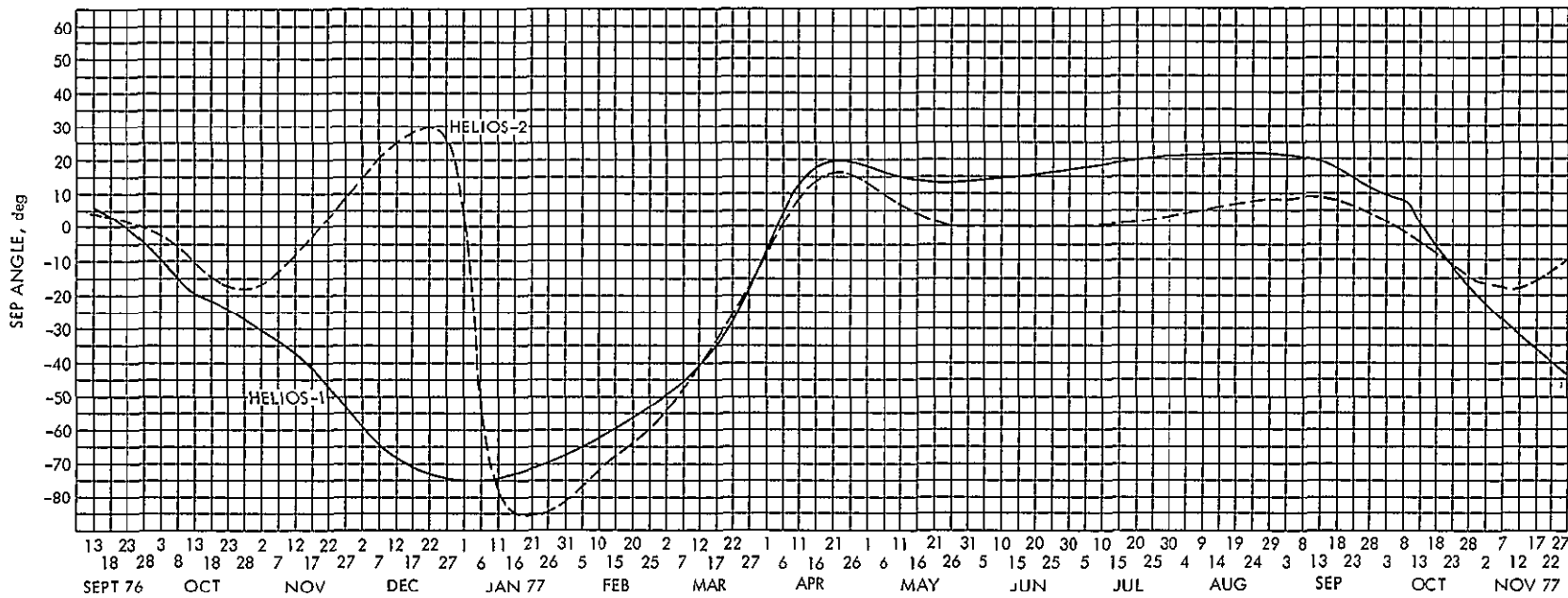
Fig. 1. Relationship of Helios-1 and -2 SEP angles vs time
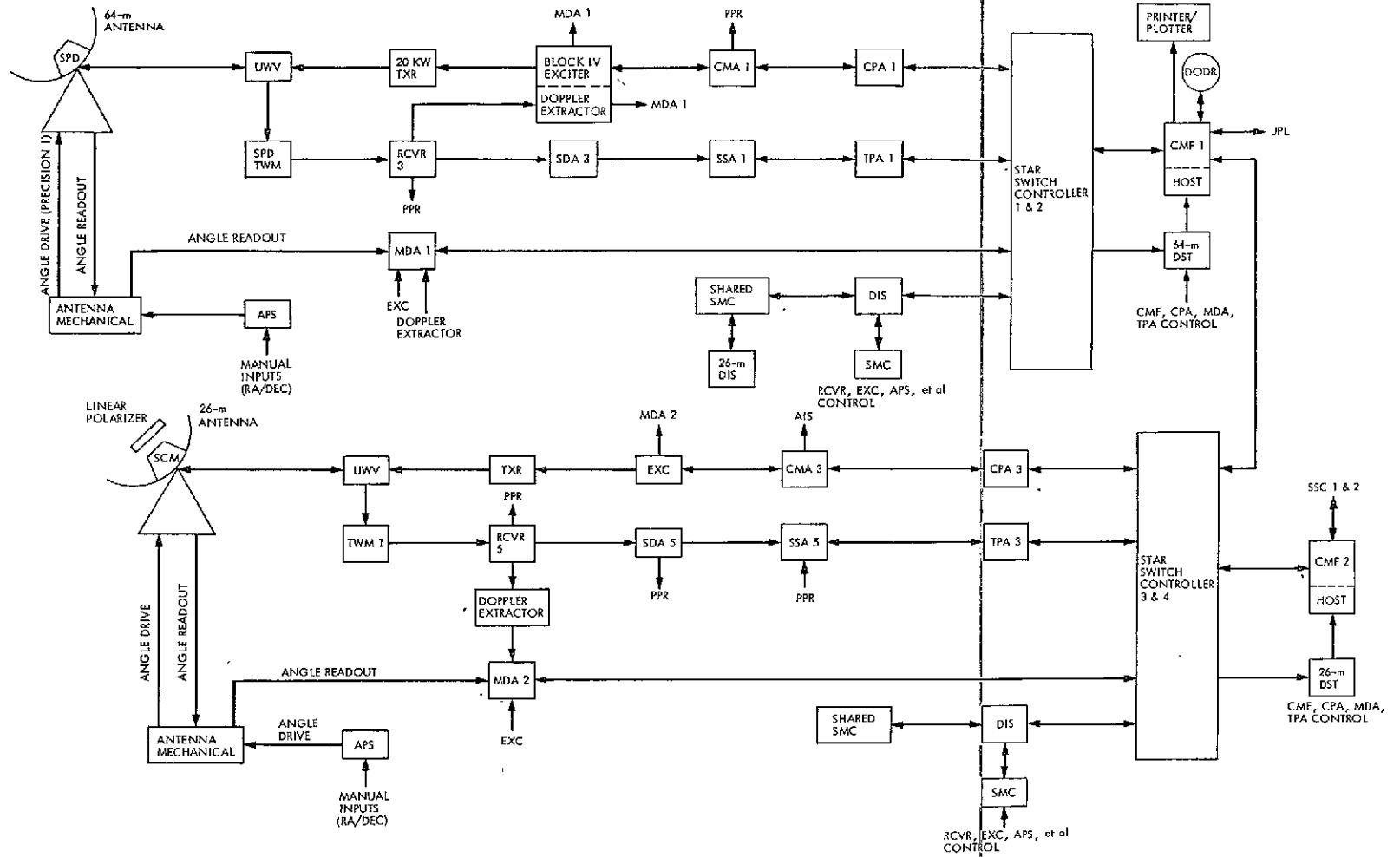
Fig 2. Standard Helios configuration for DSSs 42/43 and 61/63

		1977		
		OCTOBER	NOVEMBER	DECEMBER
		2 6 10 14 18 22 26 30	2 6 10 14 18 22 26 30	2 6 10 14 18 22 26 30
	HELIOS-1			
1	SEP ANGLE < 3 deg MAX TRACKING COVERAGE REQUESTED			
2	PERIHELION 6 (MOST INTERESTING PHASE OF HE-1)			
3	SOLAR WIND EXPERIMENT			
4	RADIAL LINEUP HE-1 AND HE-2			
5	SPIRAL LINEUP HE-1 AND HE-2			
6	SOLAR OCCULTATION			
7	SPECIAL INTEREST TRAVELING INTERPLANETARY PHENOMENA (STIP) PERIOD IV (MAX COVERAGE REQUESTED)			
	HELIOS-2			
1	SEP < 3 deg, 30 SEPT TO 11 OCT			
2	PERIHELION 4 (MOST INTERESTING PHASE HE-2)			
3	SOLAR WIND			
4	RADIAL LINEUP HE-1 AND HE-2			
5	SPIRAL LINEUP HE-1 AND HE-2			
6	SPECIAL INTEREST TRAVELING INTERPLANETARY PHENOMENA (STIP) PERIOD IV (MAX COVERAGE)			
7	SOLAR OCCULTATION			

Fig 3 Helios high activity period

N78-24167

A First-Principles Derivation of Doppler Noise Expected From Solar Wind Density Fluctuations

P S Callahan

Tracking Systems and Applications Section

The level of Doppler noise (DN) expected from solar wind (SW) density fluctuations (DF) is derived beginning with the expression for refractive index variations The calculation takes account of up- and downlink paths and of the method actually used to produce the DN values The usual assumptions that the DF are frozen in, that the large-scale radial variation can be separated from the DF, that the DF power spectrum is a power law with "outer scale" k_o, and that the DF are homogeneous on scales less than $2c\Delta t$, Δt = sample time, are made The result agrees quite well with the observations of DN by Berman (Refs 4, 6, and 7). Corrections for the finite number of points used in the actual algorithm are discussed

I. Introduction

The present discussion is meant to give a clearer understanding of the relationship of Doppler noise (DN) to density fluctuations (DF) in the solar wind (SW) by providing a detailed first-principles derivation The analysis is similar to that of Refs 1, 2, and 3, but is adapted specifically to the round-trip case and to the actual method used to obtain DN This analysis will also clarify the usefulness of DN for radio science (Ref. 4)

II. Basic Principles of Doppler Noise

The phase variations measured by DN are produced by refractive index variations along the path which occur because the index of a plasma is proportional to the electron density N

$$\mu^2 = 1 - \frac{e^2 N}{\pi m f^2} = 1 - \frac{AN}{f^2} \tag{1}$$

where f is the radio frequency and $A' = 80.6$ in MKS units Local variations of N on time scales $\gtrsim 1$ hour are nearly 100% in the SW The total change in phase for a reference point in traveling to a spacecraft and back is

$$\Phi_0 = \int_{raypath} \frac{f \, ds}{v_\phi} = \frac{f}{c} \int \frac{ds}{[1 - (A/f^2)(N + \delta N)]^{1/2}} \cong \frac{f}{c} \int ds \left[1 + \frac{AN}{2f^2} + \frac{A\delta N}{2f^2} \right] \tag{2}$$

where c is the speed of light The approximation is very good for S-band propagating in the solar wind.

Because we are interested in phase fluctuations the result is not sensitive to the average value of N but only to the fluctuations δN For this analysis we will assume that the spacecraft is at rest so there is no ordinary Doppler tone This latter assumption is an accurate approximation of the mechanization of DN predicts are subtracted from the observed Doppler and then a linear fit is done to 15 points to remove any remaining trends Because of this DN will not be sensitive to slow ($\gtrsim 30 \, \Delta t$, $\Delta t \equiv$ sample time) changes in the refractive index

In summary, we are interested in the phase change

$$\delta\Phi = \frac{f}{c} \int_{raypath} \left(\frac{A}{2f^2} \right) \delta N \, ds \tag{3}$$

where δN is a function of time and position along the raypath δN is defined so that $\delta\Phi$ has a mean of 0 At any instant one would measure a phase deviation $\delta\Phi(t)$ However, Doppler is not an instantaneous measurement but is accumulated (or averaged) over some sample time Δt To work in the "accumulation picture" one uses the time derivative of Eq (3) so that the phase deviation from t_1 to $(t_1 + m\Delta t)$ is

$$\Delta\Phi(t_1, m\Delta t) = \int_{t_1}^{t_1 + m\Delta t} dt \int_{raypath} \left(\frac{A}{2fc} \right) \dot{\delta N} \, ds \tag{4}$$

where the dot denotes the time derivative of δN Doppler is produced by differencing two adjacent phase accumulations and dividing by the sample interval. Because we have assumed that there is no velocity-induced Doppler tone, the "Doppler" produced in this case is immediately the material for producing Doppler noise (mean-squared phase fluctuation)

$$DN(t_1, \Delta t, M) = \frac{1}{M} \sum_{m=0}^{M-1} \left[\frac{\Delta\Phi(t_1, (m+1)\Delta t) - \Delta\Phi(t_1, m\Delta t)}{\Delta t} \right]^2 Hz^2 \tag{5}$$

where M is the number of points included in the linear fit Note that what we are calling DN is the square of the experimental quantity reported by Refs 4, 6, and 7

If we carry out the prescription of Eq (5) using Eq. (4), we have

$$DN(t_1, \Delta t, M) = \left(\frac{A}{2fc\Delta t} \right)^2 \frac{1}{M} \sum_{m=0}^{M-1} \left[\int_{t_1 + m\Delta t}^{t_1 + (m+1)\Delta t} dt \int_{raypath} \dot{\delta N} \, ds \right]^2 Hz^2 \tag{6}$$

An obvious simplification results if the order of integration is interchanged so that δN is evaluated at the two endpoint times The interchange is allowed as long as the DF are homogeneous on scales $<2c\Delta t$, and the round-trip light time is not so large as the time scale on which the magnitude of δN changes (~ 1 day in the SW) The first requirement is a statement of the Nyquist theorem that

data sampled at Δt contain no information about frequencies $> 1/2*\Delta t$ Recall that DN is also not sensitive to long-term trends $> 2M\Delta t$

We use the above assumption to carry out the time integral in Eq. (6). We also explicitly exhibit the up- and downlink parts of the raypath Time is measured at the receiver and the geometry is shown in Fig 1 The result is

$$DN(t_1, \Delta t, M) = \left(\frac{A}{2fc\Delta t}\right)^2 \frac{1}{M} \sum_{m=0}^{M-1} \left\{ \int_0^L dz \left[\delta N\left[r, t_1 + (m+1)\Delta t - (2L-z)/c\right] \right.\right.$$

$$- \delta N\left[r, t_1 + m\Delta t - (2L-z)/c\right] + \delta N\left[r, t_1 + (m+1)\Delta t - z/c\right]$$

$$\left.\left. - \delta N\left[r, t_1 + m\Delta t - z/c\right] \right] \right\}^2 Hz^2 \tag{7}$$

where r is the heliocentric position vector

To proceed with the evaluation of DN we must have a way of characterizing the sixteen products represented in Eq (7) We approximate the sum over m by an integral over t. We assume that the time and space integrals may be interchanged. This is valid if the correlation scale of the medium is $\ll L$, and for the "frozen-in" assumption which will be used later We show these operations in just the first term of Eq. (7)

$$DN(t_1, \Delta t, M) = \left(\frac{A}{2fc\Delta t}\right)^2 \int_0^L dz \int_0^L dz' \frac{1}{T_M} \int_0^{T_M} \left\{ \delta N\left[r, t_1 + t + \Delta t - (2L-z)/c\right] \right.$$

$$\left. \delta N\left[r', t_1 + t + \Delta t - (2L-z')/c\right] \right\} dt$$

where $T_M = M\Delta t$ and the two terms of the product are distinguished by primed and unprimed coordinates In the limit $T_M \to \infty$ the t-integral gives the autocorrelation function of δN, $F(\Delta r, \tau)$, which depends only on the separation in time and/or space of the DF The limit $T_M \to \infty$ requires that $T_M \gg T_0$, where T_0 is the correlation time of the medium For $M = 15\text{-}18$ and $\Delta t \leqslant 60$ sec as in the DN algorithm this condition is not accurately fulfilled in the SW ($T_0 \geqslant 1$ hr, for the larger changes, $\delta N/N \sim 1$). Therefore, we will do an approximate analysis consisting of two terms the first, the result for $T_M \to \infty$, the second, a correction (involving the autocorrelation function as an approximation for the mean-squared density change) for the fact that $T_M \leqslant T_0$. The autocorrelation function is symmetric, so we have only 8 terms

$$DN(t_1, \Delta t, M) \cong \left(\frac{A}{2fc\Delta t}\right)^2 2 F_1(t_1) \int_0^L dz \int_0^L dz' \left\{ 2 \left[F\left[r - r', (z - z')/c\right] \right.\right.$$

$$\left. + F\left[r - r', (2L - z - z')/c\right] \right] - \left[F\left[r - r', -\Delta t + (z - z')/c\right] \right.$$

$$+ F\left[r - r', -\Delta t + (2L - z - z')/c\right] + F\left[r - r', \Delta t + (z - z')/c\right]$$

$$\left.\left. + F\left[r - r', \Delta t + (2L - z - z')/c\right] \right] \right\}$$

$$-\left(\frac{A}{2fc\Delta t}\right)^2 2F_1(t_1)\int_0^L dz \int_0^L dz' \int_{T_M}^\infty \frac{dt}{T_M}\left\{2\,[F\,[r-r',\,t+(z-z')c]]\right.$$

$$\left.\right\}\,Hz^2 \tag{8}$$

where the second term contains all the F's of the first with the arguments modified by the addition of t. The factor $F_1(t_1)$ is to account for the fact that the general level of activity may vary on a time scale longer than T_0 (i.e., if we use a yearly average value for $F(\Delta r, \tau)$, the daily value of $DN(\Delta t, T_M)$ could easily be a factor of 2 higher or lower than we would expect). The terms with L arise because we are considering round-trip measurements. The Δt's occur because of the phase accumulation time. Reference 3, in doing a one-way analysis of range data, uses only the first term of Eq (8).

So far there has been no use made of any particular properties of the SW. The effect of any fluctuating plasma, whose statistical properties satisfy the restrictions discussed above, on round-trip Doppler data is given by Eq (8).

III. Doppler Noise From Solar Wind Density Fluctuation

We now proceed to investigate Eq (8) for the case of SWDF. First, we note that the SW has a large-scale radial variation which should be separated from the autocorrelation function, just as the long-term time variations were. We take

$$F[r-r',\tau] = b(r)\,G[r-r',\tau] \tag{9}$$

where b(r) gives the radial variation of the mean-squared density,

$$b(r) = \delta N_1^2 (A_1/r)^{4+2\gamma} \tag{10}$$

where δN_1 is the *total* RMS DF at radius A_1 and γ allows for radial variations different from r^{-2} (see Section IV).

Time and position for the SWDF are usually related by the "frozen-in" assumption because the speeds at which disturbances propagate are much less than the bulk velocity. Thus, $G(r,\tau) = G(r - v\tau)$, where v is the bulk SW velocity. For simplicity we will assume that v is not a function of $|r|$ and that it is only in the radial direction. We take the raypath to be in the x-z plane (see Fig 1) so that $v = (v_x, o, v_z)$; note that the components of v are functions of position along the raypath. Equation (8) may be rewritten as

$$DN(t_1, \Delta t, M) = B^2 \int_0^L dz\,b(r)\int_z^{z-L}(-d\ell)\left\{2\left[G\,[R-v\ell/c]\right.\right.$$

$$\left.+\,G\,[R-v(2L-2z+\ell)/c]\right] - \left[G\,[R-v(-\Delta t + \ell/c)]\right.$$

$$+\,G\,[R-v(-\Delta t + (2L-2z+\ell)/c)] + G\,[R-v(\Delta t + \ell/c)]$$

$$\left.\left.+\,G\,[R-v(\Delta t + (2L-2z+\ell)/c)]\right]\right\}$$

$$-B^2 \int_0^L dz\, b(r) \int_z^{z-L} (-d\ell) \int_{T_M}^{\infty} \frac{dt}{T_M} \left\{ 2 \left[G\left[R - v(t + \ell/c) \right] \right. \right.$$

$$+ \ldots \left.\vphantom{\int} \right\} Hz^2 \qquad (11)$$

where $\ell \equiv z - z'$, $R \equiv (o, o, \ell)'$ $B^2 = 2F_1(t_1)(A/2fc\Delta t)^2$, and the second term contains all the G's of the first with the arguments modified by t

The well-studied characteristic of SWDF is not the autocorrelation but its Fourier transform, the power spectrum. The relationship between the two is

$$g(k) = \int_{-\infty}^{\infty} G(R)\, e^{-ik\cdot R}\, d^3 R \qquad (a)$$

$$\qquad (12)$$

$$G(R) = \int_{-\infty}^{\infty} g(k)\, e^{+ik\cdot R}\, \frac{d^3 k}{(2\pi)^3} \qquad (b)$$

where k is the wavenumber vector of the DF Experimentally it is found that the spectrum can be well represented by

$$g(k) = \frac{k_o^{\beta-3}}{[k_o^2 + a_x^2 k_x^2 + a_y^2 k_y^2 + a_z^2 k_z^2]^{\beta/2}} \qquad (13)$$

where k_o is the "outer scale" of the DF, $k_o = 2\pi/\ell_o$, $\ell_o \cong 10^6$ km, the a's allow for the possibility that the spectrum is anisotropic (there is no good experimental evidence that they differ from 1, but they are easy to keep in the computation), and the spectral index $\beta = 3\ 5 - 4\ 0$ (see Section IV) We use Eq (12b) and Eq (11) to obtain

$$DN(t_1, \Delta t, M) = 2B^2 \int_0^L dz \int_{-\infty}^{\infty} \frac{d^3 k}{(2\pi)^3}\, g(k) \int_z^{z-L} (-d\ell)\, e^{i\ell(k_z - k\cdot v/c)}$$

$$\left\{ [1 + e^{-i2k\cdot v(L-z)/c}]\, [1 - e^{-ik\ v\Delta t}] \right.$$

$$\left. - \int_{T_M}^{\infty} \frac{dt}{T_M}\, e^{-ik\cdot vt}\, [1 + e^{-i2k\cdot v(L-z)/c}]\, [1 - e^{-ik\ v\Delta t}] \right\} Hz^2 \qquad (14)$$

where use has been made of the fact that G is real, so we need consider terms of only one sign in Δt

In the SW at heliocentric distances greater than a few solar radii the distance scale is much greater than the scale of the DF. The limits on the ℓ-integral can then be approximated as $\pm\infty$, so it gives a delta function $2\pi\delta(k_z - k \cdot v/c)$ The delta function can be used to do the k_z-integral with $k_z \rightarrow k_x v_x/c\,(1 - v_z/c) \equiv k_x v_x V/c$ and $k \cdot v = k_x v_x V$, giving

$$DN(t_1, \Delta t, T_M) = 2\,B^2 \int_0^L dz\, V\, b(r) \int_{-\infty}^{\infty} \frac{d^2 k}{(2\pi)^2}\, g(k_x, k_y, k_x v_x V/c)$$

$$\times \left\{ \left[1 + e^{-i2k_x v_x V(L-z)/c} \right] \left[1 - e^{-ik_x v_x \Delta t} \right] \right.$$

$$- \int_{T_M}^{\infty} \frac{dt}{T_M} e^{-ik_x v_x V t} \left[1 + e^{-i2k_x v_x V(L-z)/c} \right] *$$

$$\left. \left[1 - e^{-ik_x v_x \Delta t} \right] \right\} Hz^2 \tag{15}$$

where k_y drops out of the exponentials because $v_y \equiv 0$

For $\dot{g}(k)$ of the form of Eq (13) the k_y-integral can be carried out to give

$$DN(t_1, \Delta t, T_M) = 2 B^2 \int_0^L dz\, b(r) \frac{V k_0^{\beta-3} \sqrt{\pi}\, \Gamma(\beta - 1/2)}{a_y (2\pi)^2 \, \Gamma(\beta/2)}$$

$$\times \int_{-\infty}^{\infty} \frac{dk_x}{[k_0^2 + k_x^2 (a_x^2 + a_z^2 V^2)]^{(\beta-1)/2}} \left\{ \left[1 + e^{-i2k_x v_x V(L-z)/c} \right] * \right.$$

$$\left[1 - e^{-ik_x v_x \Delta t} \right] - \int_{T_M}^{\infty} \frac{dt}{T_M} e^{-ik_x v_x t} \left[\quad \right] \left[\quad \cdot \right] \right\} Hz^2 \tag{16}$$

where the second brackets are the same as the first

The four parts of the first term of Eq (16) can be integrated using

$$\int_{-\infty}^{\infty} \frac{dx\, e^{-ixy}}{(1 + x^2)^{(2n+1)/2}} = 2 \left(\frac{y}{2} \right)^n \frac{\sqrt{\pi}}{\Gamma(n + 1/2)} K_n(y) \tag{17}$$

For Eq (17) we have $\beta - 1 = 2n + 1$ or $n = (\beta - 2)/2$, and

$$x = k_x (a_x^2 + a_z^2 V^2)^{1/2}/k_0 \equiv k_x a/k_0$$

Before doing the k_x-integral of the second term, we must consider the effect of the t-integral It is easily carried out to give a factor $[e^{-ik_x v_x VT_M}/(-ik_x v_x VT_M)]$. For $|k_x| \geqslant k_M \equiv 2\pi/2v_x T_M$ the exponential term varies rapidly so that there is little contribution to the integral This effect is important if $2v_x T_M < \ell_0$ ($k_M > k_0$), because the k_x-integral of this (correction) term is not cut off before reaching the sloping part of the spectrum To repeat when $2v_x T_M < \ell_0$, the mean-squared phase fluctuation will depend on the averaging time $M\Delta t$ We approximate the second term of Eq (16) by finite limits on the k_x-integral and have

$$DN(t_1, \Delta t, T_M) = 2B^2 \int_0^L \frac{dz\, b(r) V}{a\, a_y \pi \Gamma(\beta/2)\, 2^{n+1}} \left\{ \left[2^{n-1} \Gamma(n) \right. \right.$$

$$- \left(\frac{k_o v_x V \Delta t}{a}\right)^n K_n(\ ) \right] + \left[\left(\frac{2k_o v_x V(L-z)}{ac}\right)^n K_n(\ )$$

$$- \left(\frac{k_o v_x V(\Delta t + 2(L-z)/c)}{a}\right)^n K_n(\ ) \right] \right\} + 4B^2 \int_0^L dz\, b(r) *$$

$$\left[\frac{V k_o^{\beta-3} \sqrt{\pi}\, \Gamma\left((\beta-1)/2\right)}{a_y (2\pi)^2 \Gamma(\beta/2)}\right] \left\{ \int_0^{k_M} \frac{dk_x \left[1 + e^{-i2k_x v_x V(L-z)/c}\right]}{[k_o^2 + a^2 k_x^2]^{(\beta-1)/2}} * \right.$$

$$\left[1 - e^{-ik_x v_x \Delta t}\right] \right\} Hz^2 \tag{18}$$

where Γ is the gamma function, K_n is the modified Bessel function of order n, and the arguments of the K's are the same as the respective factors in front of them. This result is similar to that of Ref 3, but contains all the terms required to describe two-way Doppler data. The analysis of the second term requires some care and is deferred until the basic result for long averaging times $(T_M \to \infty, k_M \to 0)$ is completed

We are now faced with the task of integrating Eq (18) along the raypath. First, we assume that only $b(r)$ and v_x (the velocity across the raypath) depend on z. A much greater simplification occurs when the order of magnitudes of the arguments are considered. We take typical numerical values $k_o = 2\pi \times 10^{-6}$ km^{-1}, $v_x = 400$ km/sec, $\Delta t = 60$ sec, $L = 3 \times 10^8$ km, $a = a_y = V = 1$ and find $k_o v_x \Delta t = 0.15$, $2k_o v_x L/c = 5.0$, $L/c\Delta t = 17$. Thus, except for $z = L$, $\Delta t \ll (L-z)/c$, and for $z = L$ the coefficient $b(r)$ will make the contribution small. In this limit we may treat the two differences in Eq (18) as derivatives. The only z dependence in the first term is the variation of v_x along the raypath

We proceed to simplify the geometric expressions in order to integrate along the raypath. From Fig 1 we have

$$r^2 = (z - q\mu_1)^2 + q^2 = q^2(\mu^2 + 1)$$

$$v_x = v_o/(1 + \mu^2)^{m/2}$$

$$dz = q\, d\mu \tag{19}$$

where v_o is the radial velocity of the SW and m slightly different from 1 allows for nonradial velocities. We ignore the variation of v_z along the raypath since it always occurs as $v_z/c < 10^{-3}$. We will also suppose that the a's are constant along the raypath as there is no evidence to the contrary. For $k_o(r)$ we chose $k_o(r) = k_1(q/A_1)^\ell (1 + \mu^2)^{\ell/2}$ to find the effects of an outer scale which changes with heliocentric distance. Recalling the form for $b(r)$ from Eq (10) and using Bessel function relations to reduce the derivatives introduced, we have

$$\cdot DN_1(t_1, \Delta t, T_M) = 2B^2 \left[\frac{V \delta N_1^2 (A_1/q)^{4+2\gamma} q k_1 (v_o \Delta t)^2}{\pi a_y a\, \Gamma(\beta/2) 2^{n+1}}\right] \int_{-\mu_1}^{\mu_2} d\mu \left\{ \left[2^{n-3} \Gamma(n-1) \frac{V^2}{a^2} * \right.\right.$$

$$(q/A_1)^\ell (1 + \mu^2)^{-2-\gamma-m+\ell/2} \right] + \left[\frac{c (1 + \mu^2)^{-2-\gamma-\ell/2}}{2q (k_1 v_o \Delta t)^2 (q/A_1)^\ell}\right] *$$

$$\frac{d}{d\mu} \left\{ \left[\left(\frac{2k_1 \, (q/A_1)^\ell \, v_o Vq \, (\mu_2 - \mu)}{ac(1+\mu^2)^{(m-\ell)/2}} \right)^n K_n \, (\,) \right] \right\} \quad Hz^2 \tag{20}$$

Because of the large power of μ in the denominator (~ 5), so long as $\mu \geqslant 3$, i.e., $q \leqslant 0.3$ AU, the limits on the integral can be considered as $\pm\infty$ for the first term, and the second term will be less than the first. The second term is integrated by parts, and the only contribution is for $\mu = \mu_1$. The result of the integration along the raypath is

$$DN_1 \, (t_1, \Delta t, T_M) = F_1 \, (t_1) \left(\frac{A}{2fc\Delta t} \right)^2 \left[\frac{\delta N_1^2 \, (A_1/q)^{4+2\gamma} \, k_1 q \, (v_o \Delta t)^2 \, V^3}{\pi a_y \, a^3 \Gamma \, (\beta/2)} \right] *$$

$$\left\{ \left[\frac{\sqrt{\pi} \, \Gamma(n-1) \, (q/A_1)^\ell \, \Gamma \, ((3+2\gamma+2m-\ell)/2)}{2\Gamma \, ((4+2\gamma+2m-\ell)/2)} \right] \right.$$

$$\left. + \left[\frac{a^2 c \, (1+\mu_1^2)^{-2-\gamma-\ell/2}}{2^n \, q k_1 v_o^2 \, \Delta t \, V^2 \, (q/A_1)^\ell} \right] \left[\left(\frac{2k_1 \, (q/A_1)^\ell \, v_o \, VL}{ac(1+\mu_1^2)^{(m-\ell)/2}} \right)^n K_n \, (\,) \right] \right\} \quad Hz^2 \tag{21}$$

where $n = (\beta - 2)/2$. For a long averaging time $T_M \to \infty$, this gives the mean-squared Doppler noise in terms of the mean-squared density fluctuation at 1 AU (A_1) appropriate to the time of observation $F_1(t_1)\delta N_1^2$, the outer scale size k_1, the radial solar wind velocity v_o, and the sampling time Δt. Note that to first order the sampling time drops out completely. This result will be discussed further in Section IV.

We now return to the correction term for finite averaging times in Eq (18). The important point is that $k_M > k_o$, so we divide all the k's by k_M. This shows the basic $(k_M^{\beta-2})^{-1} \propto \Delta t^{\beta-2}$ dependence that we wish to evaluate. We note that $k_M v_x \Delta t \ll 1$, so the second term in the integral can be expanded. The overall correction term is

$$DN_2 \, (t_1, \Delta t, T_M) = 4B^2 \int_0^L \frac{dz \, b(r) \, V \, \sqrt{\pi} \, k_o^{\beta-3}}{(2\pi)^2 a \, a_y \, \Gamma(\beta/2) \, k_M^{\beta-2}} \int_0^1 \frac{dx \, [-(\pi x/Ma)^2 + (i\pi x/Ma) \, e^{-i x p}]}{[x_o^2 + x^2]^{(\beta-1)/2}} \quad Hz^2 \tag{22}$$

where $x \equiv ak_x/k_M$, $x_o \equiv k_o/k_M$, $p = \pi(L - z)/aMc\Delta t$, and we have made use of the fact that the final result must be real

The x-integral in Eq (22) can be evaluated approximately, though we note that it is mainly a numerical factor (there is z-dependence in the second term) of order 1. Finally, we use Eqs (10) and (19), the expression for $k_o(r)$ following Eq (19), and the approximation $\mu_2, \mu_1 \to \infty$ to arrive at the correction term

$$DN_2 \, (t_1, \Delta t, T_M) \cong F_1 \, (t_1) \left(\frac{A}{2fc\Delta t} \right)^2 \left[\frac{\delta N_1^2 \, (A_1/q)^{4+2\gamma} \, k_1 q \, (v_o \Delta t)^2 \, V^3}{\pi a_y \, a^3 \Gamma \, (\beta/2)} \right] *$$

$$\left\{ \left[\frac{2a}{V^2} \left(\frac{M}{\pi} \right)^{\beta-3} \frac{(k_1 v_o \Delta t)^{\beta-4} \, (q/A_1)^{\ell(\beta-3)} \, \Gamma(n_2 - 1/2)}{(\beta - 3) \, \Gamma \, (n_2)} \right] * \right.$$

$$\left. \left[\frac{\sin p_o \mu_2}{(1 + x_o^2)^{(\beta-3)/2}} - p_o \mu_2 \, (\cos p_o \mu_2) \, \ell n \, (1 + \sqrt{1 + x_o^2}) \right] \right\} \quad Hz^2 \tag{23}$$

where $n_2 \equiv 2 + \gamma - \ell(\beta - 3)/2 + m(\beta - 2)/2$, $p_o \equiv \pi q/aMc\Delta t$, and all other terms are as before Note that the coefficient in front of the braces is the same as in Eq. (21). It should be emphasized that this form of the correction term applies *only* for $2Mv_o\Delta t < \ell_o$, or $\Delta t \lesssim 60$ sec, for $M = 15-18$ The result shows the Δt-dependence $\Delta t^{\beta-4}$ that DN can be expected to have when the averaging time $M\Delta t$ is less than the correlation time ℓ_o/v_o

IV. Discussion and Conclusions

The sum of Eqs. (21) and (23) gives the mean-squared Doppler noise (DN) in Hz^2 expected from solar wind (SW) density fluctuations (DF) Because the DF are functions of both time and position, considering them as a factor times the local average density $\delta N(R,t) = \epsilon(r,t)N(r)$ would not be useful as the important information would be contained in the correlation function of ϵ Thus, it is difficult theoretically to relate DN to the total columnar content. If a proportionality exists (Refs 6, 7) further analysis of the structure of SWDF will be needed to find the physical basis of the proportionality However, it will be shown below that the theory developed above provides a completely adequate explanation of DN. It also shows that DN can be useful for studying the spectrum and amplitude of SWDF, and perhaps also the SW velocity near the sun.

We proceed to a numerical evaluation of Eqs. (21) and (23). First, we set $a = a_y = V = 1$, as they are not known to differ much from 1. For the SW parameters we take $\delta N_1 = 5$ cm^{-3}, $v_o = 400$ km/sec, $k_1 = 2\pi \times 10^{-6}$ km^{-1} A number of observations of DF (Refs 5, 6) suggest $\gamma \cong -0$ 2; however, for now it will be kept as a parameter. We will use the geometric parameters $q = 0.1A_1$, $L = 2A_1$, and recall the restriction $\mu_1 \geqslant 3$ For the sampling parameters we take $M = 15$, $\Delta t = 60$ sec, $f = 2$ 2 GHz Since the Γ functions are not very sensitive, we use $\beta = 4$, $\gamma = 0$, $\ell = 0$, $m = 1$ in them We then find

$$DN(t_1, \Delta t, T_M) \cong F_1(t_1) \left(\frac{4\ 47 \times 10^{-3}\ 10^{2\gamma}\ (\delta N_1/5)^2\ (v_o/400)^2}{(q/0\ 1\ A_1)^{3+2\gamma}} \right) \times$$

$$\left\{ 0\ 589\ (0\ 1)^\ell\ (q/0\ 1\ A_1)^\ell + \left(\frac{2\ 64 \times 10^{-4}\ (q/0\ 1\ A_1)^2}{(\Delta t/60)^2} \right) \times \right.$$

$$\left[(0.503\ (q/0\ 1\ A_1)\ (L/2\ A_1))\ K_1(\ ) \right]$$

$$\left. - \left(\frac{5.08}{(7\ 2 \times 10^4)^{4-\beta}\ (\Delta t/60)^{4-\beta}} \right) \left[\sin\left(\frac{5\pi}{9(\Delta t/60)} \right) - \left(\frac{5\pi}{9(\Delta t/60)} \right) \cos\left(\frac{5\pi}{9(\Delta t/60)} \right) \right] \right\} Hz^2 \quad (24)$$

where critical dependences on q, Δt, β, γ, and ℓ have been retained, and $A_1 = 1$ AU. We see that, except for the largest values of q ($\cong 0\ 3\ A_1$), the second term is not important The value of the last bracket is +0 56 for $\Delta t = 60$ sec and -0 50 for $\Delta t = 10$ sec

What do observations tell us about the remaining free parameters β, γ, ℓ, in Eq (24)? Many observations of SWDF (Refs 2-6) find that $3\ 4 \leqslant \beta \leqslant 4\ 0$ It will be shown below that DN observations seem to further restrict this range Reference 5 finds that SWDF power spectra decline as $q^{-2\ 6\pm0\ 4}$ ($\gamma = -0\ 2 \pm 0\ 2$) for Viking S-X Doppler data from August to December 1976 Reference 7 finds DN $\propto q^{-2\ 6}$ for a longer span of Viking data Reference 6 interprets this dependence of DN as $\gamma = +0\ 3$, $\ell = 1$ Such an interpretation is compatible with Eq (24), however, several points should be made in this regard First, the uncertainty of γ (unstated by Ref 6) is as large as the value, and systematic effects will tend to lead to the observed slow decline; so any specification of parameters must be viewed with caution Second, Ref 3 finds $\gamma \cong 0$ for the decline of the average density. Third, there is no support in the literature for a strong dependence of the *outer scale* on heliocentric distance Fourth, the acceleration of the SW near the sun has been ignored in this analysis and will tend to produce the observed slow falloff (DN $\propto (\delta Nxv)^2$) Finally, the amplitude of Eq (24) would not agree with observations for $\gamma = +0\ 3$, $\ell = 1$. Thus, for the remainder of the discussion we take $\ell = \gamma = 0$.

The fact that Ref 4 is able to determine the dependence of DN on sample time indicates that $\beta < 4$ Reference 4 finds DN $\propto \Delta t^{-0.6}$ (for the squared quantity used in this article), implying $\beta \cong 3.4$ A numerical evaluation of Eq. (24) shows that for such a low value of β, the third term is much less than the first so that no sample time effect would be seen. On the other hand, for $\beta \geq 3.8$, the third "correction" term would be larger than the first. DN observations then lead to $3.5 < \beta \leq 3.7$. These are fairly tight limits on an important parameter of SWDF and are in good accord with many other measurements (Refs 2-6)

As we have now fixed all the parameters in Eq. (24), we need to check that it gives reasonable results for DN With the parameters chosen and for 60-sec sample times only the first term is important, so we have

$$DN(t_1, \Delta t, T_M) \cong F_1(t_1) \left(\frac{4.47 \times 10^{-3} (\delta N_1/5)^2 (v_o/400)^2}{(q/0.1A_1)^3} \right) (0.589) \, Hz^2$$

$$= 2.6 \times 10^{-3} \left(\frac{F_1(t_1) (\delta N_1/5)^2 (v_o/400)^2}{(q/0.1A_1)^3} \right) Hz^2 \tag{25}$$

Figure 2 is taken from Ref 7, and points evaluated from Eq (25) are plotted with the data and the model of Ref. 7. The agreement is quite good considering that nominal values of δN_1, v_o, $\gamma(= 0)$, $F_1(t_1) = 1$ were used It seems likely that with large amounts of data these parameters could be refined by fits to DN Thus, DN could be a useful radio science tool putting limits on $(\delta N_1 \times v_o)$, β, and γ, and the residuals from such a model would provide estimates of $F_1(t_1)$ for correlation with solar features

The relationship between solar wind density fluctuations and Doppler noise has been derived It is shown that with nominal, well-known values for SW parameters the agreement between theory and observation is quite good

References

1 Callahan, P S, 1974, *Ap J, 187* "Interpretation of Columnar Content Measurements of the Solar Wind Turbulence "

2 Woo, R., 1975, *Ap J, 201*, 238, "Multifrequency Techniques for Studying Interplanetary Scintillations "

3 Muhleman, D O, Esposito, P. B, and Anderson, J D, 1977, *Ap J., 211*, 943, "The Electron Density of the Outer Corona "

4. Berman, A L, 1977, August 14, *The Deep Space Network Progress Report 42-40*, "Phase Fluctuation Spectra — New Radio Science Information in the DSN Mark III-77 Data System "

5 Callahan, P. S, 1977, *The Deep Space Network Progress Report 42-39*, 23, "A Preliminary Analysis of Viking S-X Doppler . Measurements of the Solar Wind Turbulence."

6 Berman, A L, 1977, April 14, *The Deep Space Network Progress Report 42-38*, 172, "Proportionality Between Doppler Noise and Integrated Signal Path Electron Density Validated by Differenced S-X Range "

7 Berman. A L and Wackley, J A, 1977, April 15, *The Deep Space Network Progress Report 42-38* 152 "Viking S-Band Doppler RMS Phase Fluctuations Used to Calibrate the Mean 1976 Equatorial Corona "
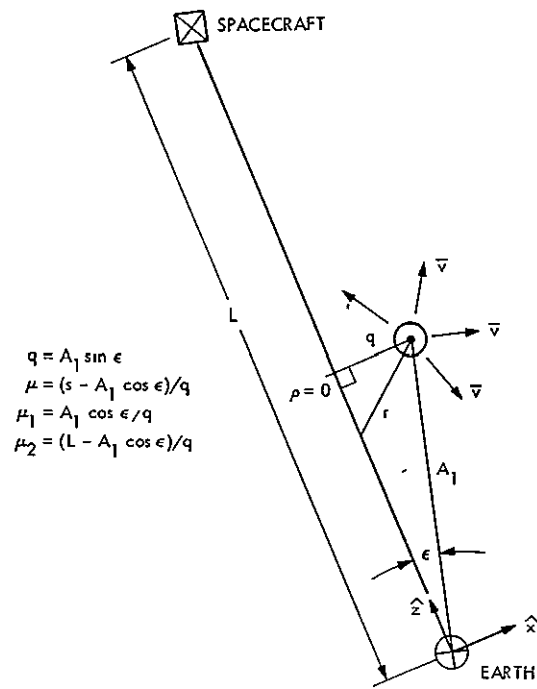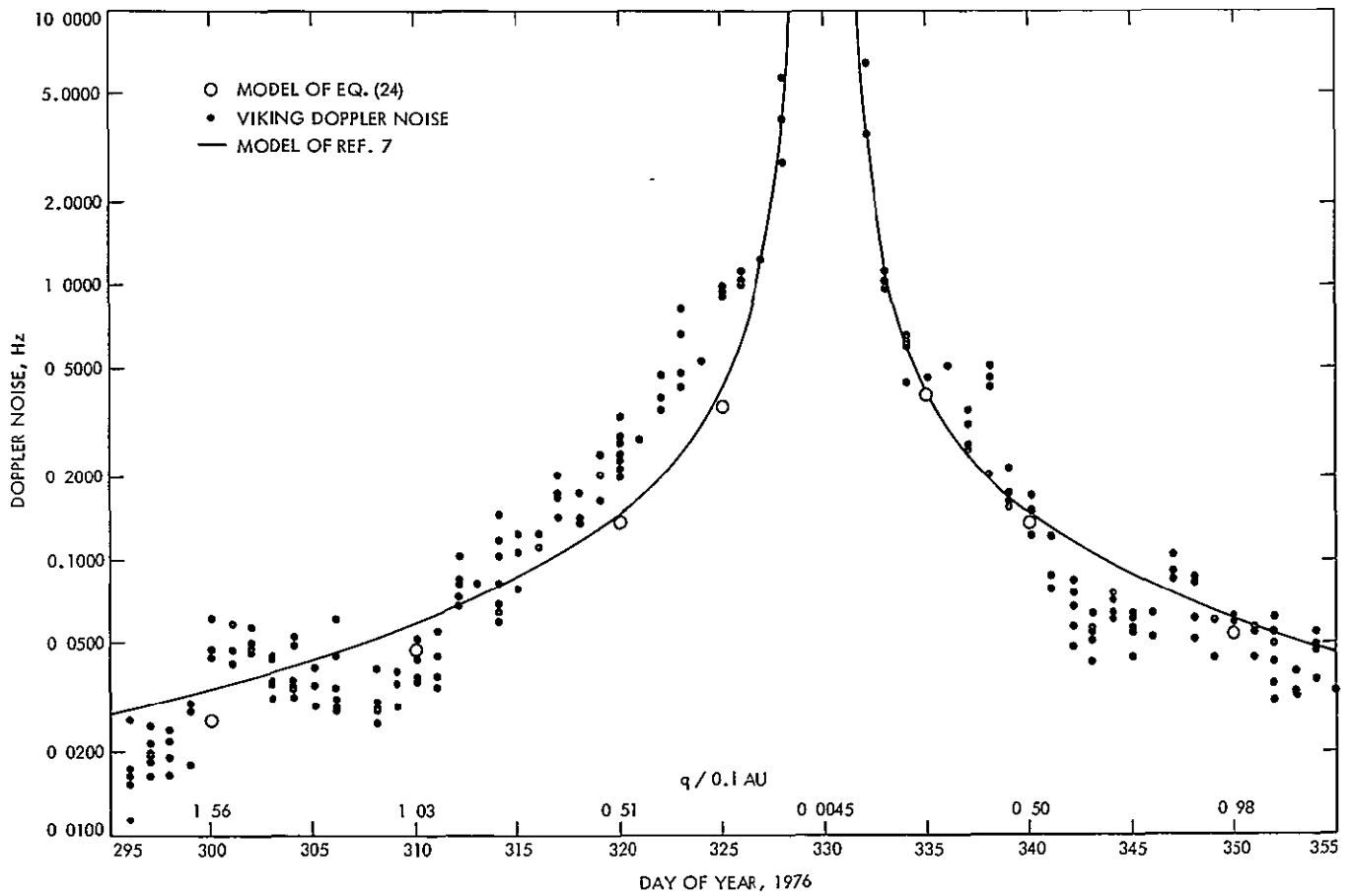
Fig. 1. Earth — spacecraft geometry

Fig. 2. Viking Doppler noise and the ISEDC model vs. day of year (295 to 355) (from Ref. 7)

N78-24168

VLBI Instrumental Effects, Part I

J W Layland and W J Hurd
Communications Systems Research Section

Very Long Baseline Interferometry (VLBI) is a method for observation of extragalactic radio sources which appears to have potential for precise long-distance Earth surveying, clock synchronization and spacecraft navigation For the past several years, many researchers at JPL and elsewhere have been working to establish the accuracy of VLBI observations The intent of the work reported here has been to review the principal components of the VLBI instrument in order to estimate and/or bound the systematic error contributions In this first of a series of articles, we establish the definitions and tools which we need in order to apply filter transfer-function analysis to the VLBI receiver, and we use it to estimate the sensitivity of the VLBI receiver to plausible filter variations

I. Introduction

Very Long Baseline Interferometry (VLBI) is a method for observation of extragalactic radio sources which appears to have potential for precise long-distance Earth surveying, clock synchronization and spacecraft navigation (Ref. 1) For the past several years, many researchers at JPL and elsewhere have been working to establish the accuracy of VLBI observations The intent of the work reported here has been to review the principal components of the VLBI instrument in order to estimate and/or bound the systematic error contributions In this first of a series of articles, we establish the definitions and tools which we need in order to apply filter transfer-function analysis to the VLBI receiver, and we use it to estimate the sensitivity of the VLBI receiver to plausible filter variations We also estimate the error contributions due to uncertainty in modeling of the receiver channels with bandwidth synthesis processing In the second article of this series, we will estimate

error contributions from channel modeling with full-band sampling

Section II of this article is an overview description of the VLBI instrument In section III we develop the expected cross-correlation of the interferometer samples in terms of the receiving filter transfer functions and the sampling clock parameters, and we review features of the delay estimation process which admit systematic errors Supporting transform analysis for this development appears in Appendix A The sensitivity of the VLBI time delay to filter variations is estimated in section IV The principal result of this section is that quite plausible variations in these filters can result in changes in the VLBI time delay of 5-15 cm In section V, the last section of this article, we estimate the error potential inherent in the necessary receiver channel modeling for bandwidth synthesis data A phase calibrator which is itself

assumed perfect is used in some parts of this analysis The principal result of this section is that errors due to channel modeling, which can be on the order of 0.5 to 1 m without calibration, can be held to generally below 1 cm if two tones from a "perfect" phase calibrator are placed in each of the synthesis channels. Evaluation of a real phase calibrator is another subject

II. The VLBI Receiving-Processing System

Figure 1 shows the portion of the VLBI system which is of concern here The radio-source and transmission path, while shown, are not explicitly of concern, and are included as a reference platform for the behavior of the system The radio source is assumed to be a point source, and the transmission path nondispersive

The radio source emits a low-level white noise process which travels by separate paths to receiving stations The transmission path delays, 'd_1' and 'd_2', are time-varying, in general, as are the oscillator reference phases, 'ϕ_1' and 'ϕ_2', and the delays into the samplers, 'q_1', and 'q_2' The station frequency and time references provide a coordinate system for the description of the received signals The delays to the stations are specified as "backward-looking," with respect to their time of arrival at the receiving stations As expressed in general coordinate time,

$$e_1'(t) = e[t - d_1(t)]$$

$$e_2'(t) = e[t - d_2(t)] \qquad \cdot \quad (1)$$

The reconciliation between this general coordinate time and the two station time-coordinates is a part of the job of the parameter estimator

Each receiving system adds its own (independent) white gaussian noise process, of temperature approximately 20 K at the maser amplifier. The maser amplifier contains the filter $H_i(s)$, with a variable gain and bandwidth A plausible model for the maser-amplifier when operating in wideband mode is a double-tuned filter plus a transmission line The total maser delay is ~16 m (Ref 2)

The output of each maser amplifier, still at microwave frequencies, is mixed with a local-oscillator before subsequent filtering by $G_i(s)$ and sampling The filters $G_i(s)$ are assumed to be at least zonal-low-pass, so that second-harmonics are rejected The mixer itself has a noise temperature of several

thousand K, which is negligible as long as we are near the high-gain region of $H_i(s)$

For wideband-sampling (WBS), the filters $G_i(s)$ represent the (50-MHz) IF filters of the Block III or Block IV Receivers For bandwidth-synthesis (BWS) processing (Ref. 3), the $G_i(s)$ represent the final narrow-band channel filters, while the pertinent portions of the IF filters are absorbed into the RF filters $H_i(s)$. When needed, we will include other details of the physical system, such as the implicit filtering of the quadrature SSB demodulator into the two-filter model shown by appropriate interpretation of the $H_i(s)$, $G_i(s)$ parameters

The sampling of the data at the output of the filters $G_i(s)$ establishes a firm and manipulable coordinate system within which the subsequent cross-correlation and processing are performed Proper interpretation of the correlation products requires a precise understanding of the continuous and time-varying time coordinates within which the receiver filters and the problem geometry are separately defined. Jitter of the sampling operation per se and pseudorandom transport lags of the receiving system are included within quantizer delays $q_i(t_i)$ The correspondence between station times t_1, t_2, which establishes the coordinate base for the data processing, and the general coordinate time within which the problem geometry is intrinsically defined, will be established by a redefinition of the geometric time delays

III. Correlation and Estimation for VLBI DATA

In this section we derive the cross-correlation to be observed between the two sampled data streams as a function of the physical filters which precede the sampling

At the sampler, the station clock which controls the sampling places an absolute and incorruptible time base into the data Except for phase noise, this same time base is also coherent with the local oscillator and any calibration system which may be used It is convenient, furthermore, to consider the filters at a given station as defined within the time reference system of that station's clock This is consistent with our belief that the best knowledge of the filter characteristics at a station will come through measurements during or in conjunction with a VLBI experiment Such measurements will of necessity specify these filter characteristics with respect to the station time-base

Let the input to the receiver's low-noise-amplifier be specified as $a_1(t_1)$ within the reference frame of the station 1

clock. The input to the station 1 sampler $c_1(t_1)$ can be written by inspection as

$$c_1(t_1) = \int_{-\infty}^{t_1-q_1(t_1)} g_1[t_1 - q_1(t_1) - \eta_1]$$

$$\left\{ \cos [\omega_1 \eta_1 + \phi_1(\eta_1)] \int_{-\infty}^{\eta_1} h(\eta_1 - \xi_1) a_1(\xi_1) d\xi_1 \right\} d\eta_1 \tag{2}$$

where $g_1(x)$, $h_1(x)$ are the impulse responses of the filters $G_1(s)$, $H_1(s)$, and $q_1(t_1)$, and $\phi_1(\eta_1)$ are the sampler input delay and the local-oscillator phase, respectively

To develop $c_1(t_1)$ further, in terms of the radio-source emissions, and permit the calculation of the cross correlation, $a_1(t_1)$ needs to be expressed in terms of $e(t)$ and $d_1(t)$, both of which are known as functions of general coordinate time Let the function $\Delta u_1(t_1)$ represent the correction term Station 1 clock-time minus general coordinate time; i e , if

$$t_1 \text{ is Station 1 clock time}$$

then $$\tag{3}$$

$$t = t_1 - \Delta u_1(t_1)$$

is the corresponding general coordinate time

In general coordinate time t, the radio-source signal at the station 1 antenna $e_1'(t)$ is

$$e_1'(t) = e[t - d_1(t)] \tag{4}$$

where $e(t)$ is the radio source emission at time t, and $d_1(t)$ is the backward looking time delay of the path to station 1 from radio source

Let us define a clock-adjusted delay function $k_1(t_1)$ to be

$$k_1(t_1) = \Delta u_1(t_1) + d_1[t_1 - \Delta u_1(t_1)] \tag{5}$$

As both $d_1(t)$ and $\Delta u_1(t_1)$ are slowly varying functions, so too is $k_1(t_1)$ The input to the Station 1 receiver is then expressed in Station 1 clock time as

$$a_1(t_1) = e[t_1 - k_1(t_1)] + n_1(t_1) \tag{6}$$

A completely parallel notation applies to the signals at Station 2.

Let us expand $k_1(\xi_1)$ in the neighborhood of t_1, such that

$$k_1(\xi_1) = k_1(t_1) + \sum_{l=1}^{\infty} k_{1l}(t_1) \cdot (\xi_1 - t_1)^l \tag{7}$$

From physical considerations, we expect that $|k_{11}(t_1)|$ will be less than 10^{-5}, $|k_{12}(t_1)|$ less than 10^{-11}, and subsequent terms correspondingly smaller We note further that the filters $G_1(s_1)$, $H_1(s_1)$ are relatively wideband and thus have short memory Let $g_1 \odot h_1(t_1 - \xi_1)$ denote the combined impulse response of these filters as in Eq (2) We expect the magnitude of $g_1 \odot h_1(t_1 - \xi_1)$ to be such that the contribution to $c_1(t_1)$ from $a_1(\xi_1)$ is negligible (e g , below 10^{-10} of the total) for all ξ_1 such that $|t_1 - \xi_1| > 10^{-4}$ From the anticipated magnitude of the $k_{1l}(t_1)$ terms in Eq. (7), the error in estimating $k_1(\xi_1)$ by a linear approximation in the neighborhood of t_1, i e., $|k_1(\xi_1) - k_1(t_1) - k_{11}(t_1) \cdot (\xi_1 - t_1)|$, is negligible (e g , below 10^{-18}) for all $|t_1 - \xi_1| < 10^{-4}$ Thus, we have

$$k_1(\xi_1) \approx k_1(t_1) + k_{11}(t_1) \cdot (\xi_1 - t_1) \tag{8}$$

as a valid approximation to $k_1(\xi_1)$ for use in evaluating the needed cross-correlations via Eqs. (2) and (6) The precise level of accuracy of this approximation is a function of the specific filters (and processing) used, and can be evaluated later, if desired. The validity of this approximation within the context specified permits the use of transform-domain techniques for performing the convolutions in Eq (2) For notational convenience, we will define new constants p_1, and p_{11}, which are implicitly functions of t_1, and reinstate the explicit dependence when necessary Define

$$p_1 = k_1(t_1) - k_{11}(t_1) \cdot t_1$$

$$p_{11} = k_{11}(t_1)$$

so

$$k_1(\xi_1) \approx p_1 + p_{11} \cdot \xi_1 \tag{9}$$

in the neighborhood of t_1

We also need to assume that $q_1(t_1)$ and $\phi_1(\eta_1)$ are slowly varying, and that $\phi_1(\eta_1)$ is well approximated by $\phi_1(t_1)$ within the context of the convolutions in Eq (2) The

corresponding definitions and assumptions apply to Station 2 filters and data.

Within this context, the input to the Station i receiver is

$$a_i(t_i) = e(t_i - p_i - p_{i1}t_i) + n_i(t_i) \qquad (10)$$

and the input to the Station i sampler-limiter is

$$c_i(t_i) = \int_{-\infty}^{t_i - q_i} g_i(t_i - q_i - \eta_i) \left[\cos(\omega_i \eta_i + \phi_i) \right.$$

$$\int_{-\infty}^{\eta_1} h_i(\eta_i - \xi_i)$$

$$\left. \cdot \left[e(\xi_i - p_i - p_{i1}\xi_i) + n_i(\xi_i) \right] d\xi_i \right] d\eta_i \qquad (11)$$

where we have suppressed the explicit dependence upon t_1 and t_2 for the functions q_i, ϕ_i, as well as for p_i, p_{i1}, as declared earlier

The processing of VLBI data is performed upon a sampled hard-limited version of the signals $c_i(t_i)$ The cross-products of data samples from the two stations exist only at discrete and regularly spaced values of t_1 and t_2 Calculation of the expected value of these cross-products from the foregoing definitions is straightforward but tedious, and is performed in Appendix A Denote this expected value as $S'_L(\tau_3, \phi_3 \; t_1, t_2)$ when written in terms of the two station clock-time indices For weak signals, the typical case, we have from the appendix that

$$S'_L(\tau_3, \phi_3 \; t_1, t_2) \simeq \frac{2}{\pi} \frac{S'_c(\tau_3, \phi_3 \; t_1, t_2)}{\sqrt{A_{c1}(0,0) \cdot A_{c2}(0,0)}} \qquad (12)$$

where $S'_c(\cdot)$ is the cross-correlation for nonlimited samples, $A_{ci}(\cdot)$ are the ith receiver autocorrelations, and with some manipulation,

$$\tau_3 = \frac{t_2 - t_1 - k_2 + k_1}{1 - k_{21}} + q_1 \cdot \frac{1 - k_{11}}{1 - k_{21}} - q_2 \qquad (13)$$

$$\phi_3 = \omega_2 \cdot t_2 + \phi_2 - \omega_1 \cdot t_1 - \phi_1 - \omega_2 \left(\frac{t_2 - t_1 - k_2 + k_1}{1 - k_{21}} \right)$$

$$- q_1 \left(\omega_2 \frac{1 - k_{11}}{1 - k_{21}} - \omega_1 \right)$$

$$S'_c(\tau_3, \phi_3 \; t_1, t_2) = \frac{N_e}{8} \cdot \frac{1}{1 - k_{21}} \int_{-j\infty}^{+j\infty} \frac{d\eta}{2\pi j} e^{-\eta\tau_3} G_2(-\eta)$$

$$\cdot \left\{ e^{-j\phi_3} H_2(-\eta + j\omega_2) \right.$$

$$\cdot H_1 \left[(\eta - j\omega_2) \frac{1 - k_{11}}{1 - k_{21}} \right]$$

$$\cdot G_1 \left[(\eta - j\omega_2) \frac{1 - k_{11}}{1 - k_{21}} + j\omega_1 \right]$$

$$+ e^{+j\phi_3} H_2(-\eta - j\omega_2)$$

$$\cdot H_1 \left[(\eta + j\omega_2) \frac{1 - k_{11}}{1 - k_{21}} \right]$$

$$\left. \cdot G_1 \left[(\eta + j\omega_2) \frac{1 - k_{11}}{1 - k_{21}} - j\omega_1 \right] \right\}$$

$$A_{ci}(0,0) = \frac{N_i + N_e}{8} \int_{-j\infty}^{+j\infty} \frac{d\eta}{2\pi j}$$

$$\left[G_i(-\eta)H_i(-\eta + j\omega_i)H_i(\eta - j\omega_i)G_i(\eta) \right.$$

$$\left. + G_i(-\eta)H_i(-\eta - j\omega_i)H_i(\eta + j\omega_i)G_i(\eta) \right]$$

The difference in the clock-adjusted delay terms, $k_1(t_1) - k_2(t_2)$, is a combination of a diurnal sinusoid plus fixed and linear offsets and other effects due to the propagation medium Over any single VLBI observation, it can usually be assumed that this clock-adjusted differential delay is known a priori except for an unknown fixed and (small) linear offset which must be solved for in order to characterize the observation The correlation amplitude, or the radio source noise density N_e, is also an unknown to be determined The receiving instrument itself can add two more unknown parameters to the set which must be solved for, namely, the local oscillator differential phase and phase-rate relative to the

station standards As can be deduced from Eq (13), the differential delay induces a phase effect which is indistinguishable from the instrument-induced phase effect Thus, to characterize any one VLBI observation, there are five parameters correlation amplitude, delay, delay-rate, phase, and phase-rate, which are unknowns to be-solved-for In principle, these five parameters could be extracted directly from the bit-wise cross products, although in practice pre-sums (Ref. 4) are generated to reduce the amount of computing that must be done For the purposes of this present section, we will assume that this intermediate step is non-lossy, and produces a result identical to that which would be obtained directly from the bit-wise cross products

To a communications-oriented engineer, the "obvious" technique for estimating the parameters of interest is that of maximum-likelihood, or a numerically tractable approximation to it. To others, the method of minimum mean-square error (MSE) fit seems proper In either case, an assumed model for the receiver's filter structure is an important part of the estimation procedure Mismatch between this model and the actual cross-correlation appears to be the sole source for biases in the estimates The minimum MSE, or least-squares estimation procedure is at least an approximation to maximum likelihood that should produce estimates which are "close" in some sense In particular, we note that the linear term of the Barankin (Ref 5) lower bound to the RMS deviation of a parameter estimated via maximum likelihood for a process embedded in Gaussian noise is identical to the formal standard deviation for that same parameter when estimated by the method of least squares

The linear least-squares procedure is defined as follows (Ref 6) Let x be an m-vector of parameters, A a k-by-m-matrix of coefficients, 'n' a k-vector of noise perturbations, and y a k-vector of observations, such that

$$y = A \cdot x + n \qquad (14)$$

Assume that n has zero mean with covariance matrix

$$V = \langle n \cdot n^T \rangle \qquad (15)$$

where $\langle \ \rangle$ denotes expected value, and T denotes transpose Then the least-squares solution for x, $\hat{X}$ is given by

$$\hat{X} = (A^T V^{-1} A)^{-1} A^T V^{-1} y \qquad (16)$$

which has formal error covariance on X given by

$$\langle \hat{X}_e \cdot \hat{X}_e^T \rangle = (A^T V^{-1} A)^{-1} \qquad (17)$$

when

$$\hat{X}_e = \hat{X} - \langle \hat{X} \rangle$$

A non-linear problem such as that posed by parameterizing Eq. (13) may be solved by assuming that it is incrementally linear in the neighborhood of some approximate solution and then solving an iterative series of (hopefully converging) linear least-squares problems. If such linearization is valid at the final solution point, and if the norm of the formal error covariance Eq (17) is small, then the formal error covariance of the linearized problem is also the formal error covariance of the nonlinear base problem. The A-matrix is to be interpreted as the matrix of partial derivatives of the k observation values with respect to the m parameters.

The $l + 1^{st}$ step of this iterative procedure is given by

$$\hat{X}_{l+1} = \hat{X}_l + (A_l^T V^{-1} A_l)^{-1} A_l^T V^{-1} [y - \hat{Y}(\hat{X}_l)] \quad (18)$$

where the subscript on A_l indicates that the partial derivatives which comprise this matrix are evaluated at $\hat{X}_l$, the prior best estimate of the parameters X. $\hat{Y}(\hat{X}_l)$ is the modeled expected value of the observable y, evaluated at the parameter point $\hat{X}_l$ Convergence is indicated when no significant change occurs in $\hat{X}_{l+1}$ This will occur at the "true X" if the functional dependence of $\hat{Y}(X)$ upon X is correctly specified, but may occur almost anywhere else if our model is wrong

This feature of the processing implies that there is in fact *no* bias built into the system until the estimation of parameters Even phenomena as apparently insidious as multipath are but linear filtering operations which can be modeled and their effect eliminated as long as this effect is not so severe as to destroy the 1 1 mapping of input to output They may cause severe degradations, but not bias errors, if properly modeled

In later sections, when we attempt to evaluate the biases which result either from our lack of knowledge about the system, or laziness in developing the model used to estimate parameters, we will assume that such biases are small, within the linear range of the final iteration step Eq (18) With this assumption, we can compute the bias for a model mismatch directly from Eq (18) by replacing the observed y with a correct model for Y($\hat{X}_l$) Furthermore, if the bias is not large, we could equally well approximate the bias for some "pro-

IV. Sensitivity to Receiver Filter Variations

As noted earlier, bias errors in the estimation of the VLBI cross-correlation parameters arise predominantly from mismatch between the model for the receiver filter structure and the receiver itself For this section, we will assume that we know exactly the *form* of the receiver filters, but know the filter parameters with some small error. This error could arise from variations in filter component values during manufacture, from errors in measurement of the parameters, or from environmental effects (predominantly thermal) during operation of the system Such error is of particular interest when we are *not* using real-time calibration If properly done, calibration should remove most of the variation observed

For specificity, we will assume that the maser front-end amplifier and mixer-amplifier $H_i(s)$ correspond to three pole-pair filter functions which were observed in a VLBI experiment (Ref 7) For bandwidth synthesis operation, the final-filters $G_i(s)$ correspond to 7-pole Butterworth filters with 2-MHz passbands (Ref 8) Filter functions for the quad-hybrids which implement a physical single sideband (SSB) demodulator are assumed to be very simple 4-pole networks covering 0 1 to 2 MHz (e.g , Ref. 9)

Variations in the discrete component filters can be reasonably anticipated to be on the order of one part in 10^3 due to environmental changes Variations in manufacture could be more than one part in 10^2 unless special care is taken in selecting components The low-noise maser amplifier is considerably more stable than this, but is subject to manual tuning, so variations between experiments could be on the order of a few parts in 10^3 Within any one experiment, laboratory evidence (Ref 2) suggests that variations can be held to one part in 10^5 or 10^6 But recent field tests in preparation for the Pioneer Venus atmosphere wind experiment (Ref 10) observed narrow-band group-delay variations on the order of a nanosecond, which corresponds to filter-parameter changes of a part in 10^4, far in excess of the laboratory experience

For the numerical results to be presented, the offset in correlation parameters is calculated using Eq. (18) for errors in filter pole positions of one part in 10^4 For the results to be

posed model" if we knew what the "correct model" was and solved Eq (18) using the "proposed model" as the observed vector y and the "correct model" as the model for functional dependence. This latter form is more convenient for reviewing a wide variety of proposed models, and will be used in the following sections

presented, the pre-whitening filter V^{-1} is ignored and treated as an identity matrix Poles are adjusted one at a time with the exception that complex pole pairs are moved pair-wise, with their real and imaginary parts varying individually, as befits actual physical parameter variations Variations of this magnitude appear to be within the linear range of the MMSE parameter-estimator so that parameter biases for the anticipated physical variations can be taken directly from these calculations The anticipated overall delay variation will be interpreted to be the root-sum-square (RSS) of the effects of varying the individual filter parameters, since the parameters will all move under the environmental forces, but not coherently

Our interest for this section is exclusively on the effects of filter changes, so we must avoid errors in calculation due to "end-effects" from the finite-length data record This can be done directly by working with a data record which is long enough so that whatever end-effects may exist are reduced to a negligible level relative to the complete "traces" of the cross-correlation function which occur through the middle of the record We can also approximate this long-record processing by utilizing precisely one trace of the cross-correlation function covering a delay-distance equal to the number of lags to be used in normal processing Since this "trace-mode" is computationally much cheaper, it will be used in the majority of our calculations, and the results verified by a few calculations with long records

Figure 2 (from Ref 7) shows the assumed passbands for the maser front-end amplifier and mixer amplifier. Each receiver exhibits three distinct complex pole-pairs, two of which are probably in the maser-amplifier itself, and the third in the succeeding electronics. The effect of filter pole motion on parameters estimated for the cross-correlation of these two passbands was calculated for full-band sampling using an 8-lag cross-correlation trace at doppler of 1×10^{-5} Table 1 gives the offset in delay and phase caused by changes of one part in 10^4 of the imaginary parts of the filter pole-pairs Offsets caused by the real-parts of these filter pole-pairs were observed to be typically 2 orders of magnitude smaller than those caused by the corresponding imaginary part, and thus were not included in Table 1. Identical results were obtained at 1×10^{-7} doppler This example was also calculated for a record length of 5 sec at 1×10^{-5} doppler, with a resultant RSS time delay offset of 0.22 ns, reasonably close to the 0 23 ns found by the single-trace calculation If, as discussed above, we can anticipate variation in the maser-amplifier of one part in 10^4, we should anticipate a related time-delay estimate offset of about 0 23 ns, or 7 cm, equivalent path-length, which is variable and dependent upon environmental factors.

Bandwidth synthesis operation considerably complicates the task of understanding the receiver parameter effects. Segments of the RF passband are extracted by a single sideband (SSB) demodulator with an appropriately set local oscillator and low-pass filter. We consider only the two most widely separated segments for which the synthesized time-delay estimate is the ratio of the difference of phases (of two selected segments) to the difference of center frequencies (of these two segments) The individual channel group delay is now only an auxiliary parameter. The effect of filter pole motion on parameters estimated for the cross-correlation of segments of the RF passbands was calculated at 10^{-7} doppler using a single trace of the cross-correlation function for local-oscillator (LO) frequencies ranging from 2250 to 2315 MHz Results for frequencies outside of the passbands (2265 to 2300 MHz) in Fig 2 are questionable because the noise from the mixer-amplifier (3000 K) is becoming significant with decreased gain and is not included in the calculations

Variations in the final filter of the BWS demodulator (a 7-pole Butterworth at 2 MHz) must be considered in two forms, depending upon whether a single filter is used and time-multiplexed between segments of the passband, or different filters are used in each segment In either case, the resultant effect is quite small, so a typical example will be discussed instead of a range of results. For a *common* filter, operating with LO's of 2260 and 2300 MHz, the RSS of differenced phase offsets for the 14 poles in these filters is approximately 3.6×10^{-3} m, which indicates that a synthesized delay offset of only 15 picoseconds should be expected for component variations of one part in 10^2 (Table 2). If *different* filters are used with LO's of 2260 and 2300 MHz, the RSS of the phase offsets for the 28 poles of these filters is approximately 28×10^{-3} m, which indicates that a synthesized delay offset of 0 11 nanoseconds (3 3 cm) should be anticipated for component variations of one part in 10^2 Assuming that manufacturing-related tolerances on the order of one part in 10^2 are uncompensated and uncalibrated, configuration-dependent offsets in the synthesized delay (2260-2300) of 3-5 cm can be anticipated As environmental changes to the filters should be on the order of a part in 10^3, changes in the synthesized delay should be less than 1 cm

Variations in the quad-hybrid demodulator filters also affect results differently, depending upon whether a single demodulator is time-multiplexed between channels, or multiple demodulators are used Our calculations were performed using very simple 4-pole quad-hybrids covering 0 1 to 2 MHz Since *real* quad-hybrids may have 12 or more poles (and zeros), the offsets due to their variations are likely to be twice what is observed numerically here For a *common* demodulator, operating with LO's of 2260 and 2300 MHz, the RSS of differenced phase offsets for the 8 poles in these demodulator

filters is approximately 0.43×10^{-3} m, which indicates that a synthesized delay offset of less than 2 picoseconds can result from component variations of one part in 10^2 (Table 3). If *different* demodulators are used with LO's of 2260 and 2300 MHz, the RSS of the phase offsets for the 16 poles of these filters is approximately 5.7×10^{-3} m, which indicates that a synthesized delay offset of about 23 picoseconds (0 7 cm) can result from component variations of one part in 10^2 Assuming that manufacturing-related tolerances on the order of one part in 10^2 are uncompensated and uncalibrated, configuration-dependent offsets in the synthesized delay (2260-2300) of about 1 cm can be anticipated. Environmental changes to the demodulator synthesized delay should be on the order of 1 mm Even if a realistic quad-hybrid, because of its increased complexity, has variations of twice that of the simple one used here, the offsets due to the quad-hybrid parameters are still small (in an RSS-sense) compared to the offsets due to the final filter parameters This may, however, be an overly simplistic view, as it ignores the active electronic elements which interconnect the two filters in the quad-hybrid to make up the demodulator proper Testing of a complete demodulator unit appears to be the best way to ensure a realistic understanding of demodulator variations.

The effects of the maser-front-end amplifier variations are always common between segments of the passband, and so are relatively independent of whether a single time-multiplexed demodulator and final filter or multiple ones are used The actual effects of these variations do depend significantly upon the placement of the selected channel within the passband. Figure 3 shows the channel group delay offset caused by a change of one part in 10^4 in the imaginary parts of each of the 6 RF poles as a function of the LO frequency The maximum offset is on the order of 1 nanosecond, which is approximately that observed in field experiments (Ref 10), and lends credence to the belief that anticipated physical variations should be on the order of one part in 10^4 Figure 4 shows the channel phase offset caused by a change of one part in 10^4 in the imaginary parts of each of the 6 RF poles as a function of the LO frequency The data in Fig 4 can also be presented as in Fig. 5 which shows the RSS synthesized delay offset resulting from filter pole variation of one part in 10^4 with various selected spanned bandwidths, as indicated

If we can anticipate variation in the maser-amplifier of one part in 10^4, we should anticipate a related synthesized time-delay estimate offset between 0 2 and 0.5 ns (6 to 15 cm path length), which is variable and dependent upon environmental factors The offset observed is a function of the placement of the selected channel within the passband, and it appears that we are at least as likely as not in doing BWS to select channels for which the sensitivity is 20 to 50% larger than the sensitivity of the full band sampling We note,

however, from Fig 4 that the phase sensitivity decreases *outside* of the main passband, so that *if*, for example, we could successfully operate at 2255-2315, the sensitivity appears to be only 0 034 ns for filter variations of one part in 10^4 These results are related to the physical model assumed for TWM variations, and should be verified experimentally.

We need also to be aware that we never really know the receiving filters, as has been assumed in this section, but are forced to estimate it through measurements and/or calibration The effect of channel estimation and calibration is the subject of the next two sections.

V. Channel Modeling for Bandwidth Synthesis

The intent of this section is to determine the minimum complexity receiver models for the bandwidth synthesis VLBI receiver which will yield suitably small errors in the resultant estimates We will, in the following, propose and evaluate channel models of varying complexity The results of this section should *not* be construed as representing the performance of any existing VLBI processing, although the tools employed here can be applied to any existing or proposed processing schemes

The receiver passbands of Fig. 2 are again assumed to be the RF-front-end filter. There is reason to believe that these receivers represent a somewhat pathological choice, because the mismatch between passbands, while an example of a real experiment, is nevertheless a worse condition than should be achieved in a "typical" experiment with careful tuning of the traveling-wave masers (TWM). Therefore, we believe that if a channel modeling scheme can be made to give some specific level of accuracy with this example-pair of receiver passbands, then this same level of accuracy should be achievable in practice in most experiments

The BWS final filter will be assumed to be a 2-MHz-wide 7-pole Butterworth which is itself a practical approximation to an ideal *square* passband The assumed SSB demodulator is the simple 4-pole R-C type used in Section IV

The most naive channel model we are tempted to try is the mathematical square passband, both with and without calibration Calibration consists of a very stable and well-controlled pulse train which is injected into the signal path ahead of the maser (Ref 11) In the frequency domain, this pulse train is seen as a "comb" of pilot-tones with related phases, of which at least one, or perhaps many may appear in each of the BWS channels If one tone appears in each channel, it is capable of measuring (relative to itself) the phase of the local oscillator

and approximating the phase-effect of the receiving filters A second tone gives some information about the transport lag in the receiving system It also gives some information about the relative amplitude of the receiving filters Increasing the number of tones in each channel improves the ability to measure the transfer function of the receiver filters (Ref 12). We assume, for now, that the calibrator itself is "perfect"

The models for which the bias offsets were calculated are of two general types "Type A" models incorporate a mathematically square 2-MHz passband with zero, one, or two pilot tones; "Type B" models incorporate the transfer function of a Butterworth filter and quad-hybrid demodulator, which is nominally the same as that in the assumed receiver function, along with zero, one, or two pilot tones All demodulators select upper sideband Where one pilot tone is used, it is placed 0.5 MHz from the lower band-edge. Where two pilot tones are used, they are placed 0.5 MHz from each band-edge Models A1 and B1 utilize no pilot tones, but their calculation assumes that the phase of the LO is stable and known, so that the only unknown phase is that induced by the receiving filters Models A2 and B2 utilize one pilot tone to calibrate the phase shift through the unknown receiver filters, and along with that, the phase of the LO Models A3 and B3 utilize two pilot tones to jointly calibrate the phase shift and transport-lag equivalent of the unknown receiver filters Model B4 utilizes the relative *magnitudes* of the filter responses to the two pilot tones to estimate the parameters of single-tuned-filter approximation to the RF filter $H(s)$ The residual phases of these pilot tones are then used to determine the phase-shift and transport-lag of the receiver, as in Model B3

As a practical matter, when two pilot tones are used in each channel, their frequencies would be slightly displaced from the multiples of 0 5 MHz in order to avoid harmonic interaction

The Model B4 transfer function is of the form

$$B4H(s) = \frac{A \cdot s \cdot e^{\tau s + j\phi}}{(s - y - jx)(s - y + jx)} \qquad (19)$$

where the *five* parameters A, τ, ϕ, y, and x are to be chosen to best fit the amplitude and phase at each of two pilot tone frequencies Since there is one more unknown than measurement, we complete the problem definition by assuming that the bandwidth y is as large as possible consistent with Eq (19), but not larger than some preset value y_0 We have taken $y_0 = 40$ Mrn/sec to correspond roughly to the individual poles in Fig 2 The approximate solution for the parameters x and y is as follows Let w_1 and w_2 be the (angular) pilot tone frequencies, and let $\Delta = w_2 - w_1$ Let $H1$, and $H2$ be the measured complex response of the receiver passband at w_1 and

w_2, exclusive of the final filter and demodulator Let the preliminary values for x and y be $x_0 = (w_1 + w_2)/2$ and y_0 as above Then we take

$$\rho = \left| \frac{H_1}{H_2} \right| \cdot \frac{w_2}{w_1} \cdot \sqrt{ \frac{y_0^2 + (w_1 + x_0)^2}{y_0^2 + (x_0 + w_2)^2} }$$

$$y = \min \{y_0, \Delta \cdot \rho/(\rho^2 - 1)\} \qquad (20)$$

$$x = w_1 + \frac{-\Delta + \sqrt{\rho^2 \Delta^2 - y^2 (\rho^2 - 1)^2}}{(\rho^2 - 1)}$$

to be our approximate solution to the magnitude part of Eq (19) The phase and delay parameters are determined after inserting these x and y values into Eq (19)

, The offset between the parameter estimates for these models and the assumed true receiver has been calculated using a single trace of the cross-correlation function — usually covering six lags The phase is in all cases referenced to the frequency at the passband center as determined from the assumed receiver's transfer function, and not from the pilot-tone responses In practice, this reference frequency would be determined from the autocorrelation of the recorded data.

Figure 6 shows the estimated differential phase offset for all models at a doppler of $1_{10}-7$ as a function of mixing frequency With no pilot tones, the offset phase swings by nearly 1 radian as the mixing frequency traverses the frequencies below 2270 MHz, where the two RF passbands show significant missmatch Were we to do delay synthesis using 2265-2305, a delay error of about 0 5 meter would result A single pilot tone is seen to be sufficient to reduce this swing to about 0 1 m, and the synthesized delay error to less than about 10 cm The use of transport-lag information from the second pilot tone reduces the phase swing still further to below 0 02 m And at this scale, model B4 appears perfect

At an expanded scale, Figure 7 shows the offset phase as a function of mixing frequency for models 2-4 at a doppler of $1_{10}-7$ An identical figure would be drawn for any doppler smaller than $1_{10}-7$ Increasing doppler, however, does change the offset phase as can be seen by observing Figures 8, 9, and 10 which represent dopplers of $1_{10}-6$, $3_{10}-6$, and $1_{10}-5$, respectively The largest differential doppler to be expected for two Earth-bound receivers is on the order of $3_{10}-6$ At this doppler, *all* models have shown some phase shift relative

to $1_{10}-7$ doppler, and the Type-A models show phase shift approaching 0 03 m. The effect of doppler on synthesized delay is not as large as on channel phase because the phase shift is in the same direction in channels at all frequencies Figure 11 shows the synthesized delay offset for mixing frequencies 2260-2300 as a function of applied doppler Model B4 changes by only 0 01 ns (0 3 cm) for doppler changing $1_{10}-7$ to $1_{10}-5$ Model B3 changes by 0 05 ns (1 5 cm) and models B2, A2, and A3 changes by 0.06 ns (1 8 cm) for doppler increasing from $1_{10}-7$ to $1_{10}-5$. For real dopplers restricted to below $3_{10}-6$, the synthesized delay change is negligible for model B4, and below 0 02 ns (0 6 cm) for models 2 and 3 The part of the synthesized delay offset which does not depend on doppler is approximately 0 4 ns for the No 2 models, 0 05 ns for the No 3 models, and apparently negligible for model B4.

The "end-effects" from finiteness of the data record can be greatly enhanced by considering parameter estimation for a single-trace of the cross-correlation function which has been asymmetrically truncated. Even with this exaggeration, model B4 exhibits less than 1 cm synthesized delay offset (2260-2300) when receiver and model final filters are perfectly matched. For the more normal mode, sample calculations with a record length of 15 sec and 10^{-7} doppler have exhibited no end-effect variations with any model larger than 1 mm in synthesized delay for perfectly matched receiver and model final filters End-effects should be reexamined with mismatched final filters

In the foregoing, Type-B models have been generated assuming that the transfer functions of the demodulator and final filter are exactly known At best, these filters are subject to manufacturing tolerances, and at worst, the quad-hybrid may be some company's trade secret, and its transfer function known to us only through our measurements. The exploration of this space is similar to that of Section IV, but is compounded by carrying several alternative models here Some exploration has been done which should approximate worst-case for the demodulation filters Figures 12 and 13 show the estimated channel phase which results when the demodulator transfer function of Station 1 only is scaled upward in frequency by 1'0%, for dopplers of $1_{10}-7$ and $1_{10}-5$ The shift to the No 2 models' phase is on the order of 0 01 m and varies with doppler and mixing frequency The shift to the phase of model B4, or No 3, is of the order of 0 003 m, and is again dependent upon doppler and mixing frequency Thus an unlikely large error in our knowledge of the demodulator filters results in a synthesized delay error which is at worst 1-2 cm for any of the pilot-tone models If we try at all while the equipment is being built, we should be able to know these filters to within a few percent, and hence reduce errors related

to modeling of this portion of the equipment to less than 0.5 cm in synthesized delay.

Errors in generating and/or measuring the phase calibrator tones cause channel phase errors in the relatively obvious way Phase errors of 10^{-2}m on a calibration tone induce channel phase errors of 0 5 to 2×10^{-2}m Amplitude errors of 1% on a calibration tone induce channel phase errors of roughly 10^{-3}m in model B4, with no effect on the other models There is thus a need to hold at least the differential phase errors between the calibration tones in the upper and lower bandwidth synthesis channels to well below 10^{-2}m if accuracies on the order of 1 cm are to be achieved with 40-MHz spanned bandwidth This requires careful design and fabrication of the calibrator itself, and SNR's of at least 50-60 dB on the detected calibration tones

Assuming that a suitable calibrator can be achieved, we summarize the results of this section as follows If no calibration is used, the receiver filters alone can represent as much as a 1-meter offset in direct delay if the phases of the mixing references are known A single calibration tone in each channel can reduce this offset to perhaps 10-15 cm, of which only a few cm is doppler-dependent Using two calibration tones in each channel together with modeling technique B4 can further reduce this offset to under 1 cm This last result depends upon our knowing the final filter and demodulator filters to within a few percent, and deserves to be reevaluated using the actual transfer functions of a physical device, instead of the "publication" filters employed here

VI. Discussion and Summary

Perhaps the greatest difficulty in obtaining definitive results for the biases induced by the VLBI instruments is the wide range of possible configurations and parameter values which can characterize the instrument In such a situation, the seemingly only way to get numerical results is to assume an example system which is a reasonable approximation to reality and evaluate its characteristics in detail To the extent that our example approximates some real system, our numerical results can then be used with some care to estimate the behavior of that system Our software tools may be useful for evaluating systems which are not close to the examples developed here

We evaluated the sensitivity of the VLBI estimated time delay to plausible variations in the receiver filter parameters Shifts on the order of one part in 10^4 of the RF filter poles induce delay errors of roughly 7 cm with full band sampling, and between 6 and 15 cm with bandwidth synthesis Shifts in the 2-MHz channel filters used for bandwidth synthesis were less deleterious than had been expected Environmentally caused shifts on the order of one part in 10^3 of the channel filter poles induce delay errors of less than 1 cm However, if separate channel filters are used, a fabrication tolerance of only one part in 10^2 could result in configuration-dependent delay variations of 3-5 cm.

We studied the problem of modeling the channel passbands for bandwidth synthesis If the relative phases of the BWS channel local oscillators are known, but we have no auxiliary information about the phase shift in the filter, time delay errors on the order of 0 5 to 1 m can result from these filters The use of an assumed-perfect calibrator can provide the information needed about the RF filters to reduce this error source to below 1 cm, as well as providing a definition point for time delay if the local oscillator phases are unknown

We are currently in the process of studying the problem of modeling the passbands with full band sampling In this case, the information inherent in the data appears sufficient to develop the RF filter models to within about 7 cm without external calibration The use of an assumed-perfect calibrator appears to reduce this error source to well below 1 cm. Details of these results should appear next issue
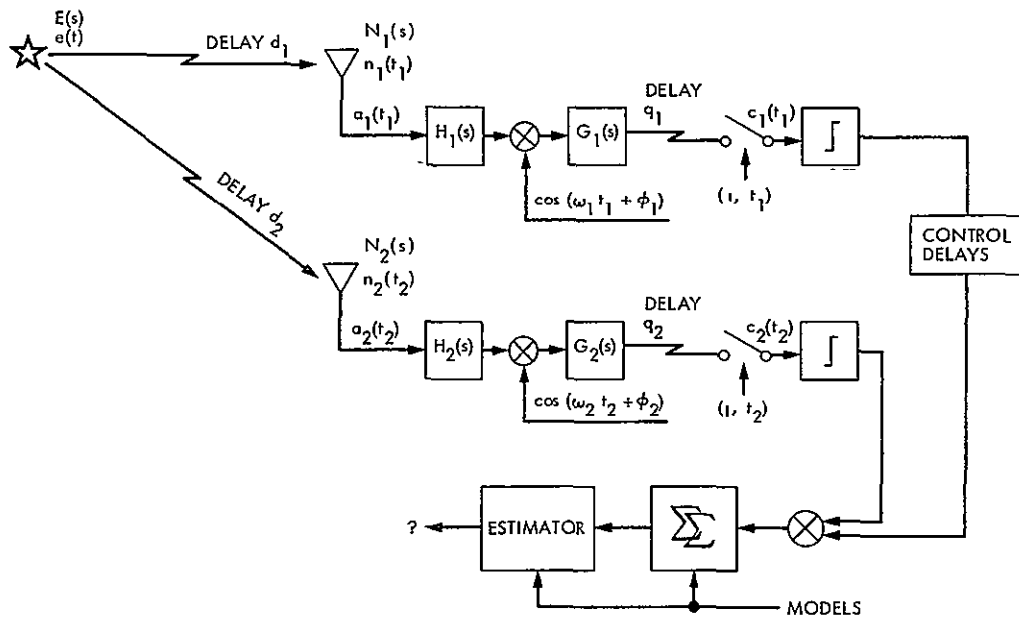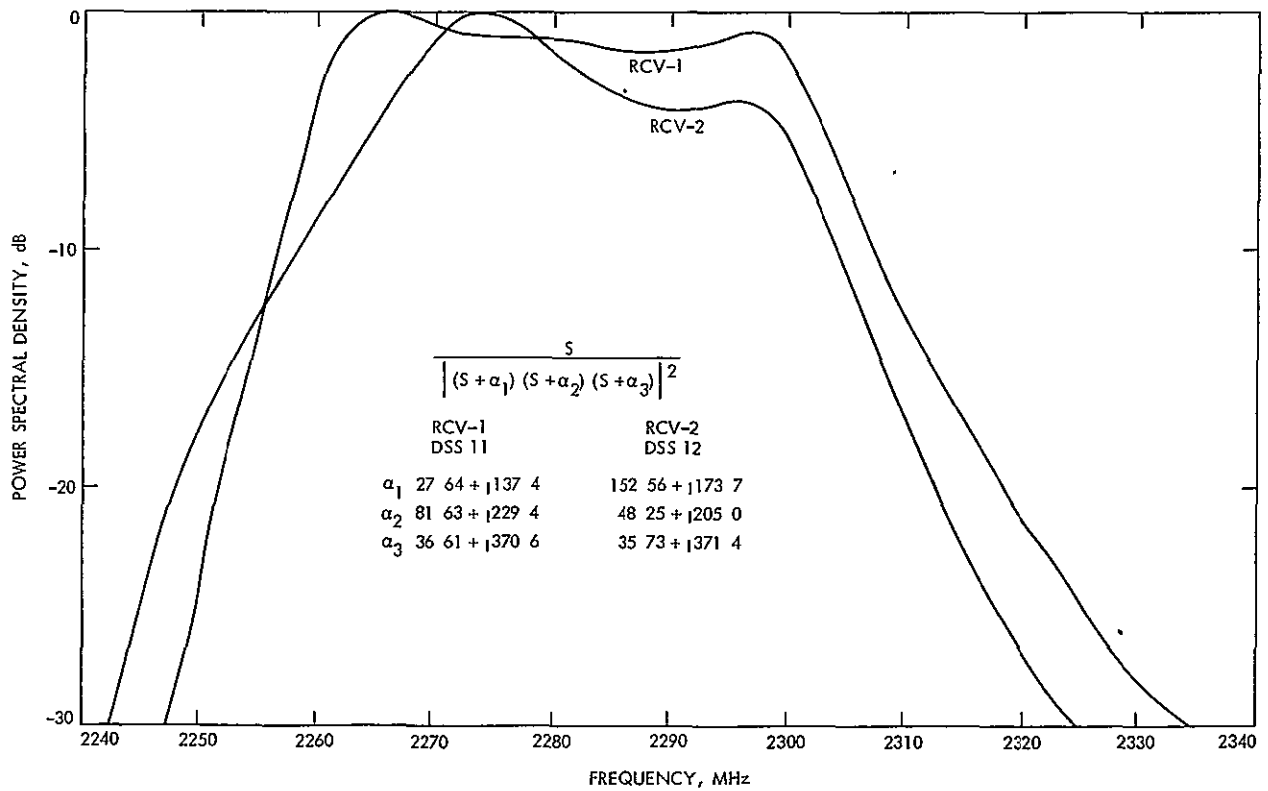
Fig. 1 VLBI system block diagram

$$\frac{S}{\left| (S+\alpha_1)\,(S+\alpha_2)\,(S+\alpha_3) \right|^2}$$

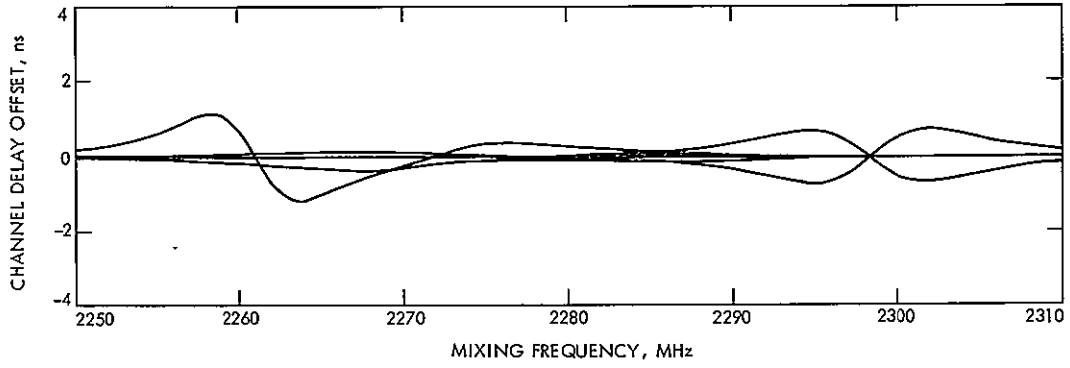|	RCV-1 DSS 11	RCV-2 DSS 12
α_1	27 64 + j137 4	152 56 + j173 7
α_2	81 63 + j229 4	48 25 + j205 0
α_3	36 61 + j370 6	35 73 + j371 4

Fig 2 Passbands of example RF filters

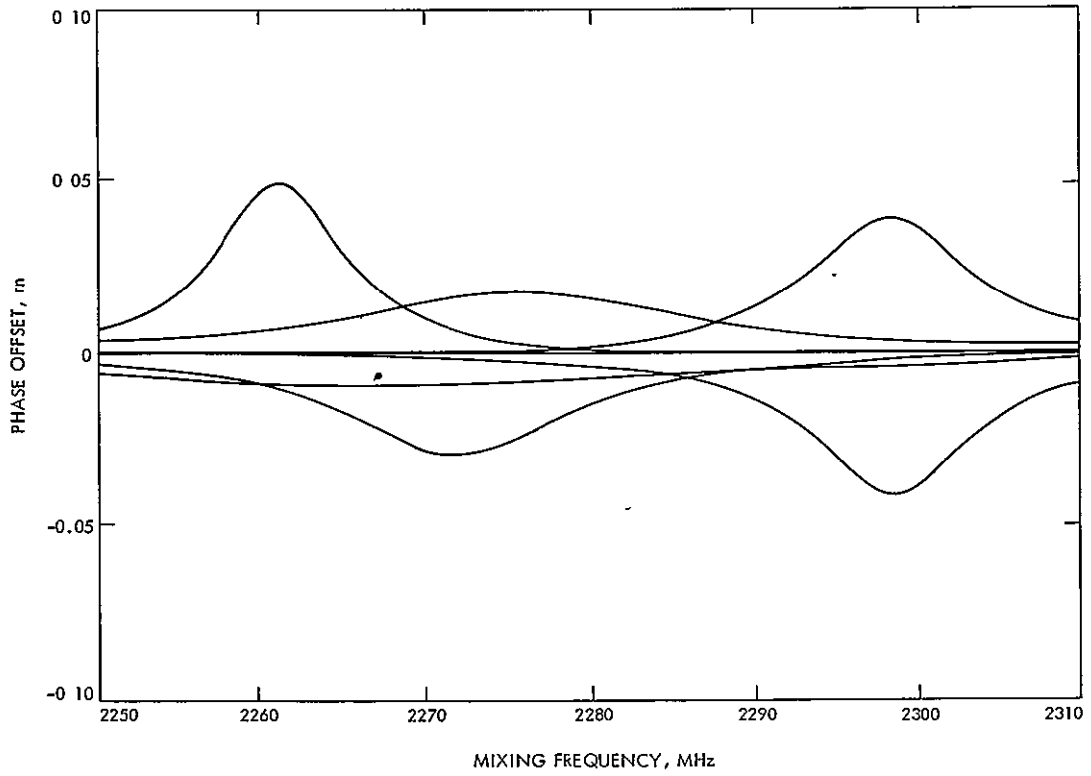**Fig. 3. Channel delay sensitivity to one part in 10^4 change in RF filter poles**

Fig 4. Channel phase sensitivity to one part in 10^4 change in RF filter poles
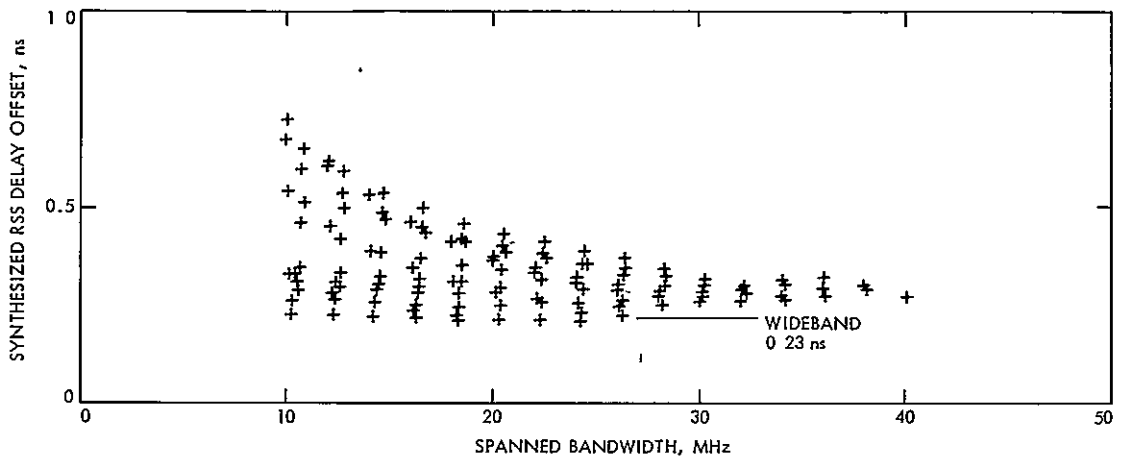
Fig. 5 Total RSS delay sensitivity to one part in 10^4 change in RF filter poles
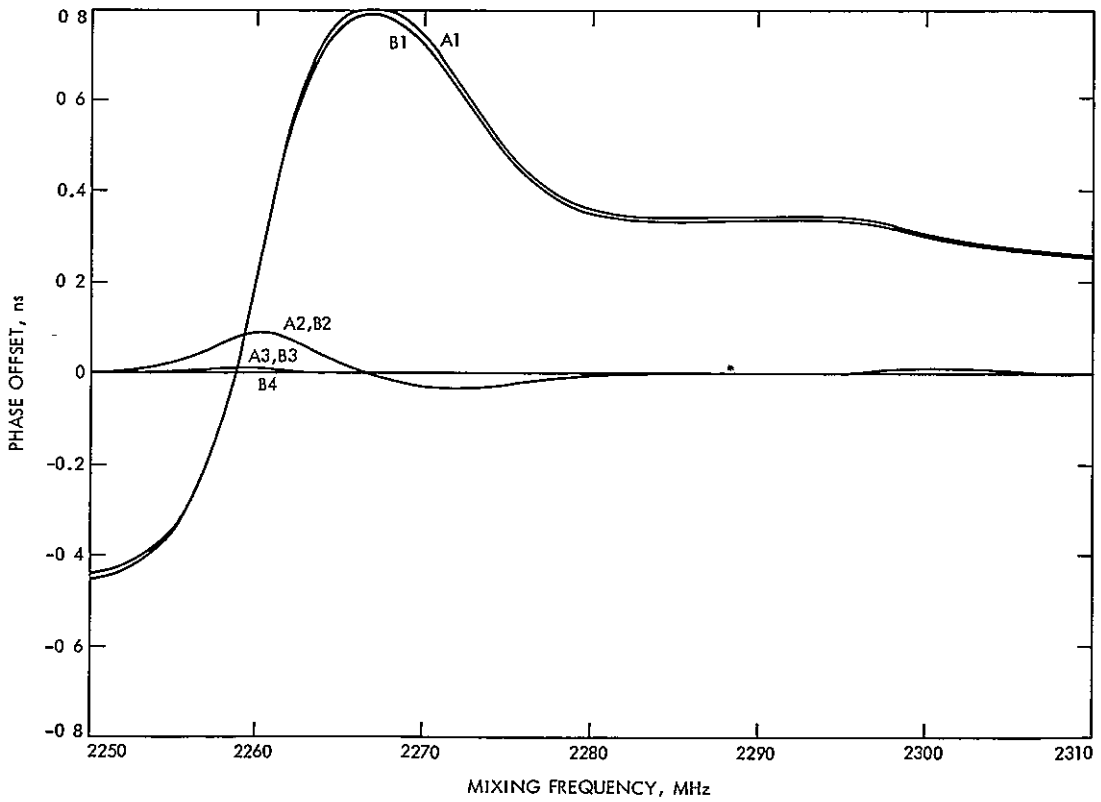
Fig. 6. Channel phase offset for channel models A1-A3, B1-B4, at 10^{-7} doppler
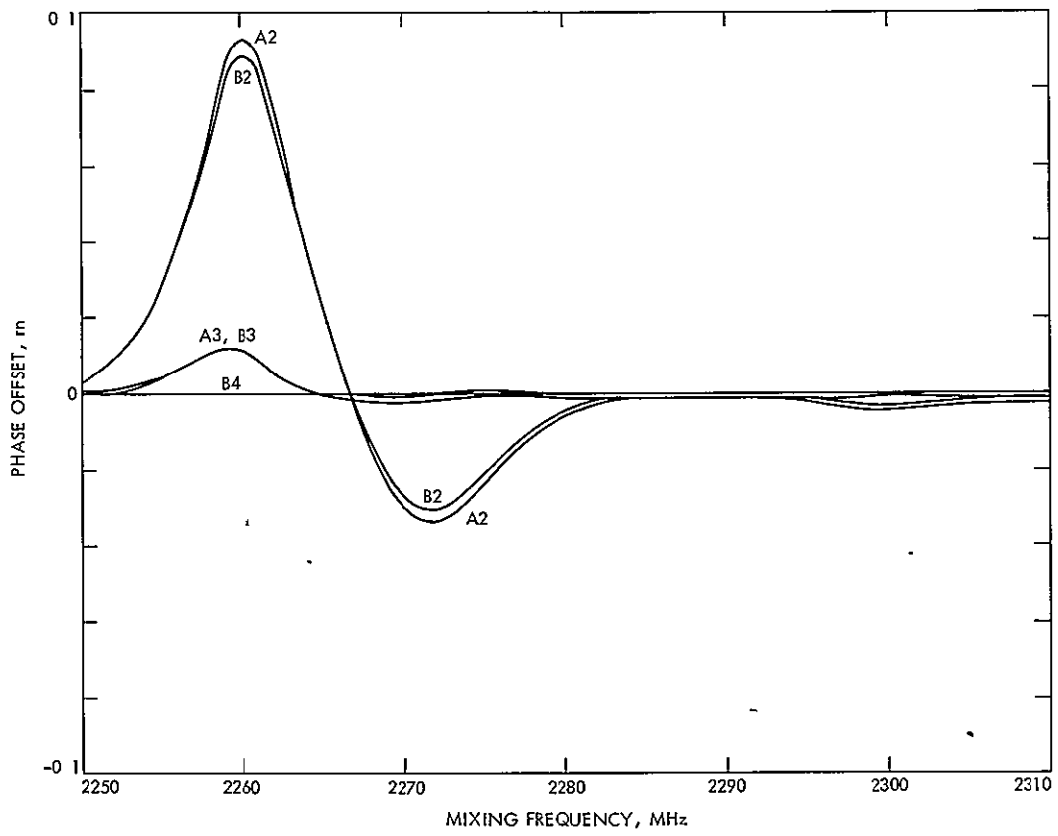
Fig. 7. Channel phase offset for channel models A2-A3, B2-B4, doppler = 10^{-7}
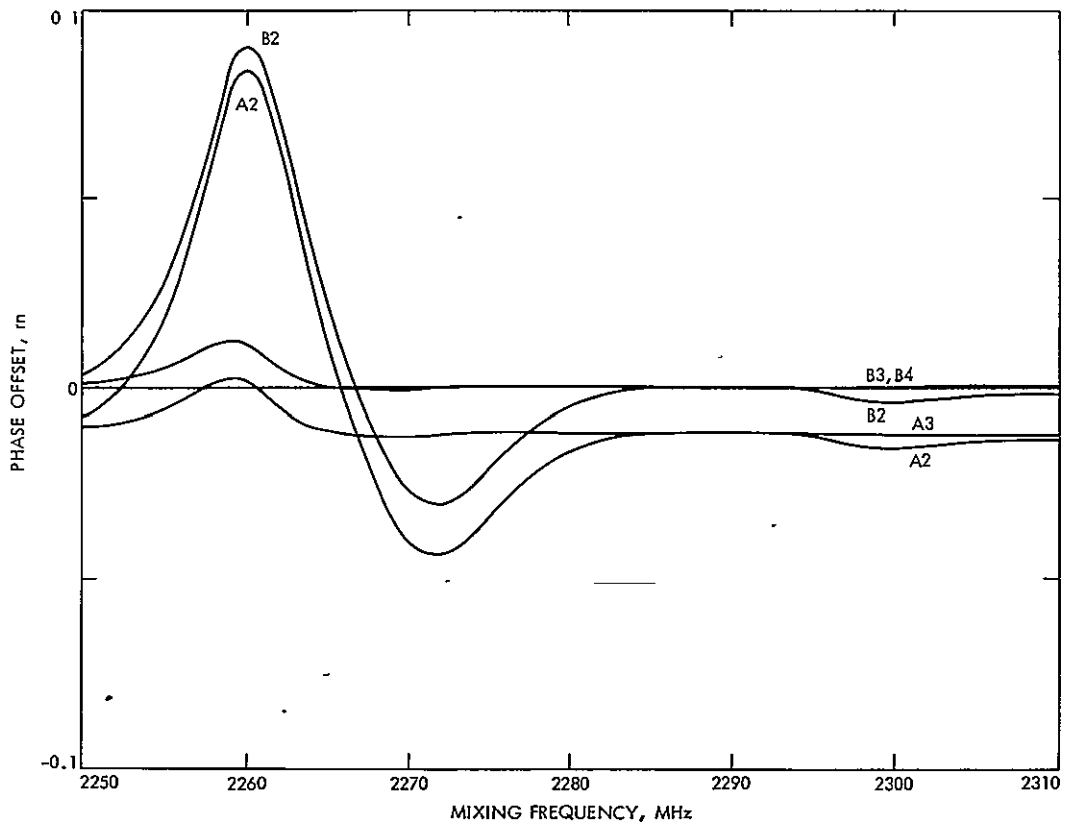
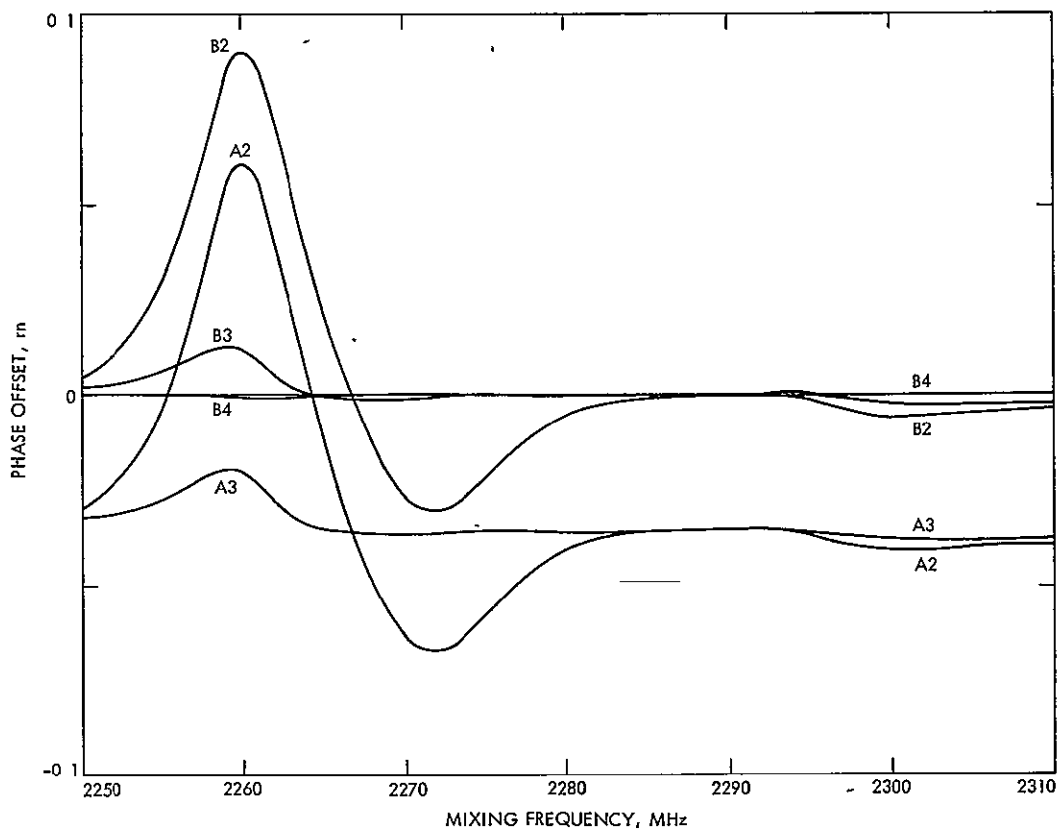Fig. 8. Channel phase offset for channel models A2-A3, B2-B4, doppler = 10^{-5}

Fig. 9 Channel phase offset for channel models A2-A3, B2-B4, doppler = 3×10^{-6}
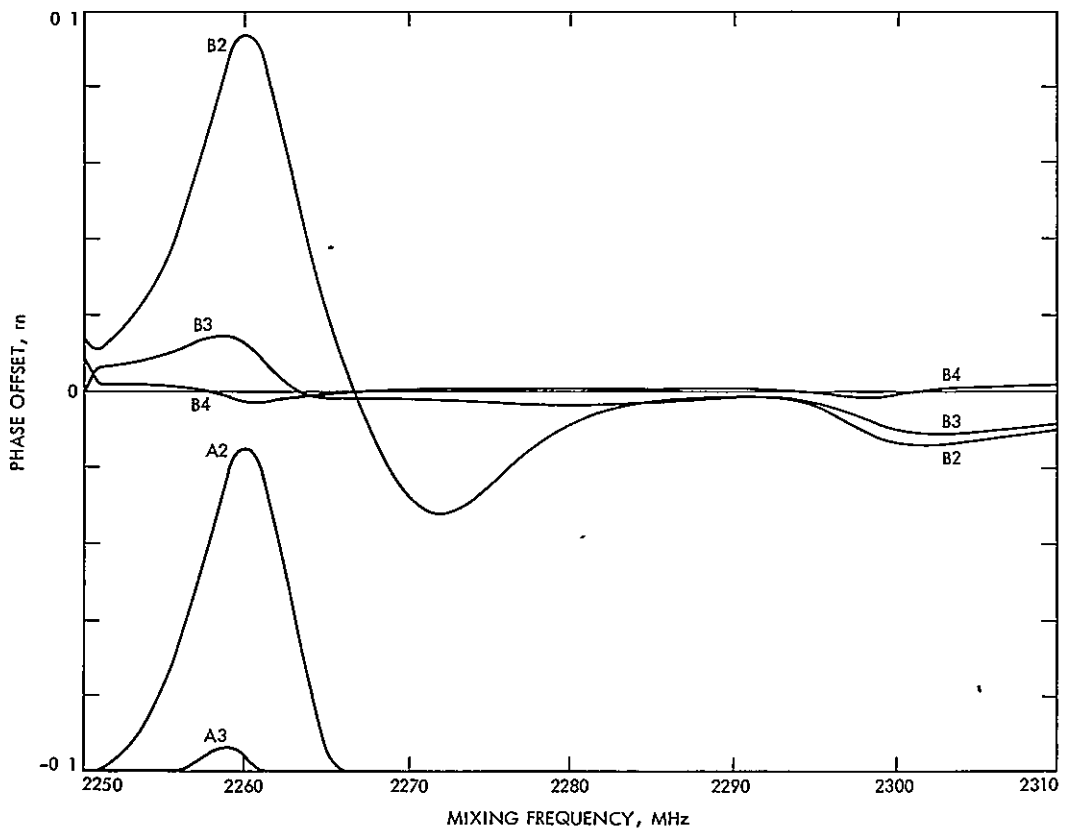
Fig. 10. Channel phase offset for channel models A2-A3, B2-B4, doppler = 10^{-5}
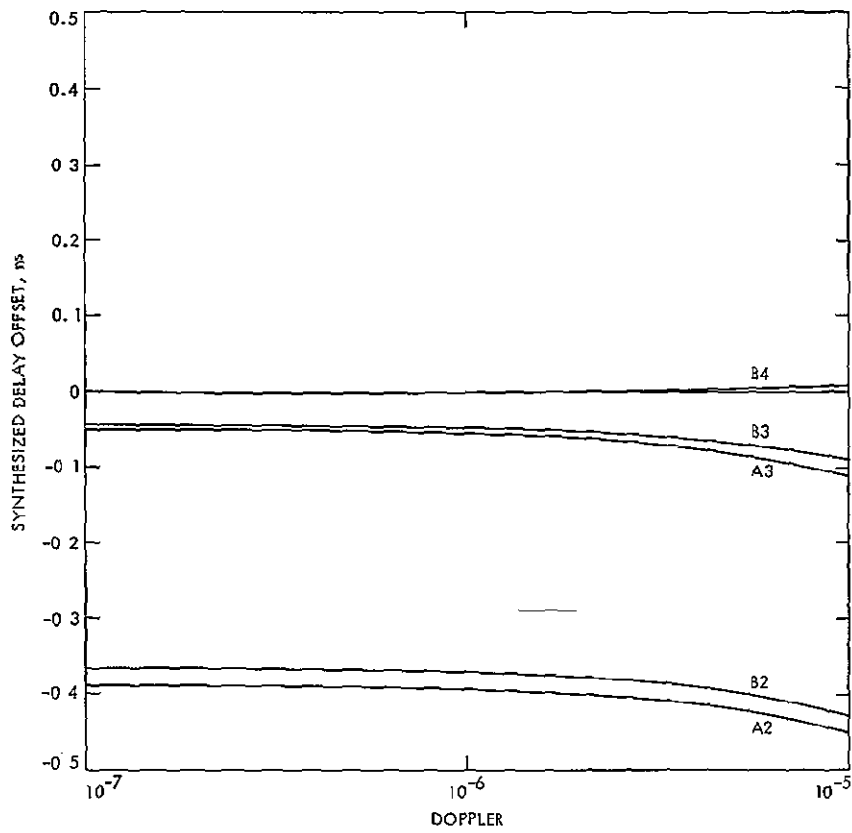
**Fig. 11. Synthesized delay offset as a function of doppler for
channel models A2-A3, B2-B4**
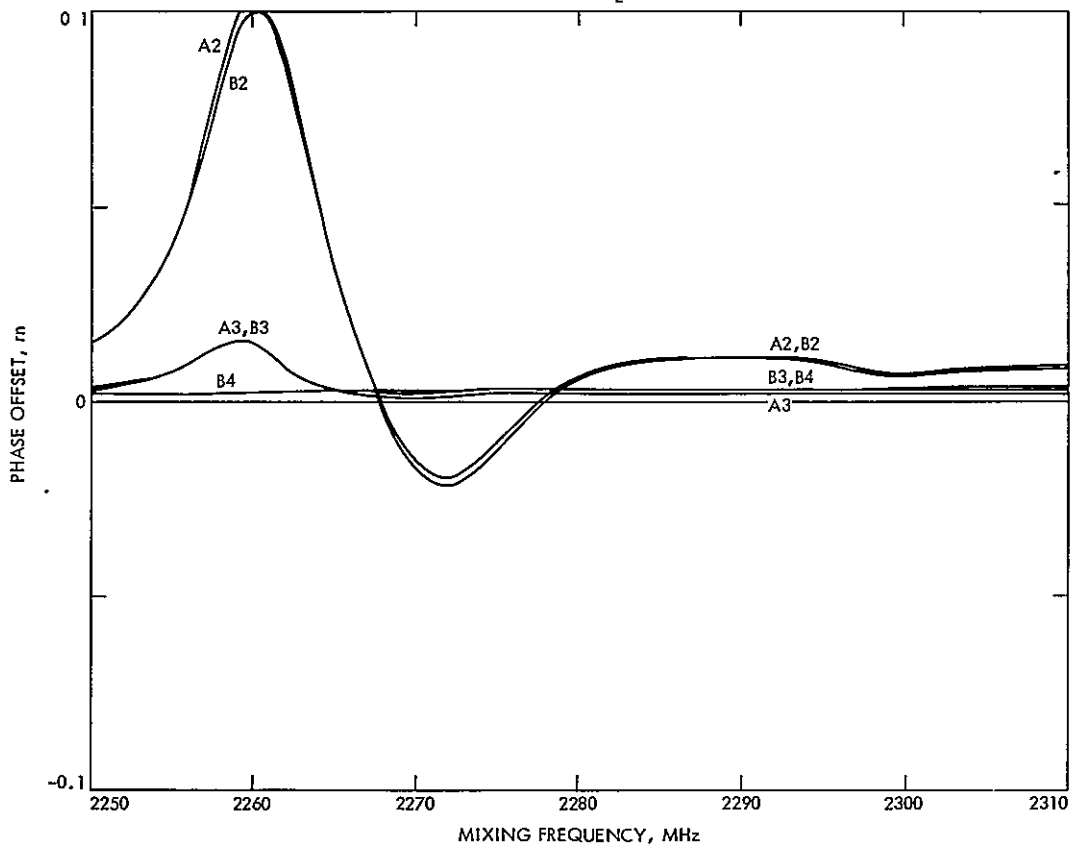
Fig. 12. Channel phase offset with 10% mismatched final filter at receiver 1,
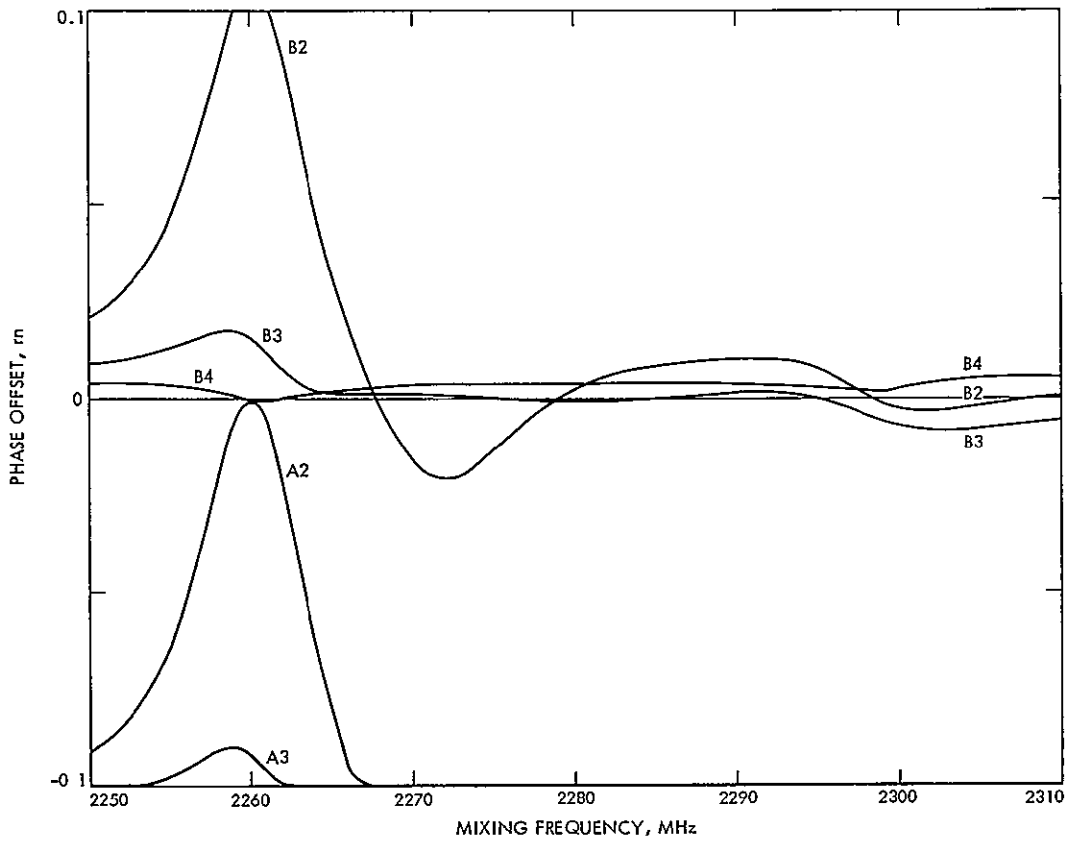for channel models A2-A3, B2-B4, doppler = 10^{-7}

Fig. 13. Channel phase offset with 10% mismatched final filter at receiver 1,
for channel models A2-A3, B2-B4, doppler = 10^{-5}

Appendix A

Expected Cross-Correlation Function
For VLBI Samples

Let the input to the ith station sampler-limiter be expressed as in Eq (11), i.e.,

$$c_i(t_i) = \int_{-\infty}^{t_i - q_i} g_i(t_i - q_i - \eta_i) \cdot \cos(\omega_i \cdot \eta_i + \phi_i)$$

$$\cdot \int_{-\infty}^{\eta_i} h_i(\eta_i - \xi_i) \tag{A-1}$$

$$\cdot \left[e(\xi_i - p_i - p_{i1} \cdot \xi_i) + n_i(\xi_i) \right] d\xi_i \, d\eta_i$$

where $g_i(\ )$, $h_i(\ )$ are impulse responses of the low-pass and RF filters, q_i is the sampler delay, $\cos(\omega_i \cdot \eta_i + \phi_i)$ is the local oscillator mixing signal at time η_i, and $p_i - p_{i1} \cdot \xi_i$ is the locally linearized propagation delay at time ξ_i, near to t_i

The cross-correlation function of the signals input to the station's sampler-limiters is defined by

$$R_c(t_1, t_2) = \left\langle c_1(t_1) \cdot c_2(t_2) \right\rangle \tag{A-2}$$

where $\left\langle \cdot \right\rangle$ denotes ensemble average, and $c_1(t_1)$, $c_2(t_2)$ are as defined by Eq (9) We will use the two-dimensional Fourier transform definitions of Papoulis (Ref 13) to manipulate this function

$$\Gamma_c(j\theta_1, j\theta_2) = \int dt_1 \int dt_2 \, e^{-j(\theta_1 t_1 - \theta_2 t_2)} R_c(t_1, t_2)$$

$$R_c(t_1, t_2) = \frac{1}{(2\pi)^2} \int d\theta_1 \int d\theta_2 \, e^{+j(\theta_1 t_1 - \theta_2 t_2)} \Gamma_c(j\theta_1, j\theta_2)$$

$$\tag{A-3}$$

This form of the cross-correlation function is rapidly varying in both coordinates It is convenient for calculations to change the coordinate system basis so that a form is obtained in which

rapid variation is suppressed in at least one coordinate Thus define

$$S_c(t, \tau) = R_c(t, t + \tau) \tag{A-4}$$

The transform of $S_c(\cdot, \cdot)$, by the definitions above, is

$$\psi_c(j\theta, j\eta) = \int dt \int d\tau \, e^{-j(\theta t - \eta \tau)} S_c(t, \tau)$$

$$= \Gamma_c(j\theta + j\eta, j\eta) \tag{A-5}$$

It is of use to calculate $R_a(\ , \cdot)$ the correlation function and its transform at the input to the two receiving systems The signal $e(t)$ is a white-noise process of density N_e when it leaves its source The signals $n_1(t_1)$ and $n_2(t_2)$ are independent white noise processes of densities N_1 and N_2. The desired correlation and its Fourier transforms are

$$R_a(t_1, t_2) = \left\langle \{ n_1(t_1) + e \, [t_1 \cdot (1 - p_{11}) - p_1] \} \right.$$

$$\cdot \{ n_2(t_2) + e \, [t_2 \cdot (1 - p_{21}) - p_2] \} \left. \right\rangle$$

$$= \frac{N_e}{2} \, \delta \, [t_1(1 - p_{11}) - p_1 - t_2(1 - p_{21}) + p_2]$$

$$\tag{A-6}$$

$$\Gamma_a(j\theta_1, j\theta_2) = N_e \cdot \pi \cdot \frac{1}{1 - p_{11}} e^{-j\theta_1 \frac{p_1 - p_2}{1 - p_{11}}}$$

$$\delta \left(\theta_1 \frac{1 - p_{21}}{1 - p_{11}} - \theta_2 \right) \tag{A-7}$$

These Fourier transforms will be extended by analytic continuation to become LaPlace transforms on the complex s-plane for manipulation of the filter functions Inversion of the extended transform is via integration along the '$j\omega$' axis, since no poles in a physically realizable filter function will fall in the right-half-plane, or on the '$j\omega$' axis

Having completed these preparations, we are now able to grind through the tedious, but not difficult, derivation of $S_c(\ ,\cdot)$. From Eq. (9), we can write by inspection the LaPlace transforms $C_i(s_i)$ at the limiter-sampler inputs

$$C_i(s_i) = e^{-q_i s_i} \cdot G_i(s_i) \cdot \frac{1}{2}\left[e^{-j\phi_i} H_i(s_i + j\omega_i) \cdot A_i(s_i + j\omega_i) \right.$$

$$\left. + e^{+j\phi_i} H_i(s_i - j\omega_i) \cdot A_i(s_i - j\omega_i) \right] \qquad \text{(A-8)}$$

for $i = 1, 2$, where $A_i(s_i)$ is the LaPlace transform of $a_i(t_i)$ Likewise, we can write the product of $c_1(t_1)$ and $c_2(t_2)$, take their expected value, and LaPlace transform in two dimensions to obtain

$$\Gamma_c(s_1, s_2) = e^{-q_1 s_1} G_1(s_1) e^{+q_1 s_2} G_2(-s_2) \cdot \frac{1}{4}$$

$$\cdot \left[e^{-j\phi_1} H_1(s_1 + j\omega_1) \Gamma_a(s_1 + j\omega_1, s_2 - j\omega_2) \right.$$

$$H_2(-s_2 + j\omega_2) e^{-j\phi_2}$$

$$+ e^{-j\phi_1} H_1(s_1 + j\omega_1) \Gamma_a(s_1 + j\omega_1, s_2 + j\omega_2)$$

$$H_2(-s_2 - j\omega_2) e^{+j\phi_2}$$

$$+ e^{+j\phi_1} H_1(s_1 - j\omega_1) \Gamma_a(s_1 - j\omega_1, s_2 - j\omega_2)$$

$$H_2(-s_2 + j\omega_2) e^{-j\phi_2}$$

$$+ e^{+j\phi_1} H_1(s_1 - j\omega_1) \Gamma_a(s_1 - j\omega_1, s_2 + j\omega_2)$$

$$\left. H_2(-s_2 - j\omega_2) e^{+j\phi_2} \right] \qquad \text{(A-9)}$$

It should be noted that for any systems we are likely to build, $G_i(s_i)$ are at least zonal low-pass, so that their response to frequencies greater than ω_i is negligible Also, we expect $\omega_1 \approx \omega_2$, and from Eq (A-7) we know that $\Gamma_a(j\theta_1, j\theta_2)$ is zero unless $\theta_1 \approx \theta_2$ These facts combine to make the first and fourth terms of the parenthesized factor in Eq (A-9) identically zero, which helps to simplify our succeeding algebra.

When rotated into the desired coordinates, the transformed cross-correlation becomes

$$\psi_c(\theta, \eta) = e^{-q_1(\theta + \eta)} G_1(\theta + \eta) e^{q_2 \eta} G_2(-\eta) \cdot \frac{1}{4}$$

$$\cdot \left[e^{-j\phi_1} H_1(\theta + \eta + j\omega_1) \right.$$

$$\Gamma_a(\theta + \eta + j\omega_1, \eta + j\omega_2) H_2(-\eta - j\omega_2) e^{+j\phi_2}$$

$$+ e^{+j\phi_1} H_1(\theta + \eta - j\omega_2) \Gamma_a(\theta + \eta - j\omega_1, \eta - j\omega_2)$$

$$\left. H_2(-\eta + j\omega_2) e^{-j\phi_2} \right] \qquad \text{(A-10)}$$

We now define the partially-inverse LaPlace transform of $\psi_c(\ ,\ )$ with respect to its first argument as

$$\psi_c^*(t, \eta) = \frac{1}{2\pi j} \int_{-j\infty}^{+j\infty} e^{\theta t}\, \psi_c(\theta, \eta)\, d\theta \qquad \text{(A-11)}$$

To evaluate this integral, we insert the definition of $\Gamma_a(\ ,\ )$ into Eq (A-10) where the factors $\Gamma_a(\theta + \eta \pm j\omega_1, \eta \pm j\omega_2)$ are obtained by substituting $\theta + \eta \pm j\omega_1$ for $j\theta_1$, and $\eta \pm j\omega_2$ for $j\theta_2$ in Eq (A-7), where the sign affixed to the mixing frequency is determined from the term selected in Eq (A-10). We integrate by using the definition of the delta function — that its integral with respect to its argument has value unity, and that the entirety of this integral arises where the argument itself is zero, i.e., at

$$\eta \pm j\omega_2 = (\theta + \eta \pm j\omega_1) \frac{1 - p_{21}}{1 - p_{11}} \qquad \text{(A-12)}$$

or

$$\theta = \pm j(\omega_2 - \omega_1) + (\eta \pm j\omega_2)\left(\frac{p_{21} - p_{11}}{1 - p_{21}} \right) \qquad \text{(A-13)}$$

By collecting terms, this integral becomes

$$\psi_c^*(t, \eta) = \frac{N_e}{8} \cdot \frac{1}{1 - p_{21}} \cdot e^{\eta\left(q_2 - q_1 \frac{1 - p_{11}}{1 - p_{21}} \right)} \cdot G_2(-\eta)$$

$$\cdot \left\{ e^{-j(\omega_2 t + \phi_2 - \omega_1 t - \phi_1)} \right.$$

$$\cdot e^{jq_1 \left(\omega_2 \frac{1-p_{11}}{1-p_{21}} - \omega_1 \right)}$$

$$\cdot e^{-(\eta - j\omega_2)\left(\frac{p_1 - p_2}{1-p_{21}} + t \frac{p_{11} - p_{21}}{1-p_{21}} \right)}$$

$$\cdot H_2(-\eta + j\omega_2) \cdot H_1\left((\eta - j\omega_2) \frac{1-p_{11}}{1-p_{21}} \right)$$

$$\cdot G_1\left((\eta - j\omega_2) \frac{1-p_{11}}{1-p_{21}} + j\omega_1 \right)$$

$$+ e^{+j(\omega_2 t + \phi_2 - \omega_1 t - \phi_1)}$$

$$\cdot e^{-jq_1 \left(\omega_2 \frac{1-p_{11}}{1-p_{21}} - \omega_1 \right)}$$

$$\cdot e^{-(\eta + j\omega_2)\left(\frac{p_1 - p_2}{1-p_{21}} + t \frac{p_{11} - p_{21}}{1-p_{21}} \right)}$$

$$\cdot H_2(-\eta - j\omega_2) \cdot H_1\left((\eta + j\omega_2) \frac{1-p_{11}}{1-p_{21}} \right)$$

$$\cdot G_1\left((\eta + j\omega_2) \frac{1-p_{11}}{1-p_{21}} - j\omega_1 \right) \right\} \quad (A-14)$$

The two terms discarded from Eq (A-10) could be developed in an identical fashion, should the receiver configuration warrant their inclusion

The desired correlation function is developed from $\psi_c^*(t,\eta)$ by transforming on η

$$S_c(t,\tau) = \frac{1}{2\pi j} \int_{-j\infty}^{+j\infty} e^{-\eta \tau} \psi_c^*(t, \eta)\, d\eta. \quad (A-15)$$

We can simplify the appearance of the following equations by inserting the auxiliary variables ϕ_3 and τ_3 which are themselves functions of t and τ

$$\tau_3 = \tau + q_1 \frac{1-p_{11}}{1-p_{21}} - q_2 + \frac{p_1 - p_2}{1-p_{21}} + t \frac{p_{11} - p_{21}}{1-p_{21}}$$

$$\phi_3 = \omega_2 t + \phi_2 - \omega_1 t - \phi_1 - \omega_2 \left(\frac{p_1 - p_2}{1-p_{21}} + t \frac{p_{11} - p_{21}}{1-p_{21}} \right)$$

$$- q_1 \left(\omega_2 \frac{1-p_{11}}{1-p_{21}} - \omega_1 \right) \quad (A-16)$$

This makes

$$S_c(\tau_3, \phi_3;\ t,\tau) = \frac{N_e}{8} \cdot \frac{1}{1-p_{21}} \int_{-j\infty}^{+j\infty} \frac{d\eta}{2\pi j}\, e^{-\eta \tau_3}\, G_2(-\eta)$$

$$\cdot \left\{ e^{-j\phi_3} H_2(-\eta + j\omega_2) \right.$$

$$\cdot H_1\left[(\eta - j\omega_2) \frac{1-p_{11}}{1-p_{21}} \right]$$

$$\cdot G_1\left[(\eta - j\omega_2) \frac{1-p_{11}}{1-p_{21}} + j\omega_1 \right]$$

$$+ e^{+j\phi_3} H_2(-\eta - j\omega_2)$$

$$\cdot H_1\left[(\eta + j\omega_2) \frac{1-p_{11}}{1-p_{21}} \right]$$

$$\cdot G_1\left[(\eta + j\omega_2) \frac{1-p_{11}}{1-p_{21}} - j\omega_1 \right] \right\} \quad (A-17)$$

When the filters $G_i(s)$, $H_i(s)$ are expressed as rational polynomials in s, the integral in Eq (A-17) is evaluated via the Heaviside expansion theorem into a sum of exponentials in $\eta\tau_3$ evaluated at the poles of $G_i(s)$, $H_i(s)$ If $\tau_3 < 0$, the integral is a normal inverse LaPlace integral, for which the selected poles are in the left-half plane, and are those of $G_1(s)$, $H_1(s)$ If $\tau_3 > 0$, the integral is an inverse LaPlace integral for *negative* time, which selects poles in the *right*-half plane, namely, those of $G_2(-s)$, $H_2(-s)$

The autocorrelation of either $c_1(t_1)$ or $c_2(t_2)$ can be written by inspection from the cross-correlation

$$A_{ci}(t,\tau) = \frac{N_i + N_e}{8} \int_{-j\infty}^{+j\infty} \frac{d\eta}{2\pi j} e^{-\eta\tau}$$

$$[G_i(-\eta)H_i(-\eta + j\omega_i)H_i(\eta - j\omega_i)G_i(\eta)$$

$$+ G_i(-\eta)H_i(-\eta - j\omega_i)H_i(\eta + j\omega_i)G_i(\eta)] \quad \text{(A-18)}$$

The autocorrelations will be used in computing the cross-correlation at the output of the limiters

Let x, y be two gaussian random variables, and let $L(x)$ denote the limiter function that is -1 if $x < 0$, and $+1$ otherwise Then it is easy to establish that

$$\langle L(x) \cdot L(y) \rangle = \langle L(x \cdot y) \rangle$$

$$= \frac{2}{\pi} \text{Arcsin}\left(\langle x \cdot y \rangle / \sqrt{\langle x \cdot x \rangle \cdot \langle y \cdot y \rangle} \right)$$

$$\text{(A-19)}$$

where $\langle \cdot \cdot \rangle$ denotes ensemble average Note that $c_1(t_1)$ and $c_2(t_2)$ are gaussian random variables for any particular values of t_1, t_2, and hence Eq. (A-19) applies to the computation of the expected cross-correlation of the output of the limiters In almost all cases of interest to VLBI, the correlated noise from the radio source is a very small part of the total noise at the receiver, i e , $N_e \ll N_i + N_e$ for $i = 1$, or 2, so that a linear approximation to the Arcsin ($\cdot$) in Eq (A-19) is adequate Thus, if we denote as $S_L($ $)$ the cross-correlation of the limiter-output signals, then

$$S_L(\tau_3, \phi_3: t, \tau) = \frac{2}{\pi} \frac{S_c(\tau_3, \phi_3 \; t, \tau)}{\sqrt{A_{c1}(0,0) \cdot A_{c2}(0,)}} \quad \text{(A-20)}$$

The *variance* of each $S_L($ $\cdot \cdot)$ is unity, since the magnitude of $L(x)$ is identically one The covariance of $S_L($ $t, \tau)$ will be needed for SNR calculations

Appendix B

Square Passband Filters

We can obtain at least a partial check on the derivation from Appendix A by reverting to the special case of square passbands with single-sideband demodulators, for which a simpler derivation is possible Let

$$G_i(jx) = \begin{cases} 1 & \text{for } |x| < \omega_1, \omega_2 \\ 0 & \text{elsewhere} \end{cases}$$

$$\text{(B-1)}$$

$$H_i(jx) = \begin{cases} 1 & \text{for } \omega_i < |x| < \omega_i + B_i \\ 0 & \text{elsewhere} \end{cases}$$

where B_i is the bandwidth of the supposed square-passband filters Denote by $S_{SQ}(\quad)$ the form assumed by $S_c(\quad)$ for this special case

$$S_{SQ}(\tau_3, \phi_3 \ t,\tau) = \frac{N_e}{8} \cdot \frac{1}{1-p_{21}} \cdot \left\{ e^{+\phi_3} \int_{jb}^{jB} \frac{d\eta}{2\pi j} e^{-\eta\tau_3} \right.$$

$$\left. + e^{-\phi_3} \int_{-jB}^{-jb} \frac{d\eta}{2\pi j} e^{-\eta\tau_3} \right\}$$

$$\text{(B-2)}$$

where

$$b = \max\left\{ 0, \frac{1-p_{21}}{1-p_{11}}\omega_1 - \omega_2 \right\}$$

and

$$B = \min\left\{ B_2, \frac{1-p_{21}}{1-p_{11}}(\omega_1 + B_1) - \omega_2 \right\}$$

The execution of these integrals results in the anticipated $\sin(x)/x$ form, i e ,

$$S_{SQ}(\tau_3, \phi_3 \ t,\tau) = \frac{N_e}{8} \cdot \frac{1}{1-p_{21}} \cdot \frac{1}{2\pi} \cdot \frac{1}{\tau_3} \cdot \sin\left(\frac{B-b}{2}\tau_3\right)$$

$$\cdot \cos\left(\frac{B+b}{2}\tau_3 - \phi_3\right) \qquad \text{(B-3)}$$

Equation (B-3) describes a cross-correlation with a magnitude and phase factor If we let ϕ_4 be the argument of the phase factor, we can collect terms in ϕ_4 to place it into the form

$$\phi_4 = \frac{B+b}{2}\tau_3 - \phi_3$$

$$\phi_4 = \phi_x + t(\omega_1 - \omega_2) + \left(\omega_2 + \frac{B+b}{2}\right) \cdot \frac{p_{11} - p_{21}}{1-p_{21}} \cdot t$$

$$+ \frac{B+b}{2}\tau \qquad \text{(B-4)}$$

where ϕ_x is an undetermined phase angle This corresponds with the "fringe phase" of Thomas (Ref 14), if $\omega_2 + (B+b)/2$ is interpreted as the "center of the doppler-shifted passband" at RF

The autocorrelation of either receiver output is

$$\overline{A_{SQ_i}}(t,\tau) = \frac{N_i + N_e}{2} \cdot \frac{1}{2\pi} \cdot \frac{\sin\left(\frac{B_i}{2}\tau\right)}{\tau} \cdot \cos\left(\frac{B_i}{2}\tau\right) \quad \text{(B-5)}$$

If we denote as $S_{LQ}(\quad)$ the cross-correlation at the output of the limiters with square passband filters, and use Eq (B-5) with the weak-signal approximation to Eq (A-19),

$$S_{LQ}(\tau_3, d_3 \ t,\tau) = \frac{N_e}{\sqrt{N_1 N_2}} \cdot \frac{2/\pi}{1-p_{21}} \cdot \frac{\sin\left(\frac{B-b}{2}\tau_3\right)}{\frac{\sqrt{B_1 B_2}}{2} \cdot \tau_3}$$

$$\cdot \cos\left(\frac{B+b}{2}\tau_3 - \phi_3\right) \qquad \text{(B-6)}$$

is the expected value of the cross-correlation function observed in VLBI processing

Acknowledgments

References

1 Counselman, C C III, "Very-Long Baseline Interferometry Techniques Applied to Problems of Geodesy, Geophysics, Planetary Science, Astronomy, and General Relativity," *Proc. IEEE*, Vol 61, No 9, Sept 1973, pp 1225-1230

2 Clauss, R, et al, "Low Noise Receivers Microwave Maser Development," *DSN Progress Reports*, TR 32-1526, Vol XI, Jet Propulsion Laboratory, Pasadena, Calif, Oct. 15, 1972, pp 71-80

3 Rogers, A E E, "Very Long Baseline Interferometry with Large Effective Bandwidth for Phase-Delay Measurements," *Radio Sci*, Vol 5, No 10, Oct 1970, pp. 1239-1247

4 Hurd, W J, "DSN Clock Synchronization by Maximum Likelihood VLBI," *DSN Progress Report* TR 32-1526, VOL X, Jet Propulsion Laboratory, Pasadena, Calif, Aug 15, 1972, pp 82-95

5 Barankin, E W, "Locally Best Unbiased Estimates," *Ann Math Stat*, Vol 20, 1949, pp 477-501

6 Cramer, H, *Mathematical Methods of Statistics*, Princeton Univ Press, 1945

7 Hurd, W J, "Preliminary Demonstration of Precision DSN Clock Synchronization by Radio Interferometry," *DSN Progress Report 42-37*, Feb 15, 1977, pp 57-68

8 Rogers, A E E, et al, "Very Long Baseline Interferometry Hardware," Final Report for Contract NAS5-20777, Feb 1976, Part 7, "An IF to Video Converter", Haystack Technical Note 1975-5.

9 Weaver, D K, "Design of RC Wide-Band 90-Degree Phase-Difference Network," *IRE Proc.*, Apr 1954, pp 671-676

10 Urech, J. M., et al., "S-Band Maser Group Delay Measurements and Stability Report," Madrid Deep Space Station, Oct. 1976.

11 Rogers, A E E, et al, "Very Long Baseline Interferometry Hardware," Final Report for Contract #NAS5-20777, Feb 1976, Part 13 "A Receiver Phase and Group Delay Calibration System", Haystack Technical Note 1975-6

12 Thomas, J B, "The Tone Generator and Instrumental Calibrations in VLBI Measurements," JPL Internal Report EM-315-31, July 15, 1977

13 Papoulis, A, *Probability, Random Variables, and Stochastic Processes*, Sec 12-2, McGraw-Hill Book Company, New York, 1965

14 Thomas, J B, "System Noise Effects in VLBI Measurements," JPL Internal Report EM 315.6, Oct 25, 1976

Table 1. Offset in estimated group delay and phase for $1_{10}-4$ offset in filter pole position with full band sampling

Pole no.		Δ delay, ns	Δ phase, rn
1a		−0.099	0.0067
1b		−0.027	0.0135
1c		0.124	0 0079
2a		0.032	−0 0068
2b		0.099	−0.0130
2c		−0.132	−0 0081
	RSS (all)	0.23	0 024

Table 2. Change in estimated channel phase for $1_{10}-2$ change in final filter pole position. (Rn $\times$ 10^{-3})

Pole	Phase at 2260	Phase at 2300	$|\Delta\phi|$
1a	3 34	3 18	0 16
1b	5 07	4 66	0 41
1c	1.91	1 90	0 01
1d	1 27	0 80	0 47
1e	6.71	6 33	0 38
1f	−1.62	−1 74	0 12
1g	11 2	9.13	2 1
2a	−3 65	−3 17	0 48
2b	−5 45	−4 65	0 80
2c	−2 15	−1 89	0 26
2d	−1 12	−0 80	0 32
2e	−7 47	−6 30	1 17
2f	2 15	1 72	0 43
2g	−11 9	−9 11	2 8
RSS	22 2	18 0	3 6

Table 3. Change in estimated channel phase for $1_{10}-2$ change in quad-hybrid filter pole positions (rn x 10^{-3})

Pole	Phase at 2260	Phase at 2300	$|\Delta\phi|$
1a	0 323	0 405	0 08
1b	1 69	1 82	0 13
1c	1 07	1 31	0 28
1d	1 79	1.73	0 06
2a	−0 376	−0.404	0 03
2b	−1 92	−1 81	0 11
2c	−1 24	−1 30	0 06
2d	−1 97	−1 72	0 25
RSS	4 08	4 03	0 43

VLBI Clock Sync and the Earth's Rotational Instability

J W Layland and A N Mathews
Communications Systems Research Section

The DSN is currently preparing to monitor the stability of its clocks and frequency standards in the 64-meter net by means of VLBI Since variations in the Earth's rotation rate represent an error source to VLBI clock synchronization, we calculated the Allan Variance of the Earth rotation to find that, in a long-term sense at least, these variations do not noticeably increase the differential instability of two clocks as measured by Intercontinental VLBI.

I. Introduction

The DSN is currently preparing to monitor the stability of its clocks and frequency standards in the 64-meter net by means of VLBI Since variations in the Earth's rotation rate represent an error source to VLBI clock synchronization, it is not immediately clear that such frequency standards monitoring is possible to the precision desired We calculated the Allan Variance of the Earth rotation to find that, in a long-term sense at least, the instability of the Earth's rotation does not cause the differential instability of two widely separated clocks as measured by Intercontinental VLBI to measurably exceed that intrinsic to the clocks themselves, which is on the order of one part in 10^{14}

II. The VLBI Time Delay

Roughly, the time delay difference measured in a VLBI experiment for any particular radio source observed at UTC (Universal Time-Coordinated) = t is given by (Ref. 1)

$$\Delta Tm(t) = \Delta Tc(t) + Z_b \sin \delta_s$$

$$+ r_b \cos \delta_s \cos (\alpha_s - \lambda_b - \alpha_G(t)) \qquad (1)$$

$$- (UT_1 - UTC)) + \Delta T_i(t)$$

The various elements of Eq (1) are defined as follows

$\Delta Tc(t)$ the difference between clocks at the stations

Z_b the projection of the baseline between the two stations upon the instantaneous spin axis of the Earth

r_b the projection of the baseline into the instantaneous equatorial plane of the Earth

λ_b the longitude of the baseline

$\alpha_G(t)$ Greenwich Sidereal Time at $UTC = t$

α_s and δ_s the right ascension and declination of the radio source

$(UT_1 - UTC)$ the deviation in the phase of the Earth's rotation relative to UTC, measured in radians of Earth rotation

$\Delta T_i(t)$ the difference in incidental time delays such as propagation medium and instrumentation

Those elements of Eq (1) of principal interest here are the clock differences $\Delta Tc(t)$, and $(UT_1 - UTC)$. The equation is clearly nonlinear in the $(UT_1 - UTC)$ parameter for large

excursions, but is linear for small ones with a coefficient on the order of 2 μs of time delay per second of UT_1 for an individual delay measurement The effective coefficient can be somewhat reduced for slow variations in $(UT_1 - UTC)$ by solving for $(UT_1 - UTC)$ using observations of a number of appropriately located radio sources, but fast variations can masquerade equally well as fast variations in the clock differences irrespective of such techniques.

III. Instability Statistic

The Allan Variance (Refs 2 and 3) is routinely used to measure instability of an oscillator. Let

$$y(t) = a \sin\left(2\pi\nu_0 t + \phi(t)\right) \qquad (2)$$

be the signal emitted by the oscillator at nominal frequency ν_0 The two-sample Allan Variance with measurement interval T may be computed as

$$\sigma_\phi^2(T) = \frac{1}{2N} \sum_{i=1}^{N} \left[\frac{\phi(t_i) - 2\phi(t_i + T) + \phi(t_i + 2T)}{2\pi\nu_0 T}\right]^2 \qquad (3)$$

The square-root of this statistic is an estimate of the fractional error in time as counted by this oscillator, or of the fractional error in oscillator frequency. The instability measure of the DSN Hydrogen Maser is essentially constant at 5×10^{-15} for $T > 30$ sec (Ref. 4, Fig 3)

The Earth itself is an oscillator which operates at a nominal rate of one cycle per "day." Its instabilities take two forms· motion of the poles or spin axis relative to the Earth's crust, and changes in the rotation rate about the instantaneous position of the spin axis. Motion of the spin axis is measured in a rectangular coordinate system (X,Y) centered at the mean pole of 1903; variations in the phase of rotation appear in $(UT_1 - UTC)$ Polar motion is implicit in Eq. (1) in the definition of Z_b, r_b relative to the instantaneous spin axis Our data for X, Y, and $(UT_1 - UTC)$ comes via the US Naval Observatory Time and Frequency Bulletins, Series 7, and is computed by the Bureau International de l'Heure (BIH) based on optical observations by a world-wide observatory network The so-called "Rapid Service" values are published for one-day intervals within a week of the actual date, and can be expected to be somewhat noisier than the "Final Values," which are published for five-day intervals after a month of additional observing

Figure 1 shows the fractional instability of the Earth's rotation as computed from the Rapid Service data for the

interval from January 1976 to July 1977. For comparison, the polar motions X and Y are scaled in fractional Earth rotations (days), as is $(UT_1 - UTC)$ The region of UT_1 for $T < 3$ days, which decreases as $1/T$, is representative of a white noise error on individual determinations, and is of a magnitude which is at least conceptually consistent with the 4-ms error (Ref. 5) attained by individual observatories in one night The peak at around 70 days could be from the seasonal variations in UT_1, which are known to exist but hard to predict.

Figure 2 shows the fractional instability of the Earth's rotation as computed from the Final Values for the same interval. Statistically, the difference between Rapid Service and Final Values is that all of the apparent white noise of observations is removed in the Final Values, along with most short-term variations.

Figure 3 shows the fractional instability of the Rapid Service UT_1 from February 1972 through June 1977. The 1-sigma confidence intervals shown correspond to the number of distinct T-day segments in the data record For $10 < T < 100$ days, this figure is essentially the same as Fig 1 For $T > 200$ days, $\sigma(\Delta T/T)$ is approximately constant, possibly representing a "flicker" noise component of 2×10^{-9} This is consistent with the observation in Ref 6 that variations in $UT_2 - A$ 3 during 1956-1965 were flicker-like

We should be cautious in obtaining conclusions based upon these figures for two reasons First of all, the data set we have analyzed is short relative to some of the known variations Secondly, we are at the mercy of the instrumentation and averaging methods used by the BIH, so that the estimated instability will include some instrumental noise, and it could be missing some real variations due to the averaging Thus, if conclusions are to be formed from this data, a sizeable margin should exist relative to the calculated statistics.

IV. Implication for VLBI Clock Sync

As noted earlier, errors in UT_1 could masquerade as clock errors in VLBI time delay measurements to the level of at worst 2 μs clock error per second of UT_1 error. The fractional instability of the VLBI-measured clock contains terms due to UT_1 variations and to the clocks themselves. These terms are shown in Fig 4. If we assume that the BIH Final Values represent the actual Earth motion, then the noise induced in a VLBI-measured clock by use of the Rapid Service data corresponds to the noise of the difference UT_1 (Rapid Service) $- UT_1$ (Final) For short time intervals, such as a single VLBI observing pass, we cannot tell absolutely whether short-term variations in UT_1 represent a problem or not, because we do not know whether the white phase noise in

Rapid Service UT_1 for $T < 3$ days is really in UT_1 or is an artifact of the optical instruments currently used to measure it. This matter could be resolved by attempting to use VLBI to solve for UT_1 on a shorter time interval than can be done with the optical data

For time scales in excess of 3 days, it appears in Fig 4 that instability of the frequency standards themselves is comparable to or greater than even the worst-case statistical variations due to the Rapid Service data Both are below the 10^{-14} level, and thus the Earth's rotational instability should cause no problem in monitoring the frequency standards' long-term performance to a few parts in 10^{14}, even without concurrently solving for UT_1.

References

1 Williams, J. G, "Very Long Baseline Interferometry and Its Sensitivity to Geophysical and Astronomical Effects," JPL-SPS 37-62, Vol II, pp 49–55, March 1970

2. Barnes, J. A., et al, *Characterization of Frequency Stability*, NBS Technical Note 394, October 1970.

3 Allan, D. W, "Statistics of Atomic Frequency Standards," *Proc IEEE*, Vol 54, pp 221–230, February 1966

4 Dachel, P R., et al, "Hydrogen Maser Frequency Standards for the Deep Space Network," *DSN-PR 42-40*, pp 76–83, August 15, 1977 (Also PTTI Conference, Proceedings, December 1976)

5 *Explanatory Supplement to the Astronomical Ephemeris and the American Ephemeris and Nautical Almanac*, London, Her Majesty's Stationery Office, 1961, p 83

6 Barnes, J A, and Allan, D W, "An Approach to the Prediction of Coordinated Universal Time," *Frequency 5*, No 6, pp 15–20, Nov–Dec 1967.
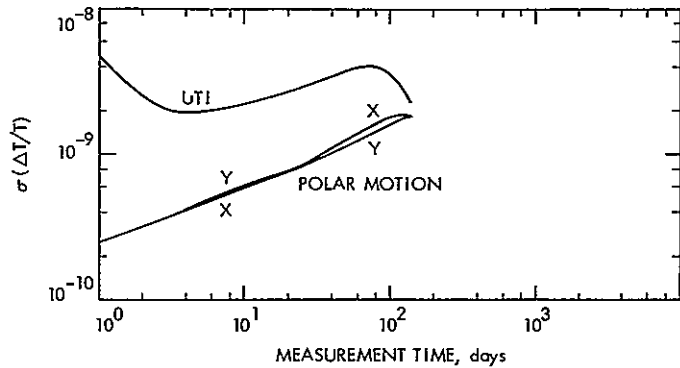
Fig 1. Stability of Earth rotation, BIH Rapid Service data, January 1976 to June 1977
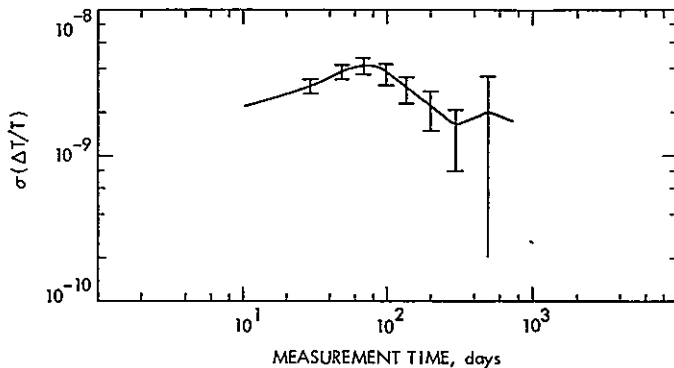

Fig. 2. Stability of Earth rotation, BIH Final Data, January 1976 to June 1977

Fig. 3. Stability of Earth rotation, BIH data, February 1972 to June 1977

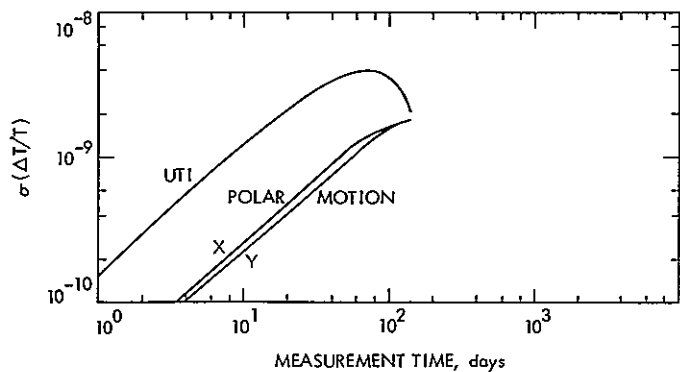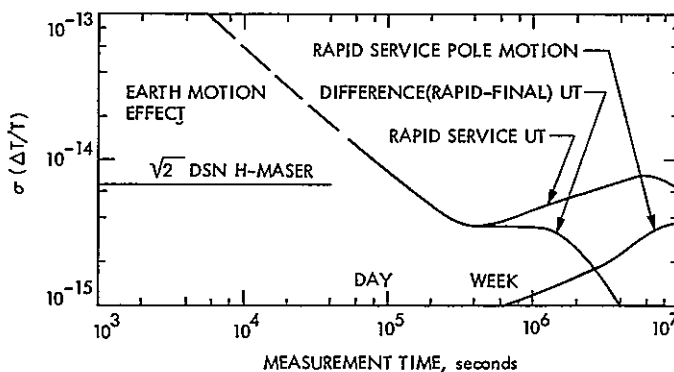Fig. 4. VLBI-measured clock rate variations

X- and K-Band Maser Development: Effects of Interfering Signals

R. C. Clauss

Radio Frequency and Microwave Subsystems Section

Signals at levels exceeding −90 dBmW at the input connection of a traveling-wave maser can affect maser performance in a variety of ways Both S-band and X-band masers are considered where interfering signals are (1) within the maser bandpass, (2) near the maser bandpass, and (3) far from the maser bandpass, where mixing with the maser pump can occur

I. Interference to Maser Operation

Signals at levels exceeding −90 dBmW at the input connection of a traveling-wave maser (TWM) affect maser performance in a variety of ways, depending upon the amplitude and frequency of the interfering signal The particular masers considered here are the S-band Block III (2270-2300 MHz) and the X-band (8400-8500 MHz) TWMs.

The first situation considered is where a signal exceeding −90 dBmW is at a frequency located within the maser signal bandpass The −90 dBmW signal is amplified by the maser (net gain = 45 dB) and leaves with an amplitude of −45 dBmW in the normal manner Signal levels greater than −85 dBmW cannot be amplified by the same amount (45 dB) because the output level would exceed −40 dBmW The maser material spin system is in an inverted population condition to provide amplification, typically the population inversion begins to degrade at a TWM output signal level of −40 dBmW and the maser gain therefore decreases This gain loss is referred to as maser saturation.

The presence of a saturating signal in the maser bandpass does not necessarily produce intermodulation products during the amplification process of another signal within the bandpass. A demonstration involving two large signals within the maser bandpass (partially saturating but not completely eliminating maser gain) produced no detectable intermodulation products. The signals were spaced 1 MHz apart in frequency and the measurement of resolution extended 60 dB below the level of the test signals The ability of a large, saturating signal to produce intermodulation in a maser depends on its proximity to other signals The difference frequency between the two interfering CW signals must have a period that approaches the spin relaxation time involved in the maser process (typically 0 05 sec) in order to cause substantial intermodulation A large (partially saturating) signal with low frequency amplitude modulation (less than 10 kHz AM) is capable of modulating the maser gain at the AM rate, thereby transferring the AM to other signals in the maser bandpass. Excessive reduction in maser gain caused by a large interfering signal degrades the system noise temperature, this occurs at first as an increase in the effective input noise temperature contribution of the amplifier or receiver behind the maser

The second situation considered involves signals near the maser bandpass. Maser saturation occurs as a function of signal level and frequency separation between the maser bandpass and the interfering signal. Safe levels vary from −90 dBmW at the band edge to −30 dBmW when the signal is removed by 100 MHz from the maser band edge This sensitivity to saturation occurs in a manner that can be approximated to be decreasing at the rate of 0 6 dB/MHz for the first 100 MHz and then at a lesser rate of 0 1 dB/MHz for the next 300 MHz. In general, at frequencies more distant than 400 MHz from the band edge the maser performance is not disturbed by signal levels lower than 1 mW At levels above 1 mW heating can reduce maser gain in proportion to the power level of the interfering signal

An exception to the general insensitivity of the maser to out-of-band interfering signals is the third situation considered Out-of-band signals mixing with the maser pump or pumps (dual pumps are used at X-band) can cause interference at the signal frequency and maser gain reduction. Masers are pumped at frequencies required by the paramagnetic energy level system at power levels of 0.1 watt (nominal) Pump energy is supplied by free-running klystrons or gunn oscillators which are frequency modulated at rates of 20 to 120 kHz with frequency deviations as great as 220 MHz (see Table 1). The difference frequency between maser pump and signal frequencies is referred to as the idler frequency, electron spin resonance in the maser material occurs at the idler frequency (or frequencies). Masers are particularly susceptible to interfering signals at the idler frequency Interfering signals at the maser idler frequency result in a complete loss of maser gain when amplitudes are greater than −10 dBmW

At lower levels maser gain reduction occurs and mixing produces interfering signals at the difference frequency between the idler interference signal and the frequency modulated maser pump. At idler interference levels below −40 dBmW the maser gain remains normal, but mixing occurs with a conversion loss of 90 dB. For example in an S-band maser a −40 dBmW signal at 10.4 GHz will mix with the 12 7 GHz maser pump, producing an interfering signal at 2300 MHz with a level of −130 dBmW when referred to the maser input This mixed product will be frequency modulated (like the maser pump) and may appear as broadband noise on an ordinary spectrum analyzer. Safe levels for interfering signals at the maser idler frequency depend upon the overall receiving system sensitivity and should be computed with regard to the information given above Measurements at +10 dBmW have resulted in detectable maser gain reductions at frequencies within 200 MHz of the idler frequency. Other mixing in a maser structure is noticeable when signals are introduced at levels above +10 dBmW at frequencies that could mix, or multiply and mix, with the maser pump. This mixing phenomenon is not believed to be caused by the maser material. Resonance isolator material and joints involving oxide layers which could form tunnel junctions in the maser structure can provide the nonlinear elements needed for this mixing phenomenon (Refs. 1 and 2) Maser signal frequency ranges, pump ranges, idler ranges and some typical candidate ranges for mixing due to nonlinearities are shown in Table 1.

References

1 W Higa, R Clauss, P Dachel, "Low Noise Receivers Theory of "Noise Bursts" on Large Antennas," in *The Deep Space Network Progress Report for March and April 1973*, California Institute of Technology, Jet Propulsion Laboratory, Technical Report 32-1526, Volume XV, pp 80-83, June 15, 1973.

2 R C. Clauss, "Low Noise Receivers, Microwave Maser Development, Second-Generation Maser," in *The Deep Space Network Progress Report for the period May 1 to June 30, 1968*, California Institute of Technology, Jet Propulsion Laboratory, Space Programs Summary 37-52, Vol II, pp. 58-61, July 31, 1968.

Table 1. Maser signal, pump, idler and mixing ranges

Maser signal frequency range	2270-2300 MHz	8400-8500 MHz
Maser pump frequency range	12.65 to 12.73 GHz	19 15 to 19.28 GHz $(f_{p\ 3\text{-}4})$ and 23 96 to 24.18 GHz $(f_{p\ 1\text{-}3})$
Maser idler frequency ranges	10.35 to 10 46 GHz $(f_p - f_s)$	10 65 to 10 88 GHz $(f_{p\ 3\text{-}4} - f_s)$ and ‑15.46 to 15.78 GHz $(f_{p\ 1\text{-}3} - f_s)$
Mixing ranges due to nonlinearities (typical)	14 92 to 15 03 GHz 7 46 to 7 52 GHz	‾27.55 to 27 78 GHz 32 36 to 32 68 GHz

N 78 - 2 4 1 7 1

Complex Mixer System Modifications

G L Stevens

Communications Systems Research Section

Modifications of the complex mixer system to increase bandwidth and number of channels have been made Three modified complex mixers have been installed at DSS 14 and were used to process planetary radar signals in March and April of 1977

I. Introduction

The complex mixer system is an integral part of the R&D spectrum analyzer and is described in detail in Ref 1. A third complex mixer module has been installed in the system, and all complex mixer modules have been redesigned to provide baseband bandwidth of DC to 2 MHz The three independent channels can be operated in either of two modes, accepting the 10-MHz IF of the DSN receivers or the 2 5-MHz IF of the experimental receiver or microwave link

II. Complex Mixer Module

A block diagram of a complex mixer module is presented in Fig 1 The phase-locked loop and the SIN-COS generator of the original design were retained The complex mixer section has been redesigned to increase the output bandwidth from 1 MHz to 2 MHz

Figure 1 shows that the IF signal is applied to two separate channels At the input of each channel is an isolation amplifier needed to prevent the modulation products generated by the mixers from contaminating the input source The buffered IF signal is then mixed with the locally generated SIN and COS signals to translate the IF signal to baseband and generate the complex modulation products Following the mixers are lumped constant passive low-pass filters which pass the

difference frequencies (the desired baseband signal) while attenuating the sum modulation products and local oscillator leakage

A two-section elliptic low-pass filter was chosen because it could supply the necessary selectivity with a minimum number of components, minimizing the problems of filter tuning to achieve the desired phase and amplitude tracking over the passband range Ripples exist within and without the pass-band, and this was used to advantage by carefully placing one of the attenuation peaks of the stopband at exactly 2 5 MHz In doing so, the 2 5-MHz local oscillator feedthrough was significantly suppressed The passband ripple of these filters is 0 25 dB

The filtered baseband signals are then amplified and fed to 50-Ω output buffers designed to drive 50-Ω coax cables terminated with 50-Ω loads

III. Packaging

Three printed circuit boards (PCBs) are contained within each complex mixer module The phase-locked loop and the SIN-COS generator occupy two of these boards and were not modified A new PCB was designed to accommodate the circuitry of the 2-MHz complex mixer Outside dimensions,

mounting hole locations and electrical connection layouts were made the same as the old boards to facilitate easy retrofitting of the new boards

Figure 2 shows the 2-MHz complex mixer PCB All microcircuits are on sockets for easy field maintenance Gain and DC offset adjustment potentiometers for each channel are provided on the PCB and are accessible through holes drilled in the module cover plates Each low-pass filter is comprised of two ferrite torroidal inductors and five capacitors Each capacitor is formed by paralleling up to three glass capacitors to achieve the desired value Input and output connections to each filter are established by inserting plug-in jumpers Installation of the jumpers in one set of sockets connects the filters into the complex mixer circuitry Plugging the jumpers into an alternate set of sockets transfers the filter input and output connections to 50-Ω bulkhead connectors This arrangement permits easy connection of the filter terminals to external test equipment This is necessary when testing the two filters on each board for amplitude and phase tracking across the DC to 2-MHz band. Although the input-output phase relationship of these filters varies from 0 degrees at DC to over 100 degrees at 2 MHz, the filters track in phase to better than 1 degree over the entire range

IV. Performance

Table 1 summarizes the typical characteristics of the modified complex mixer module In each complex mixer, the real and imaginary outputs are balanced in gain to within 0 2 dB and in phase to within 6 degrees over the entire operating range of DC to 2 MHz

V. Conclusion

A third complex mixer module has been added to the complex mixer system All complex mixer modules have been modified to increase the output bandwidth to 2 MHz. The complex mixer system was used to process planetary radar signals during March and April of 1977.

Reference

1 Constenla, L C , *Complex Mixer System*, Technical Report 32-1526, Jet Propulsion Laboratory, Pasadena, California, December 15, 1972.

Table 1. Complex mixer module specifications

Parameter	Value	Comment
Input impedance	50 Ω	
Output impedance	50 Ω	
Bandwidth	DC to 2 MHz	
Voltage gain	2	Single sideband gain with 50-Ω output loads
Baseband freq response	±0 5 dB	DC to 2 MHz
Amplitude tracking	0 2 dB	DC to 2 MHz
Phase tracking	< 6 deg	DC to 2 MHz
Maximum input voltage	1 VPP	
L O leakage	< 2 mVRMS	2 5 or 10 MHz mode
Maximum undistorted OP vol	2.8 VPP	
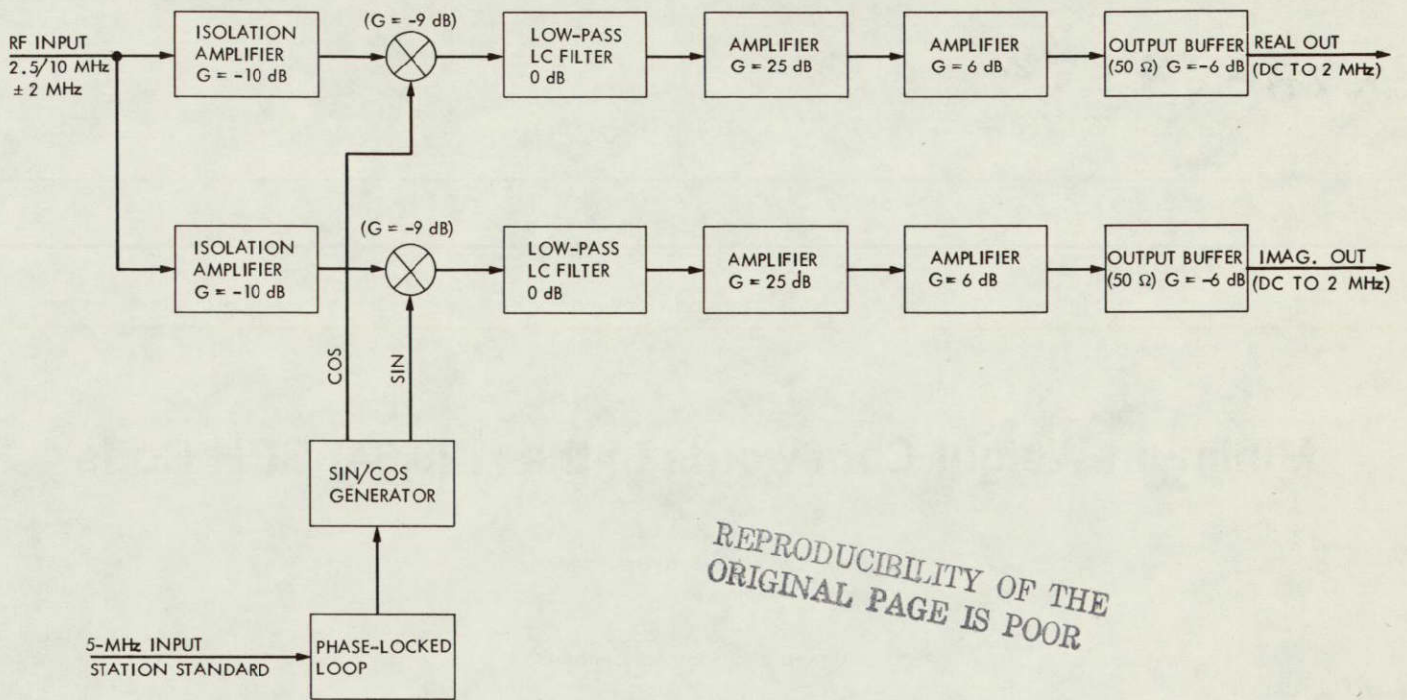
Fig. 1. Block diagram of complex mixer module

Fig. 2. 2-MHz complex mixer circuit board

Minimum-Weight Codewords in the (128,64) BCH Code

L. D. Baumert
Communications Systems Research Section
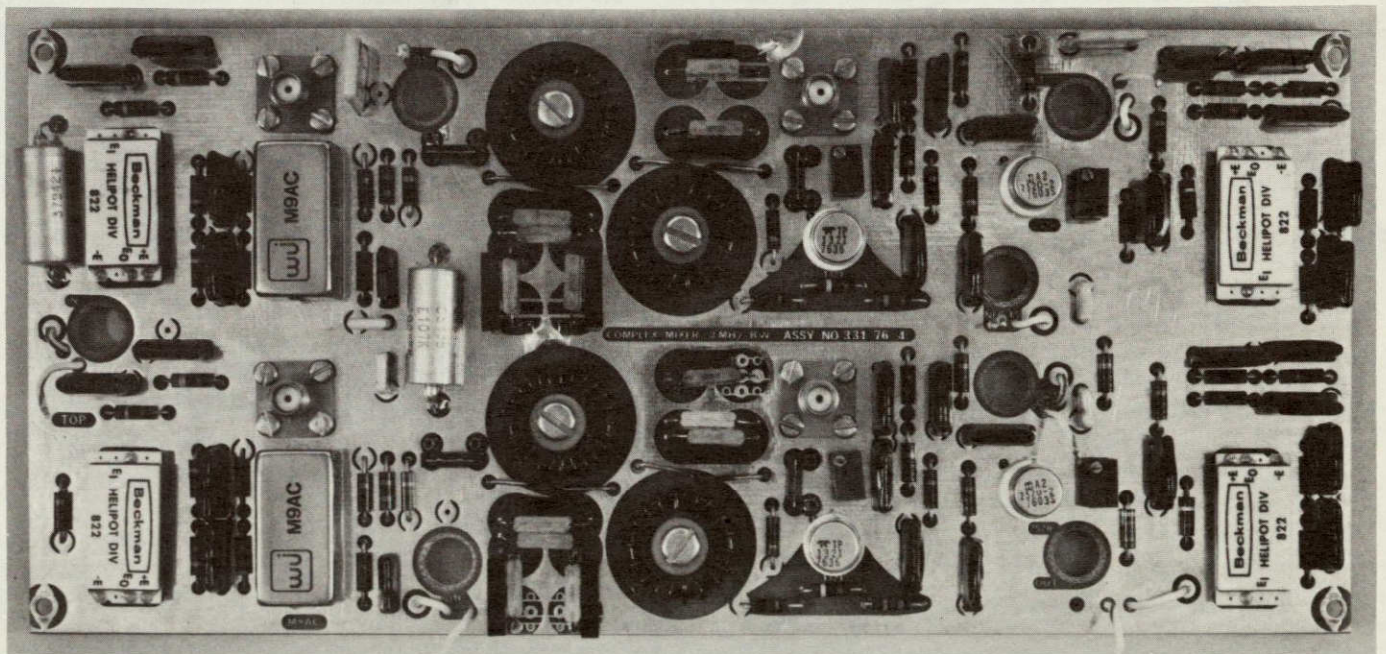
L. R. Welch
University of Southern California

*In this article we determine the number of weight 22 codewords in the (128,64) BCH
code which is being studied for use on future deep-space missions.*

I. Introduction

Perhaps the most promising candidate deep-space telemetry coding system which is markedly superior to the short-constraint-length convolutional code on Voyager is a (128,64) BCH (Bose-Chaudhuri-Hocquenghem) block code equipped with a soft-decision decoding algorithm (Ref. 1). The minimum distance of this code is known to be 22, but in order to get accurate estimates of the code's performance it is necessary to know the exact number of codewords of weight 22. In this article we will combine techniques of combinational algebra and computer simulation, and conclude that the number of such codewords is almost certainly 243,840.

Our proof rests on the fact that the BCH code is invariant under a certain group of coordinate permutations of order $2^7 \cdot 7 \cdot 127 = 113,792$. Thus the words of any fixed weight are distributed into conjugacy classes under the action of this group. In this paper we will show that for weight 22 codewords one such class contains 16256 codewords, but all other classes contain 113,729 codewords. Our computer simulations of decoding algorithms have generated 85 weight-22 codewords; these have all been contained in just three classes: the small class of size 16256 and two larger classes. Thus the number of weight-22 codewords is almost surely 16256 + 113792 + 113792 = 243840.

II. Preliminary Information

The (128,64) BCH code has an automorphism group G of order $113,792 = 7 \times 127 \times 128$ consisting of the transformations $\tau : x \to \gamma x^{2^k} + \delta (k = 0,1, \ldots, 6; \gamma, \delta$ in $GF(2^7), \gamma \neq 0)$ acting on the elements of $GF(2^7)$ (Ref. 2). The codeword symbol position labels are $\alpha^0, \alpha^1, \alpha^2, \ldots, \alpha^{126}, 0 = \alpha^\infty$, where α is a primitive root of $GF(2^7)$ and the action of τ on these labels determines the codeword permutation. So any element of G can be described in terms of a permutation of the symbols $0,1, \ldots, 126, \infty$. Thus each element of G can be described by a product of disjoint cycles of the symbols $0,1, \ldots, 126, \infty$. The order of an element is the least common multiple of the lengths of these cycles. Two conjugate permutations have the same number of cycles of each size and hence the same order. If a codeword w is fixed by the transformation τ, then the codeword $w\emptyset$ is fixed by the conjugate transformation $\emptyset^{-1}\tau\emptyset$.

The weight of any codeword is of course fixed by the transformations of G; thus in particular the words of minimum weight 22 are distributed into classes according to whether or not they are transformed into each other by G. Thus a collection of representative words, one from each of these classes, suffices to determine all words of weight 22 in the code. In order to determine these words of weight 22 it is useful to

know whether there are any small classes (i.e , are they all of size 7 × 127 × 128 or are some smaller?)

Equivalently, one may ask whether any word w of weight 22 in the code is fixed by a transformation τ of G We shall show that there is a single class of weight 22 codewords containing 127 × 128 = 16,256 codewords and that the other weight 22 codewords all occur in full classes of size 7 × 127 × 128

Since conjugate elements of G perform similarly for these purposes, it suffices to examine a single element of each conjugacy class of G

III. The Conjugacy Classes of G

Lemma Every element of G is conjugate to one of the following transformations

(1) Identity $x \to x$		order 1
(2) Translation $x \to x + 1$		order 2
(3) $x \to \gamma x, \gamma \neq 0,1$		order 127
(4) $x \to x^{2^k}, k = 1, \quad , 6$		order 7
(5) $x \to x^{2^k} + \delta, k = 1, \quad , 6, Tr(\delta) = 1$		order 14

In particular, if α satisfies $\lambda^7 + x^3 + 1 = 0$ over $GF(2)$, then $Tr(\alpha^7) = 1$, and $\delta = \alpha^7$ may be used in (5) The cycle structure for (4) is 2 of length 1 and 18 of length 7, and for (5) there is one cycle of length 2 and 9 cycles of length 14

Proof Let us first note the general form of a conjugate $\emptyset\tau\emptyset^{-1}$ Let

$$\tau \quad x \to \gamma x^{2^k} + \delta \quad \emptyset \quad x \to a x^{2^l} + b$$

then

$$\emptyset^{-1} \quad x \to a^{-2^l} x^{2^l} + \left(\frac{b}{a}\right)^{2^l}$$

where $0 \leqslant j \leqslant 6$ and $i + j \equiv 0$ modulo 7 So

$$\emptyset\tau\emptyset^{-1} \quad x \to a^{-2^j}(\gamma^{2^j} a^{2^{k+j}} x^{2^k} + \delta^{2^j} + \gamma^{2^j} b^{2^{j+k}} + b^{2^j})$$

Note that the exponent on x is preserved by conjugation, so transformations having different exponents are necessarily in different conjugacy classes

Trivially, the identity forms its own conjugacy class Note that $\emptyset \quad x \to ax$ transforms $\tau \quad x \to x + 1$ into $\emptyset\tau\emptyset^{-1} \quad x \to x + a^{-1}$ Since a is arbitrary $(a \neq 0)$ we have shown that all translations (save the identity) belong to the same conjugacy class Obviously these translations have order 2 Let $\tau \quad x \to \gamma x + \delta (\gamma \neq 0,1)$ then $\emptyset \cdot x \to x + \delta/(\gamma + 1)$ transforms τ into $\emptyset\tau\emptyset^{-1} \quad x \to \gamma x$ All these transformations $(\gamma \neq 0,1)$ thus must have order dividing 127, and since it cannot be 1 it must be 127

For $k = 1, \quad ., 6$, conjugate $\tau \quad x \to x^{2^k}$ by $\emptyset. x \to ax + b$, this yields $\emptyset\tau\emptyset^{-1} \quad x \to a^{2^k-1} x^{2^k} + a^{-1}(b^{2^k} + b)$ Since $a(a \neq 0)$ is arbitrary, so is a^{2^k-1} As b ranges over $GF(2^7)$ note that $b^{2^k} + b$ covers all elements of trace 0 exactly twice Thus all mappings $x \to \gamma x^{2^k} + \delta$ such that $Tr(\sigma\delta) = 0$, where σ is the unique solution of $x^{2^k-1} = \gamma$, are conjugate to $x \to x^{2^k}$

Conjugating $\tau \quad x \to x^{2^k} + \delta (k = 1, \quad , 6, Tr(\delta) = 1)$ by $\emptyset$ $x \to ax + b$ yields

$$\emptyset\tau\emptyset^{-1} \quad x \to a^{2^k-1} x^{2^k} + a^{-1}(b^{2^k} + b + \delta)$$

Thus, as above, we get all mappings $x \to \gamma x^{2^k} + \delta$ such that $Tr(\sigma\delta) = 1$, and our lemma is proved provided we establish the cycle structures and the orders of the mappings in these last two classes

Let $\tau \quad x \to x^{2^k} + \delta (k = 1, \quad , 6)$ then $\tau^7 \quad x \to x + Tr(\delta)$, thus if $\delta = 0$ as in (4) we see that the order of τ must divide 7 and, as it is not 1, must indeed be 7 Since $x = 0,1$ are the only solutions of $x = x^{2^k}$ in this field, the cycle structure here must be 2 of length 1 and 18 of length 7. Similarly if $Tr(\delta) = 1$, $\tau^{14} \quad x \to x + 1 + Tr(\delta) = x$, thus the possible orders for τ are 1,2,7, and 14 Not 1 obviously, and $\tau^7 \quad x \to x + Tr(\delta) = x + 1$, so not 7 Now $\tau^2 \quad x \to x^{2^{2k}} + \delta^{2^k} + \delta$, but if these are equal $x^{2^{2k}} + x = \delta^{2^k} + \delta$ Since $x^{2^{2k}} + x$ maps $GF(2^7)$ doubly onto its elements of trace 0, we see that there are precisely two solutions to this equation These two solutions must appear in à cycle of length 2 since no cycle of odd length exists (for j odd x and $\tau^j(x)$ necessarily are of different trace so they cannot be equal) Thus $\tau \quad x \to x^{2^k} + \delta$ where $Tr(\delta) = 1$ must have 1 cycle of length 2 and 9 cycles of length 14 In particular, it is of order 14 as asserted

IV. The Codewords of Weight 22

If a codeword of weight 22 is fixed by a transformation τ, then τ must have distinct cycles whose lengths add to 22 Thus no transformation conjugate to (3) $x \to \gamma x(\gamma \neq 0,1)$ can fix a codeword of weight 22 since its cycle structure is necessarily 1 of length 127 and 1 of length 1 The cycle structure for (5) $x \to x^{2^k} + \delta$, $Tr(\delta) = 1$, rules these conjugacy classes out also A

translation $x \to x + \delta$ necessarily has 64 cycles of length 2 of the form (i,j) corresponding to α^i and $\alpha^j = \alpha^i + \delta$ Thus a codeword of weight 22 would have its 1's in positions specified by 11 such cycles.

So with codeword $C_0, C_1, \dots, C_{127}$ we would have

$$\Sigma C_i \alpha^i = \sum_{i=1}^{11} \delta \neq 0$$

for $\delta \neq 0$, which contradicts the definition of a BCH code So $x \to x + \delta (\delta \neq 0)$ fixes no words of weight 22 in this code.

Since the $\tau_k \quad x \to x^{2^k} (k = 1, \dots, 6)$ are all powers of each other, they fix the same codewords, if any Thus it suffices to examine $x \to x^2$ Since the cycle structure here (2 cycles of length 1, 18 cycles of length 7) allows codewords of weight 22, all possibilities were examined by computer and it was found that 2 such codewords exist These are transformed into each other by $x \to x + 1$ The 127 X 128 images under G of either of these are all distinct Thus the words of weight 22 in

the (128,64) BCH code occur in full classes of size 7 X 127 X 128 = 113,792 except for the 127 X 128 = 16,256 indicated above. Testing the 85 weight 22 codewords which occurred during our simulation of this code indicates that there are just 2 further classes of size 113,792 Thus we conclude

The (128,64) BCH code has 243,840 codewords of weight 22 These codewords may be constructed by applying G to the following representatives

A = (0) (3,6,12,24,48,96,65) (23,46,92,57,114,101,75) (43,86,45,90,53,106,85),

B = 1,2,6,11,17,18,30,33,36,39,40,45,61,68,82,99,101, 103,106,112,115,119,

C = 1,13,22,25,26,37,44,47,56,65,67,80,83,85,86,88,99, 105,115,119,120,122

The first one (obviously) corresponds to the single small class of size 16,256

References

1 Baumert, L D , and McEliece, R J , "Performance of Some Block Codes on a Gaussian Channel," Proceedings of the 1975 International Telemetering Conference, pp 189-195, McGregor and Werner, Washington, D C , 1975

2 vanLint, J H Coding Theory, Springer Lecture Notes in Mathematics No 201, Springer-Verlag, Heidelberg, 1971

N78-24173

A High-Speed Computer Link for Moderate Distances and Noisy Environments

M W Sievers

Communications Systems Research Section

To satisfy the need for a fully duplex high-speed computer data link for the antenna automation project at DSS 13, a very simple and inexpensive scheme was employed. The link requires two coaxial cables over which is sent a unipolar "digital frequency modulated" signal in which a logical 1 has twice the frequency of a logical 0 Optical isolators and filters reduce ground loop effects and increase noise immunity Tests conducted in various environments and over different cable lengths at JPL, DSS 14 and DSS 13 have indicated that the link is highly effective

I. Motivation

As part of the automation project being conducted at DSS 13, a need arose for a high-speed, fully duplex communication link between a microprocessor located in the teepee of the 26-meter antenna and a minicomputer located approximately 500 meters away in the control room The harsh electrical environment at DSS 13 necessitated incorporating circuitry that was resistant to ground loops and large noise spikes

It was desired to make the link hardware as insensitive to environmentally induced faults as possible while keeping it reasonably simple The philosophy taken was to accept faults occurring with low to moderate probability but with high coverage (coverage is the conditional probability that a system can recover from a fault given that a fault has occurred) So fault detection is as important in the link design as fault prevention. Clearly, since the most probable type of fault, i e , single bits, burts, etc , is a function of the nature of the electrical environment, a provision was made for incorporating various fault detection schemes or combinations of schemes in

the link design to permit the use of the link in environments other than that at DSS 13.

II. Link Implementation

The link was implemented using identical modules at each computer consisting of transmitter and receiver submodules One computer transmits to the other computer via one coaxial cable and receives from the other computer via another coaxial cable In each transmitter and receiver submodule, a first-in-first-out (FIFO) data buffer facilitates achieving the full duplex nature of the link as well as providing a means for synchronizing the computers to the link

Link data are encoded into a "digital frequency modulation" (DFM) signal, which encodes a logical one at twice the frequency of a logical zero Figure 1 illustrates the modulation technique as well as the timing used in the DSS 13 link As shown, each bit period is divided into two subperiods The clock subperiod (C) signals the start of a bit period and is

followed by a data subperiod (D). The duty cycle of the pulses as well as the separation between pulses was chosen so that the transient effect of charging the coaxial cable by a given pulse had sufficient time to decay before the occurrence of the next pulse

A Poisson distribution was assumed for the nature of the environmental noise at DSS 13. That is, it was assumed that the probability that a given noise spike has duration t is $e^{-\lambda t}$ for some λ, a constant. It was further assumed that 95% of all noise spikes would be of duration 200 nanoseconds or less ($\lambda = 0.015$), so that if a lowpass filter eliminated all pulses of less than 300 nanoseconds, about one noise spike in 100 has a chance of being passed by the filter if no other precautions are taken.

Although this result by itself is not acceptable, when coupled with the probability of a pulse of duration greater than 300 nanoseconds having sufficient amplitude to be incorrectly interpreted, the link fault rate is reduced to an acceptably small level Since noise spikes tend to result in common mode noise, a differential receiver front end cancels most of the effect of a noise spike. In the link, an optical isolator serves the dual function of a ground loop desensitizer and differential receiver

It is not known at this time what the actual link fault rate is The link has not yet made an error in approximately 10^8 bits during several hours of testing at JPL, DSS 14 and DSS 13

III. Link Transmitter

A block diagram of the link transmitter is shown in Fig. 2. The host specific interface connects the transmitter section to the host computer that drives it This interface communicates with the FIFO input control logic, which strobes data into a 256 by 8 FIFO data buffer This buffer was constructed from Advanced Micro Devices 2841A 64X4 FIFO chips The operation of the FIFO buffer is asynchronous with respect to its input and output, and thus the host computer may be entering data into the FIFO while the link is removing data.

A transmit enable flip-flop in the output control-data formatter enables data from the FIFO buffer output and parity encoder to be shifted out The 9-bit even parity serial word is output to the coaxial cable via a high-current 75450 series driver terminated in the characteristic impedance of the coaxial cable

At the heart of the output control-data formatter is a glitchless three-phase clock, illustrated in Fig 3. A 4-bit binary counter counts block pulses applied to it The three most

significant bits are decoded by a four- to ten-line decoder A single output of the decoder becomes true as a function of the four input lines The enable line connected to the most significant input of the four- to ten-line decoder is derived from the transmit enable flip-flop.

The output of the decoder is inverted and clocked into D flip-flops by the least significant bit from the counter. This guarantees glitch-free clock pulses with phase $\phi1$ present first, followed by $\phi2$ then $\phi3$.

The parallel to serial shift register is clocked by the trailing edge of $\phi1$ Each time a new word is to be loaded into the shift register, a flip-flop in the output control-data formatter is set This flip-flop holds the load enable line true on the shift register, which is then loaded by the trailing edge of $\phi1$. $\phi2$ clears the load enable flip-flop and is output as the clock pulse. At $\phi3$, the output of the shift register is gated out and a bit counter within the output control-data formatter is incremented The bit counter is decoded and determines when to advance the FIFO output and when to load the next word into the shift register The output process continues until the FIFO is empty or the transmit flip-flop is cleared by the host interface.

The output control-data formatter also signals the host interface when the FIFO buffer has been cleared This signal is used by the host interface to generate an interrupt to give the computer an indication of when it may send the next data block. In the DSS 13 configuration, this interrupt is used to fill the transmit buffer with new data if any is to be sent, but the transmit flip-flop is not set to transmit at this time. The link depends on a software handshake process for synchronizing input and output A sending computer must wait for a message from the receiving computer signaling that it can accept a new transmission Upon receipt of this message, the sending computer may send another block

It should be noted that while this handshaking method is simple and effective, if not carefully applied, it can lead to a deadlock problem, e g., neither computer is transmitting because both are waiting for an acknowledge message from the other What was done at DSS 13 was to give the minicomputer master status. It sends a request to the microprocessor, which acts as a slave, for data and waits for that data before sending the next request The microprocessor does not send data to the minicomputer unless it is requested to do so.

IV. Link Receiver

After isolation and filter circuits, the DFM signal is split into data and clock pulses in the data-clock pulse separator (Fig 4) This module assumes that the first pulse it receives is

always a clock pulse Internally, a data bit latch circuit is cleared by each clock pulse and set if a data pulse is present. A strobe pulse is issued after a delay sufficiently long to guarantee that a data pulse is latched. The strobe pulse is used to clock the output of the data bit latch into a serial to parallel shift register. The parallel word is scanned for the presence of a synchronization (sync) word If a correct parity sync word is found, the sync detector latch is set and data may be strobed into the FIFO buffer. If the data stream vanishes for a "long" period of time, e g., 16 clock periods, the sync detector latch is cleared.

The FIFO input control waits for the sync detector to find the sync word It strobes the sync word into the FIFO buffer and starts a bit counter Each time a new word is available in the shift register, it strobes that word into the FIFO. FIFO input control also monitors the FIFO buffer status and signals the host specific interface when the FIFO is filled This interface issues a computer interrupt to indicate that data is available to be read.

The host interface reads data from the FIFO buffer under computer control and signals the FIFO output control when it has transferred the data word to the computer. Output control then signals the FIFO to present the next word at its output.

Any time the parity check circuitry detects a bad parity word after the sync detector is set, it signals the host interface This signal is used by the host interface to generate a computer interrupt

As noted in Section I, fault detection and recovery have been left to the software. Although sophisticated detection-correction schemes are possible, the DSS 13 link employs a simple 16-bit check sum for fault detection This scheme detects all errors not a multiple of 2^{16}. Recovery can be simply accomplished by retransmission of the data block in error As noted in the previous section, a software handshake is performed to synchronize the sending and receiving computer. The acknowledge message sent by the receiving computer contains a word that lets the sending computer know if the block it just sent was received with an error Normally, this error message could be used to request that the same block be retransmitted. This is not presently done at DSS 13 since, in this particular application, it is not required
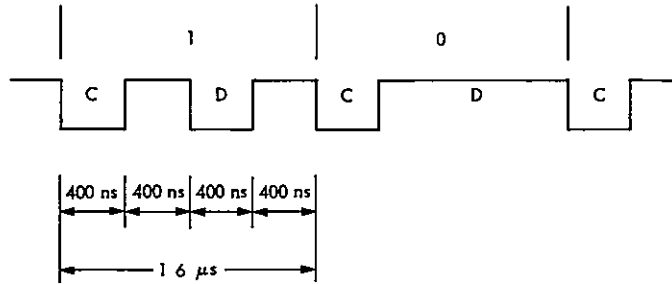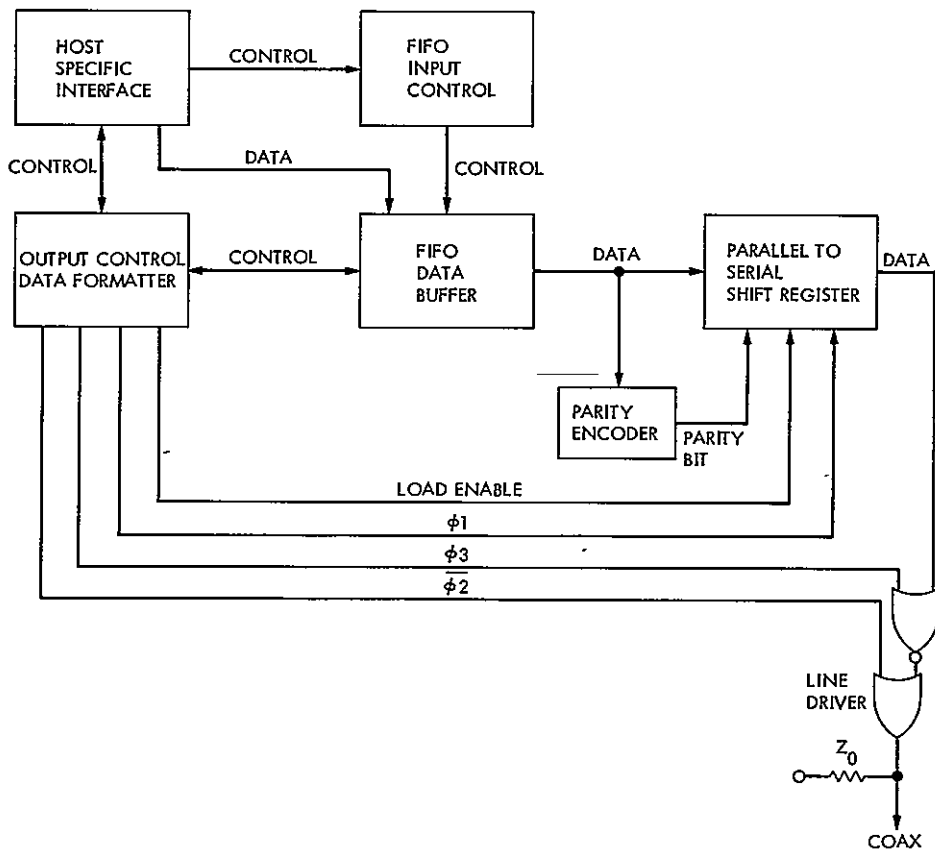
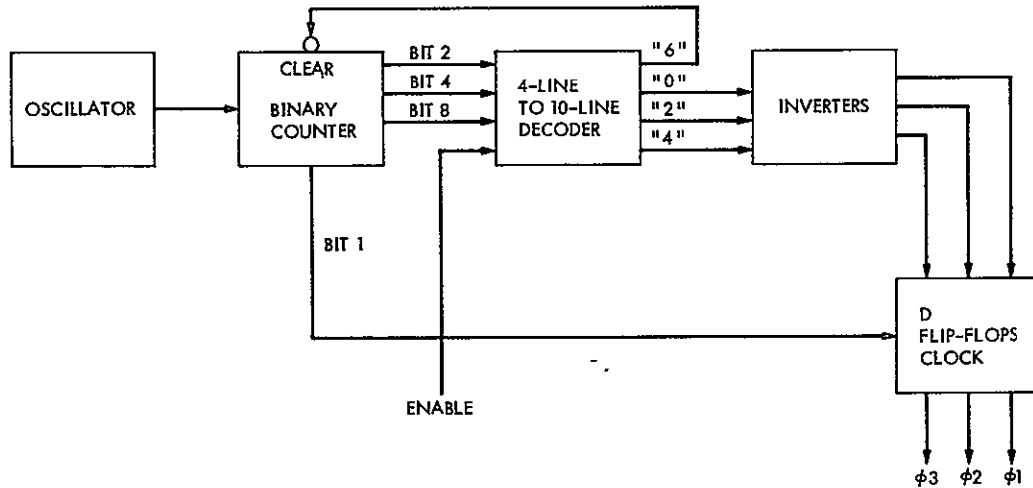Fig.1. Digital frequency modulation

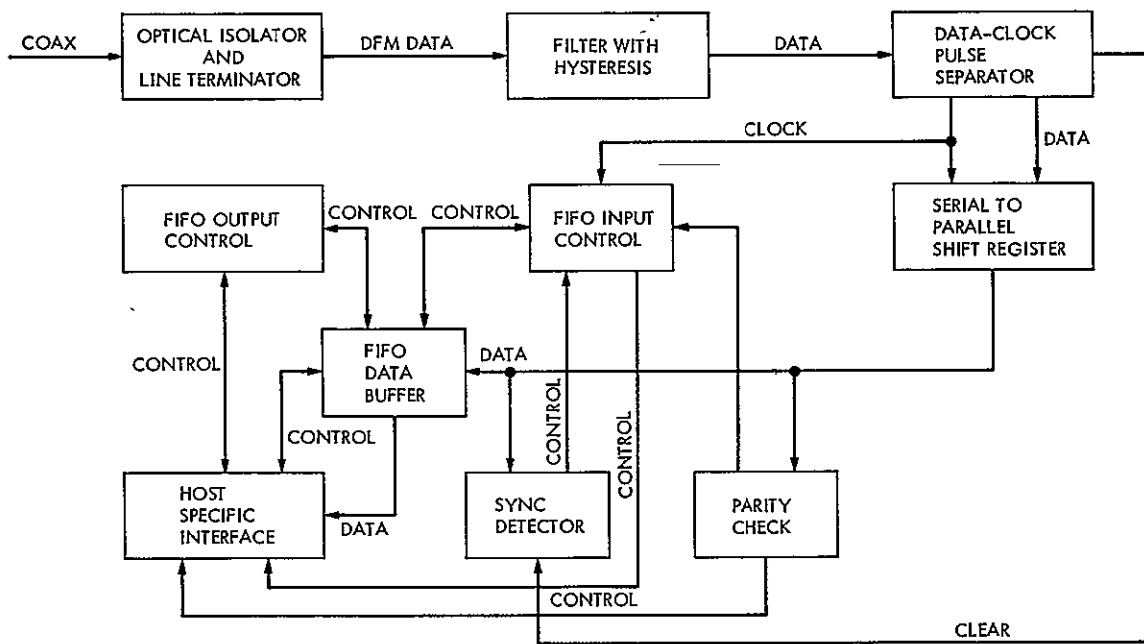Fig. 2. Transmitter module

Fig. 3 Three-phase clock

Fig. 4 Receiver module

N78-24174

DSS 13 Automated Antenna Pointing Subsystem Phase 1 Hardware

M W Sievers
Communications Systems Research Section

An automated antenna pointing subsystem (APS) is being installed at DSS 13 as part of the unattended station project. The function of the APS is to track an instructed position with the 26-meter antenna and to monitor the antenna servo system and meteorological conditions to ensure a proper operational environment. This article will discuss the now-completed first phase of the digital hardware portion of the APS development

I. Introduction

An antenna pointing subsystem (APS) is being designed as part of the unattended station project now in progress at DSS 13 The function of the APS is to provide control and monitoring of the 26-meter antenna. The development has been divided into three phases

Phase 1   Design and install hardware and software required to slew the antenna to a given source, to track that source, and to provide the minimum set of monitoring functions required by the tracking function.

Phase 2·   Design and install hardware and software to monitor the antenna environment to ensure safe unattended operation

Phase 3.   Refine servo models used in phase 1 and design and install hardware and software to connect the APS to the station controller

Phase 1 has now been completed, and the monitor hardware for phase 2 has been installed This article will concentrate on the phase 1 hardware system

II. Phase 1 Functional Requirements

Phase 1 functions can be classified into two categories tracking, and the monitor and display needed to support tracking.

The tracking function requires that there be a means to move the antenna to a selected source and to track that source as a function of time Specifically, this function is composed of the following subfunctions

(1) Selection of source to be tracked

(2) Calculation of the azimuth and elevation positions of this source as a function of time

(3) Determination of the present antenna azimuth and elevation and calculation of an error signal

(4) Moving the antenna to correct for the error calculated in (3)

(5) Determination of when the antenna is pointed at the source

(6) The particular configuration of the DSS 13 antenna requires

   (a) Ability to set and reset azimuth and elevation brakes, to select azimuth and elevation high or low speed, and to turn on the hydraulic system

   (b) Ability to sound a warning prior to moving the antenna

   (c) Provide a signal to the servo system that indicates whether the digital system is functional.

The monitor and display requirements for phase 1 are

(1) Antenna wrap-up and pre-limit indicators

(2) Brake and speed monitors

(3) Indicator that APS has control of antenna

(4) Warning displays

(5) Current antenna position and tracking error display

III. APS Phase Hardware Structure

A system that satisfies the requirements of Section II is shown in Fig 1 At the heart of the phase 1 hardware is a Modcomp II minicomputer configured with a floating point arithmetic unit, a moving head disk, a terminal device, a quad Standard Interface Adaptor (SIA), and a dual digital-to-analog converter (DAC). A multiplexer-demultiplexer (MUX-DEMUX) connects the minicomputer to a display device interface, an antenna angle encoder interface, and the servo system monitors and control interface via one of the Standard Interface Adaptors The instructed position is input through the terminal device and the dual DACs provide the azimuth and elevation rate commands which are amplified to drive the antenna. MUX-DEMUX details may be found in Section IV, and the interface descriptions are found in Sections V through VIII.

Universal time (UT) is produced by the UT generator in a 30-bit BCD format In addition to time, the UT generator also supplies pulse trains of one pulse per second (1 PPS) and 50 pulses per second (50 PPS) Both the 1-PPS and the 50-PPS signals are synchronized with the units of seconds. These signals are provided as interrupts for the APS software (Ref 1)

IV. Multiplexer-Demultiplexer

The purpose of the multiplexer-demultiplexer is to connect several device interfaces to the APS minicomputer via a single Standard Interface. The front end of this device is a Standard Interface compatible module (Fig 2) Through a simple gating arrangement, the Standard Interface signals are buffered and made to look like a bus configuration Device interfaces connect to this bus and communicate with the minicomputer at its request. Control information on the bus is derived from the interface function bits $\overline{F}_0$ and $\overline{F}_1$ as well as the data bits Device interfaces are initialized by a simple 74121 power-up reset circuit

When not outputting to the minicomputer, the MUX-DEMUX is always prepared to accept command information and data from it MUX-DEMUX status information may be jammed into the minicomputer at any time, but a data transmission must be requested The MUX-DEMUX always acknowledges a command by sending the minicomputer its status

A watchdog timer, which is part of the servo control hardware (see Section V), must periodically be refreshed by the computer to indicate that the program is intact and executing Should this timer fail, the MUX-DEMUX will send the computer its status Since the act of sending status causes a computer interrupt, the action on watchdog timer expiration is performed in the hope that sufficient information is present for the program to respond to the interrupt and attempt recovery.

Referring to Fig 2, the minicomputer signals its desire to send information to the MUX-DEMUX by asserting $\overline{STC}$ This signal is received and filtered by a 75182 integrated circuit (IC) chip. The 75182 output gates on the response signal $\overline{RSP}$ and is inverted to inhibit the MUX-DEMUX data ready $(\overline{RDY})$ and function code $(\overline{F}_1\overline{F}_0)$ 5438 drivers and the data $(\overline{D}_0 - \overline{D}_7)$ 75138 drivers. Additionally, the 75182 output enables one input of a 7400 NAND gate, the other input of this gate is connected to the 7404 that receives the $\overline{RDY}$ signal

After the minicomputer receives the $\overline{RSP}$ signal, it places data on $\overline{D}_0 - \overline{D}_7$, the function code on $\overline{F}_1\overline{F}_0$, and asserts $\overline{RDY}$ When $\overline{RDY}$ is received by the 7400 discussed above, that gate's output goes low This signal is inverted by a 5438 and filtered by a 75182.

The output of the 75182 gates on a 7411 AND and starts another 5438-75182 time delay circuit. This delay eventually turns the 7411 off and disables the $\overline{RSP}$ signal The 7411 output is a strobe signal that indicates that the data and function code being sent are stable

The minicomputer generates a 11 function code when it is sending the MUX-DEMUX a command byte. A 7408 AND detects the 11 function code, and its output is gated with the strobe from the 7411 to enable a 74S138 decoder and set a status jam flip-flop. (Note that this flip-flop is also set by the time-out signal from the watchdog timer.) Three data bits at the input of the 74S138 select one of eight interfaces to which the minicomputer is sending a command. The five remaining bits are interpreted as command information by the selected interface

After the minicomputer releases $\overline{STC}$, to acknowledge the command just received, the status jam flip-flop output is gated to assert $\overline{STD}$ with a 11 function code. The minicomputer responds to the asserted $\overline{STD}$ by signalling $\overline{RSP}$ In the MUX-DEMUX, $\overline{RSP}$ is gated and filtered through the same circuitry that gated and filtered $\overline{RDY}$ in the discussion above This time, however, no strobe is issued and the MUX-DEMUX places its status on the $\overline{D}_0 - \overline{D}_7$ data lines and signals $\overline{RDY}$. $\overline{RDY}$, the function codes, and data are held asserted as long as the minicomputer is asserting $\overline{RSP}$.

When the minicomputer sends a full word to the MUX-DEMUX, the function code bits determine whether the Data Acquisition Interface or the Plasma Display Interface is to receive the data word. A pair of 7411s gate a strobe to the Data Acquisition Interface if $\overline{F}_1 F_0$ is true or to the Plasma Display Interface if $F_1 \overline{F}_0$ is true. Note that when a full word is being sent, all bits may be interpreted by the receiving interface and that the status jam flip-flop is not set

If the command byte or full word sent to the MUX-DEMUX is a request for data from the selected device, that device issues a data ready signal $\overline{DTARDY}$ when it has data available and places its data on the output data bus The $\overline{DTARDY}$ signal is latched in the data ready flip-flop, the output of which is gated to produce an $\overline{STD}$ signal and also enables the output data bus onto $\overline{D}_0 - \overline{D}_7$ by bringing the 75138 strobe lines low The handshake process mentioned in the status byte jam discussion is started to transfer data bytes to the minicomputer, with the following differences

(1) Data bytes are transferred to the minicomputer as long as the data ready flip-flop is set. It is the responsibility of the sending interface to clear the flip-flop when it has transferred all of its data by issuing $\overline{DONE}$

(2) The status jam flip-flop being false enables the trailing edge of the $\overline{RSP}$ signal to fire a 74123 one-shot. The one-shot output, labeled NXTBYT, is a signal to the sending interface to place its next data byte onto the output data bus if one is available.

(3) The function code is 00

Each interface capable of sending data to the minicomputer has an established number of bytes that it will transfer. Since the minicomputer has a priori knowledge of that number, it can prepare its input hardware accordingly.

V. Servo Control Hardware Interface

The Servo Control Hardware Interface connects the minicomputer to azimuth and elevation speed and brake control relays, the hydraulic pump starter, and the warning horn relay. Additionally, it provides the servo control system with an indication that the APS software and hardware are functional, i e., the watchdog timer. The minicomputer controls these functions via command bytes.

In Fig. 3, brake and speed control information is stored in a 74175 register. This register is clocked by a signal from the 74S138 interface selection decoder in the MUX-DEMUX. Four data bits on the input data bus are clocked into the 74175 and buffered by 75453s to drive brake and speed control relays. High speed and brakes released is indicated by a low signal at the 75453 outputs.

A 74S138 decoder in the Servo Control Interface decodes command bytes from the minicomputer to refresh the watchdog timer, turn the hydraulic pumps on or off, and sound the warning horn. The watchdog timer consists of a 74123 retriggerable one-shot with a one second delay and a 75452 driver The driver pulls in a relay in the servo control system. As long as the relay is held on by the timer, the minicomputer has control of the servo system. Should the watchdog time out, the relay is dropped out and a time out signal from the watchdog timer is issued to the MUX-DEMUX. Once the relay has been turned off, the minicomputer no longer has control of the servo system and reset must be done manually.

The hydraulic pumps are controlled by a 74S112 flip-flop and 75453 driver. When the driver output is low, the pumps are on, and off otherwise.

Finally, the minicomputer can actuate a warning horn The horn circuitry consists of a 555 oscillator, a 74191 counter, a 74S112 flip-flop and a 75453 driver A single command byte from the minicomputer sets the 74S112 and enables the 555 Each pulse from the 555 sounds the horn and increments the 74191. When the horn has been sounded three times, the 74S112 is cleared and the 555 disabled. The horn on time is approximately one second with an on-to-off ratio of about 2:1.

VI. Plasma Display Interface

A Burroughs Self-Scan plasma display panel was made part of the APS so messages could be quickly displayed. Interface circuitry (Fig 4) provides control signals for cursor manipulation, character input-output, and screen clear. The interested reader should consult a Burroughs Self-Scan manual for a signal glossary and timing diagrams.

Command byte information is used for cursor operations and screen clear Data bytes are separated into cursor pre-load addresses and characters. This is done by examining the most significant bit of a data word. If the bit is set, the circuitry generates signals to pre-set the cursor If not set, a write command is issued. This permits mixing cursor addresses and characters in a single transmission

VII. Angle Encoder Interface

The angle encoder interface (Fig. 5) consists of registers to hold the azimuth and elevation data words and circuitry to send these coordinates to the MUX-DEMUX in 8-bit bytes

The angle encoder is made by Northern Precision Laboratory and generates a 20-bit azimuth and a 20-bit elevation word. The encoder produces a data ready signal when it has data available. The data ready signal is filtered and used to strobe a set of 74174 registers when these registers are not being read by the minicomputer

A 74109 flip-flop is set when the minicomputer is reading angle encoder data from the 74174s. This flip-flop output disables an input of a 7408 AND, thus preventing the data ready from clocking the 74174 registers Data is placed on the output data bus by 74253 tristate data selectors A 74193 counter is decoded to select the byte to be placed on the bus Each time NXTBYT is received by the 74193, a new byte is placed on the bus When all bytes have been transferred to the minicomputer, the decoder issues the DONE signal

VIII. Data Acquisition Interface

The Data Acquisition Interface was designed to control a Data Acquisition Device This device, shown in Fig. 6, is a 64 differential channel analog-to-digital converter The device is made of Burr-Brown components SPM 851 eight differential channel, 12-bit analog-to-digital (A-D) converter, MXP 321 and MXP 320 analog multiplexers, and 74365 tristate buffers

The MXP 321 contains a binary counter which may be incremented by a strobe signal or randomly loaded by a strobe signal with load enable asserted. The output of this counter selects the analog channel to be sampled The MXP 320 contains an analog multiplexer only

In the SDM 851, another differential multiplexer selects analog data from one of the MXP 320 or the MXP 321. It also contains all circuitry necessary to start the A-D conversion and indicate when the conversion is complete The SDM 851 has been set up to start an A-D conversion after a new channel has been selected either by incrementing the channel address or loading a new one.

The interface that controls the Data Acquisition Device is shown in Fig. 7 A command byte sent by the minicomputer is interpreted in the interface to produce a strobe to the Data Acquisition Device. A full word sent to the interface causes it to bring the channel address load enable signal low and then issue a strobe pulse Data sent in the full word is used for the channel address data

The end-of-conversion signal from the SDM 851 is filtered and gated to produce the data ready signal to the MUX-DEMUX. A 74S112 flip-flop controls the select line on a pair of 74257 tristate data selectors. The NXTBYT signal clocks the 74S112 and is gated with its output to produce the DONE signal

Data is sent to the minicomputer left adjusted. In this form, it is convenient for the using software to select either a logical or arithmetic shift to correctly align the data

Reference

1 Sievers, M. W., "An Automated Tracking System for the ARIES Antenna," in *The Deep Space Network Progress Report 42-32*, pp 139-150, Jet Propulsion Laboratory, Pasadena, California, April 15, 1976.

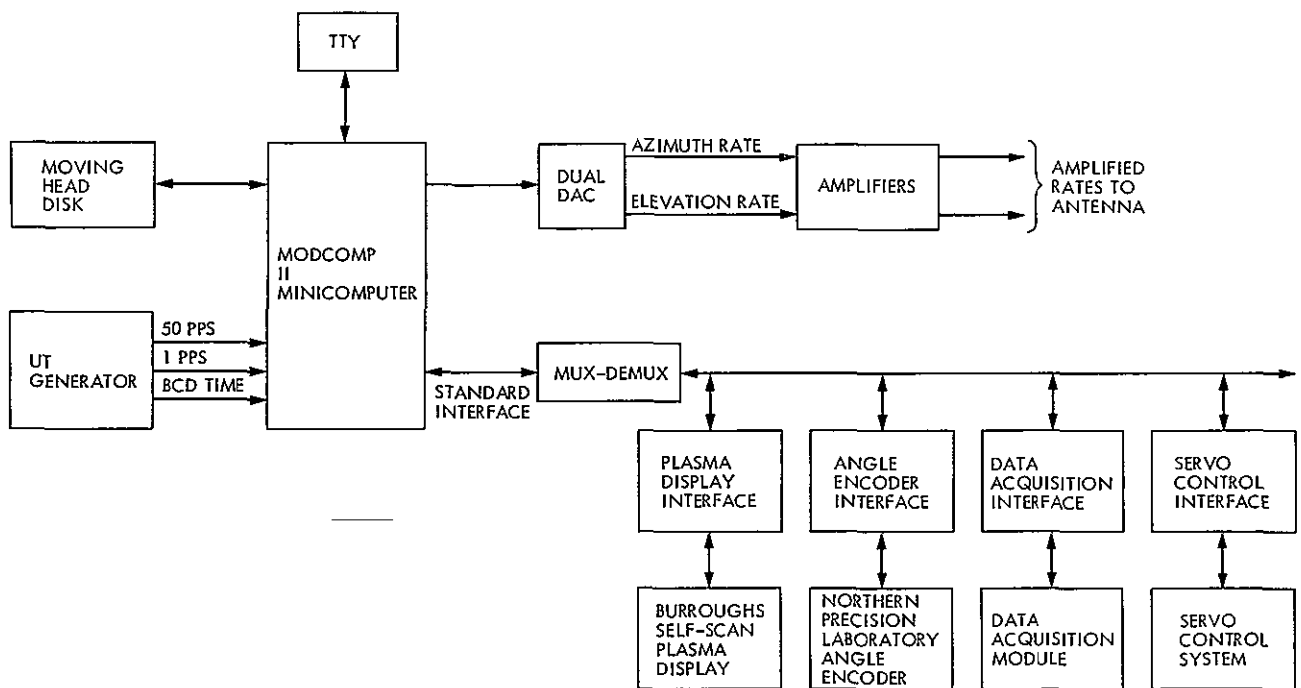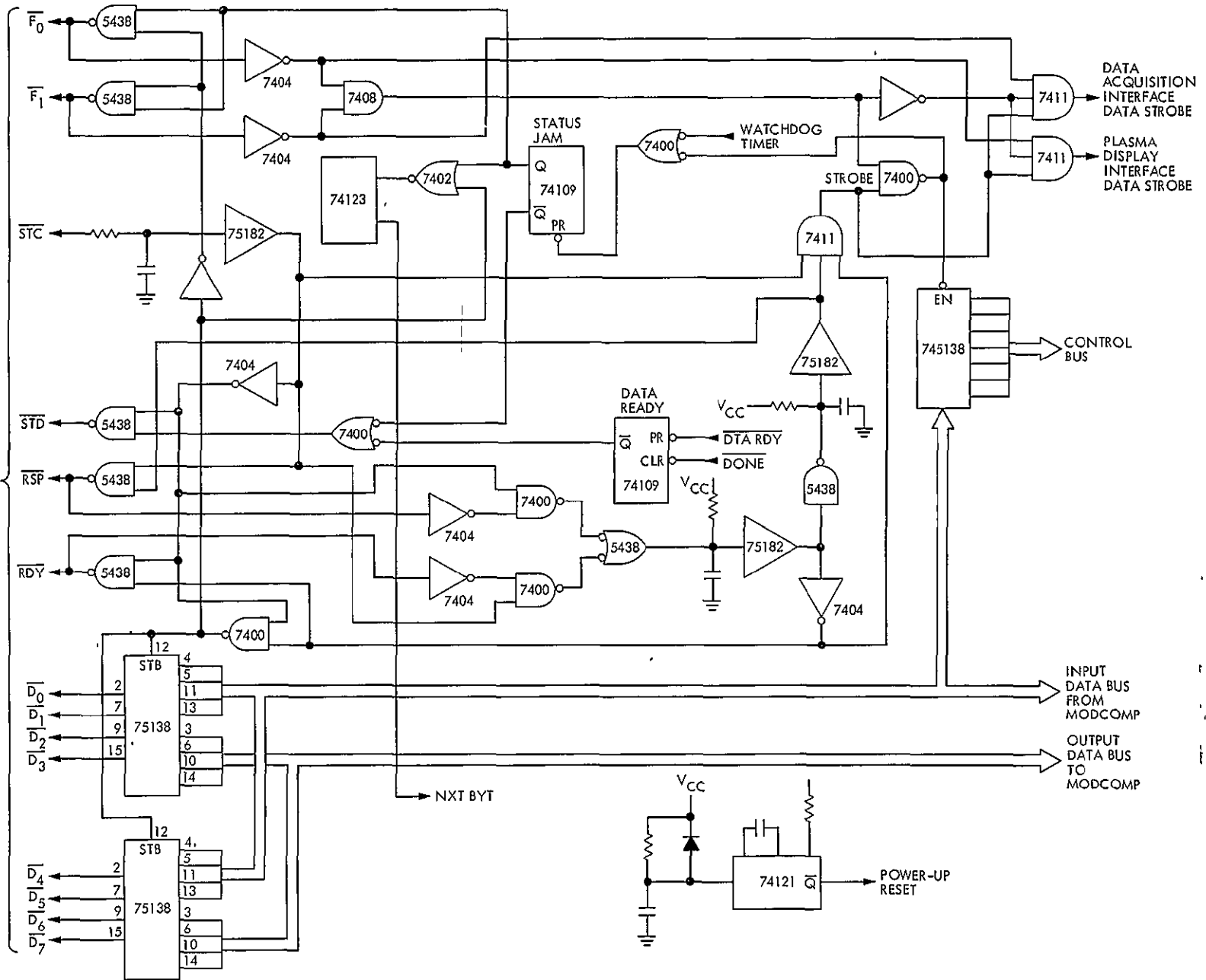Fig. 1. APS phase 1 block diagram

Fig. 2. Simplified MUX-DEMUX logic
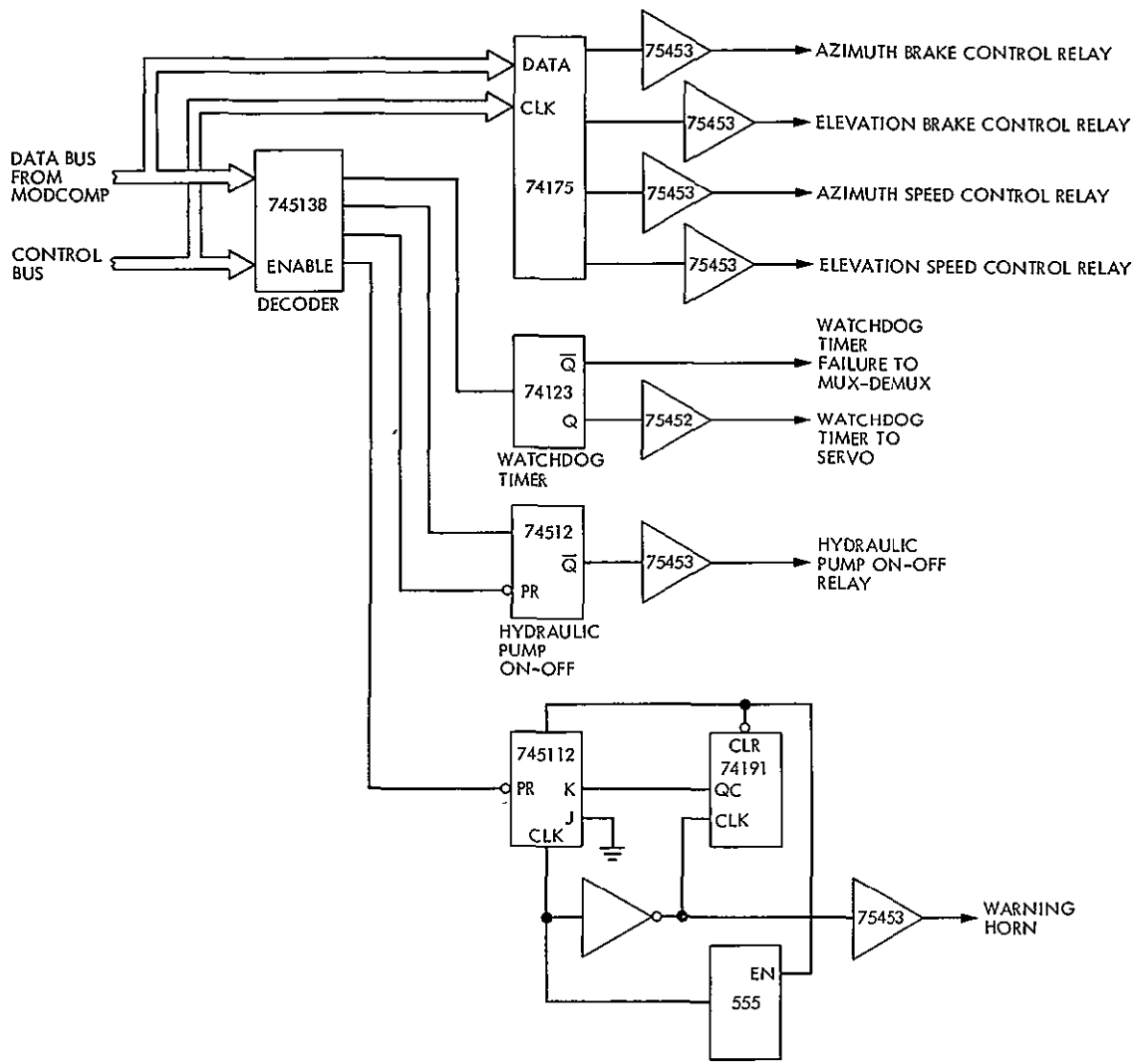
Fig. 3. Servo control interface logic
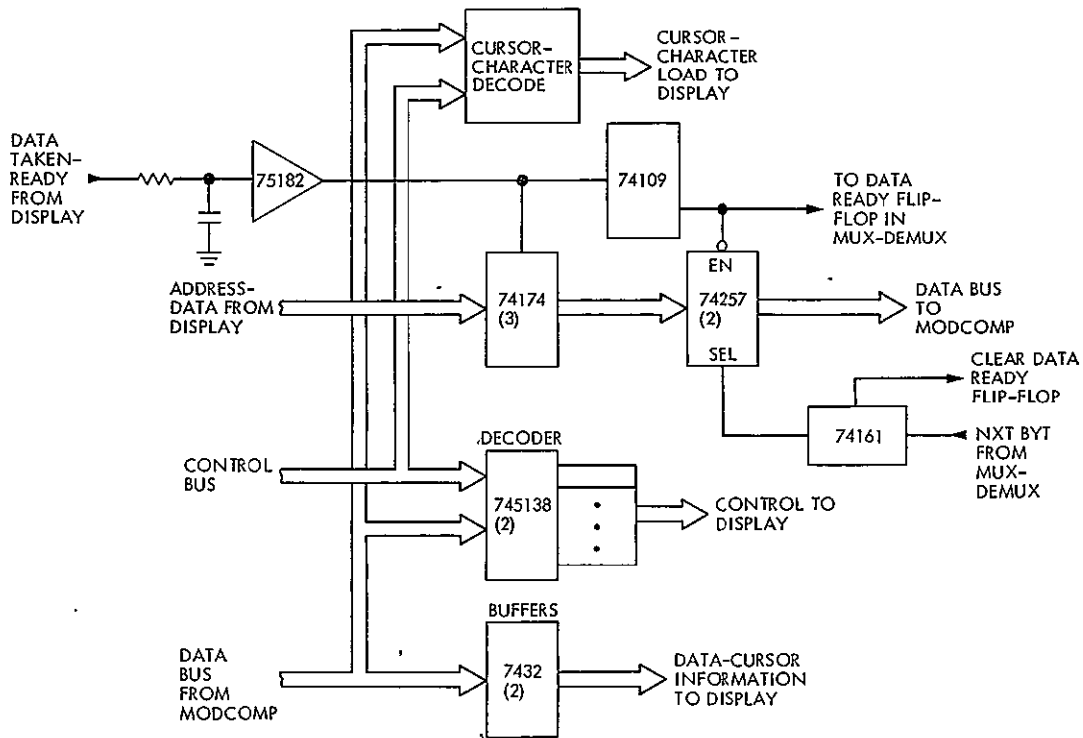
Fig. 4   Plasma display interface
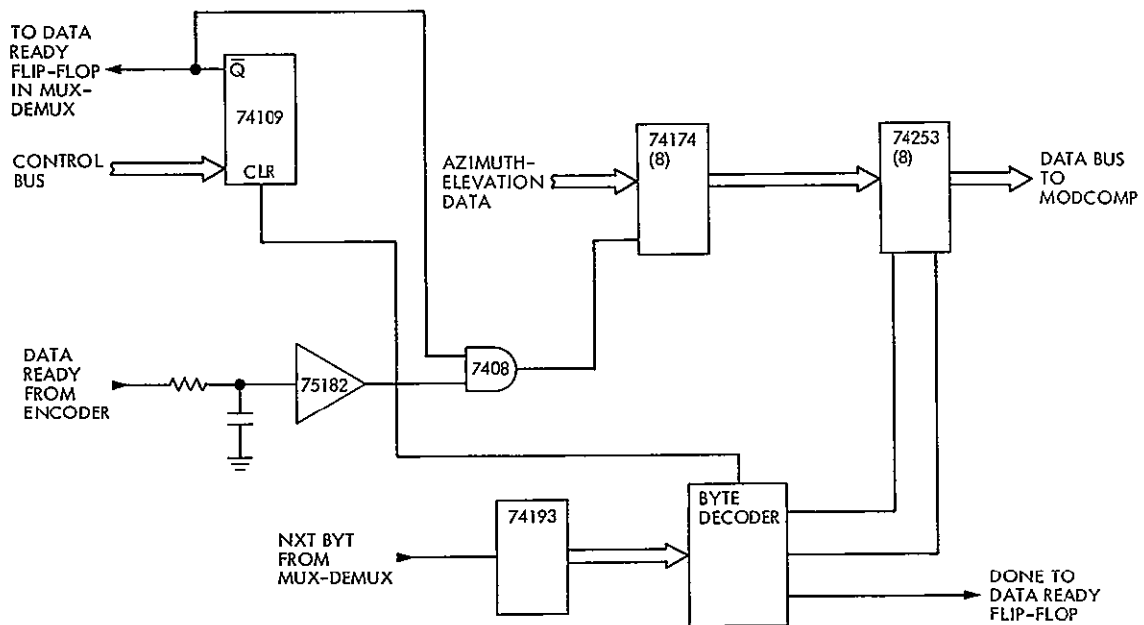
Fig 5   Angle encoder interface
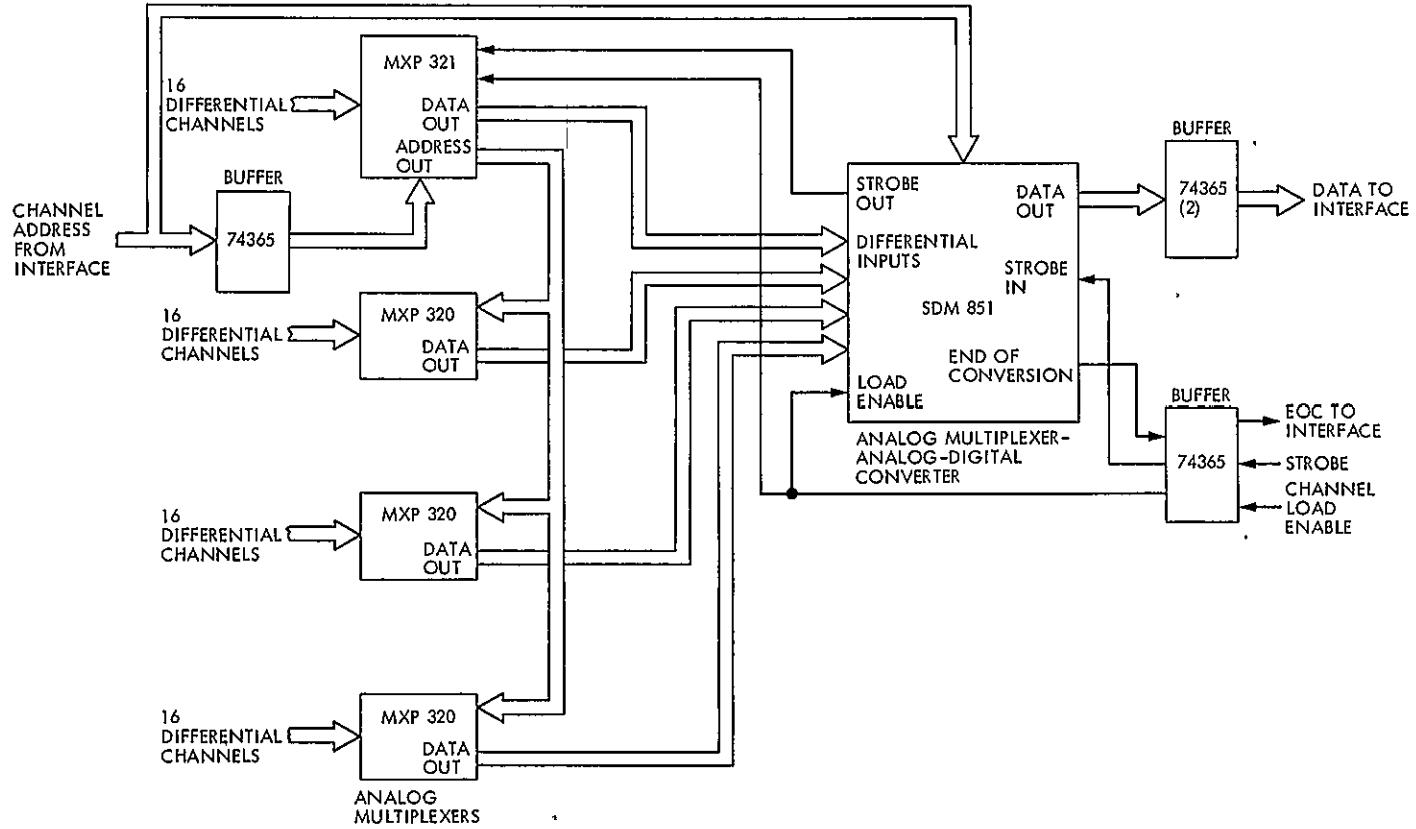
Fig. 6. Data acquisition device
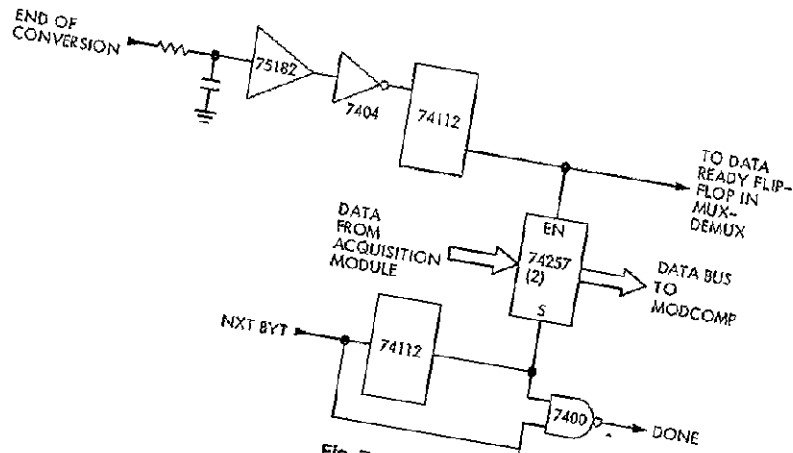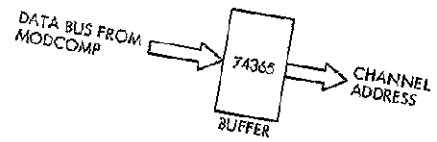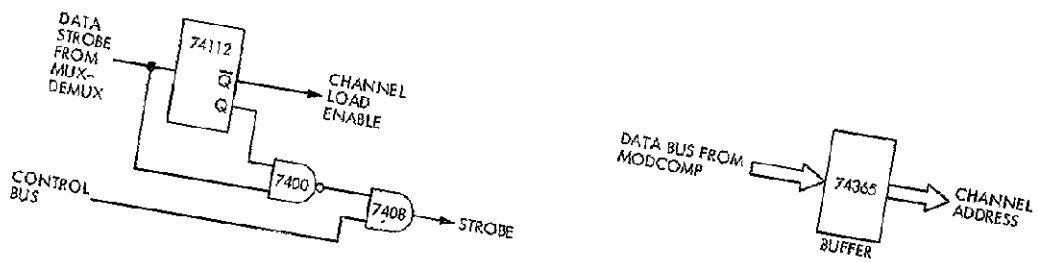
Fig. 7. Data acquisition interface

Digital High Density (80 Mb/s) Tape

M. D Donner
Communications Systems Research Section

This article describes work with a state-of-the-art high density digital PCM tape recorder- reproducer system recently purchased by JPL The tape recorder is designed for 80 Mb/s operation at an overall bit error rate of 10^{-5} and for 40 Mb/s operation at 10^{-6}. The article describes the process of measuring the error rate Also detailed is a data rate buffer designed for use in recent radar experiments and generalizable to most potential uses of the recorder system.

I. Tape Transport

Nothing is more crucial to the performance of a high density tape recording system than the tape transport. In standard computer applications, the transport is taken for granted, but in this system with narrower tracks on wider tape moving faster than computer tape recorders, the transport is critically important.

Each data track is 0.635 mm (0 025 in.) wide with 0 254-mm (0 010-in) spacing between tracks Tape speed is 152 or 305 cm/s (60 or 120 ips). The system data rate using all 28 tracks is 86.8 Mb/s (Megabits per second) at 305 cm/s (120 ips) and 43.4 Mb/s at 152 cm/s (60 ips) Omitting the two edge tracks (which have a higher error rate than the inside tracks) the data rate to 80.6 Mb/s at 305 cm/s (120 ips) and 40.3 Mb/s at 152 cm/s (60 ips) The tape is 25 mm wide and the transport can accept reels up to 38 cm in diameter. A 38-cm reel holds about 3300 meters of 25-micron-thick tape

Tape tension is maintained with tension arms whose position errors are fed back to the reel hub motors Tape motion is controlled by a capstan-and-pinch roller system. Tape speed is controlled by a servo which phase locks the capstan tachometer signal (derived from a rotating patterned wheel and an optical sensor mounted on the capstan motor shaft) to a crystal reference.

All the tape guides are mounted on roller bearings Both tape guides and reel hubs are mounted on platforms with small jackscrews so that they may be aligned.

Alignment of the guides and hubs is very critical because the guides provide no restoring force to keep the tape centered in the tape path. Strict parallelism must be maintained between the axes of all the rotating elements (hubs and guides) and the axis of the capstan. If parallelism is not maintained, the two edges of the tape are subjected to different tensions resulting in scalloping of one edge of the tape.

The restoring force problem is very important to this system because of the narrowness of the tracks With tracks only 0 635 mm wide, separated by 0.254 mm, it only takes 0 127 or 0.254 mm of sideways motion to cause a 6-dB loss of signal amplitude and the resultant increase in error rate. Excessive skew can raise the system error rate by a factor of 10 to 100.

The record and reproduce heads are IRIG standard inter-leaved 28-track two-section heads. The odd numbered tracks are on one set of heads and the even numbered tracks on another. An earlier version of the transport with single in-line heads was found to be unacceptable, because the track widths were reduced to 0 318 mm due to problems in making a 28-track in-line head.

II. Data Electronics (Fig. 1)

User data is delivered to the recorder at 3 1 MHz when operating at 305 cm/s (120 ips) or 1.6 MHz when operating at 152 cm/s (60 ips) on 30 differentially driven twisted pairs, 28 data lines and two clock lines The recorded data is blocked into 512 bit blocks made up of 496 bits of user data plus 15 bits of synchronization character plus one bit of parity Room for the 16 overhead bits is made by increasing the clock rate internally by a factor of 32/31 using a PLL. Overhead represents about 3 1% of all data actually on tape

The data, now at a clock frequency of $\binom{3 \ 2}{1 \ 6}$ MHz is mixed with a PN sequence of period $2^{17} - 1$. The purpose of this is to eliminate the DC component of the user's data

This data stream is now converted to NRZ-M and is amplified and sent to the record heads Recording is done without any added bias signal

On playback the signal from the reproduce heads goes through several stages of amplification, filtering, and a limiter to recover a binary signal In this scheme the data clock is not recorded explicitly on a separate track as is done on many lower data rate systems. Packing density is so high (12,000 bits/cm/track = 30,000 bits/inch/track) that intertrack skew completely destroys the utility of an explicit clock track Instead, the data clock is recovered by phase locking an oscillator to the transitions in the reproduced data. Each track has its own PLL to recover its clock. Next, the data stream is extracted from the PN sequence by a parity check scheme The primitive polynomial used for the PN sequence in this machine is $X^{17} + X^{14} + 1$ Thus, the parity check network (mod 2 adder) takes three taps off a shift register containing the scrambled data One consequence of this scheme is that all single bit errors that occur between the PN encoder and decoder will appear as three bit errors in the output data. In our preliminary testing we did observe that errors occurred in bursts of three

The clock from one track (track 9 in this system) is arbitrarily assigned as the master clock and the final deskew operation uses this clock.

Due to skew problems, the 28 bits coming off the repro-duce heads at any one instant are probably not the same 28 that were recorded simultaneously Thus, a method is needed for realigning the data streams so that the 28 bits that went in simultaneously on record come back out simultaneously on playback. In order to do this, the synchronization characters inserted in the data stream on record must be recognized and sufficient buffer space must be provided to permit the system to wait for markers on all tracks before playing the data out without running out of buffer space first Data block length must be large enough that the probability of slipping one whole block on any track with respect to the others is kept very small Block length should be kept as small as possible to minimize deskew memory requirements.

Thus, blocks are 512 bits long (496 bits of data, 15 bits of synchronization character, 1 bit of parity) and 1K bits of memory are provided per track for deskew buffering This system is capable of reproducing the input data smoothly and evenly with no gaps or discontinuities caused by having to wait for a late synch character In earlier versions of the tape recorder the manufacturer experimented with shorter deskew buffers but found 1K to be best. Note that the particular value of block and buffer size are critically dependent on the skew characteristics of the tape transport.

III. Error Rate Testing of the Data System

The first problem to be addressed after delivery of the system was the characterization of its overall error perfor-mance The contractor's own testing was fairly low level and his test equipment did not have much resolution of error location A significant problem in tape recording systems is the presence of bad spots on the tape Bad spots contribute significantly to the overall error rate. The primary cause of bad spots is imperfections in the tape occurring during the manufacturing process Other sources of bad spots or dropouts are fingerprints, dust and dirt, and so on In order to distinguish errors due to bad spots on the tape from other errors, it is necessary to be able to identify a tape location very precisely

Another major type of error source is the track dropout in which one particular data track makes a lot of errors (i.e., more than the average for normal tracks) Track dropouts can result from loss of lock by the PLL in the data electronics or from improper equalization of the filter in the low level amplifier section. The ability to identify errors on a track by track basis is another desirable feature in an error tester (Fig 2)

Error testing with this system is a two-pass operation On the first pass the tape is recorded On the second pass the test

data is played back, compared with the original, and errors are counted.

The tester is interfaced to an SDS 930 computer through the Pin/Pot system The computer can load or control all the internal registers as well as most of the control logic flip-flops The user, through the computer, controls the configuration of the tester

A. Test Data Format

Two different types of data were selected for testing purposes pseudo-noise sequence and DC. For the PN sequence data each track on the recorder receives a different phase of the same PN sequence. Eight different sequences are available ranging in length from $2^{16} - 1$ to $2^{23} - 1$ (i.e., $2^n - 1$, $n = 16$, 17, ..., 23).

The primitive polynomials used are

$$X^{16} + X^5 + X^3 + X^2 + 1$$

$$X^{17} + X^3 + 1$$

$$X^{18} + X^7 + 1$$

$$X^{19} + X^6 + X^5 + X + 1$$

$$X^{20} + X^3 + 1$$

$$X^{21} + X^2 + 1$$

$$X^{22} + X + 1$$

$$X^{23} + X^5 + 1$$

For the DC data type each track receives a single bit from a 28-bit reference word which is loaded from the computer Thus, except for synchronization characters inserted by the tester, the data on each track's input does not change

Synchronization characters are inserted with both data types The spacing between characters is determined by the PN sequence generator Once each cycle of the PN sequence the sync character is inserted. The sync character contains block number information (a 16-bit number) so that longitudinal location on tape is determined by block number and bit number within the block. Figure 3 illustrates the test data formats

The block number contained in a sync character is associated with the following data bits Thus a location on tape is Block F, bit B, as in Fig. 4.

Note that the sync character used by the tester is completely unrelated to the sync information generated internally by the Sangamo data electronics The Sangamo sync character is invisible to the user and there is no interaction with it

The synchronization character is made up of three parts. Four tracks receive the parts of a 63-bit PN sequence broken into four 16-bit sections (with one extra bit added to make it 64). These four tracks are the synchronization tracks Another seven tracks receive identical copies of the 16-bit block number. All the other tracks receive 16 one bits or 16 zero bits.

During playback/error count the tester searches for the sync character. The data from the synchronization tracks are cross-correlated with the 64 bits of the sync character When the correlation coefficient is higher than a threshold which is controlled by the 930, the synchronization character is "detected." The block number acquired simultaneously is loaded into the block number register and an error count cycle is initiated The block number is reconstructed by majority vote of the seven block number tracks

During an error count cycle each reproduced bit is compared with the predicted bit for that location. Disagreements are accumulated in a register.

B. Data Acquisition and Analysis

The next problems we had to address after designing and constructing the error tester described above were. What are some meaningful measurements of the system's performance? How do we go about making these measurements?

Some considerations that bore heavily on the decision-making process which answered those questions were

(1) The XDS 930 computer used to collect information from the error tester is much slower than the tester Although the tester's resolution is 1 bit, the computer cannot examine the tester's registers fast enough to realize that resolution

(2) What resolution is meaningful and useful in evaluating the performance of the tape system? How large physically are the bad spots on tape and how far apart are they? Also, what good comes from knowing an error's location down to the nearest 0 76 micron (30 micro-inches) when the tape transport's position resolution is only 30 cm.

(3) As we look closer and closer at the tape the amount of data we have to process grows With a tape speed of

305 cm/s (120 ips) and a data rate of 3 1 X 10^6 28-bit words per second the tester can produce 3 1 X 10^6 5-bit numbers per second Each 5-bit number is the total number of errors detected in one particular 28-bit word on tape. Thus, an error counting run of a 3300-meter reel of tape (a standard size) would produce 3×10^9 5-bit words. To store all this information would require about 1.5×10^{10} bits of memory Of course this error record would be very sparsely inhabited If the actual error rate was close to the $1 0 \times 10^{-5}$ specified for 305 cm/s (120 ips) operation, the table would only have about 8×10^5 non-zero entries

The physical length of a block of test data generated using the 16th-order polynomial is about 6 4 cm (2 5 in). There are about 48,000 test data blocks in a 3300-meter reel of tape We decided that tabulating errors on a block by block basis was a good compromise between computer memory limitations, transport position accuracy, and physical tape defect size Since our early experiments indicated that even a block error count table would be quite sparse, we decided to note in the table only those blocks with non-zero error count Thus, we discovered that 6000 memory locations were quite sufficient to hold error information generated from a 3300-meter tape (three locations per noted block)

Among the statistics we generated were

(1) Running overall bit error rate

(2) 100 frame boxcar — error rate over a 100-block-long "boxcar" which slides along

(3) 1000 block boxcar

(4) 300-meter boxcar.

We also generated two types of histograms

(1) A histogram in which bin #n contains the total number of blocks with n errors noted.

(2) A histogram in which bin #n contains the number of times n errorless blocks occurred between two successive blocks containing errors

IV. Results and Conclusions

A. Test Data and Error Performance

The results of our preliminary error testing of the tape system are enlightening and useful The histogram in which bin #n contains the total number of blocks with n errors has

shown us the threefold multiplication of single bit errors which results from the PN decoding scheme used in the recorder/reproducer's playback electronics (Fig. 6)

The clear run histogram (bin #n contains the number of times exactly n blocks have passed between two successive error blocks) has exposed tape difficulties which produce low-frequency bursts of errors This can result from a warped flange rubbing against the tape once each revolution of the reel Figure 7 is one such histogram exhibiting a strong periodicity at about 17 blocks

Multiple passes over one reel of tape have demonstrated our ability to locate bad spots on tape as we had hoped Our results indicate that half of all errors are caused by these bad spots

At 152 cm/s (60 ips) the overall bit error rate is about $1 0 \times 10^{-6}$. From tape to tape and from run to run it varies from as low as $0 2 \times 10^{-6}$ to as high as $10 0 \times 10^{-6}$ Problems with tracking at 305 cm/s (120 ips) have prevented us from doing much work at this speed

B. Problems With the Electronics

Our main difficulties in getting the data electronics to perform reliably were the result of poor quality control in the construction of the electronic modules. The infant mortality rate for the data electronics system was extremely high Between August of 1976 and March of 1977 we replaced at least 35 active components (realization of the importance of this statistic came late, so perhaps five or ten component replacements went undocumented) out of a total of 2450 active components in the data system One particular transistor (2N4126) experienced 13 failures out of a total of 252 2N4126's in the system During this time the data electronics were "burned in" for about 2100 hours

Adjustment of the analog sections of the data electronics is complex and time consuming The adjustments drift enough that equalization must be rechecked every three or four weeks This drift may be caused by changes in the head characteristics due to wear

C. Problems With the Tape Transport

Of all the parts of this tape system the transport is probably the weakest We had no trouble with the servo electronics, which performed well and reliably, but almost every other part of the transport gave us trouble

Primary among the transport problems is the fact that the tape is not guided in any way Neither the capstan nor any of the "guide" rollers provides any restoring force to keep the

tape centered on the tape path. Alignment of the tape path is extremely critical. If the tape on the reel is not precisely lined up with the tape path, the tape skews across the heads and the tape wraps very unevenly on the reel. This causes numerous dropouts as well as damage to the tape. This alignment problem is so severe that we are currently unable to record or playback at 305 cm/s (120 ips). The problem is less severe at 152 cm/s (60 ips) and we are able to use the recorder at this speed (and presumably below 152 cm/s (60 ips).

Alignment of the tape path is extremely delicate and the construction of the adjusting screws does not lend itself to easy or reproducible changes

The ability to align all the tape guide rollers parallel to the capstan is questionable because the aluminum plate on which all are mounted and to which all should be referenced (according to the factory) is not flat Our measurements indicate that the surface deviates from flatness by 0.38 to 0 5 mm, though whether this is due to paint on the surface or to damage is not clear

Overall it is clear that the transport is not up to the job of delivering the kind of performance required for this application

D. Ideas for the Future

High-density digital tape recording has a lot of potential for future performance This system as a whole is fairly well designed and, except for the transport, is certainly capable of meeting its specifications More attention must be given in future efforts to the tape transport because a system of this type stands or falls by the transport's performance A transport with vacuum column buffering and air bearing guides should show improved tracking over a tension arm/roller guide model such as this one

To prevent the infant mortality problems we suffered an extensive burn-in is indicated The manufacturer should emphasize control of component quality to prevent being stuck with a marginal quality production lot of components

Despite the grim picture, we are obtaining satisfactory performance at 40 Mb/s and we may be able to get the full 80 Mb/s in the future by working on the transport alignment

problems. It should be possible in the future, given the knowledge we have acquired here, to procure a better system and get excellent performance.

V. Data Buffer

While the data rate of the tape system is quite high, the format is rigidly fixed. The two data rates available are about 40 Mb/s at a tape speed of 152 cm/s (60 ips) and 80 Mb/s at 305 cm/s (120 ips). In particular, the recorder will only accept 28 tracks of data at 3.1 MHz (305 cm/s = 120 ips) or 1.55 MHz (152 cm/s = 60 ips). If the user has, for example, 8 bits of data at 2 MHz something must be done to reformat the data. The first step toward a general-purpose buffer to interface any user to the tape system was taken with the construction of a special-purpose buffer for use in this year's Venus radar track (Fig 5).

The Venus radar data was available as three synchronous 9-bit channels at about 800 kHz. We decided to run the recorder at 152 cm/s (60 ips) to minimize wasted capacity and because there were problems with the transport's tracking at 305 cm/s (120 ips)

The synchronizer (Fig. 5) gathers the three channels together and builds a 28-bit word for the tape system. The data channels are at the same frequency but exhibit a slight phase drift (about one cycle per day) Each channel is the digitized radar return from one of three stations.

The memory is used to organize the data into 256 word blocks The memory is organized as two banks of 256 X 28 static RAM and they are commutated between read and write, while one is outputting to the tape, the other is accepting radar data. Each time a RAM bank is filled a block write is initiated First, an 8-word synchronization character is written, followed by the 256 words of data.

In between blocks a square wave of half the frequency of the record clock is recorded This minimizes the DC component of the data sent to the tape recorder. The system error rate of the tape recorder is very sensitive to any DC component of the input data, so this has proved necessary

Detection of the sync character during playback is similar to that in the error rate tester

RECORD ELECTRONICS

REPRODUCE ELECTRONICS
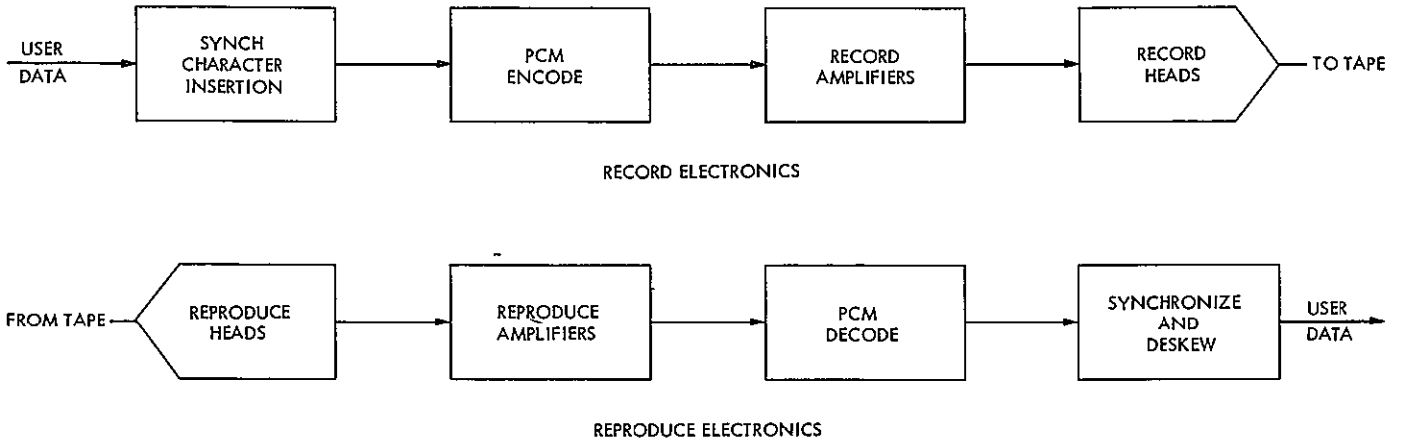
Fig 1. Block diagram — HDR PCM system
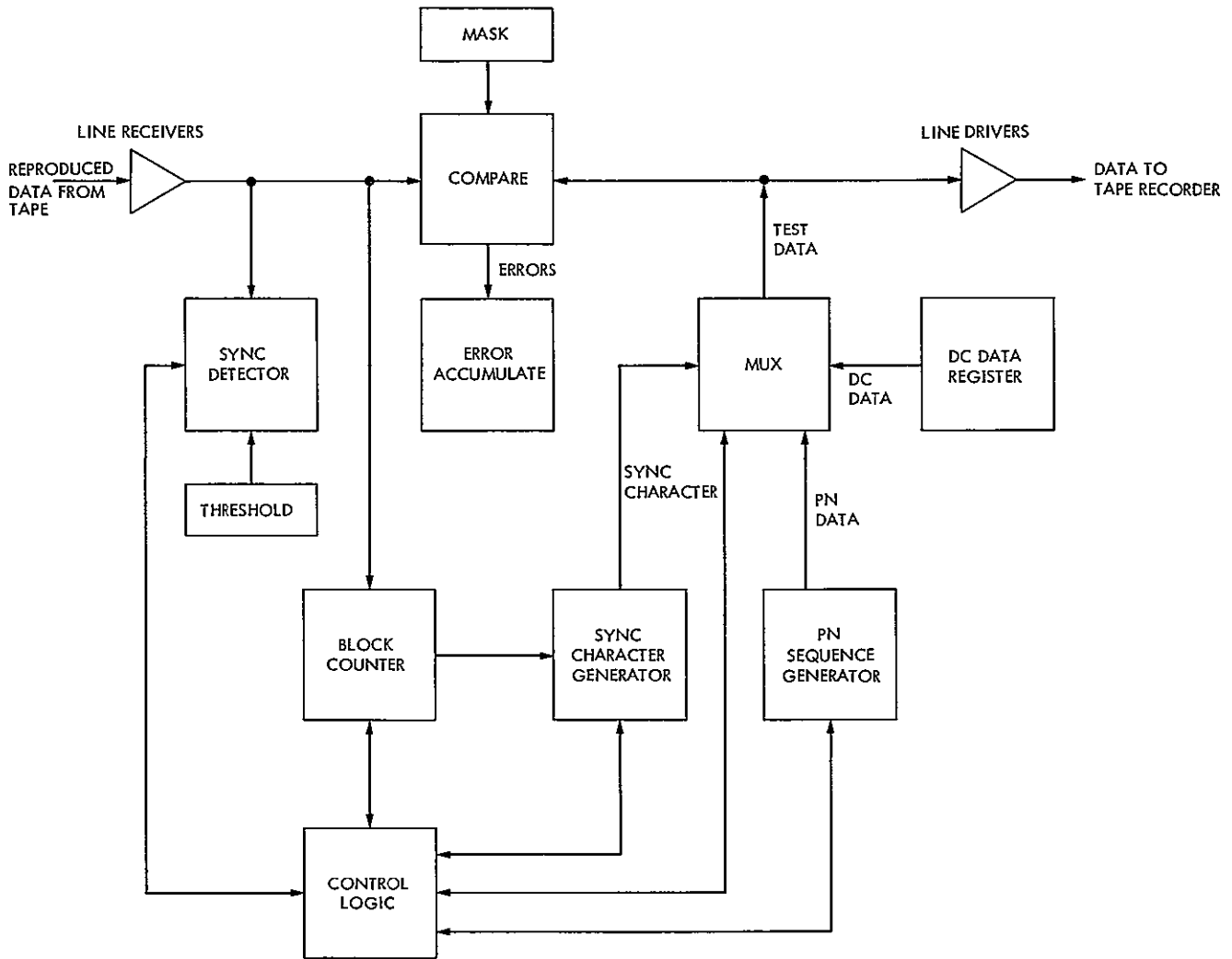
Fig. 2. Error rate tester block diagram
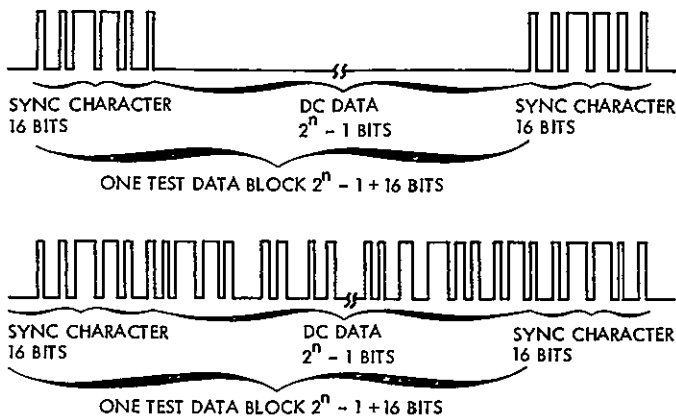
Fig. 3. Test data format
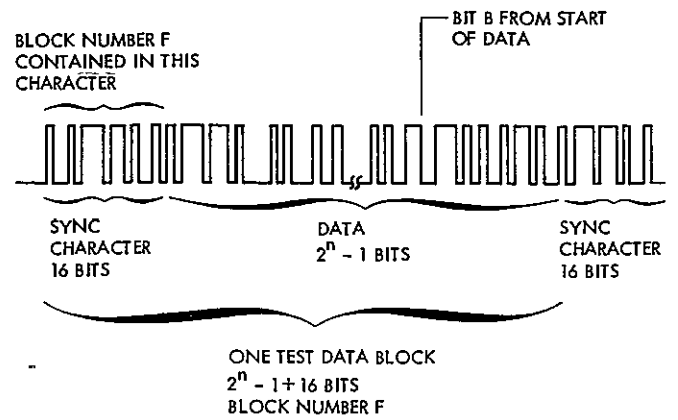
Fig 4. Tape position addressing
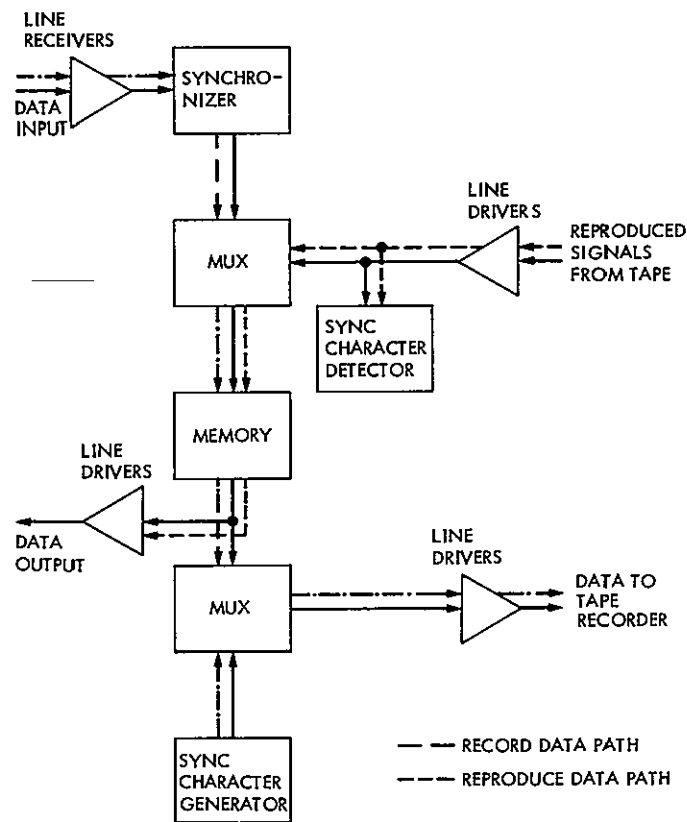
Fig. 5 Radar data buffer block diagram

ERROR HISTOGRAM/1

0	1	2	3	4	5	6	7	8	9
4	1	2	65	5	4	34	5	2	19
8	0	15	3	0	12	9	2	4	2
3	3	2	3	3	2	1	6	0	1
2	4	1	1	0	1	0	2	1	5
4	0	2	1	1	0	0	4	2	1
1	2	3	1	3	4	4	3	0	0
0	2	3	3	1	2	2	1	0	2
1	0	1	1	0	2	2	1	0	1
0	1	2	5	4	2	0	1	1	3
4	1	0	0	1	0	1	2	3	0
2									

PEAK VALUE =   65 LINEAR SCALE
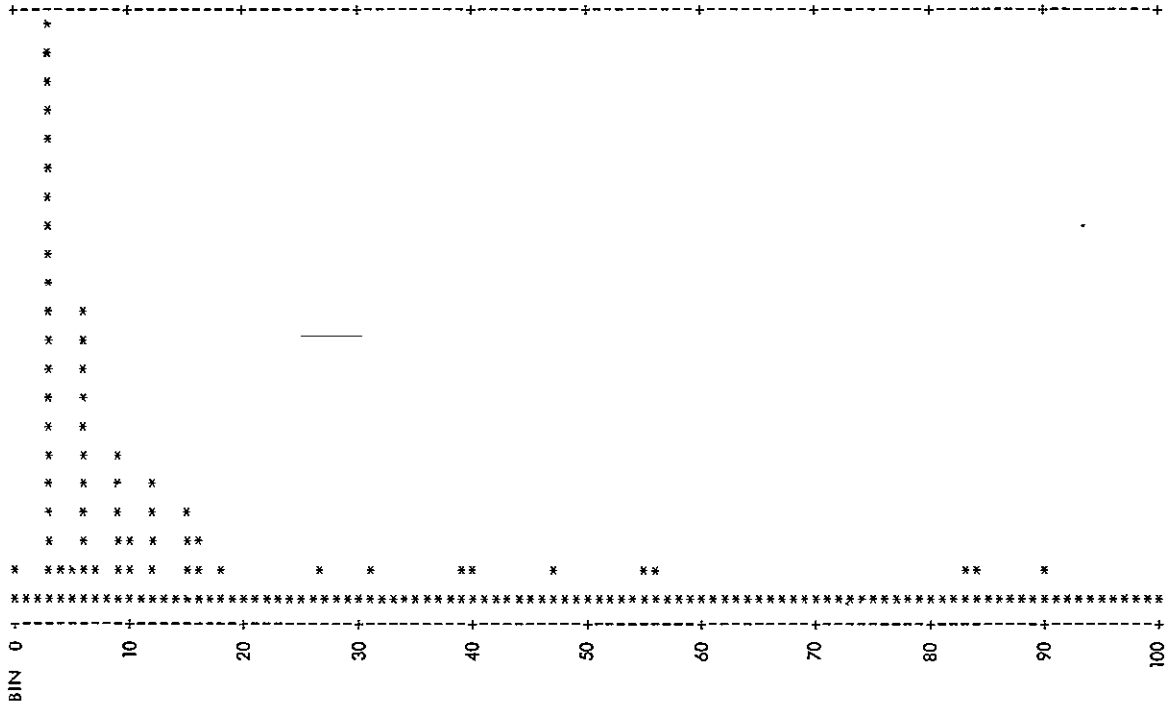
Fig. 6. Error histogram sample

CLEAR RUN HISTOGRAM/1

0	1	2	3	4	5	6	7	8	9
0	18	21	7	17	47	47	14 BIN	4	6
16	16	21	6	4	2	3	⟨207⟩ 17	2	1
1	0	2	2	0 BIN	0	1	0	1	5
1	2	0	0	⟨20⟩ 34	0	0	0	2	2
0	0 BIN	0	1	1	0	0	0	0	1
1	⟨9⟩ 51	1	0	0	0	1	0	0 BIN	2
0	0	2	0	0	0	0	0	⟨7⟩ 68	1
0	2	0	0	0	0	0	1	0	2
0	0	1	0	1	0 BIN	2	0	0	0
0	0	0	0	0	⟨4⟩ 85	1	0	0	0
0					0				

PEAK VALUE =   207 LINEAR SCALE

```
+---------+---------+---------+---------+---------+---------+---------+---------+---------+---------+
          *
          *
          *
          *
          *
          *
          *
          *
          *
          *
          *
          *
          *
          *
          *
          *
    **    *
    **    *
 *  **    *     *
** ****  ***    *
*********************************************************************************************************
+---------+---------+---------+---------+---------+---------+---------+---------+---------+---------+
0        10        20        30        40        50        60        70        80        90       100
BIN
```
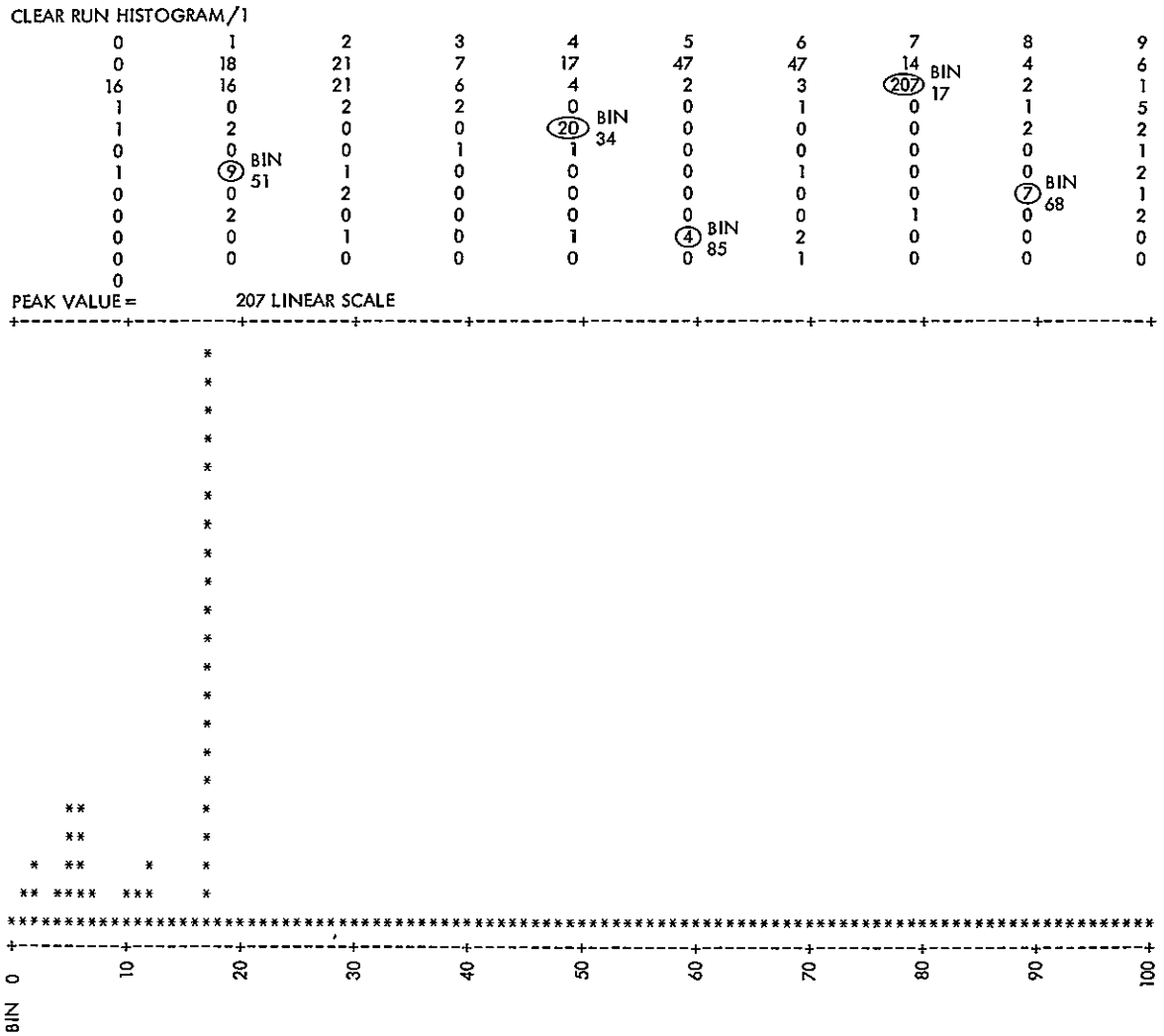
Fig. 7. Clear run histogram sample

N78-24176

Dynamic Spares Provisioning for the DSN

I Eisenberger and G Lorden
Communications Systems Research Section

A method is proposed to maintain cost-effective spares stockpiles for an entire DSN station or complex as new modules or subsystems are continuously added Levels of spares are calculated individually for each new module type so as to conform to an established standard for the entire spares pool. Finding the spares levels is computationally simplified and in many cases is reduced to consulting a Down-Time Ratio Chart. A simple modification permits taking into account a criticality factor

I. The Spares Provisioning Algorithm

Cost-effective sparing algorithms have been proposed by the authors in Refs 1 through 4. These were designed to provide optimal spares packages for systems or subsystems by taking into account for each module type the mean-time between failures (MTBF), unit cost, number operating, and number redundant Each spares package is optimal in the sense that it minimizes the cost of attaining its up-time ratio (UTR). The choice of a suitable package among optimal ones is made by trading off cost against UTR

The benefits of using such an algorithm flow from the fact that every dollar spent on spares buys the right choice of module type to maximize the UTR A difficulty arises, however, when new subsystems or parts of subsystems are introduced and the algorithm is used to determine the spares needed. A spares package with cost C and up-time ratio U might be chosen this year and another "optimal" package with cost C' and UTR U' may be chosen next year for new equipment The combination of the two will generally be suboptimal and could be improved upon by considering the two procurements together, thus spending the right relative amounts on the two to maximize the *overall* UTR Since it is

obviously impractical to make all new procurements at the same time or to recompute the entire spares stockpile of a station every time a new type is added, a method of dynamic spares provisioning is needed to insure that overall cost-effectiveness is maintained

To outline such a method it is convenient to work with the down-time-ratio ($DTR = 1 - UTR$) of a system, the fraction of the time that the system is not operable due to unavailability of spares. Let $A > 0$ be chosen as the "sparing" standard" (discussed below) Then when a new module type with unit cost C_i is added to the spares pool, the number of spares it requires is the *smallest* number such that

$$DTR_i < A \cdot C_i, \qquad (1)$$

where DTR_i denotes the down-time ratio of the ith module type One computes DTR_i for 0 spares, 1 spare, 2 spares, etc, until a value smaller than $A \cdot C_i$ is obtained (The computation of up-time, hence down-time, ratios is easily made by the algorithm in Ref. 1) Thus, $A \cdot C_i$ is a "ceiling" for the down-time ratio of module type i

The advantage of the method using relation (1) is that it is applied to each module type without regard for which others are determined at the same time, the resulting spares being the same as if the entire spares complement of a station (or complex) were recomputed each time a new module type is added

The disadvantages of the method are

(1) It is only approximately optimal.

(2) The value of A must be chosen in advance (as described in the next section).

The nonoptimality results from the intentionally simplified character of relation (1), not from considering each module type separately Investigation of actual procurement examples previously computed using the optimal package approach indicates that the sacrifice of strict optimality has negligible effect the method based on relation (1) often yields the optimal packages and, even when it does not, incurs minimal degradation in cost-effectiveness

II. Choice of a Sparing Standard

The role of the sparing standard A in determining the spares complement is basically one of establishing the level of the tradeoff between total spares cost and overall UTR A rough idea of the meaning of the A-value can be obtained from the following upper bounds on the overall DTR

$$DTR = 1 - UTR = 1 - \prod_i UTR_i = 1 - \prod_i (1 - DTR_i)$$

$$< \sum_i DTR_i < A \sum_i C_i,$$

using relation (1) for the last inequality

Thus,

$$A > \frac{DTR}{\sum_i C_i}, \tag{2}$$

where $\sum C_i$ is the cost of a "unit spares package" (one spare of each module type). In typical cases, the two sides of inequality (2) are within a factor of 2 or so, thus, A is roughly the ratio of the overall DTR to the cost of a unit spares package (Note that the use of this rough interpretation is conservative, i e., actual DTR's are smaller than the interpretation suggests)

Although the rough interpretation of the sparing standard A is helpful, it is not accurate enough to be a completely satisfactory basis for choosing the value of A. That choice should be based upon a fully informed tradeoff between cost and up-time ratio for an entire spares pool For this purpose one has to compute spares for all modules using a range of values of A and then compare the resulting costs and UTR's This computation can be performed piecemeal, taking modules singly or in convenient groups. Once A is chosen, the process need not be repeated for some time

Periodically it may be necessary or desirable to set a new value for the sparing standard in order to adapt to changes in performance requirements or cost constraints Also, if the amount of equipment increases significantly, then the overall UTR will go down and it may be decided that more spares should be procured using a smaller value of A.

Without changing A, one can recalculate the sparing needs of individual modules from time to time based upon better estimates of their MTBF's If, for example, a module's failure history indicates a lower MTBF than specified by the manufacturer, then an appropriate number of additional spares can be determined by recalculating DTR's using the more realistic MTBF

III. Calculation of Down-Time Ratios

The actual determination of spares levels using the method of Section I reduces to the calculation of down-time ratios for given numbers of spares The algorithm in Ref 3 calculates DTR's with or without redundancies among operating modules. In the case of multistation spares pools, the UTR's for the various stations will generally *not* be equal and the geometric mean of the station UTR's is the most convenient measure of overall performance. Thus, one defines the "average DTR" by

$$DTR = 1 - [UTR(1) \times \ldots \times UTR(s)]^{1/s}$$

where s = number of stations and $UTR(j)$ = up-time ratio at station j A similar definition is given for DTR_i, the average DTR of module type i It is easily verified that the method of sparing based on relation (1) yields an overall DTR satisfying the upper bound in inequality (2)

The use of pooled sparing or redundancy, while highly cost-effective, does not lead to calculations that can be summarized in graphs or tables In the simplest sparing situation, however, where a module type is operating without redundancy and without pooling, a simple computation easily expressed in graphs, or tables, can be used to determine the

down-time ratios and, hence, the number of spares required for a prescribed A value.

In terms of the *operating ratio*

$$V = \text{no. of modules operating} \times \frac{MTTR}{MTBF} \text{(in same units)}$$

The *reciprocal* DTR is expressible as follows

No spares	$\dfrac{1}{DTR}$
0	$1 + \dfrac{1}{V}$
1	$\left(1 + \dfrac{1}{V}\right)\dfrac{2}{V} + 1$
2	$\left[\left(1 + \dfrac{1}{V}\right)\dfrac{2}{V} + 1\right]\dfrac{3}{V} + 1$
n	$\displaystyle\sum_{k=0}^{n+1} \frac{n+1}{(n+1-k)} v^{-k} =$

$$\left\{\left[\left(1 + \frac{1}{v}\right)\frac{2}{v} + 1\right]\frac{3}{v} + . \quad \right\}\frac{n+1}{v} + 1$$

It is easy to carry out these computations on a pocket calculator. At each stage simply multiply the last answer by $n + 1$, divide by V, and add 1 When the result exceeds $1/(A \cdot C_i)$, the number of spares required according to relation (1) is n

Alternatively, one can use a Down-Time Ratio Chart (like the one in Fig 1) that plots $1/DTR$ as a function of

$$V^* = \text{no operating} \times \frac{MTTR \text{ (weeks)}}{MTBF \text{ (k-hr)}} = 5\,952\,V$$

rather than V for greater convenience of computation Locate the point with coordinates V^* on the horizontal axis and $1/(A \cdot C_i)$ on the vertical axis The number of spares required

is determined by the region in which that point falls For example, the point with $V^* = 0\,4$ and $1/(A \cdot C_i) = 3000$, shown as P in Fig 1, lies in the region above the $1/DTR$ curve for 1 spare and below the curve for 2 spares Hence, the goal for $1/DTR$, which is 3000, is not reached by using 1 spare but is exceeded by using 2 spares Thus, the region in which P falls is labeled "2 spares" and the other regions between curves are labeled similarly

IV. An Example

Table 1 lists the results of computations for a pooled sparing example with no redundancy The data on module types were obtained by selection from a spares calculation on actual DSN equipment Note in Table 2 that the configurations of the stations differ and the DTR's differ correspondingly The value of $A = 6\,42 \times 10^{-7}$ was chosen based on inequality (2) with a DTR goal of 1% The actual average DTR for the three stations came out 0.48%, which is roughly a factor of 2 smaller (as is typical, see the discussion in Section II) The spares package obtained in this example is actually an optimal one as was verified by using the algorithm of Ref 3 A repair time of two weeks was assumed for all modules

Note that module type 5, requiring the most spares, has a unit cost in the middle of the range and an MTBF roughly as good as three of the other modules However, the number operating is high for a module with this MTBF level, so that the number operating/MTBF (= total number of failures per 1000 hours of operation) is relatively high. Type 4, which requires the second highest number of spares, is distinguished by very low cost The relatively high spares level determined for type 4 produces an extremely low DTR (0 003%), but these spares are still "needed" because of their cost-effectiveness in maximizing system UTR Type 2, by contrast, is quite expensive and is spared at a level which gives it a relatively high DTR.

V. Criticality Factors

A useful sparing algorithm should be capable of taking into account differences in criticality of different module types Down-time due to shortage of spares may be much less critical for some modules than for the most essential modules

To represent such differences mathematically, let each module type be assigned a *criticality factor* K_i, where $0 < K_i < 1$ The interpretation is that down-time of module type i is assigned a weighting factor K_i on a scale from 0 to 1,

with higher K_i's thus denoting higher criticality. The modified algorithm replaces relation (1) by

$$K_i \cdot DTR_i < A \cdot C_i \qquad (3)$$

This modification essentially minimizes $\Sigma_i K_i \cdot DTR_i$ rather than $\Sigma_i DTR_i$ for the dollars spent

Another interpretation of relation (3) is that one follows the algorithm in relation (1) but with C_i, the unit cost, replaced by C_i/K_i, the *cost-criticality ratio*. Modules of low criticality wind up being treated as if their cost were much higher, whereas the costs of modules of maximum criticality, 1, are unchanged.

This method can greatly enhance the flexibility of the sparing algorithm in dealing with diverse types of equipment. One way of implementing it would be to classify all module types into, say, two or three categories with appropriately specified criticalities

VI. Conclusions

The method of sparing proposed in this article offers both simplicity and cost-effectiveness. It is easy to understand and flexible in applications, permitting consideration of criticality as well as redundancy and pooled sparing It also enables sparing determinations to be made for new modules without reconsidering the entire spares stockpile With suitable software implementation, this method should prove highly useful in DSN spares provisioning

References

1 Eisenberger, I , Lorden, G , and Maiocco, F , "A Preliminary Study of Spares Provisioning for the Deep Space Network," *DSN Progress Report*, TR 32-1526, Vol XVIII, Jet Propulsion Laboratory, Pasadena, Calif , Dec. 15, 1973

2. Eisenberger, I , Lorden, G , and Maiocco, F., "Cost-Effective Spares Provisioning for The Deep Space Network," *DSN Progress Report 42-20*, Jet Propulsion Laboratory, Pasadena, Calif., Apr 15, 1974.

3 Eisenberger, I., and Lorden, G , "Cost-Effectiveness of Pooled Spares in the Deep Space Network," *DSN Progress Report 42-38*, Jet Propulsion Laboratory, Pasadena, Calif , Aug 15, 1975.

4 Eisenberger, I , and Lorden, G., "Priority Repair Schemes in the Deep Space Network", *DSN Progress Report 42-30*, Jet Propulsion Laboratory, Pasadena, Calif., Dec 15, 1975.

Table 1. Data for sparing example

No.	No operating[a]	MTBF, k-hr	No op. MTBF	Unit cost, $	No spares	Avg.[a] DTR_i, %
1	21	13	1 62	4000	3	0834
2	51	50	1.02	5200	2	1830
3	21	15	1 40	2150	3	0494
4	63	49	1 29	236	4	0030
5	42	10	4 20	2000	5	1254
6	6	10	60	2000	2	0397
Total				15586	19	4833

[a]See Table 2 for individual stations

Table 2. Breakdown by station

Module No	No operating			DTR_i, %		
	Station 1	Station 2	Station 3	Station 1	Station 2	Station 3
1	8	9	4	0952	1065	0486
2	17	14	20	1831	1516	2144
3	9	8	4	0632	0564	0287
4	25	25	13	0036	0036	0019
5	8	16	18·	0744	1428	1590
6	4	2	0	0789	0401	0
Overall	71	74	59	4976	5002	4520
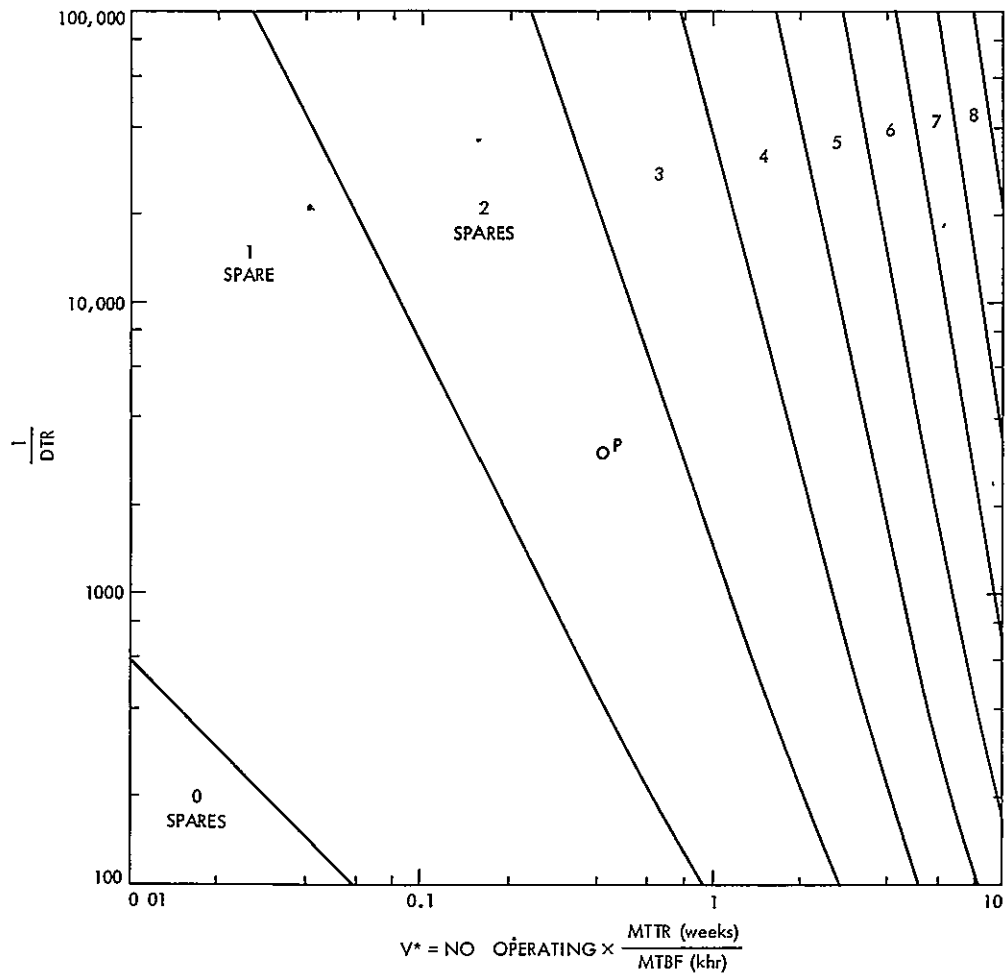
Fig. 1. Down-Time Ratio Chart

N78-24177

Planetary Atmosphere Modeling and Predictions

A. L. Berman

TDA Engineering Office

The capability to generate spacecraft frequency predictions which include the refractive bending effects induced during signal passage through a planetary atmosphere is a pivotal element of the DSN Radio Science System. This article describes the current implementation effort to develop planetary atmosphere modeling and prediction capability

I. Introduction

Prior to the Pioneer Venus Orbiter mission, Radio Science data was obtained during planetary occultations via the use of fixed frequency open loop receivers The open loop receiver bandwidth was selected so as to encompass the received frequency (f_a) dynamic range (plus uncertainties) during the occultation phase (on the order of 10 KHz to 100 KHz total at S-band level), and the resultant receiver output was recorded in analog form on magnetic tapes. These tapes were shipped to the Compatibility Test Area (CTA 21) where they were digitized and formatted into computer compatible magnetic tape for delivery to the Radio Science experimenters For the Pioneer Venus Orbiter mission, the large number of occultations (~100) and the large dynamic frequency range (up to 100 KHz at S-band) would result in extremely high processing costs and an excessive amount of manual tape handling, if the occultation data were acquired and processed as in previous missions In the way of a less costly alternative, the idea was conceived of driving the first local oscillator in the open-loop receiver with the predicted frequency (f_p), and subsequently passing a greatly reduced bandwidth containing the mixed frequency ($f_a - f_p$)[1] through a narrow filter (on the order of several KHz) The receiver output bandwidth could then be digitized in real time and stored, with transmission of the digitized radio science data to the Network Operations Control Center (NOCC) via High Speed Data Line (HSDL) occurring subsequent to the occultation event

Since processing costs are approximately proportional to recorded bandwidth, this new system could be expected to greatly decrease processing costs and the manual handling and shipment of a very sizeable number of magnetic tapes Descriptions of this new system can be found in previous issues of the DSN Progress Report (Refs 1 and 2), and a detailed description of the new subsystem implementation (the DSS Radio Science Subsystem) which supports this task is planned for a future DSN Progress Report issue

---

[1] The Radio Science experimenter recovers the actual frequency by adding back the predicted frequency to the mixed frequency ($f_a - f_p$) $+ f_p = f_a$

Pivotal to this new method of acquiring radio science data is the predicted frequency, which must now include the refractive bending of the spacecraft signal as it passes through a planetary atmosphere – in sharp contrast to the standard spacecraft frequency predictions currently available The present implementation effort to add a planetary atmosphere model to the existing spacecraft frequency prediction capability will hence be the subject of the following sections

II. Implementation of a Planetary Atmosphere Model Capability

The current method of generating spacecraft frequency predictions begins with the delivery by a Flight Project to DSN Network Operations of a spacecraft Probe Ephemeris Tape (PET) The PET tape is first processed by the Fast Phi-Factor Generator Program (FPGP), which resides on the Xerox Data Systems (XDS) Sigma 5 computer in the NOCC Support Subsystem The FPGP output is a Polynomial Coefficient Tape (PCT), which contains the station-dependent, frequency-independent spacecraft observables The PCT is then input to the PREDIK program (also residing on the NOCC Support Subsystem XDS Sigma 5 computer), which produces the final frequency-dependent spacecraft observables.

Early in 1977 a tradeoff study was conducted to determine the optimum method, from an implementation and subsequent operations viewpoint, of developing a planetary atmosphere prediction capability The method selected was·

(1) The modification of an existing general-purpose navigation software program ("POEAS") to include planetary atmosphere effects and to produce as an output a PCT

(2) The modification of the PREDIK program to output spacecraft frequency predictions in a form specifically designed for the DSS Radio Science Subsystem

The POEAS program, which resides on the Univac 1108 computer, will be operated by DSN Network Operations The required input to the POEAS program is a (spacecraft) state vector, which will thus become the Flight Project – DSN interface when generating "Radio Science" predictions The standard tracking prediction configuration is compared to the new radio science prediction configuration in Fig 1. A Radio Science Prediction and "Radio Science Data"[2] flow diagram is presented in Fig 2

---

[2]"Radio Science Data" includes both the recorded open-loop receiver data and the frequency used to drive the programmed (first local) oscillator

III. POEAS Program Planetary Atmosphere Capability Requirements

The functional requirements in regard to the modification of the POEAS software program to develop a planetary atmosphere modeling capability are as follows

(1) Planetary atmosphere modeling will be available for at least the following planets and satellites

    (a) Venus
    (b) Jupiter
    (c) Saturn (including rings)
    (d) Callisto
    (e) Titan
    (f) Uranus

    It is a design goal to accommodate all planets and satellites

(2) An event corresponding to a defined transition time between top of atmosphere and free space will be computed.

(3) Signal level degradation will be computed as an analytic function of available program parameters

(4) The (spacecraft) virtual earth direction in an inertial coordinate system will be computed

(5) A user input (run-time control) will be available to allow switching at discrete times between different limb signal exit points for oblate planet occultations

(6) Spacecraft apparent velocity and acceleration will be computed.

IV. PREDIK Program Planetary Atmosphere Capability Requirements

The functional requirements in regard to the modification of the PREDIK software program to develop a planetary atmosphere prediction capability are as follows

(1) The PREDIK program will accept a new event flag which corresponds to a defined transition between the top of the atmosphere and free space, and will include the event in the prediction computer printout

(2) The PREDIK program will contain an algorithm which, beginning with the starting frequency, sequentially

proceeds to select frequencies throughout the user-requested time period, in each case selecting the longest sample output interval, such that

(a) The maximum difference between the instantaneous predicted frequency and the resulting linearly interpolated frequency over the interval will be less than Δf

(b) Δf will be a user input.

(c) Δf will be restricted to 1 Hz $\leqslant \Delta f \leqslant$ 10,000 Hz (S-band).

(3) The user will have the (input) capability to switch the prediction output at discrete times between tracking modes·

(a) D1 (one-way)

(b) D2 (two-way)

(c) D3.XX (three-way with station XX)

(4) The basic output of the PREDIK program will consist of time-tagged S-band frequencies at the proper digitally controlled oscillator (DCO) level (~46 MHz)

(a) The output sample interval will be variable, but subject to a minimum output sample interval of one second

(b) Samples will be output on the even second

(5) The PREDIK program will contain an algorithm for the purpose of verifying correct transmission between PREDIK program output and input to the CTA 21 and DSS Radio Science Subsystems.

(6) Whenever the output sample interval is one second, the PREDIK program will output the maximum difference between the instantaneous predicted frequency and the resulting linearly interpolated frequency over the interval.

(7) The user will have the capability to select a time subinterval (t_1, t_2) for which there may be specified starting (t_1), ending (t_2) and several discrete interior $(t_1 < t < t_2)$ frequencies Exterior to the subinterval, the automatic algorithm will apply

V. Planned Implementation Schedule

The planned implementation schedule to meet the Pioneer Venus and Voyager mission requirements is as follows

(1) POEAS transfer to operations

(a) April 1, 1978 — Venus capability only

(b) September 1, 1978 — full capability

(2) PREDIK transfer to operations

April 1, 1978 — full capability

References

1 Miller, R. B , "Pioneer Venus 1978 Mission Support," in *The Deep Space Network Progress Report 42-38*, Jet Propulsion Laboratory, Pasadena, California, April 15, 1977

2 Mulhall, B D L , "DSN Radio Science System Description and Requirements" in *The Deep Space Network Progress Report 42-39*, Jet Propulsion Laboratory, Pasadena, California, June 15, 1977
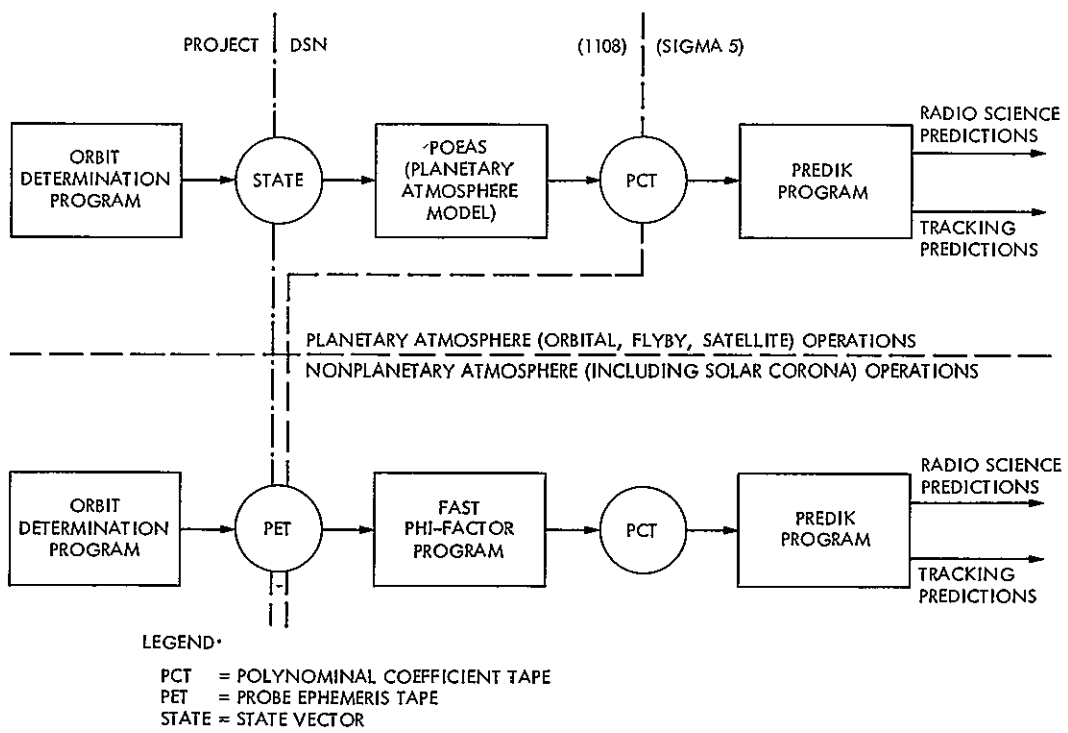
Fig. 1. Project/DSN prediction interface
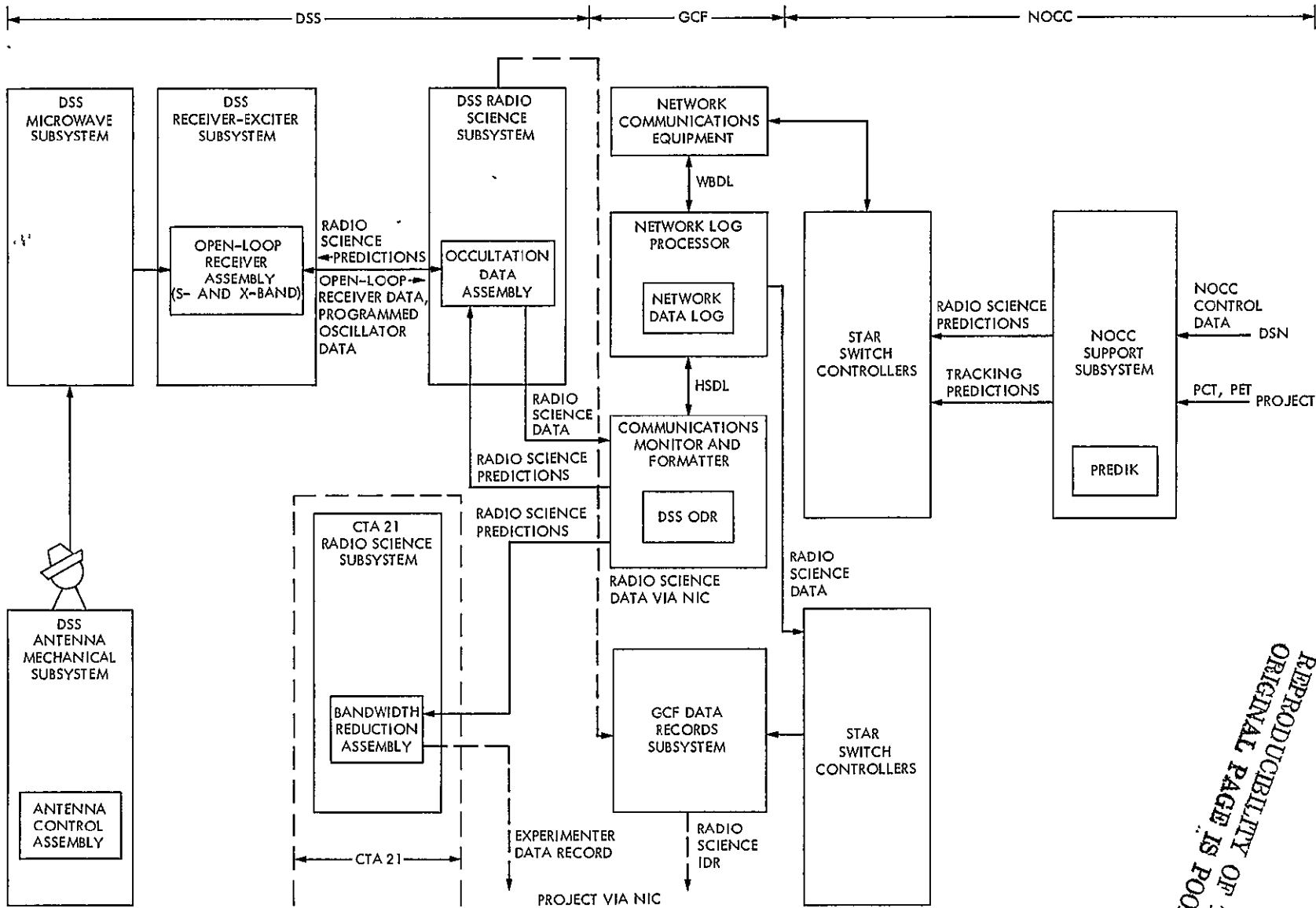
Fig. 2. Planetary atmosphere predictions data flow

An Empirical Model for the Solar Wind Velocity

A L Berman

TDA Engineering Office

An analytic expression for the average radial component of the Solar Wind velocity between 1 solar radius and 1 AU is developed as follows

$$v_r(r) = \left[\frac{440}{r^{-0\,3} + 3\,35 \times 10^{-7}\,r^{-4\,0}} \right] \text{ km/second}$$

where r is the radial distance in AU. The model is constructed by (1) Assuming the conservation of particle flow-in the Solar Wind and (2) Application of a twelve-year average measured value of the Solar Wind radial velocity at 1 AU

I. Introduction

Starting with the work of Parker in the late 1950s, many coronal investigators have attempted to formulate a model of the Solar Wind. These attempts usually take the form of making certain assumptions which define the applicable equations, and then solving these equations in the region between 1 solar radius and 1 AU. In the final step, boundary values at 1 solar radius based on observations or assumptions are incorporated, and the model predicted values of the observables (density, Solar Wind velocity, proton temperature, electron temperature) at 1 AU are compared to the corresponding in situ measurements To date, none of the theoretical attempts have been able to correctly predict the in situ measured average values of all four observables Of the four parameters, only electron density has been experimentally determined (by a variety of methods) over the full range of radial distances from 1 solar radius to 1 AU. Considering that particle flow is conserved in the Solar Wind (Ref 1),

$$N_e(r)v_r(r)r^2 = K$$

where

$N_e(r)$ = Electron density

$v_r(r)$ = Radial component of the Solar Wind velocity

r = Radial distance

one can immediately write the radially dependent expression for $v_r(r)$ in terms of $N_e(r)$ Although this empirical process adds nothing to the theoretical understanding of the Solar Wind, it is here considered that the generation of such an analytical expression for the radial component of the Solar Wind velocity would-

(1) Produce the most accurate model in the sense of being the most closely tied to actual observations (of electron density).

(2) Produce a very convenient model for use in modelling other coronal parameters, such as spectral broadening

II. The Model

To begin, one requires an electron density model For this purpose, the electron density model determined from S-band Viking doppler phase fluctuations (Ref 2) will be adopted

$$N_e(r) = \frac{2\,39 \times 10^8}{r^6} + \frac{1.67 \times 10^6}{r^{2.30}}$$

where $N_e(r)$ is the electron density in electrons/cm^3 and r is the radial distance in solar radii. This model yields the following values

r, solar radii	$N_e(r)$, electrons/cm^3
1	$2\,41 \times 10^8$
10	8610
215	7.2

At $r = 1$ the model is in good agreement with eclipse observations (Table I, Ref 1), at $r = 10$ the model is in good agreement with eclipse observations and pulsar time delay measurements (Ref 3), and at 1 AU the model is in good agreement with in situ density measurements (Ref. 4)

Next, one requires a boundary value for the Solar Wind radial velocity, the obvious choice is the average measured value of $v_r(r)$ at 1 AU Gosling (Ref 5) has recently reported average Solar Wind velocities for the period 1962–1974, the average value for the entire 12-year period is

$$v_r(r = 215) = 440 \text{ km/second}$$

The above value will be adopted here

Combining the electron density function with the boundary value of the radial Solar Wind velocity at 1 AU, one arrives at

$$v_r(r) = \left[\frac{440}{r^{-0\,3} + 3\,35 \times 10^{-7}\,r^{-4\,0}}\right] \text{ km/second}$$

where r is the radial distance in AU This model for the radial Solar Wind velocity is applicable over the region 1 solar radius to 1 AU and yields

r, AU	$v_r(r)$, km/second
(1/215)	0.61
(10/215)	170
(215/215)	440

It is of interest to briefly compare these values to theoretical results Four models in Ref 6 at 1 solar radius yield an average value of

$$v_r(1/215) = 2\,9 \text{ km/second}$$

with values ranging from 0 3 to 5.8 km/second Three models mentioned in Ref 3, produce an average value at 10 solar radii of

$$v_r(10/215) = 172 \text{ km/second}$$

with individual values ranging from 160 to 185 km/second Figure 1 compares the empirical velocity model to a theoretical model of Brandt, Wolff and Cassinelli (Ref 7), while Fig 2 makes a similar comparison to the "two fluid" models of Hartles and Barnes and Wolff, Brandt, and Southwick

131

References

1. Cuperman, S, and Harten, A., "Some Physical Implications of Recent Solar Wind Measurements," in *Solar Wind*, edited by Sonett, C. P, Coleman, P. J Jr., and Wilcox, J.-M., National Aeronautics and.Space.Administration, Washington, D.C, 1972.

2 Berman, A L, and Wackley, J. A., "Viking S-Band Doppler RMS Phase Fluctuations Used to Calibrate the Mean 1976 Equatorial Corona," in *The Deep Space Network Progress Report 42-38*, Jet Propulsion Laboratory, Pasadena, California, April 15, 1977

3 Berman, A. L., "Electron Density in the Extended Corona: Two Views," in *The Deep Space Network Progress Report 42-41*, Jet Propulsion Laboratory, Pasadena, California, October 15, 1977

4 Hundhausen, A. J., Bame, S. J., Asbridge, J. R., and Sydoriak, S. J., "Solar Wind Proton Properties Vela 3 Observations from July 1965 to June 1967," *Journal of Geophysical Research, Space Physics,* Vol. 75, No 25, September 1, 1970

5 Gosling, J. T, Asbridge, J R, Bame, S J, and Feldman, W C., "Solar Wind Speed Variations 1962-1974," *Journal of Geophysical Research,* Vol 81, No 28, October 1, 1976

6 Hundhausen, A J, "Solar Wind and Coronal Expansion," in *Physics and Chemistry in Space*, Vol 5, Springer-Verlag, Berlin, Heidelberg, New York, 1972.

7 Brandt, J C, *Introduction to the Solar Wind*, W H Freeman and Company, San Francisco, 1970.
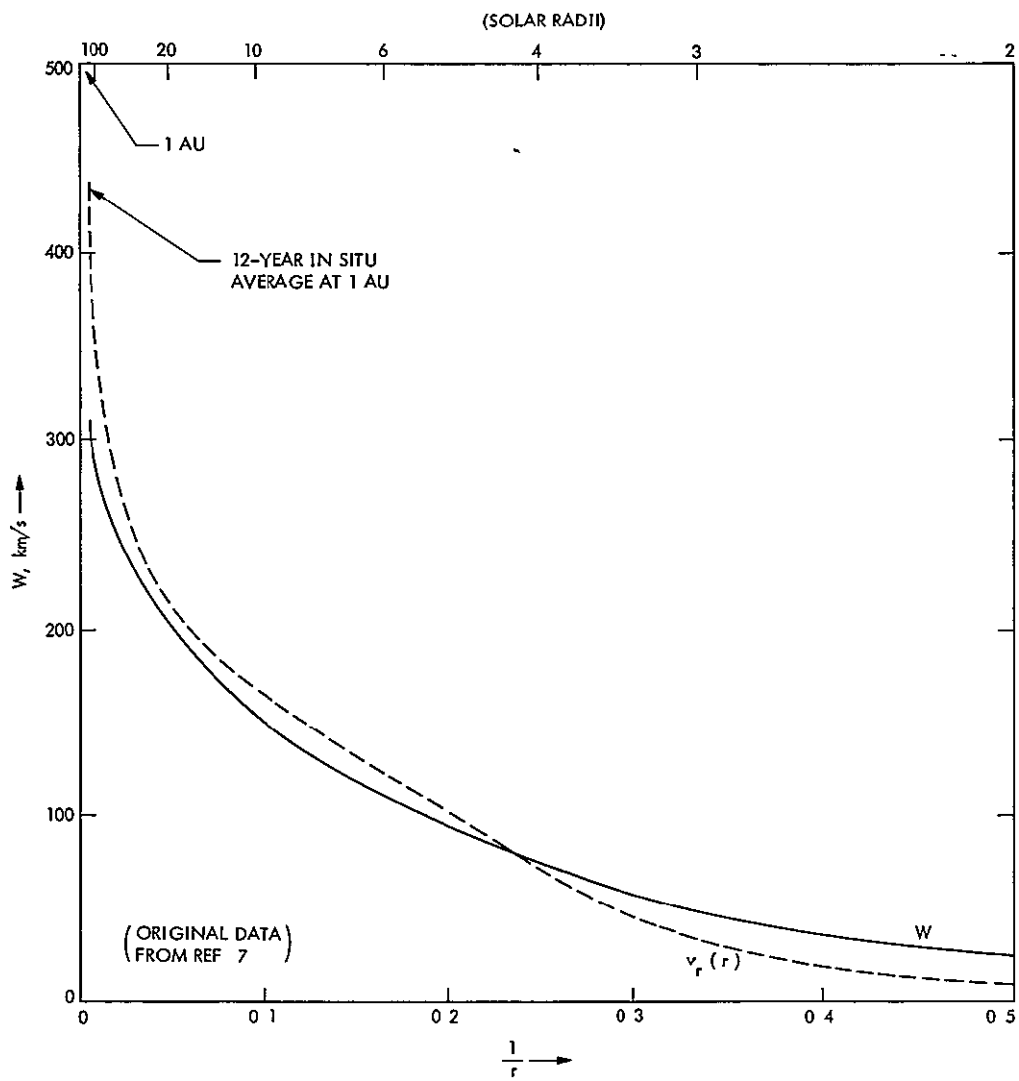
Fig. 1. Empirical Solar Wind velocity model $(v_r(r))$ compared to
theoretical model of Brandt, Wolff, and Cassinelli (W)
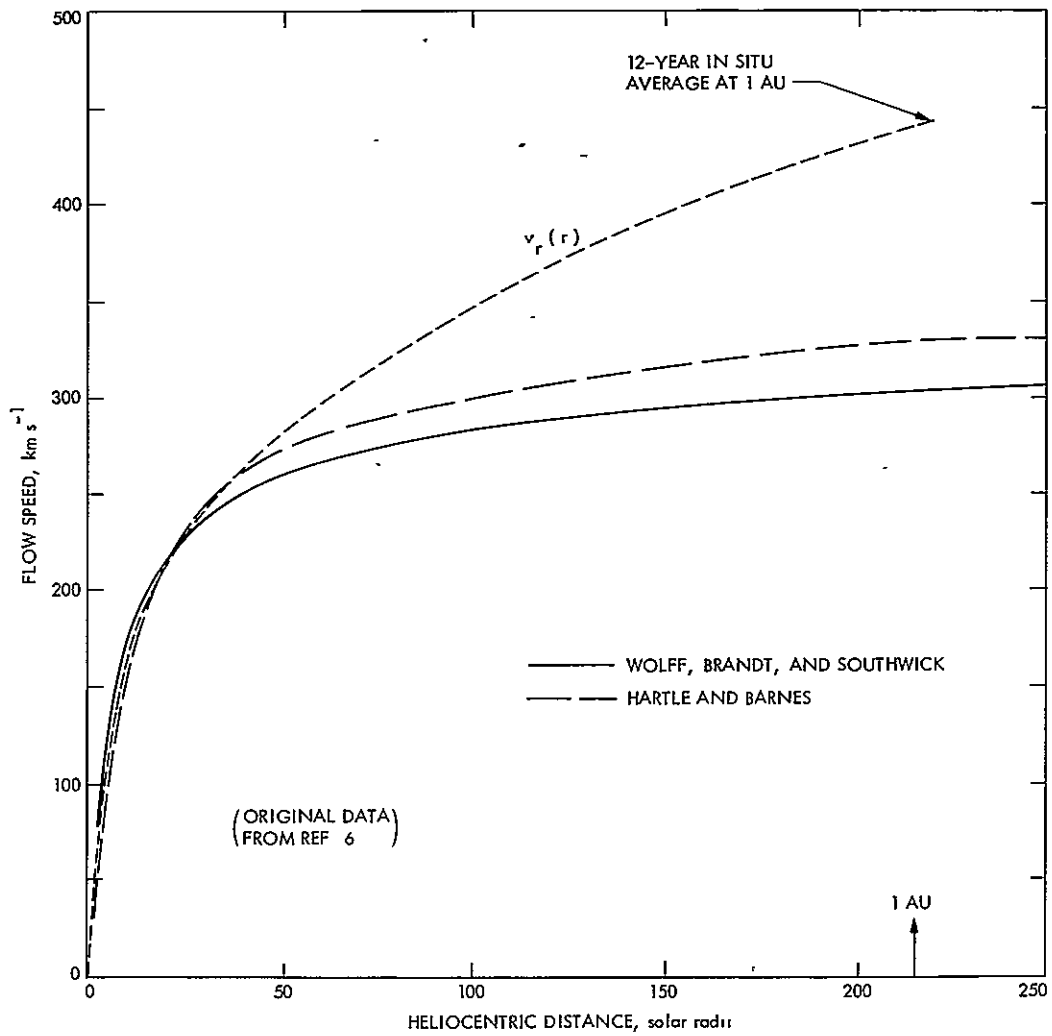
Fig. 2. Empirical Solar Wind velocity model (v_r (r)) compared to the two fluid models of Hartles and Barnes and Wolff, Brandt, and Southwick

RMS Electron Density Fluctuation at 1 AU

A L Berman

TDA Engineering Office

Analytic expressions at 1 AU for the average RMS Electron Density Fluctuation and the ratio of RMS Electron Density Fluctuation to Electron Density, both as functions of the observational time scale, are constructed from average spacecraft in situ density measurements at approximately 1 AU and columnar phase fluctuation measurements over a wide variety of signal closest approach points Additionally, the (one-dimensional) Electron Density Fluctuation spectrum and the Doppler phase fluctuation "scale" are derived, and various extrapolations to the region interior to 1 AU are made

I. Introduction

⸱ Solar Wind modeling is essential for predicting the effects of the Solar Wind upon spacecraft telecommunications, particularly for those spacecraft in various phases of. Solar Conjunction Fundamental to the process of modeling the Solar Wind is a description of the time-scale-dependent Electron Density Fluctuation There now exist substantial in situ measurements of electron density (as a function of time) at approximately 1 AU and columnar phase fluctuation measurements (also as a function of time) at a wide variety of signal closest approach points, the two of which can be reconciled and subsequently synthesized to construct "average" analytic expressions to describe Electron Density Fluctuation In pursuit of this goal, in situ Electron Density measurements by the Mariner 5 and Vela 3 spacecraft will be combined with Viking and Helios Doppler Phase Fluctuation observations.

II. The Ratio of RMS Electron Density Fluctuation to Mean Electron Density

It is convenient to start with a description of the relevant parameters as in Ref 1

$N_e(r,t)$ = instantaneous electron density, electrons/cm^3

r = radial distance

t = time

such that the mean electron density becomes.

$$N_e(r) = \frac{1}{t} \int_0^t N_e(r,t)dt$$

and the RMS electron density fluctuation is hence

$$n(r) = \left[\frac{1}{t}\int_0^t \{N_e(r,t) - N_e(r)\}^2 dt\right]^{1/2}$$

The ratio of "local" electron density fluctuation to mean electron density is simply defined as

$$\epsilon \equiv \frac{n(r)}{N_e(r)}$$

As was pointed out in Ref 1, the most frequent abuse of the parameter ϵ is that it is treated as a constant, in fact, it must be treated as a function of the time-scale over which the RMS value is computed

$$\tau_n = \text{RMS time-scale}$$

$$\epsilon = \epsilon(\tau_n)$$

In the following section, the time-scale-dependent form of ϵ will be obtained at 1 AU.

III. The Time-Scale-Dependent Form of ϵ at 1 AU

The work of Goldstein and Sisco (Ref 2) shows that the in situ (one-dimensional) power spectrum of electron density begins to fall off after one solar rotation, or approximately 2.4×10^6 seconds For time-averaging periods longer than this, one would expect the value of ϵ to be nearly constant To compute a long-term value of ϵ, one can use the following

(1) Mariner 5 data (5 months) (Ref 2)

$$N_e \,(1 \text{ AU}) = 9.2 \text{ electrons/cm}^3$$

$$n \,(1 \text{ AU}) = 5.6 \text{ electrons/cm}^3$$

$$\epsilon \,(1 \text{ AU}) = 0.609$$

(2) Vela 3 data (2 years) (Ref. 3)

$$N_e \,(1 \text{ AU}) = 7.7 \text{ electrons/cm}^3$$

$$n \,(1 \text{ AU}) = 4.6 \text{ electrons/cm}^3$$

$$\epsilon \,(1 \text{ AU}) = 0.597$$

The following value of ϵ at 1 AU will hence be adopted

$$\epsilon(\tau_n) = 0.6$$

$$\tau_n > 2.4 \times 10^6 \text{ seconds}$$

One now desires the value of ϵ for time-scales less than one solar rotation The form of the temporal columnar fluctuation spectrum (P) is well known to be power law with fluctuation frequency (ν).

$$P(\nu) \propto \nu^{-K_0}$$

The average value of K_0 from Helios and Viking Doppler phase fluctuations (Ref 4) is [1]:

$$K_0 = 2.42$$

One knows (Cronyn, Ref 5) that if a temporal columnar fluctuation spectrum is of the form

$$P(\nu) \propto \nu^{-K_0}$$

then the equivalent in situ fluctuation spectrum (P_n) will be

$$P_n(\nu) \propto \nu^{-K_0 + 1}$$

hence, one writes for the in situ density fluctuation spectrum

$$P_n(\nu) \propto \nu^{-1.42}$$

The relationship between fluctuation frequency and time-scale is

$$\nu \propto \tau_n^{-1}$$

and the relationship between the RMS density fluctuation and the density fluctuation spectrum is therefore

$$\left[n(\tau_n) \right]^2 = \int P_n(\nu)\, d\nu$$

$$\propto \int \nu^{-1.42}\, d\nu$$

$$\propto \nu^{-0.42}$$

$$\propto \tau_n^{0.42}$$

Finally, one arrives at

$$n(\tau_n) = K_1 \tau_n^{0.21}$$

for the electron density fluctuation dependence upon τ_n at 1 AU Assuming a constant value of N_e at 1 AU and applying

---

[1]Coincidentally, $k_0 = 2.42$ is the exact average of the six experiments detailed in Table I of Ref 4

the value of $\epsilon = 0.6$ at $\tau_n = 2.4 \times 10^6$ seconds, one would have for $\epsilon(\tau_n)$:

$$\epsilon(\tau_n) = 0.6\left(\frac{\tau_n}{2.4 \times 10^6}\right)^{0.21} \quad \tau_n < 2.4 \times 10^6 \text{ seconds}$$

$$\epsilon(\tau_n) = 0.6 \quad \tau_n > 2.4 \times 10^6 \text{ seconds}$$

Using the average value of N_e at 1 AU (Ref. 6)

$$N_e(1 \text{ AU}) \simeq 7.5 \text{ electrons/cm}^3$$

one would have for the electron density fluctuation at 1 AU:

$$n(\tau_n) = 4.5\left(\frac{\tau_n}{2.4 \times 10^6}\right)^{0.21} \text{ electrons/cm}^3$$

$$\tau_n < 2.4 \times 10^6 \text{ seconds}$$

$$n(\tau_n) = 4.5 \text{ electrons/cm}^3$$

$$\tau_n > 2.4 \times 10^6 \text{ seconds}$$

For example, considering the time-scale applicable to 60-second sample interval Doppler noise (15 samples), one has

$$\tau_n = 900 \text{ seconds}$$

$$n(900) = 0.86 \text{ electrons/cm}^3$$

$$\epsilon(900) = 0.11$$

By way of comparison to actual spacecraft (in situ) results, one has for a 10^4-second ($\sim$2.8 hours) time scale

$$\epsilon(10^4) = 0.19$$

This is compared in Fig 1 to typical in situ spacecraft electron density measurements over 10^4 seconds.

Combining the ideas presented in this section with the following nominal electron density model (Ref 7)

$$N_e(r) = \frac{2.39 \times 10^8}{r^6} + \frac{1.67 \times 10^6}{r^{2.30}}$$

$$r = \text{heliocentric distance, solar radii}$$

one can obtain the following radially dependent electron density fluctuation

$$n(\tau_n) = 0.6\left(\frac{\tau_n}{2.4 \times 10^6}\right)^{0.21}\left\{\frac{2.39 \times 10^8}{r^6}\right.$$

$$\left. + \frac{1.67 \times 10^6}{r^{2.30}}\right\} \text{ electrons/cm}^3$$

$$\tau_n < 2.4 \times 10^6 \text{ seconds}$$

$$n(\tau_n) = 0.6\left\{\frac{2.39 \times 10^8}{r^6} + \frac{1.67 \times 10^6}{r^{2.30}}\right\} \text{ electrons/cm}^3$$

$$\tau_n > 2.4 \times 10^6 \text{ seconds}$$

and additionally, the following radially dependent (one-dimensional) electron density fluctuation spectrum ($P_n(\nu)$):

$$P_n(\nu) = 3.2 \times 10^{-4}\nu^{-1.42}\left\{\frac{2.39 \times 10^8}{r^6}\right.$$

$$\left. + \frac{1.67 \times 10^6}{r^{2.30}}\right\}^2 \text{cm}^{-6} \text{ Hz}^{-1}$$

$$\nu > (2.4 \times 10^6)^{-1}$$

$$P_n(\nu) = 0$$

$$\nu < (2.4 \times 10^6)^{-1}$$

$$\nu = \text{fluctuation frequency, Hz} = \tau_n^{-1}$$

This average spectrum is compared to the Mariner 5 results of Ref 2 in Fig. 2.

IV. The Scale of Doppler Phase Fluctuation

In Ref. 6, the scale for Doppler phase fluctuation is given as

$$L(a) = \frac{0.43}{\epsilon^2}\left(\frac{a}{r_0}\right)\left(\frac{\tau}{60}\right)^{1.4}, \text{ km}$$

where

L = scale, km

a = signal closest approach point

r_0 = solar radius

τ = Doppler sample interval ($\tau_n = 15 \times \tau$), seconds

Substitution for ϵ yields:

$$L(a) = 100 \left(\frac{a}{r_0}\right)\left(\frac{\tau}{60}\right), km \qquad \tau_n < 2.4 \times 10^6 \text{ seconds}$$

and.hence the Doppler phase fluctuation scale is seen to be:

$$L \propto a$$

and

$$L \propto \tau \qquad \tau_n < 2.4 \times 10^6 \text{ seconds}$$

$$L \neq f(\tau) \qquad \tau_n > 2.4 \times 10^6 \text{ seconds}$$

References

1 Berman, A. L., "Proportionality Between Doppler Noise and Integrated Signal Path Electron Density Validated by Differenced S-X Range," in *The Deep Space Network Progress Report 42-38*, Jet Propulsion Laboratory, Pasadena, California, April 15, 1977

2 Goldstein, B., and Sisco, G L., "Spectra and Cross Spectra of Solar Wind Parameters From Mariner 5," in *Solar Wind*, edited by Sonett, C. P., Coleman, P J, Jr.; and Wilcox, J M, National Aeronautics and Space Administration, Washington, D C, 1972.

3. Hundhausen, A J., Bame, S. J, Asbridge, J. R, and Sydoriak, S J, "Solar Wind Proton Properties Vela 3 Observations from July 1965 to June 1967," *Journal of Geophysical Research, Space Physics*, Vol 75, No. 25, September 1, 1970

4 Berman, A. L, "Phase Fluctuation Spectra — New Radio Science Information to Become Available in the DSN Tracking System, Mark III-77, in *The Deep Space Network Progress Report 42-40*, Jet Propulsion Laboratory, Pasadena, California, August 15, 1977.

5 Cronyn, W M., "Density Fluctuations In the Interplanetary Plasma Agreement Between Space Probe and Radio Scattering Observations," *Astrophysical Journal*, Vol. 171, February 1, 1972

6 Berman, A. L, "Electron Density in the Extended Corona Two Views," in *The Deep Space Network Progress Report 42-41*, Jet Propulsion Laboratory, Pasadena, California, October 15, 1977

7. Berman, A L., and Wackley, J A, "Viking S-Band Doppler RMS Phase Fluctuations Used to Calibrate the Mean 1976 Equatorial Corona," in *The Deep Space Network Progress Report 42-38*, Jet Propulsion Laboratory, Pasadena, California, April 15, 1977

8 Brandt, J. C, *Introduction to the Solar Wind*, W. H. Freeman and Company, San Francisco, 1970.
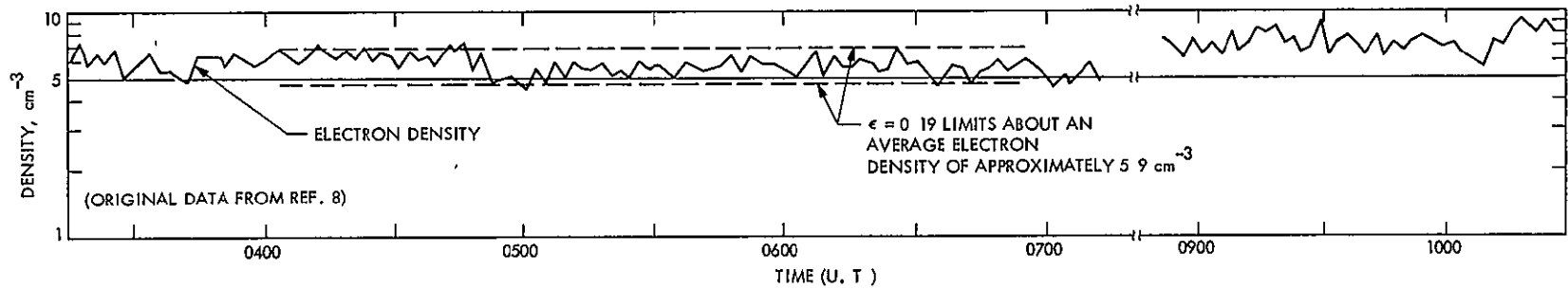
Fig 1. Comparison of ratio of electron density fluctuation to electron density (ϵ) to actual spacecraft in situ electron density measurements for $\tau_n = 10^4$ seconds
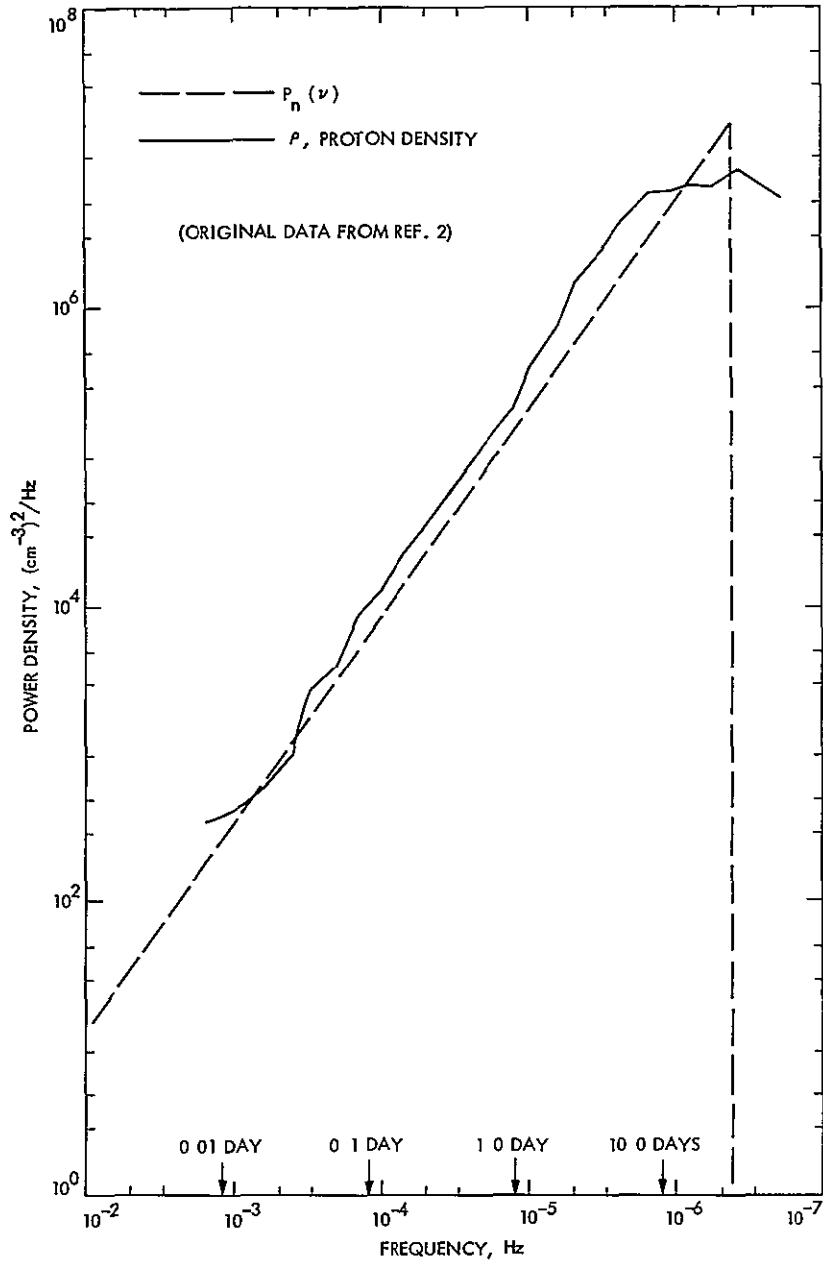
Fig 2 Comparison of the (one-dimensional) electron density fluctuation spectrum at 1 AU to the actual Mariner 5 proton density spectrum at approximately 1 AU

N78-24180

S-X Conversion for the Block III Receiver-Exciter

R E Weller

Radio Frequency and Microwave Subsystems Section

An S-X conversion modification has been designed for the Block III receiver-exciter to be used in the 26-meter S-X Conversion Project The description, design, specifications and data are presented

I. Introduction

The basic purpose of adding an X-band receive capability to the existing DSN 26-meter subnetwork is to maintain the DSN capability to support NASA flight projects — both those currently approved and those that are anticipated to be initiated in the near future

Deep space missions are phasing over their downlink radio frequency communications from S-band to X-band in order to meet mission navigation and science data return requirements, particularly from the planet Jupiter and beyond Equally important is the need for spacecraft transmission frequencies that are (presently) clear of other users. The extremely weak signals received from spacecraft in deep space are highly susceptible to radio interference from spacecraft located closer to Earth, such as those in Earth orbit These two factors — adequate data returns from the outer planets and protection from radio frequency interference — are sufficient cause for space flight projects to employ X-band in addition to S-band

At the present time, only the three DSN 64-meter-diameter antenna stations are equipped with X-band receive capability The increasing requirements for X-band support creates an overload on these stations while simultaneously creating an underload on the two 26-meter station subnets The purpose of the 26-meter S-X Conversion Project is to relieve the 64-meter subnet overload by adding X-band capability to one of the existing 26-meter subnets

The 26-meter S-X Conversion Project which will provide X-band receiver capability (Ref 1) includes a modification to the Block III receiver-exciter subsystem The receiver changes required to accomplish this modification are described in this article

II. Overall Description

To provide X-band receive capability in the Block III receivers at the 26-meter stations in the most cost-effective manner, two basic guidelines were followed namely, to maximize the use of existing station equipment that is consistent with performance and/or lifetime requirements, and minimize the maintenance cost impact through the utilization of X-band equipments already in service at the 64-meter stations The Block III receiver can be used as is, if a down converter from X- to S-band is inserted ahead of it This approach was used Three methods of down-converting were examined (Fig 1). These differ in the technique used to derive the reference signal and are discussed below

Method 1, Fixed Frequency Reference Signal

In this method the full 35-MHz bandwidth of the X-band signal is translated to S-band The Block III receiver does not have the capability of handling this bandwidth and modifications to the first local oscillators and receiver front end would be required.

Method 2, Adjustable Frequency Reference Signal

By providing the capability of selecting the frequency of the reference signal, the converter output frequency can always be adjusted to fall within the Block III receiver input bandwidth However, this mechanization would add complexity to the doppler extractor

Method 3, Coherent Frequency Reference Signal

Generating a reference signal whose frequency is coherently related to the exciter will provide an output frequency from the down-converter that is always within the receiver passband and yet not add any complexity to the doppler extractor

Method 3 was selected for the down-converter design and is discussed in more detail later in the article

In addition to a down-converter, it is necessary to add an X-band doppler extractor and a coherent X-band test signal (for receiver testing) to make the modification complete The functional block diagram of the 26 meter S-X conversion of the Block III receiver-exciter is presented in Fig 2 The new assemblies required for the S-X conversion are shown in solid squares while the existing equipment is shown in broken lined squares Each of these assemblies is also discussed in more detail

The general requirements for the X-S conversion is that the performance at X-band shall be equivalent to or better than the present performance of the Block III receiver-exciter at S-band Table 1 presents the functional requirements, specifications, and test data for the S-X conversion performance

III. Detailed Description

A. X-S Converter

Figure 3 shows the simplified block diagram of the X-S down-converter. The coherent reference to the down-converter appears at the output of the X96 frequency multiplier. The input signal to the times-96 frequency multiplier (X96) is obtained from the 320/221 frequency shifter (320/221), which in turn is driven by the exciter synthesizer multiplied by

X2 Therefore, the frequency at the input to the X96 multiplier is $f_T/48 \times 320/221$ where f_T is the S-band transmitted frequency The X96 module is a commercial multiplier that was developed for JPL by Zeta Lab Special attention was given to the method of mechanizing the X96 multiplier to assure that no coherent S-band output appears such as the X36 harmonic

The output of the X96 is followed by a bandpass filter to remove any undesired harmonics, and the signal is then applied to the mixer as the local-oscillator signal The signal at this point is $f_T/48 \times 320/221 \times 96$, or $f_T\ 640/221$.

The input signal received from the X-band maser is applied to a commercial amplifier. This amplifier was selected both for the low noise figure and to provide sufficient gain to mask the losses of the mixer, power divider, and cables, plus the Block III receiver noise figure The amplifier is followed by a bandpass filter used as a preselector, and the output of the filter is applied to the mixer This input signal is coherent with the transmitted signal and is $f_T\ 880/221 \pm D_x$, where D_x is X-band doppler.

The output of the mixer when mixed with the local-oscillator signal $f_T\ 640/221$ is $f_T\ 240/221 \pm D_x$ The output of the mixer is applied to a power divider and each output of this power divider is then applied to a switch As can be seen from Fig 2, each receiver may either select an S-band signal from the maser or an X-band signal that has been down converted to S-band

Figure 4 is a photo of the X-S Converter Assembly with the door removed The module at the top right is the X96 frequency multiplier while the module located top-left is the X-band amplifier. The X-band mixer is the dark square module located at bottom left. The dc voltages required for this assembly are supplied by power supplies located in the X-S Translator Assembly The X-S Converter Assembly will be mounted in the antenna dec house close to the existing Block III receiver-exciter

B. Doppler Extractor

Figure 5 shows the block diagram of receiver 1 doppler extractor. A second output that is used for receiver 2 doppler extractor is shown for the 240/220 output of the 320/221 module and also for the 45-MHz synthesizer and the 49/51 reference modules These doppler extractor modules are mounted in the Block III receiver located in the control room.

The reference frequency for the doppler extractor applied to the input of the 320/221 frequency shifter if $f_T/48$ and the

output of the 240/221 port is then $f_T/48 \times 240/221$ This reference signal is applied to the doppler mixer The doppler signal applied to the doppler mixer is derived from the receiver VCO through a $\times 2$ frequency multiplier This doppler signal is $[f_T \cdot 240/221 - 50 \pm D] 1/48$, where $(240/221 \, f_T - 50)$ is the first local oscillator signal When these two signals are applied to the doppler mixer as well as the 49/51-MHz and the 45-MHz references, the mixer produces doppler biased at both 1 MHz and 5 MHz

C. S-X Band Translator

Figure 6 shows the simplified block diagram of the translator. The signal applied to the 2636/221 frequency shifter is obtained from the exciter distribution amplifier and is $f_T/48$ The output of the frequency shifter is then amplified by the UHF amplifier and applied to the $\times 12$ frequency multiplier. The output of the $\times 12$ is applied to the mixer as the local oscillator (LO) signal and is identified as $f_T/48 \times 2636/221 \times 12$, or $f_T \, 659/221$

The signal for the mixer may be obtained either directly from the exciter or after the exciter output has been amplified by the transmitter This signal is f_T When these two signals are

present, the output of the mixer is $f_T \, 659/221 + f_T$, or f_T 880/221, which is the spacecraft transponder ratio, and this signal is identified as the X-band receiver test signal.

The design of the S-X translator assembly is adapted from the Block IV receiver-exciter design and uses the same components. The S-X translator assembly is shown in Fig 7 with the door removed. The three square modules at the top are power supplies; the large module to the left is the 2636/221 frequency shifter The small module in the bottom center is the UHF amplifier, while the module at bottom right is the $\times 12$ frequency multiplier and the horizontal module located in the center is the mixer.

IV. Conclusion

The evaluation of an engineering model has been completed. The fabrication of the first production system is in process and is scheduled for completion by January 1, 1978 The hardware will be installed in the lab receiver for testing and then shipped on March 1, 1978, for installation at DSS 12

Reference

1. Lobb, V. B., "26-Meter S-X Conversion Project," in *The Deep Space Network Progress Report 42-39*, pp 157-167, Jet Propulsion Laboratory, Pasadena, Calif., June 15, 1977

Table 1. Functional requirements, specifications, and test data

Parameter	Requirements	Specifications	Test data
Frequency range	8 4 – 8 44 GHz	8 4 – 8 44 GHz	8 4 – 8 43 GHz[a]
Noise figure	⩽ 10 dB	⩽ 10 dB	8 0 dB
Doppler phase error noise	< 12 deg	< 12 deg	8 deg
Doppler shift during mission lifetime	80 km/sec	80 km/sec (X = 4 51 MHz) (S = 1 267 MHz)	X = 4 6 MHz S = 4 6 MHz
Doppler shift during single pass	1 0 km/sec	1 0 km/sec (X = 56 3 kHz) (S = 15 4 kHz)	150 kHz
Doppler rate near Earth	100 m/sec²	100 m/sec² (X = 5630 Hz/sec) (S = 1540 Hz/sec)	5630 Hz/sec with 32 deg phase error
Doppler rate planetary encounter or orbit	0 1 m/sec² (< 10° error when 10 dB above receiver 12 Hz threshold)	0 1 m/sec² (X = 5 63 Hz/sec) (S = 1 54 Hz/sec)	< 10 deg phase error
Doppler stability 5 × 10⁴ second averaging	0 4 m	0 4 m X = 8100 deg	0 4 m 625 deg[b]
Group delay	1 4 m	1 4 m (9 3 nanosec)	0 5 ns[b]

[a]8 43 – 8 44 GHz noncoherent mode
[b]Added instability due to S-X conversion over Δt of 5°C

144

Fig. 1. Down-conversion techniques

X-BAND
$f_x = \frac{11}{3} f_s$

DOWN CONVERTER

S-BAND

BLOCK III RECEIVER
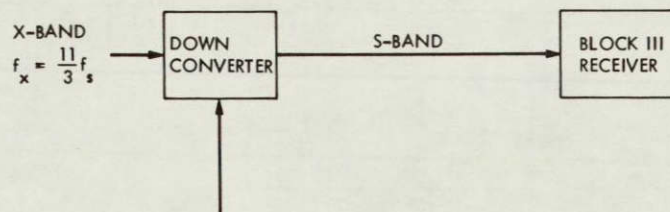
METHOD A. FIXED FREQUENCY REFERENCE
METHOD B. ADJUSTABLE FREQUENCY REFERENCE
METHOD C. COHERENT FREQUENCY REFERENCE $(\frac{8}{3} f_s)$
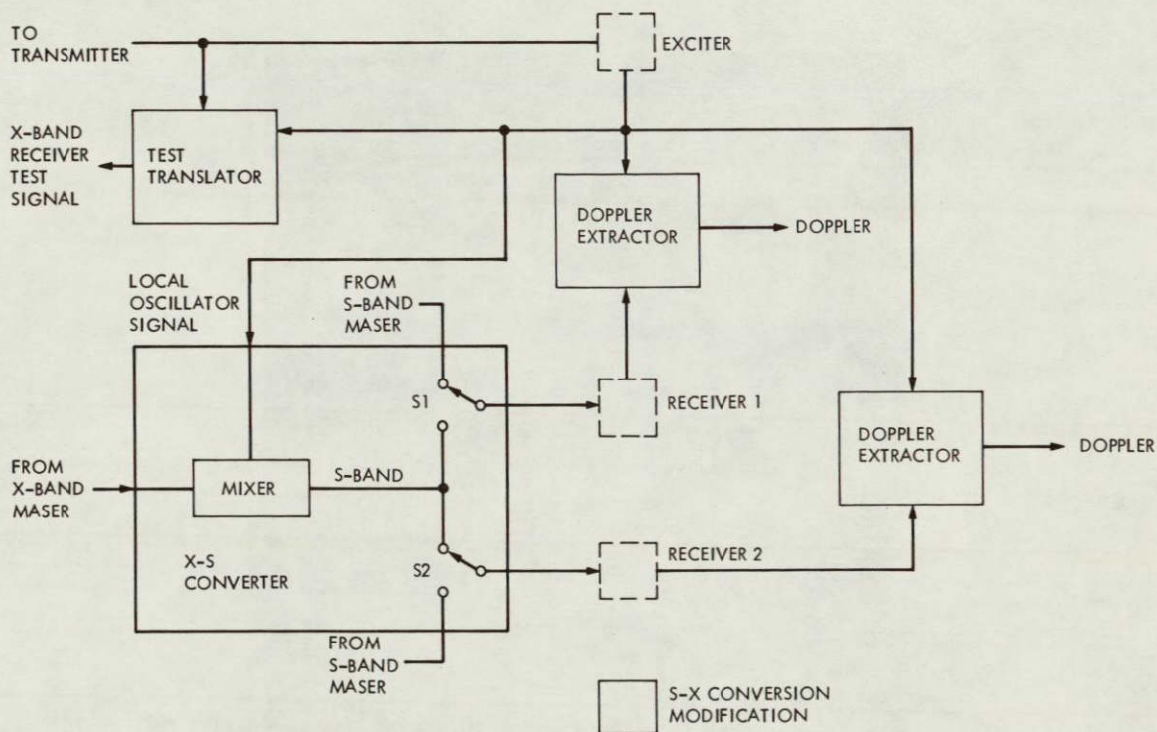
Fig. 2. S-X conversion modification — functional block diagram

Fig. 3. X-S converter simplified block diagram
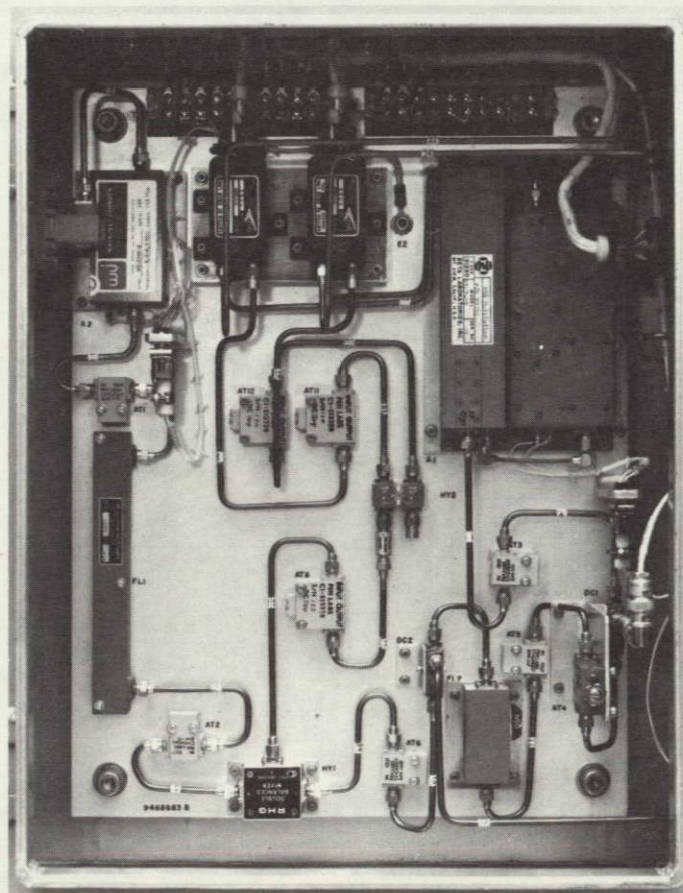
Fig. 4. X-S converter assembly with door removed
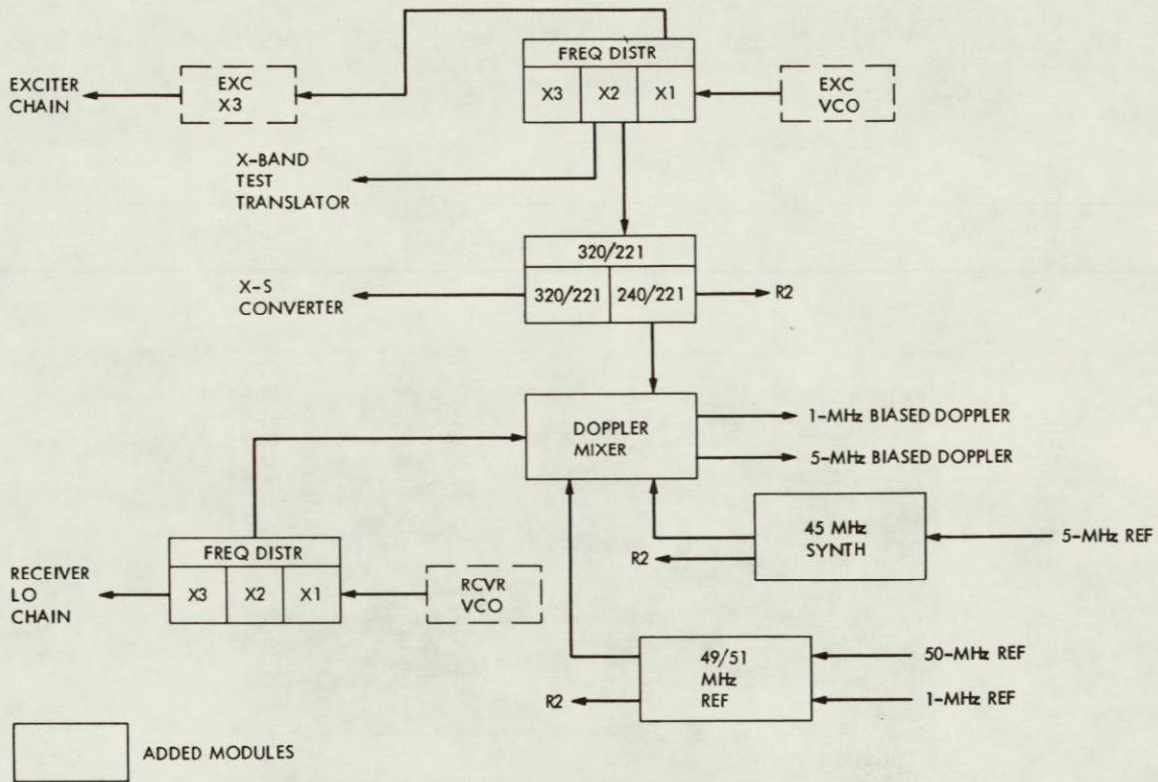
Fig. 5. Doppler extractor block diagram

Diagram labels:

FREQ DISTR — X3 X2 X1

EXC X3 → EXCITER CHAIN

EXC VCO

X-BAND TEST TRANSLATOR

320/221 — 320/221 | 240/221 → R2

X-S CONVERTER

DOPPLER MIXER → 1-MHz BIASED DOPPLER
→ 5-MHz BIASED DOPPLER

45 MHz SYNTH ← 5-MHz REF
R2 ←

FREQ DISTR — X3 X2 X1

RECEIVER LO CHAIN

RCVR VCO

49/51 MHz REF ← 50-MHz REF
R2 ← ← 1-MHz REF

ADDED MODULES
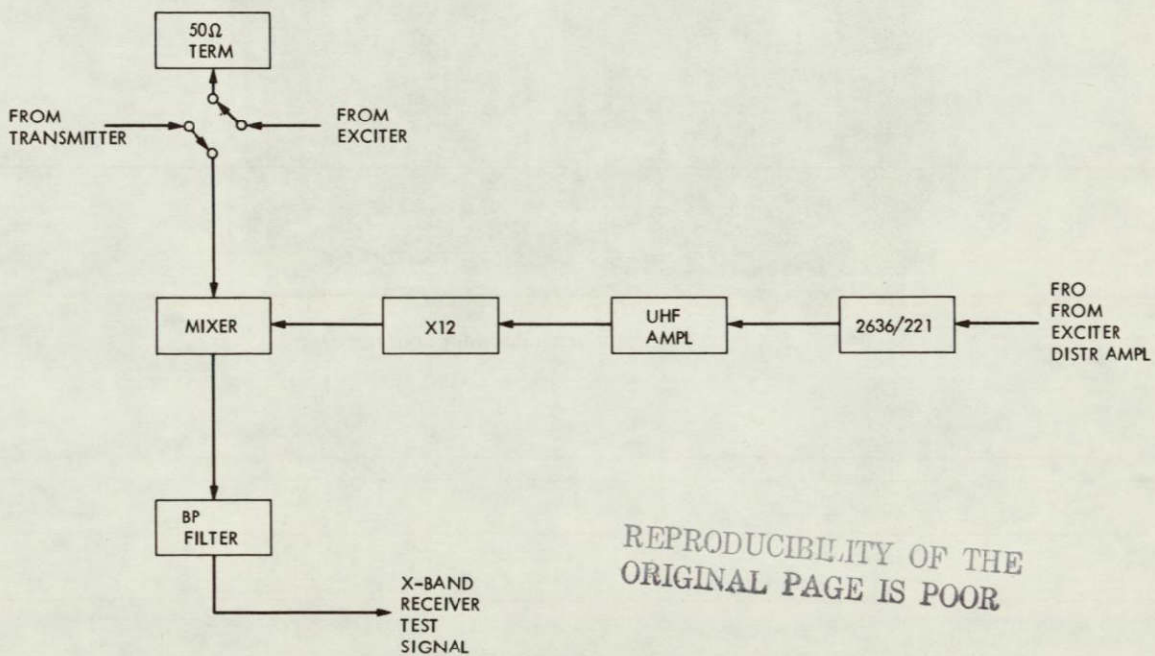
Fig. 6. S-X band translator block diagram

Diagram labels:

50Ω TERM

FROM TRANSMITTER

FROM EXCITER

MIXER ← X12 ← UHF AMPL ← 2636/221 ← FRO FROM EXCITER DISTR AMPL

BP FILTER → X-BAND RECEIVER TEST SIGNAL

REPRODUCIBILITY OF THE ORIGINAL PAGE IS POOR

147
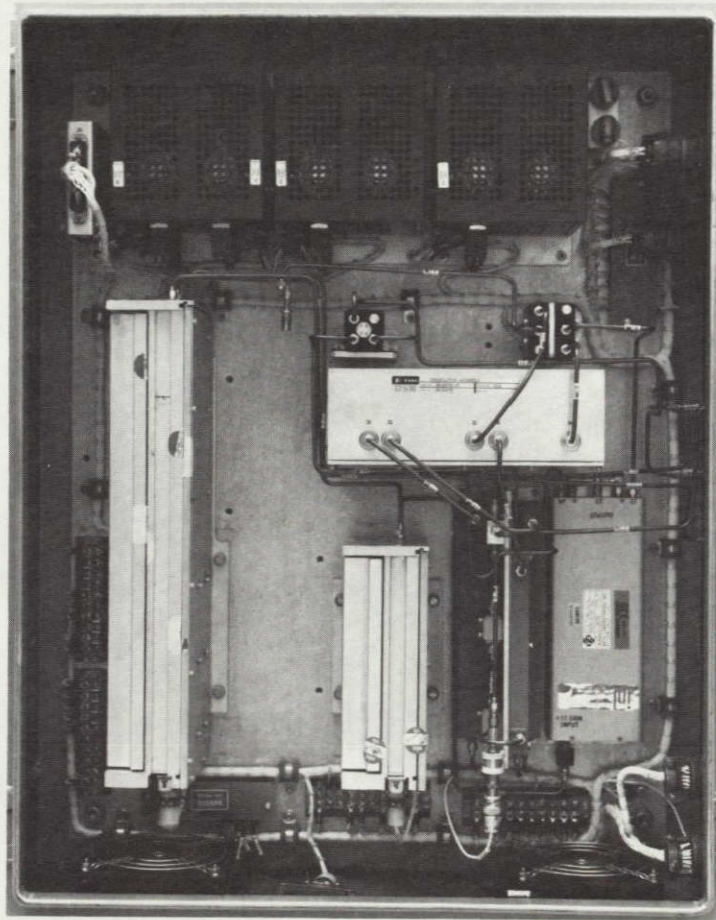
Fig. 7. S-X band translator assembly with door removed

N78-24181

DSN Telemetry System Performance Using a Maximum Likelihood Convolutional Decoder

B Benjauthrit and R Kemp

TDA Engineering Office

This report describes results of telemetry system performance testing conducted at Goddard Merritt Island Space Flight Station using DSN equipment and a Maximum Likelihood Convolutional Decoder (MCD) for code rates 1/2 and 1/3, constraint length 7 and special test software The test results confirm the superiority of the rate 1/3 over that of the rate 1/2 The overall system performance losses determined at the output of the Symbol Synchronizer Assembly are less than 0 5 dB for both code rates Comparison of the performance is also made with existing mathematical models Error statistics of the decoded data are examined. The MCD operational threshold is found to be about 1 96 dB

I. Introduction

In the past, numerous papers have been written on the subject of DSN telemetry system performance using a code rate 1/2, constraint length 7[1], Maximum Likelihood Convolutional Decoder (MCD) (Refs 1-3) However, recent attention has been focused on the use of the built-in rate 7 1/3 decoding capability of the MCD for improved telemetry system performance. This may provide an alternate approach to other enhancements being considered, for example, it may allow the use of S-band rather than X-band for some phases of a mission

In order to verify and analyze the rate 7 1/3 performance of the MCD, tests were conducted at the Merritt Island Goddard Space Flight Center Station using DSN equipment for both code rates. Results and analyses of these tests are provided herein.

---

[1]For convenience, we shall write this as "a code rate 7 1/2" or simply "a rate 7 1/2 "

II. Test Objectives and Implementation

The objectives of the tests were

(1) To obtain the decoding performance of the MCD, i e , to obtain plots of bit error probability or bit error rate (BER) vs ST_B/N_0 at the input of the decoder. The BER's of interest are between 10^{-6} and 10^{-2} and the expected ST_B/N_0 is from +1 0 to +5 0 dB

(2) To obtain the system decoding performance, i e., to obtain plots of BER vs ST_B/N_0 at the input of the receiver

(3) To discover the minimum operational point of the telemetry system

(4) To discover the mechanisms that limit the operating system to this minimum operational point

(5) To obtain node synchronization change frequencies, i.e., the number of node synchronization changes per the number of decoded bits

The data rates selected for these tests were 3.6, 5.6, 6 4, and 7 2 kbps The test conditions are given in Table 1.

To achieve the above objectives, typical DSN telemetry system test equipment consisting of the Simulation Conversion Assembly (SCA), microwave equipment (UWV), Receiver Assembly (RCV), Subcarrier Demodulator Assembly (SDA), Symbol Synchronizer Assembly (SSA), and the Telemetry Processor Assembly (TPA)/MCD was used (see Fig 1). All tests were configured with the S-band Block III receiver using 12–Hz design point loop noise bandwidth range, Block III SDA at medium-loop bandwidth, Block III SSA at narrow/narrow-loop bandwidth, modulation index of 72 deg (carrier suppression of -10 2 dB), and PN code data pattern for both code rates The ST_B/N_0 values were established at the receiver input using the Y-factor technique (Ref. 4). The system operational software was employed to provide SSA symbol signal-to-noise ratio (SNR) To determine the MCD BER and error statistics, use was made of a program called MCDPEP to record decoded telemetry data and another program called MDAP to analyze the recorded data (Ref. 3). To obtain MCD SER, the BER line (original symbols) from the SCA to the SSA was connected

The output of MDAP contained normalization rate (NR,a mechanism in the decoder used to indicate the quality of the input data (Refs 2 and 8)), MCD BER, MCD SNR (a quantity derived from the decoder normalization rate), number of node sync changes, and burst error statistics

For each bit rate and ST_B/N_0 value, a data run was made for the rate 1/2 and then for the rate 1/3 This was accomplished by merely reconfiguring the SCA and the MCDPEP software. This method was utilized to reduce the possibility of introducing errors in the Y-factor setup. After each pair of data runs, the Y-factor was checked for drift In addition, the receiver AGC was monitored continuously for drift

III. Analysis

A short discussion of system loss and the experimental test results are presented in this section.

A. System Loss

Mathematical loss models of the various telemetry subsystems (i e , radio loss, subcarrier demodulation loss, bit sync and detection loss, and waveform distortion loss) have been extensively proposed in the past (Refs 5 and 6), they will not be repeated here A software implementation of selected loss models, called TAP, is described in Ref. 6. For insight and comparison, a typical printout of this loss-model program for radio (receiver) loss, SDA loss, SSA loss, and other important system parameters is tabulated in Table 2 for the same conditions as stated in Table 1 for the experimental tests. Table 3 provides summaries of Table 2. Note that the loss-model program contains no waveform distortion loss calculation capability.

B. Test Results

The test results in terms of BER, number of normalizations per bit, average normalization rate, number of bursts per bit, average number of errors per burst, average burst length, maximum burst length of each run, number of error-free runs (EFR) per bit, total number of error-free runs, SSA output SER, and node synchronization change frequency (Refs.1-3) are tabulated in Table 4 Five runs were made for each of tests A4, B4, C4, and D4 This is to provide confidence in determining node sync change frequencies The results were consistent; the averages and standard deviations of these tests are given in Table 4 In order to confirm the first run results, a rerun was obtained for tests A5, A6-1/3, and B6-1/3 Averages and standard deviations of these tests are also shown in Table 4. The accuracy of a Y-factor setting for a specific ST_B/N_0 is approximately ±0 5 dB (based on output SNR's calculated by the MCD and SSA) Furthermore, it was discovered that (see Table 5)

(1) The system operational software could only handle ST_B/N_0 levels above 1 96 dB (believed to be due to the MCD operating threshold), below which the SSA initialized with the software would not achieve lock

(2) The system losses at the Merritt Island station (MIL-71) were about one decibel worse than those at JPL Pasadena Compatibility Test Area (CTA-21)

Therefore, tests with ST_B/N_0 levels of 1 0, 1 7, and 2 0 dB could not be performed

It should be pointed out that the SSA SNR and MCD SNR printed out at the Terminet are provided by two special programs contained in the TPA operational software program

The first program is used to correct the bias of the SSA SNR at low SNR (<5 dB) It is based on a curve fit of Fig 21 in Ref 7 for an internal SSA SNR of 26 dB (measured at CTA-21), giving the estimated SSA SNR (dB) as[2]

$$R_e = -10 \log \left(10^{-R_i/10} + 10^{-R_0/10} \right) \qquad (1)$$

---

[2]Developed by G L Dunn and R Bunce

where

R_i = internal SSA SNR = 26 dB

$$R_0 = \frac{-(2 - R_a) + \sqrt{(2 - R_i)^2 + 4(R_a + 5)}}{2} \qquad (2)$$

and

R_a = actual input SSA SNR (dB)

Using Eqs (1) and (2) to estimate the SSA SNR output instead of the exact results from Ref 7 yields an error of less than 0 14 dB over the range of −5 to 50 dB By solving Eqs. (1) and (2), the actual SNR expressed in terms of the estimated SSA SNR is as follows

$$R_a \text{ (dB)} = \frac{(R + 1)^2 - 6}{R + 1} \qquad (3)$$

where

$$R = \begin{cases} -10 \log \left(10^{-R_e/10} - 10^{-R_i/10}\right) \text{for } R_e \leqslant 5 \text{ dB} \\ R_e \text{ otherwise} \end{cases} \qquad (4)$$

where R_e and R_i have been defined previously

Equation (3), together with Eq (4), is used to correct the SSA SNR bias

The second program provides a system output SNR estimate determined from the MCD normalization rate. The program presently employs the algorithm derived from the Linkabit convolutional decoder model LV7015 implemented in Spain as part of the early telemetry system performance analysis (Ref. 2). The algorithm is

$$ST_B/N_0, \text{dB} = \frac{2\,9664}{\bar{N}_c + 0\,08} + 5\,1218 - 0\,2252\bar{N}_c$$

where $\bar{N}_c$ is the average normalization counts (= $192\bar{N}_b$, $\bar{N}_b$ = average normalizations per bit). Due to certain design differences (Ref. 1), this algorithm provides only approximate values of ST_B/N_0 at the MCD output (see Fig 2).

Plots of BER vs receiver ST_B/N_0 (dB) for all tests (Tests 4 through 6 of test series A through E) are shown in Fig 3 The rate 1/3 performance is about one-half of a decibel better than that of rate 1/2. This is in agreement with previous simulation results (Ref. 8). The acceptance test data at 250 kbps are also shown in the figure. They were for the MCD alone and included no system losses. The experimental test data show about one decibel degradation from the above ideal data However, direct comparison of the two cannot be made due to the differences in bit rate and other test conditions

The measured and calculated losses of the telemetry system considered are shown in Fig 2. One can see that the measured losses are higher than the calculated ones This is due to the approximate loss models and the neglect of other loss effects such as the waveform distortion loss.

Figures 4 and 5 provide graphical representations of error-free run size R vs probability that R is exceeded and burst length size B vs probability that B is exceeded For comparison, each graph displays the results of both rates 1/2 and 1/3. The data indicate no clear trend for rate 1/3 to be superior to rate 1/2 with regard to error-free run data However, in all cases, rate 1/3 is superior to that of rate 1/2 for the burst length data.

Figure 6 makes comparison of the average burst length and average number of burst errors vs MCD input ST_B/N_0 for tests A4-1/2, A4-1/3, and LV7015-1/2 The other remaining tests yield a similar result and thus are not shown.

IV. Summary

Most of the test objectives were achieved The decoding performance of the MCD is shown in Fig 3 The telemetry system decoding performance is summarized in Fig 2 The minimum operational point of the telemetry system is found to be approximately 1 96.dB (MCD ST_B/N_0 for rate 1/2, see Table 5), below which the SSA initialization with the present system operational software could not be achieved (believed to be due to the MCD operating threshold) (The present system operational software does not have the capability to handle the 1/3 rate.) This leads to elimination of certain low ST_B/N_0 tests Finally, due to the nature of the decoder, the node synchronization change frequencies, i e , the number of node synchronization changes per the number of decoded bits, of only low ST_B/N_0 were obtained (given in Table 4). For high ST_B/N_0 tests, the time specified in the test conditions was not sufficiently long to generate a node sync change

References

1 Benjauthrit, B, "Final Report on DSN Telemetry System Performance with Convolutionally Coded Data Maximum Likelihood Decoding," in *DSN Progress Report 42-33*, Jet Propulsion Laboratory, Pasadena, Calif, pp 112-122, June 15, 1976.

2 Urech, J. M, et al, "DSN Performance Tests of a Maximum Likelihood Decoder," in *DSN Progress Report 42-33*, Jet Propulsion Laboratory, Pasadena, Calif, pp 131-146, June 15, 1976

3 Benjauthrit, B., et al, "DSN Telemetry System Performance with Convolutionally Coded Data Using Operational Maximum Likelihood Convolutional Decoders," in *DSN Progress Report 42-36*, Jet Propulsion Laboratory, Pasadena, Calif, pp 81-101, Dec 15, 1976.

4. Baumgartner, W. S, et al, "Multiple-Mission Telemetry System Project," in SPS 37-60, Vol II, Jet Propulsion Laboratory, Pasadena, Calif., pp 152-169

5. Edelson, R E., *Telecommunications System Design Techniques Handbook*, Technical Memorandum 33-571, Jet Propulsion Laboratory, Pasadena, Calif., 1972

6. Dunn, G L, "Telemetry Analysis Program (TAP) Update," JPL Interoffice Memorandum 421E-75-360, Sept. 5, 1975 (an internal document).

7 Lesh, J. L., "Accuracy of the Signal-to-Noise Ratio Estimator," in Technical Report 32-1526, Vol X, Jet Propulsion Laboratory, Pasadena, Calif, Aug 15, 1972

8 Gilhouser, K S, et al, "Coding Systems Study for High Data Rate Telemetry Links," Accession No N71-27786, Linkabit Corp, San Diego, Calif, Jan. 1971

Acknowledgments

Table 1. Telemetry performance test conditions

RF band S, mod index 72°, data pattern PN code, RCV BLK III at 12 Hz W_{LO}, SDA BLK III, medium, SSA BLK III, narrow/narrow, subcarrier frequency 1 44 MHz

Bit rate, kbps	Test ID	P_T/N_0, dB	ST_B/N_0, dB	Expected BER	Time, min	Expected bits	Bit errors
7 2	A1	40 03	1 0	1.2×10^{-1}	2	$8\ 64 \times 10^5$	10^5
	2	40.73	1 7	$1\ 8 \times 10^{-2}$	2	$8\ 64 \times 10^5$	$1\ 6 \times 10^4$
	3	41 03	2 0	7×10^{-3}	2	$8\ 64 \times 10^5$	6049
	4	42 03	3 0	3×10^{-4}	2	$8\ 64 \times 10^5$	259
	5	43 03	4 0	1.5×10^{-5}	30	$1\ 3 \times 10^7$	194
	6	44 03	5 0	9×10^{-7}	60	$2\ 6 \times 10^7$	23
3 6	B1	37 02	1 0	$1\ 2 \times 10^{-1}$	4	$8\ 64 \times 10^5$	10^5
	2	37 72	1 7	1.8×10^{-2}	4	$8\ 64 \times 10^5$	1.6×10^4
	3	38 02	2 0	7×10^{-3}	4	8.64×10^5	6048
	4	39 01	3 0	3×10^{-4}	4	8.64×10^5	259
	5	40 02	4 0	$1\ 5 \times 10^{-5}$	60	$1\ 3 \times 10^7$	194
	6	41 02	5 0	9×10^{-7}	120	$2\ 6 \times 10^7$	23
5 6	C1	38 94	1 0	$1\ 2 \times 10^{-1}$	2 6	$8\ 64 \times 10^5$	10^5
	2	39 64	1 7	$1\ 8 \times 10^{-2}$	2 6	$8\ 64 \times 10^5$	$1\ 6 \times 10^4$
	3	39 94	2 0	7×10^{-3}	2 6	$8\ 64 \times 10^5$	6048
	4	40 94	3 0	3×10^{-4}	2 6	$8\ 64 \times 10^5$	259
	5	41 94	4 0	1.5×10^{-5}	38 6	$1\ 3 \times 10^7$	194
	6	42 94	5 0	9×10^{-7}	77 3	$2\ 6 \times 10^7$	23
6 4	D1	39 52	1 0	$1\ 2 \times 10^{-1}$	2 3	$8\ 64 \times 10^5$	10^5
	2	40 22	1 7	$1\ 8 \times 10^{-2}$	2 3	$8\ 64 \times 10^5$	$1\ 6 \times 10^4$
	3	40 52	2 0	7×10^{-3}	2 3	$8\ 64 \times 10^5$	6048
	4	41 52	3 0	3×10^{-4}	3 3	$8\ 64 \times 10^5$	259
	5	42 52	4 0	$1\ 5 \times 10^{-5}$	33 8	$1\ 3 \times 10^7$	194
	6	43 52	5 0	9×10^{-7}	67 5	$2\ 6 \times 10^7$	23

Table 2. Typical telemetry system parameters and losses obtained from TAP[a] for both rates 7 = ½ and ⅓

Bit rate, kbps	Test ID	ST_S/N_0, dB	Code rate	SSA ST_B/N_0 estimate dB	SDA loop noise BW, Hz	Carrier loop noise BW, Hz	Carrier power, dBm	RCV loss, dB	SDA loss, dB	SSA loss, dB	System loss, dB	SER %
7 2	A4	3 0	1/2	1 33	0 38	99.17	−150 7	0 162	0 049	0.024	0.235	8 43
			1/3	0 64	0 33	99.12	−150 7	0 161	0 053	0 033	0 246	13 11
	A5	4 0	1/2	1.88	0 42	104 50	−149 7	0 134	0 042	0 020	0 196	6 04
			1/3	1 01	0 37	104.40	−149 7	0.133	0.045	0 027	0 205	10 31
3 6	B4	3 0	1/2	1 27	0 35	80 94	−153 7	0 285	0 067	0 024	0 376	8 78
			1/3	0 60	0 30	80 88	−153 7	0 280	0 072	0 034	0 386	13 49
		4 0	1/2	1 81	0 39	87 20	−152.7	0 241	0 058	0 020	0 319	6 31
			1/3	0 96	0 35	87 14	−152 7	0 236	0 062	0 028	0 326	10 63

[a]From Ref 6 under the following conditions

System noise temperature = 41 K
Block III bandwidths = RCV - narrow, SDA - narrow, SSA - medium/narrow
One-way S/X DOP offset (Hz), rate (Hz/sec), time (min) = 0 0, 0 0, 0.0.

Table 3 Percent of loss for the various telemetry subsystems, calculated, wave form loss not included

Code rate	Relative loss, %											
	7 2 kbps			3 6 kbps			5.6 kbps			6 4 kbps		
	RCV	SDA	SSA	RCV	SDA	SSA	RCV	SDA	SSA	RCV	SDA	SSA
1/2	68	22	10	76	18	6	71	20	9	70	21	9
1/3	64	23	13	73	19	8	68	21	11	66	22	12

Table 4. Telemetry system test performance results

Bit rate	Test ID	ST_B/N_0, dB	Code rate	Number of bits, $\times 10^6$	Bit error rate	Number of norms/bit, $\times 10^{-6}$	Avg norm rate	Bursts/bit	Avg errors/burst	Avg burst length	Max burst length	EFRS/bit, $\times 10^{-5}$	Number distinct EFRS	Symbol error rate %	Sync changes/ bit, $\times 10^{-6}$
7 2	A4	3 0	1/2	0 79 ±0 06	$(4\ 47\ \pm0\ 72) \times 10^{-3}$	11 35 ±0 10	11 86 ±2 43	$(6\ 47\ \pm0\ 76) \times 10^{-4}$	7 56 ±0 23	12 86 ±0 39	69 ±7	490 ±48	477 ±53	13 65 ±7 35	8 3 ±4 3
			1/3	0 81 ±0 07	$(3\ 41\ \pm0\ 19) \times 10^{-3}$	11 32 ±0 12	11 22 ±2 10	$(5\ 82\ \pm0\ 46) \times 10^{-4}$	6 15 ±0 15	9 68 ± 0 34	49 ±11	371 ±27	449 ±34	0 98 ±0 20	12 8 ±6 9
	A5	4 0	1/2	12 92 ±0 07	$(2\ 3\ \pm0\ 3) \times 10^{-4}$	10 18 ±0 02	9 88 ±0 63	$(4\ 45\ \pm0\ 42) \times 10^{-5}$	5 11 ±0 14	8 3 ±0 2	44 ±2	22 95 ±2 85	578 ±52	–	0
			1/3	12 88 ±0 11	$(1\ 62\ \pm0\ 26) \times 10^{-4}$	10 14 ±0 06	11 88 ±0 38	$(3\ 85\ \pm0\ 55) \times 10^{-5}$	4 23	6 13 ±0 13	33 ±4	16 15 ±2 55	503 ±70	0 89	0
	A6	5 0	1/2	25 92	$9\ 57 \times 10^{-6}$	10 26	5 75	$2\ 20 \times 10^{-6}$	4 35	7 28	21	0 96	62	3 68	0
			1/3	25 92 ±0 05	$(0\ 70\ \pm0\ 43) \times 10^{-5}$	10 15 ±0 02	8 13 ±0 13	$(1\ 99\ \pm1\ 14) \times 10^{-6}$	3 25 ±0.25	5 0 ±0 25	14 ±3	0 71 ±0 43	57 ±30	–	0
3 6	B4	3 0	1/2	0 89	$(3\ 30\ \pm0\ 14) \times 10^{-3}$	11 20	14 01 ±0 28	$(4\ 67\ \pm0\ 14) \times 10^{-4}$	7 16 ±0 36	12 14 ±0 72	62 ±7	335 ±15	405 ±13	2 61 ±1 6	0 90 ±0 4
			1/3	0 89	$(1\ 73\ \pm0\ 13) \times 10^{-3}$	11 20	14 76 ±0 20	$(3\ 20\ \pm0\ 16) \times 10^{-4}$	5 52 ±0 19	8 54 ±0 37	41 ±5	177 ±14	285 ±14	62 47	2 00 ±1 3
	B5	4 0	1/2	13 00	$2\ 54 \times 10^{-4}$	10 16	9 75	$4\ 92 \times 10^{-5}$	5 21	8 53	34	25 62	643	0 05	0
			1/3	13 01 ±0 04	$(3\ 34\ \pm0\ 05) \times 10^{-4}$	10 19	12 75 ±0 25	$(7\ 26\ \pm0\ 03) \times 10^{-5}$	4 61	6 94	42 ±2	33 1 ±0 5	930 ±10	0 9	0
	B6	5 0	1/2	25 92	$2\ 5 \times 10^{-5}$	10 15	6 25	$5\ 33 \times 10^{-6}$	4 68	7 73	31	2 5	145	–	0
			1/3	25 69	$1\ 14 \times 10^{-5}$	10 24	8 25	$3\ 0 \times 10^{-6}$	3 81	5 81	34	1 15	84	–	0
5 6	C4	3 0	1/2	6 21 ±6 65	$(3\ 28\ \pm0\ 51) \times 10^{-3}$	10 87 ±0 63	9 56 ±3 10	$(2\ 70\ \pm1\ 9) \times 10^{-4}$	7 02 ±1 05	11 81 ±1 89	62 ±10	202 ±152	420 ±309	10 18 ±9 79	9 3 ±10 2
			1/3	0 66 +0 46	$(1\ 88\ \pm0\ 17) \times 10^{-3}$	11 08 ±0 07	11 35 ±0 70	$(3\ 40\ \pm0\ 2) \times 10^{-4}$	5 79 ±0 24	9 02 ±0 44	47 ±12	198 ±18	340 ±36	4 38 ±0 44	3 2 ±1 3
	C5	4 0	1/2	13 18	$3\ 98 \times 10^{-4}$	10 17	10 63	$7\ 5 \times 10^{-5}$	5 30	8 72	46	39 83	976	–	0
			1/3	13 13	$1\ 65 \times 10^{-4}$	10 21	11 75	$3\ 65 \times 10^{-5}$	4 50	6 62	39	16 52	482	0 86	0
	C6	5 0	1/2	26 14	$1\ 4 \times 10^{-5}$	10 10	6 38	$3\ 33 \times 10^{-6}$	4 28	7 15	19	1 46	93	–	0
			1/3	26 61	$5\ 64 \times 10^{-6}$	10 03	8 25	$1\ 65 \times 10^{-6}$	3 41	4 82	17	0 57	50	0 33	0
6 4	D4	3 0	1/2	0 42 ±0 21	$(1\ 92\ \pm0\ 11) \times 10^{-3}$	11 20	1 98 ±0 33	$(3\ 8\ \pm2\ 7) \times 10^{-4}$	7 64 ±0 27	12 85 ±0 53	61 ±14	282 ±186	125 ±48	4 55 ±0 11	105 7 ±51
			1/3	0 99	$(3\ 64\ \pm0\ 2) \times 10^{-3}$	11 20	12 54 ±1 05	$(5\ 80\ \pm0\ 3) \times 10^{-4}$	6 58 ±0 07	10 47 ±0 08	62 ±7	381 ±23	535 ±25	10 76 ±2 99	1 8 ±0 4
	D5	4 0	1/2	13 15	$5\ 7 \times 10^{-4}$	10 19	10 86	$9\ 57 \times 10^{-5}$	5 94	9 95	55	56 88	1225	0 53	0
			1/3	13 57	$1\ 77 \times 10^{-4}$	9 73	10 75	$4\ 01 \times 10^{-5}$	4 42	6 63	55	1 77	548	6 55	0
	D6*	5 0	1/2	26 41	$5\ 45 \times 10^{-5}$	10 11	7 50	$1\ 09 \times 10^{-5}$	4 98	8 00	38	5 48	296	–	0
			1/3	26 40	$1\ 5 \times 10^{-7}$	10 04	5 38	$7\ 58 \times 10^{-8}$	2 00	3 00	5	0 02	4	–	0

*Signal too high

Table 5. Operational thresholds in dB

Code rate	SSA ST_S/N_0	JPL tech rqmt MCD ST_B/N_0	CTA-21		MIL-71		Voyager expectation, dB/BER
			Operational software MCD ST_B/N_0	MCD PEP MCD ST_B/N_0	Operational software MCD ST_B/N_0	MCD PEP MCD ST_B/N_0	
7 1/2	-5 00	3 00	1 96	2.00	3.16	3 17[a]	$2.3/5 \times 10^{-3}$
							$3 96/3 \times 10^{-5}$
7 1/3	-5 00	2 70	—	1 50	—	3.20	$1.7/10^{-2}$

[a]A rough estimate
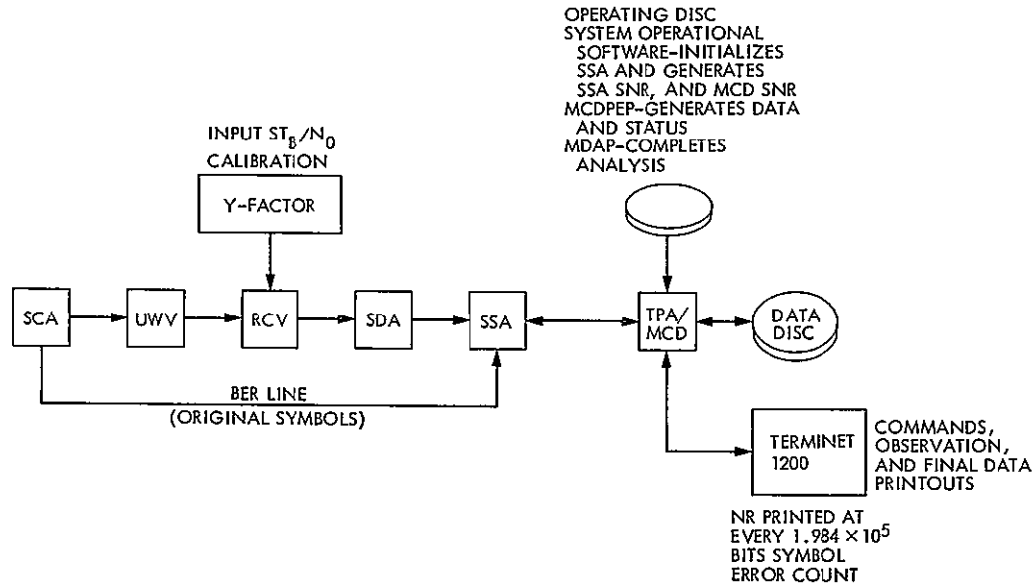
Fig. 1. DSN telemetry system test configuration

NOTES TEST A 7 2 kbps
       TEST B 3 6 kbps
       TEST C 5 6 kbps
       TEST D 6 4 kbps

Fig. 2. Measured and calculated telemetry performance for code rates 7:½ and ⅓ at various bit rates
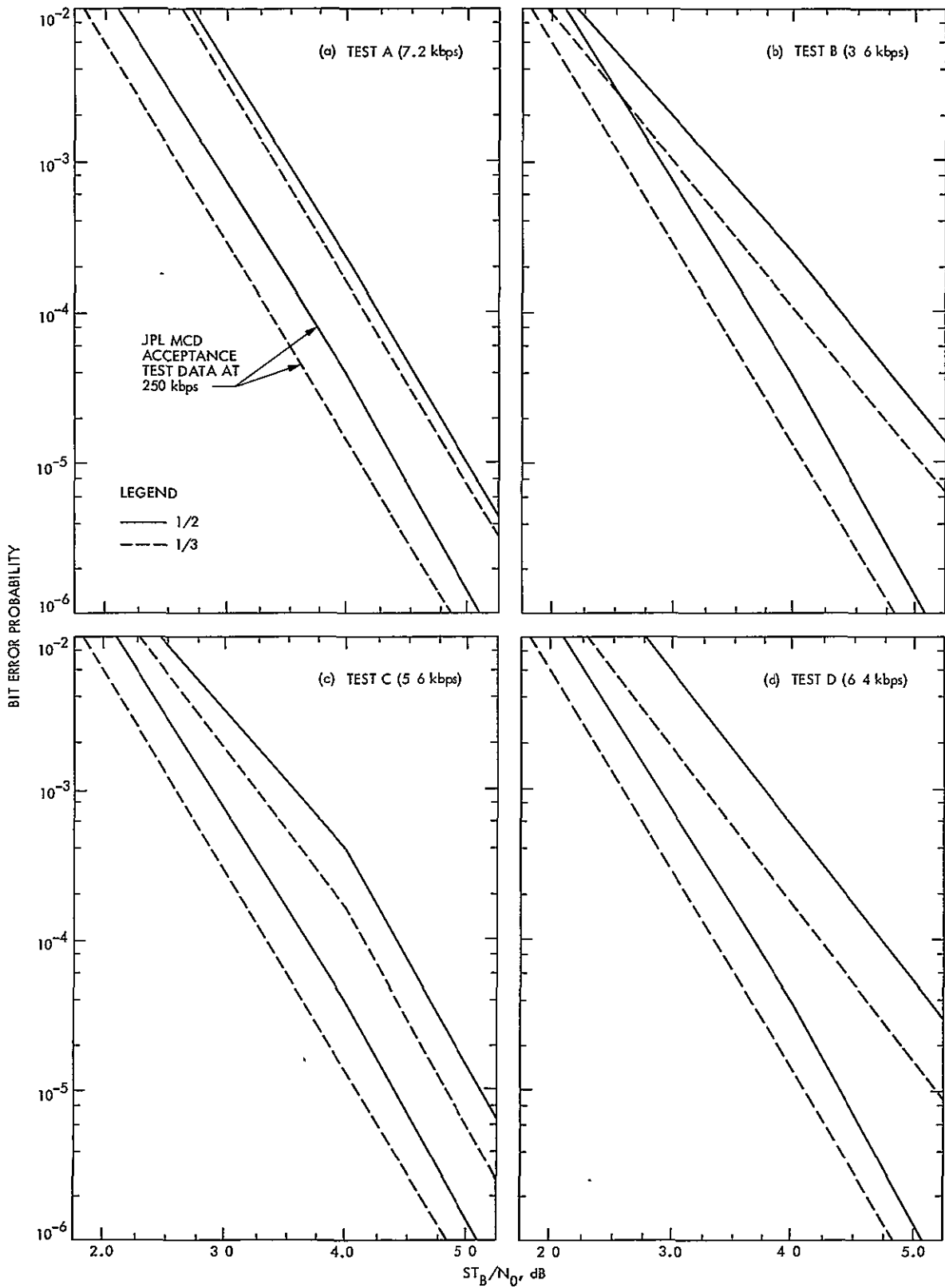
Fig. 3 Bit error probability vs receiver ST_B/N_0 by Y- factor of tests A-D for code rates 7:½ and ⅓
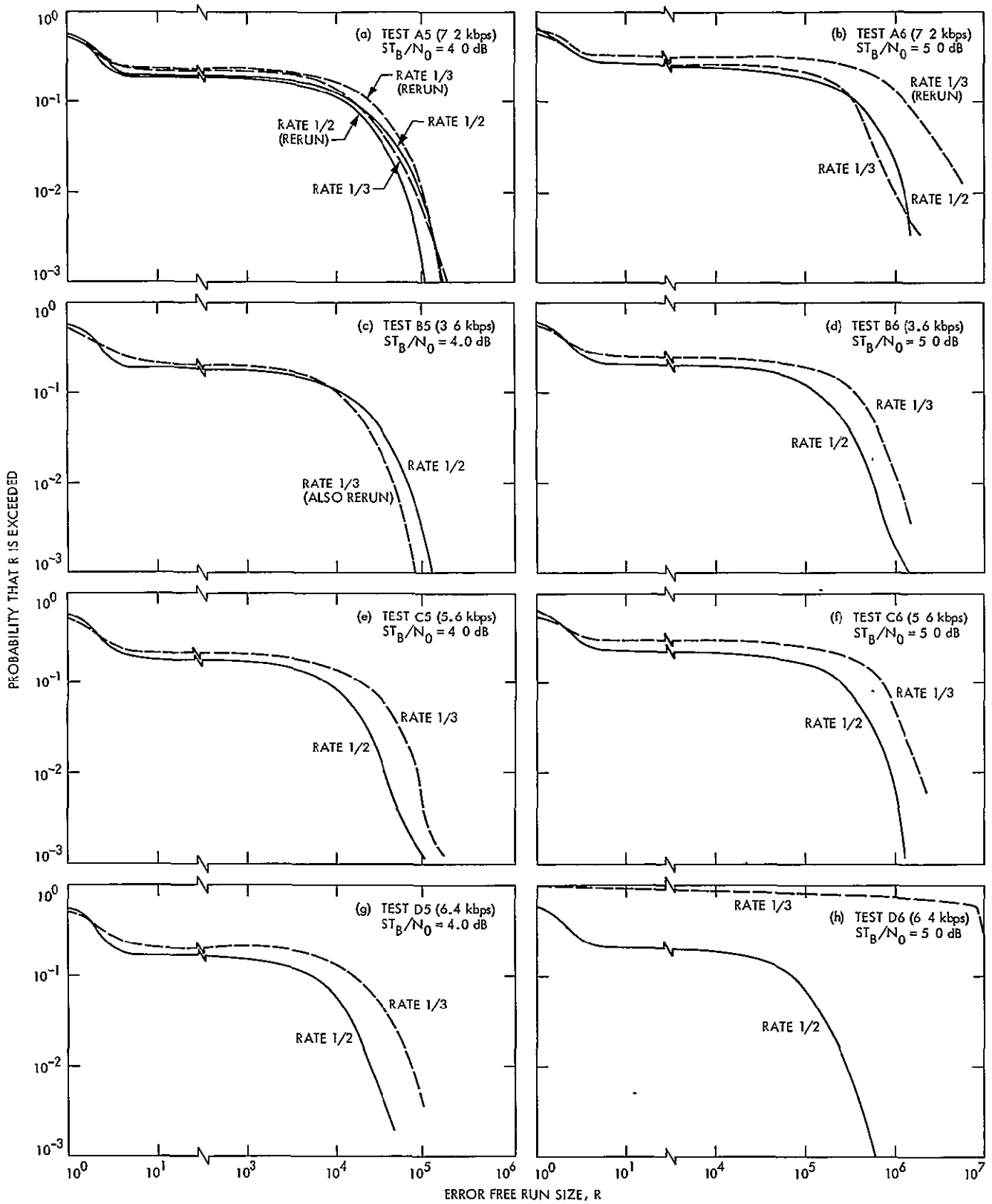
Fig 4   Error-free run size R vs probability that R is exceeded of tests A5-D6 for code rates 7:½ and ⅓
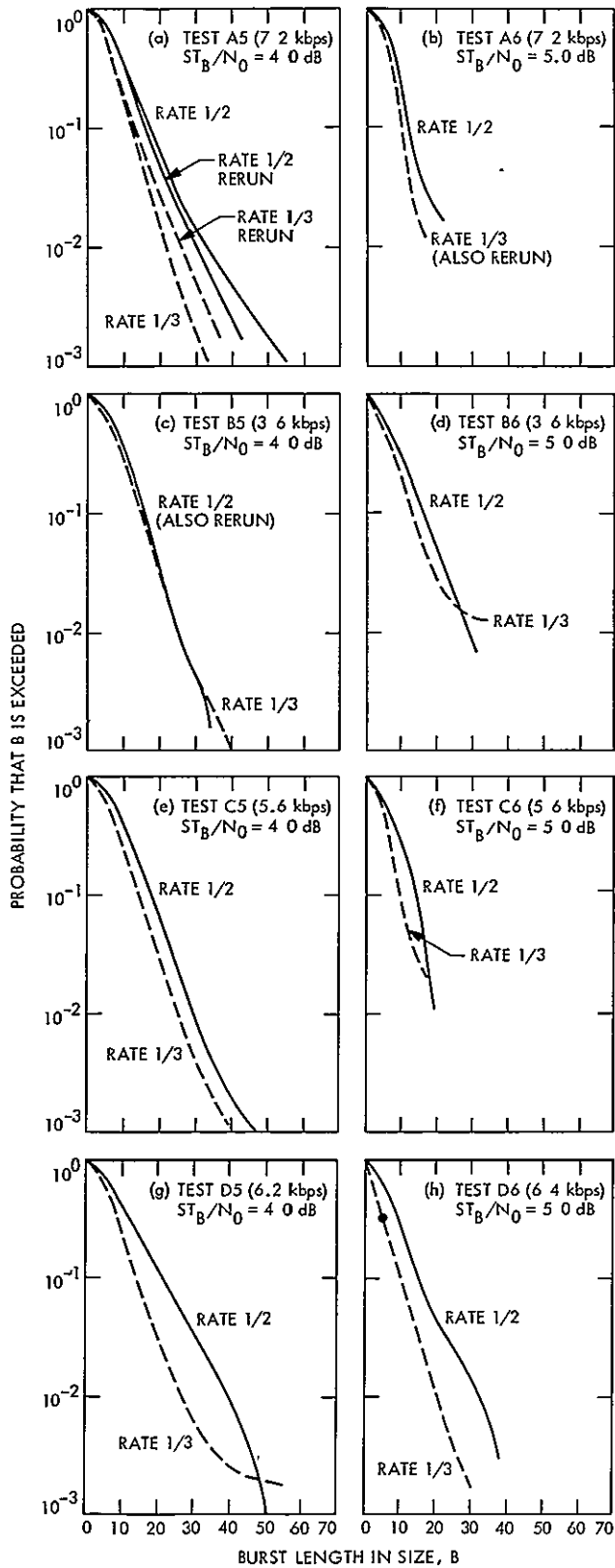
Fig. 5   Burst length size B vs probability that B is exceeded
of tests A5-D6 for code rates 7 ½ and ⅓
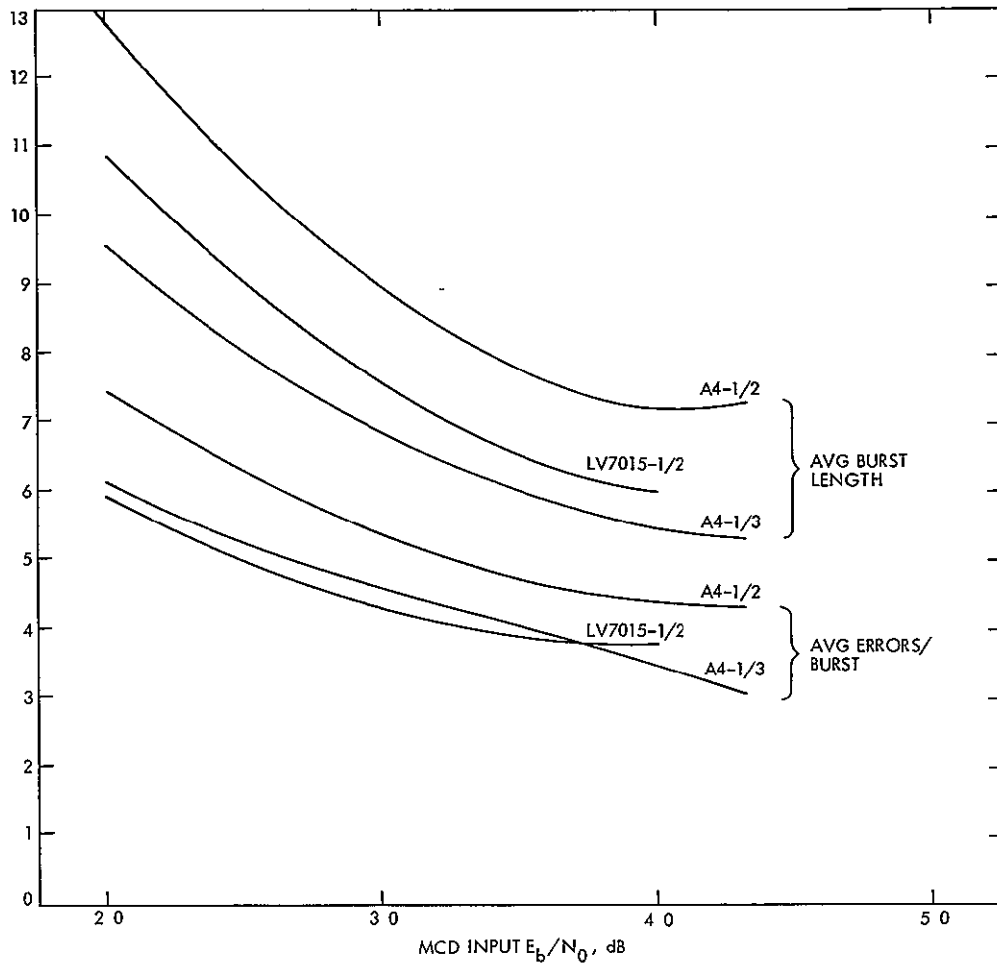
Fig. 6. Comparison of average burst length and average number of burst errors vs MCD input
E_b/N_0 for tests A4-½, A4-⅓, and LV7015-½

N78-24182

CCIR Papers on Telecommunications for Deep Space Research

N F de Groot

Telecommunication Systems Section

Three JPL papers on telecommunications for deep space research were recently adopted by Study Group 2 of the International Radio Consultative Committee (CCIR). In this article, we present a brief description of United States participation in the process of developing the technical basis for international allocation and regulation of the radio frequency spectrum. The first of the three papers is then presented in its CCIR format and style. The paper considers the telecommunication requirements for deep space research. Topics include functional requirements, methods and techniques, and equipment characteristics

In 1979 the United States will participate in a General World Administrative Radio Conference The conference will be held in Geneva under the auspices of the International Telecommunications Union (ITU), a specialized agency of the United Nations The purpose of the conference is to revise the international Radio Regulations that allocate and control the worldwide use of the radio frequency spectrum. The conclusions of the conference have treaty status and are subject to ratification by each participating nation The last major revision of the Radio Regulations occurred in 1959

Conference negotiations are based in large part on documents published by the International Radio Consultative Committee (CCIR), a part of ITU A 13-volume set of reports and recommendations is revised and published by the CCIR at approximately four-year intervals The several study groups of CCIR treat particular subjects such as propagation, broadcasting, mobile services, spectrum utilization, etc Study Group 2

deals with space research and radio astronomy The CCIR volumes are published after international discussion and approval, and thus provide an agreed-upon technical base for negotiating radio frequency allocations and regulations in consideration of social, economic and political factors

To assist the U S Department of State in the preparation for the 1979 conference, NASA is participating in CCIR work in a number of technical areas One of these is deep space research The Spectrum Engineering Group of the Jet Propulsion Laboratory is conducting studies and writing CCIR documents in connection with the allocation and protection of radio frequency bands used for deep space research These bands are shared with other services, within the United States and throughout the world

An objective of the radio regulations is the protection of radio services from harmful interference To continue and

enhance the protection of deep space research telecommunications, a rationale for band allocation must be developed and agreed upon by 150 nations in a one-country, one-vote environment

Three reports on deep space telecommunications, prepared within the Spectrum Engineering Group, were presented by the United States to the CCIR Study Group 2 Final Meeting held in Geneva during September 1977.

In Geneva, these reports were assigned to a working group with representatives from 7 countries After minor revision by the working group, the papers were recommended to the full Study Group 2 for approval. The reports were approved, and next will be presented to the CCIR Plenary Assembly Upon adoption by that body in mid-1978, they will be published as part of CCIR Volume 2, Space Research and Radio Astronomy

The three deep space papers are

(1) Doc   2/296   Telecommunication Requirements for Manned and Unmanned Deep Space Research

(2) Doc 2/269 Preferred Frequency Bands for Deep Space Research Using Manned and Unmanned Spacecraft

(3) Doc. 2/279 Protection Criteria and Sharing Considerations Relating to Deep Space Research.

The first of these papers is presented in this issue of the Deep Space Network Progress Report The other papers will appear in future issues Each paper will be reproduced in its original form to give to the reader a sense of the style and format of CCIR documents

WORKING GROUP 2-B

Draft New REPORT*
TELECOMMUNICATION REQUIREMENTS FOR MANNED
AND UNMANNED DEEP SPACE RESEARCH
(Question (AZ/2))

1.   Introduction

This report presents the characteristics of typical United States of America (U.S.) deep space research missions, the functional and performance requirements for telecommunications needed to conduct deep space research via spacecraft, and the technical methods and parameters of systems used in connection with such missions. [Edelson, 1972]

A set of deep space research missions considered probable during the 1977-2000 time period is shown in Table I.   (This set is part of a larger group being studied in the U.S.)

Considerations regarding preferred frequency bands for deep space research can be found in Doc. 2/269. Interference, protection criteria and sharing are discussed in Doc. 2/279.

2.   Telecommunication requirements

Deep space missions require highly reliable communication. As shown in Table I, this must be accomplished over long periods of time and great distances. The need for high e.i.r.p. and very sensitive receivers is a result of the large communication distance, as shown in Table I.

Table I.   Characteristics of potential U.S. missions

Mission	Launch Year	Duration (Years)	Maximum Communication Distance ($\times 10^6$ km)
Jupiter/Saturn Flyby	1977	4	2962
Venus Orbiter	1978	6	259
Lunar Polar Orbiter	1980	2	0.41
Jupiter Orbiter/Probe	1982	8	917
Saturn/Uranus Flyby	1982	7	3023
Venus Orbiter Imaging Radar	1983	2-1/2	260
Mars Polar Orbiter	1984	2-1/2	396
Dual Comet Flyby	1984	1-1/2	157
Jupiter Orbiter	1987	7-1/2	964
Mercury Orbiter	1988	5	259
Saturn Orbiter	1989	8	1580
Jupiter/Pluto Flyby	1990	7-1/2	4499
Asteroid Rendezvous	1991	2-1/2	528
Jupiter/Neptune	1992	7	4620

*This Report supersedes Report 536, which is therefore cancelled.

Continuous usage of deep space communication bands is a consequence of the several missions now in existence and others being planned. Figure 1 shows how the long duration of missions to the outer planets results in the requirement for communication capability with several deep space missions at any given time. Each spacecraft must have the capability for communication with at least one earth station at all times, particularly during mission critical times such as orbit correction maneuver, planetary flyby, orbit insertion, or emergencies such as equipment malfunction. Unplanned loss of communication may result in poor mission performance and even mission failure.

In addition, each mission may include more than one spacecraft, so that simultaneous communication with several space stations will be necessary. The U.S. Mars Orbiter/Lander (Viking) mission was designed for simultaneous operation of two Earth-to-space links and three space-to-Earth links, using a single earth station. Simultaneous coordinated communication between a space station and more than one earth station may also be required.

2.1 Telemetering requirements

Telemetering is used to transmit both maintenance and science information from deep space.

Maintenance telemetering information about the condition of the spacecraft must be received whenever needed to insure the safety of the spacecraft and success of the mission. This requires a weather independent telecommunications link of sufficient capacity. The propagation properties of the current 2 GHz allocation meet the requirement. Maintenance telemetering data rates are relatively low. For example, the Mariner Jupiter/Saturn (MJS) spacecraft to be launched in 1977 will have data rates of 40 and 1200 bits per second (bits/s).

Science telemetering involves the sending of data from measurements made by the onboard scientific instruments. The scientific data are of two types imaging (television-like), and non-imaging (general). For example, the imaging experiment on the U.S. 1975 Mars lander (Viking) consists of two facsimile cameras, non-imaging science experiments are biological, meteorological, seismological, molecular and mineral analysis. Data rates and acceptable error rates may be quite different for the two types of data.

Telemetering link capacity has steadily increased with the development of new equipment and techniques. This increase can be used in two ways (1) to gather larger amounts of scientific data about nearby planets, and (2) to permit missions to more distant planets. A figure of merit used to show telemetering capability is shown in Figure 2. The figure of merit is the product of telemetering data rate and the square of communication distance. It was calculated for four missions: Mariner Mars 1964, Mariner Mars 1969, Viking Orbiter 1975, and Mariner Jupiter/Saturn 1977. Each represents an important step in telemetering development. If the 1977 figure of merit is applied to the proposed 1983 Venus Orbiting Imaging Radar (VOIR) mission with a communication distance of 2.60×10^8 km, a data rate of 1.5 Mbits/s might be anticipated. The imaging radar experiment will need a rate of approximately 3 Mbits/s, so an improvement in figure of merit is required.

As imaging experiments become more sophisticated, even higher bit rates will be required. This is discussed in Section 4.6, including the effect on bandwidth. [Davies, 1971]

An important contribution to telemetering has been the development of coding methods that permit operation with a lower signal to noise ratio. [Forney, 1970] The coded signal requires a wider transmission bandwidth. The use of coded telemetering at very high data rates may be limited by allocation width.

2.2 Telecommand requirements

Reliability is the principal requirement of a telecommand link. Commands must be received accurately and when needed. For U.S. deep space missions the telecommand link is

required to have a bit error rate no greater than 1×10^{-5}. Commands must be received successfully, without regard to spacecraft orientation, even when the primary high gain antenna may not be pointed at Earth. For such circumstances, reception using a nearly omnidirectional spacecraft antenna is required. Very high e.i.r.p. is needed at earth stations because of low spacecraft antenna gain, and to provide high reliability.

With computers on the spacecraft, automatic sequencing and operation of spacecraft systems is largely predetermined and stored on-board for later execution. For some complicated sequences, automatic operation is a requirement. Telecommand capability is required for in-flight alteration of stored instructions, which may be needed to correct for observed variations or malfunctions of spacecraft behaviour. This is particularly true for missions of long duration, and for those circumstances where sequencing is dependent on the results of earlier spacecraft events. For example, the commands for spacecraft trajectory correction are based on tracking measurements and cannot be predetermined.

Command data rates have been as low as one bit per second, with an increase to a few kilobits per second expected in the future.

The telecommand link must be relatively free from weather effects. Reliable telecommand includes the need for weather-independent maintenance telemetering to verify if commands are correctly received and loaded into command memory. The 2 GHz allocations provide weather independence.

2.3 Tracking requirements

Tracking provides information used for spacecraft navigation and for radio science studies.

2.3.1 Navigation

The basic tracking measurements for navigation are radio-frequency Doppler shift and the round-trip propagation time of a ranging signal. The measurements must be made with a degree of precision that satisfies navigation requirements [Curkendall, 1970]. Table II lists accuracy specifications for the Viking Mars Orbiter/lander and Mariner Jupiter/Saturn (MJS) flyby missions. Future requirements for longer or more difficult missions require more accurate navigation and tracking [Melbourne, 1976].

Table II. Navigation and tracking accuracy specifications

Mission	Required Navigation Accuracy	Doppler Frequency Measurement Accuracy	Range Measurement Accuracy	Earth Station Location Estimate Accuracy
Viking Mars Orbiter/lander	300 km at Mars	±0.003 Hz	±20 m	±20 m
Mariner Jupiter/ Saturn Flyby	400 km at Jupiter	±0.001 Hz	±4 m	±2 m
	1300 km at Saturn	±0.001 Hz	±4 m	±2 m

2.3.2 Radio science

Spacecraft telecommunication links can also be important to studies of propagation, relativity, celestial mechanics, and gravity [Anderson, 1973][Hennes, 1972][Michael, 1972]. Amplitude, phase, frequency, polarization and delay measurements provide the needed information. The opportunity to make these measurements depends on the availability of appropriate allocations. Within the 2-20 GHz range, transmission delay and Faraday rotation (charged particle and magnetic field effects) decrease rapidly with increasing frequency, and thus are best studied with the lower frequencies. The higher frequencies provide relative freedom from these effects and are more suitable for studies of relativity, gravity and celestial mechanics. For these studies, calibration of charged particle effects at the lower frequencies is also needed.

Range measurements with an absolute accuracy of one or two centimetres are required for this fundamental scientific work. This ranging accuracy depends on wide band codes and the simultaneous use of multiple frequencies for charged particle calibration.

2.4 Requirements for manned deep space missions

Manned deep space missions beyond the moon have not yet been flown. The functional requirements of such a mission will be similar in kind to those for unmanned missions. The presence of human occupants in spacecraft will place additional requirements for reliability on the telemetering, telecommand and tracking functions. Given the necessary level of reliability, the significant difference between manned and unmanned missions will be the use of voice and television links for both Earth-to-space and space-to-Earth communication. From a telecommunication standpoint, the effect of this will be an expansion of transmission bandwidth in order to accommodate the video signals. Given the link performance to accomplish the required data transfer rates, telecommunications for manned and unmanned deep space research are similar enough in concept that separate discussion is generally not required.

3. Technical characteristics

3.1 Earth stations

Deep Space Network (DSN) earth station complexes are located at approximately 120 degree longitude intervals as shown in Table III. At each complex there is one 64 m diameter antenna, two or more 26 m antennae, high power transmitters with extremely precise-frequency control, sensitive phase-locked loop receivers, and associated equipment [Reid, 1973]. The DSN is interconnected via terrestrial communication lines and fixed satellite facilities to a control center in California, U.S.A

Table III. Location of DSN earth station complexes

Location	Latitude	Longitude	Height Above Mean Sea Level
Goldstone, Ca (USA)	$35^\circ 22'$ N	$115^\circ 51'$ W	1019 m (3343 ft)
Canberra, Australia	$35^\circ 28'$ S	$148^\circ 59'$ E	818 m (2684 ft)
Madrid, Spain	$40^\circ 26'$ N	$4^\circ 17'$ W	791 m (2595 ft)

Tables IV(a) through (d) list major characteristics of the earth stations. Tables IV(a) and (b) show current implementation; while I-V (c) and (d) show planned performance improvements and additions. For current 26 m stations, increase in antenna size to 34 m and the addition of 8 GHz receive capability is planned to be complete at one station in each complex by 1980. The 64 m antennae are expected to be increased to 70 m by 1984. Transmit capability near 15 GHz may be in operation by 1990.

The system noise temperatures listed in Table IV are for the specified conditions. The noise temperature varies with the operating mode, weather conditions and elevation angle. This variation must be included in performance and interference calculations. The noise contribution of the earth station receiver alone is shown in curve B of Figure 3. The curve is based on current U.S. experience in the 2 and 8 GHz bands and estimates of possible implementation at the higher frequencies.

3.2 Space stations

Spacecraft size and weight is limited by the payload capability of the launch vehicle The power of the space station transmitter and the size of the antenna are limited, in comparison with those parameters at earth stations. The noise temperature of the receiver is higher because a simple uncooled preamplifier is typically used.

The space station has a combined receiver-transmitter, called a transponder, that operates in one of two modes. In the turn-around (also called two-way) mode, the carrier signal received from an earth station is used to control the oscillator in a phase-locked signal loop. The frequency of this oscillator is then used to control the transmitter frequency of the transponder according to a fixed ratio. In the one-way mode, no signal is received from an earth station, and the transmitter frequency is controlled by a crystal oscillator.

In the two-way mode, the spacecraft transmitted frequency and phase is controlled very precisely because of the extreme accuracy and precision of the signal received from an earth station.

Table V lists major characteristics of space stations designed for the 1977 mission to Jupiter and Saturn.

The noise temperature of the space station receiver is shown by curve A in Figure 3. The curve is based on the noise temperature of the Helios spacecraft of the Federal Republic of Germany (600K at 2.3 GHz), and estimates of possible implementation at the higher frequencies.

At the present time, the power of the space station transmitter is limited by primary power available on the spacecraft, and not by transmitter technology, for the 2-20 GHz frequency range.

4. Deep space telecommunication methods

Telemetering and telecommand functions for deep space telecommunications are typically accomplished by transmission of phase modulated carriers [Viterbi, 1966]. Doppler tracking is done by phase coherent detection of the carrier. By adding a ranging signal to the modulation, the ranging function is performed. [Edelson, 1972][NASA, 1976].

4.1 Carrier tracking and Doppler measurement

As received on Earth, the frequency of a signal transmitted by the spacecraft is modified by the Doppler effect [Curkendall, 1970]. The means to measure the Doppler shift, and hence the velocity of the spacecraft with respect to the earth station, is provided by carrier phase tracking. Earth and space station receivers track the carrier signal with a phase-locked loop. In the two-way transponder mode, the frequency and phase in the space station phase-locked loop are used to develop one or more space-to-Earth frequencies. This provides signals to the earth station that are correlated with the Earth-to-space frequency, enabling precise Doppler measurement.

-6-
(Doc. 2/296-E)

Table IV (a). Current characteristics of earth stations with 26 meter antennae

Band (GHz)	Antenna Gain (dBi)	Antenna Beamwidth (deg)	Transmitter Power (dBW)	e.i.r.p. (dBW)	[1]Receiving System Noise Temperature (K)	[1]Receiving System Noise Spectral Density (dB(W/Hz))
2.1 Earth-to-space	53	0.368	43	96	-	-
2.3 Space-to-Earth	54	0.328	-	-	33	-213

[1]Clear weather, 30° elevation angle, diplex mode for simultaneous reception and transmission.

Table IV (b). Current characteristics of earth stations with 64 meter antennae

Band (GHz)	Antenna Gain (dBi)	Antenna Beamwidth (deg)	[3] Transmitter Power (dBW)	e.i.r.p. (dBW)	[2]Receiving System Noise Temperature (K)	[2]Receiving System Noise Spectral Density (dB(W/Hz))
2.1 Earth-to-space	61	0.146	50 / 56	111 / 117	-	-
2.3 Space-to-Earth	62	0.131	-	-	16	-217
8.4 Space-to-Earth	72	0.041	-	-	23	-215

[2]Clear weather, 30° elevation angle, receive only mode.
[3]+56 dBW transmitter power use during spacecraft emergencies only.

Table IV (c). Expected characteristics of earth stations including planned increase in antenna size from 26 m to 34 m.

Band (GHz)	Antenna Gain (dBi)	Antenna Beamwidth (deg)	Transmitter Power (dBW)	e.i.r.p. (dBW)	[2]Receiving System Noise Temperature (K)	[2]Receiving System Noise Spectral Density (dB(W/Hz))
2.1 Earth-to-space	55	0.292	43	98	-	-
2.3 Space-to-Earth	56	0.260			22	-215
7.2 Earth-to-space	66	0.082	43	109		
8.4 Space-to-Earth	67	0.073	-	-	25	-215
15 Example	72	0 041	To be determined	To be determined	35	-213
30 Example	76	0.026	To be determined	To be determined	To be determined	To be determined

[2]Clear weather, 30° elevation angle, receive only mode.

Table IV (d). Expected characteristics of earth stations including planned increase in antenna size from 64 m to 70 m

Band (GHz)	Antenna Gain (dBi)	Antenna Beamwidth (deg)	[3] Transmitter Power (dBW)	e.i.r.p (dBW)	[2]Receiving System Noise Temperature (K)	[2]Receiving System Noise Spectral Density (dB(W/Hz))
2.1 Earth-to-space	62	0.131	50 56	112 118	-	-
2.3 Space-to-Earth	63	0.116	-	-	16	-217
7.2 Earth-to-space	72	0.041	50 56	122 128	-	-
8.4 Space-to-Earth	73	0.037	-	-	23	-215
15 Example	76	0.026	To be determined	To be determined	33	-213
30 Example	73	0.037	To be determined	To be determined	To be determined	To be determined

[2]Clear weather, 30° elevation angle, receive only mode.
[3]+56 dBW transmitter power for use during spacecraft emergencies only.

Table V. Characteristics of 1977 U.S. space station design (MJS)

Space to Earth Band (GHz)	Antenna Size (m)	Antenna Gain (dBi)	Antenna Beamwidth (degrees)	Transmitter Power (dBW)	e.i.r.p (dBW)
2.3	3.7	37	2.3	13.6	51
8.4	3.7	48	0.64	13.2	61

Earth to Space Band (GHz)	Antenna Size (m)	Antenna Gain (dBi)	Beamwidth (degrees)	Receiver Noise Temperature (K)	Receiver Noise Spectral Density (dB(W/Hz))
2.1	3.7	36	2.6	1540	-197

In the one-way mode, the space-to-Earth frequencies are derived from the oscillator in the transponder, and the Doppler measurement is based on a priori knowledge of the oscillator frequency.

The carrier tracking process also provides the local oscillator signal used to convert the radio frequency to the receiver intermediate frequency.

4.2 Modulation and demodulation

The radio links use phase (angle) modulation of the radio frequency carrier. The baseband digital data signal is used to modulate a subcarrier, which in turn phase-modulates the radio frequency carrier. A square wave subcarrier is typically used for telemetering, for telecommand the subcarrier may be sinusoidal. The modulation index is adjusted to provide a desired ratio of residual carrier power to data sideband power. This ratio is selected to provide optimum carrier tracking and data detection in the receiver.

R.F. carrier and data subcarrier demodulation is accomplished by phase-locked loops. Data detection generally uses correlation and matched filter techniques.

Television and voice links for manned missions may use other modulation and demodulation techniques.

4.3 Coding

In a digital telecommunication link, error probability can be reduced if the information bandwidth is increased. Coding accomplishes this increase by translating data bits into a larger number of code symbols in a particular way. Some examples of coding types are block and convolutional codes [Forney, 1970][Lindsey, 1973]. After transmission, the original data are recovered by a decoding process that is matched to the code type. The performance advantage of coded transmission is related to the wider bandwidth, and can amount to 3.8 dB (convolutional coding as used on MJS, with a maximum bit error rate of 1 x 10^-3).

4.4 Multiplexing

Science and maintenance telemetering may be combined into a single digital data stream by time division multiplexing, or may be on separate subcarriers that are added to provide a composite modulating signal. A ranging signal may also be added in combination with telemetering or telecommand. The amplitude of the different data signals is adjusted to properly divide the transmitter power between the carrier and information sidebands.

4.5 Ranging

Ranging is performed from an earth station using the space station transponder in the two-way mode. Ranging modulation on the Earth-to-space signal is recovered in the transponder and used to modulate the space-to-Earth carrier. At the earth station, comparison of the transmitted and received ranging codes yields a transmission delay measurement proportional to range.

A fundamental limitation to ranging precision is the ability to measure time correlation between the transmitted and received codes. The system currently in use employs a highest code frequency of 0.5 MHz. The code period is 2 μs and resolution to 4 ns is readily achieved, assuming sufficient signal-to-noise ratio. This resolution is equivalent to 120 cm in two-way path length, or 60 cm in range. This meets the current navigation accuracy requirements of Table II.

For the 1 cm accuracy needed for future radio science experiments (Section 2.3.2), a code frequency of at least 30 MHz is required.

4.6 Link bandwidth

Earth-to-space and space-to-Earth bandwidths are governed by required telemetering data rates [Davies, 1971] and ranging precision [Couvillon, 1970]. By contrast, the telecommand spectrum width is relatively narrow as a result of the relatively low data rate.

To pass a periodic square modulation waveform with no more than 0.3 dB loss, the bandwidth must include the fifth harmonic of the modulating frequency. For the telemetering signal, the radio frequency bandwidth must be wide enough to pass the fifth harmonic of the subcarrier frequency plus the fifth harmonic of the clock rate (1/2 the bit rate). With present techniques, the subcarrier frequency must be high enough to provide 1-1/2 subcarrier cycles per data bit. The total bandwidth required is therefore

$$BW = 2 \left[(BR \times 1 \frac{1}{2} \times 5) + 5 \times \frac{1}{2} BR \right]$$

$$= 20 \ BR$$

where

$$BW = RF \ bandwidth$$

$$BR = bit \ rate$$

For example, a 1 Mbits/s uncoded data rate requires a 1.5 MHz subcarrier and 20 MHz RF bandwidth.

Figure 4 shows a curve representative of telemetering spectra.

As telemetering data rates increase, the need for a subcarrier to move the data sidebands away from the carrier tracking loop becomes less important. Direct modulation of the carrier may be used, requiring less bandwidth.

Increased telemetering data rates are expected in the future. For example, the surface imaging radar being developed to study the oceans of the Earth will gather data at 110 Mbits/s. When an instrument like this is used for study of other planets, the telemetering bandwidth required will be far beyond that available in current deep space allocations.

The current implementation of ranging uses square wave biphase modulation. The bandwidth required for the transmitted ranging signal is determined by the highest code frequency. The spectrum to the fifth harmonic is shown in Figure 5. A bandwidth equal to six times the

code frequency is usually considered acceptable. For some deep space missions, the maximum bandwidth requirement will be determined by ranging accuracy considerations. Transmission in relatively wideband allocations in the 10-20 GHz portion of the spectrum will be necessary to meet ranging accuracy required for radio science.

Link bandwidth requirements for deep space research are based on needed bit rates for the various functions shown in Table VI

Table VI.   Required bit rates for a deep space mission

Direction and Function	Link		
	Weather Independent	Normal	High Data Rate
Earth-to-space			
Telecommand (bit/s)	1-1000	1-1000	1-1000
Computer programming (kbit/s)	1-50	1-100	1-200
Voice (kbit/s)	45	45	45
Television (Mbit/s)	1-4	1-12	6-24
Ranging (Mbit/s)	1	10	100
Space-to-Earth			
Maintenance Telemetering (bit/s)	8-500	8-500	8-1000
Scientific data (kbit/s)	0.008-115	1-500	$50-10^4$
Voice (kbit/s)	45	45	45
Television (Mbit/s)	0.2-0 8	2-8	6-24
Ranging (Ranging (Mbit/s))	1	10	100

Table VII lists the bandwidth required for these bit rates, assuming the use of techniques to minimize the width of the transmitted spectrum.

Some deep-space missions use two or more spacecraft. Table VIII shows the total required bandwidth for expected deep-space missions.

4.7   Antenna gain and pointing

For the parabolic antennae typically used in space research, the maximum gain is limited by size and by the accuracy with which the surface approaches a true parabola [Ruze, 1966]. The latter limitation places a bound on the maximum frequency that may be effectively used with a particular antenna.

One factor in surface accuracy, common to both Earth and space station antennae, is manufacturing precision.

Table VII. Required bandwidths for deep-space missions

Direction and function	Link		
	Weather Independent	Normal	High Rate Data
Earth-to-space			
Channel bandwidth (MHz)	4	40	400
Telecommand (kHz)	1 to 5	1 to 5	1 to 5
Computer programming (kHz)	5 to 250	5 to 500	1 to 1000
Voice (kHz)	50 to 200	50 to 200	50 to 200
Video (MHz)	1 to 4	1 to 24	6 to 50
Ranging (MHz)	4	40	400
Space-to-Earth			
Channel bandwidth (MHz)	4	40	400
Maintenance telemetering (kHz)	1 to 5	1 to 5	1 to 10
Scientific data (kHz)	0.008 to 115	1 to 500	50 to 10^4
Voice (kHz)	50 to 200	50 to 200	50 to 200
Video (MHz)	0.2 - 0.8	2 - 8	6 - 24
Ranging (MHz)	4	40	400

Table VIII. Deep space research bandwidth requirements and frequency bands, current and planned

Period of use and type of link	Total required bandwidth MHz	Suitable space research frequency bands MHz
Weather independent 1970 ⟶	10	2,110 - 2,120 Earth-to-space
		2,290 - 2,300 Space-to-Earth
Normal 1970 ⟶	100	7,145 - 7,235 Earth-to-space
		8,400 - 8,500 Space-to-Earth
High rate data 1980 ⟶ (development starting in 1970s)	1,000	Various bands above 10,000

For earth station antennae, surface deformation is caused by wind and thermal effects. As elevation angle is varied, gravity introduces additional distortion of the surface.

For space station antennae, size is limited by space available in the launch vehicle, and by the state of the art in constructing unfurlable antennae. Thermal effects cause distortion in space station antenna surfaces.

The maximum usable gain of antennae is limited by the ability to point them accurately. The beamwidth must be adequate to allow for the angular uncertainty in pointing. All the factors that cause distortion of the reflector surface also affect pointing accuracy. The accuracy of the spacecraft attitude control system (often governed by the amount of propellant which can be carried) is a factor in space station antenna pointing.

The precision with which the location of the earth and space stations are known with respect to each other affects the minimum usable beamwidth and the maximum usable gain.

Table IX shows typical limits on antenna performance. Figure 6 shows the gain of the 64 m earth station antennae as a function of frequency and elevation angle.

Table IX. Current limitations on maximum antenna gain

Limiting Parameter	Space Station Antennae		Earth Station Antennae	
	Typical Minimum Value	Maximum Gain	Typical Minimum Value	Maximum Gain
Accuracy of Dish surface	0.024 cm rms on a 3.7 m diameter reflector	66 dB[1] at 100 GHz	0.12 cm rms on a 64 m diameter reflector	76 dB[1] at 20 GHz
Pointing Accuracy	±0.15° (3σ)	55 dB[2]	±0.016° (3σ)	75 dB[2]

[1] Gain at other frequencies will be lower.

[2] Gain of antenna with half power beam width equal to 2 x pointing accuracy (3σ). Beam of higher gain antenna will be too narrow.

4.8 Additional radionavigation techniques

Doppler and ranging measurements provide the basic tracking information needed for navigation. Additional techniques have been developed to enhance navigation accuracy.

4.8.1 Calibration of the velocity of propagation as affected by charged particles

Range and Doppler measurements are influenced by variations in the velocity of radio wave propagation caused by free electrons along the transmission path. The electrons exist in varying densities in space and in planetary atmospheres, and are particularly dense near the Sun. Unless accounted for, these variations in propagation velocity can introduce errors in navigation calculations.

The charged particles cause an increase in phase velocity and a decrease in group velocity. By comparing range change with integrated Doppler over a period of time, the charged particle effect may be determined. The effect on propagation velocity is inversely proportional to the square of the radio frequency. This frequency dependence may be used for additional calibration accuracy. Turnaround ranging and Doppler tracking can be performed with simultaneous space-to-Earth signals in two or more separate bands. The charged particle effects in the separate bands are different in magnitude, and this difference is used to improve the calibration.

The charged particle effect is discussed in Doc. 2/168.

4.8.2 Very long baseline interferometry (VLBI)

Accuracy of spacecraft navigation depends on the precise knowledge of earth station location with respect to the navigation coordinate system. A 3 metre error in the assumed station location can result in a 700 kilometre error in the calculated position of a spacecraft at Saturn distance. VLBI provides a means of improving the estimate of station location by using a celestial radio source (quasar) as a signal source at an essentially unchanging point on the celestial sphere [Rogers, 1970]. It is possible to record the quasar signals in such a way as to determine the difference in time of reception at two widely separated stations with great accuracy. Using a number of measurements the station locations can be determined to a relative accuracy of 50 cm. Frequencies near 2 and 8 GHz are used for VLBI at the present time.

The VLBI technique is also used to measure directly the spacecraft declination angle. Two accurately located earth stations separated by a large north-south distance measure the range to the spacecraft. The declination can then be calculated with great precision.

A third application of the VLBI method can be used to improve the accuracy of measurement of spacecraft angular position [Reid, 1973]. Two earth stations alternately observe a spacecraft signal and a quasar signal. By knowing time, station location, and the effect of Earth rotation on the received signals, the angular position of the spacecraft can be determined with respect to the celestial references. When fully developed the techniques will provide a significant improvement over the current accuracy of 0.01 arcseconds. The improved accuracy will permit more precise navigation [Swenson, 1968].

5. Performance analysis and design margins

Table X shows a link budget used for performance analysis. The example given is for high rate telemetering from Jupiter. Similar analysis for telecommand and ranging is done during mission planning. The earth and space station characteristics shown earlier are used as the basis for calculating a performance margin for each telecommunication function.

A most important point in the design of deep space missions is that the telemetering performance margin is quite small (3.5 dB in the example given). This small margin is a consequence of the need to obtain maximum scientific value from each spacecraft. To design with a 10 dB larger margin of safety would reduce the quantity of telemetered data by a factor of 10. The risk of using a system with small performance margin is its susceptibility to harmful interference, and for bands above 2 GHz, decreased reliability caused by weather effects.

Table X.   Performance budget. Spacecraft-to-Earth from Jupiter

Mission: Mariner Jupiter/Saturn 1977
Mode: Telemetering, 115.2 kbits/s, coded, 8.45 GHz carrier

Transmitter Parameters
RF power, dBW (21W) 13.2
Circuit loss, dB ..... -0.2
Antenna gain, dBi (3.7m) 48.1
Pointing loss, dB ..... -0 2

Path Parameters
Free space loss between isotropic antennae, dB ..... -290.4
8.45 GHz, 9.3 x 10^8 km

Receiver Parameters
Antenna gain, dBi (64m, 30° elev angle) 72.0
Pointing loss, dB ..... -0.3
Weather attenuation, dB ..... -0.1
System noise spectral density, dBW/Hz (22.6K) ..... -215.1

Total Power Summary
Link loss, dB ..... -171.1
Received power, P(T), dBW ..... -157.9

Carrier Tracking Performance (two-way)
Carrier power/total power, dB ..... -15.4
Received carrier power, dBW ..... -173.3
Carrier threshold noise bandwidth, dB (10 Hz) 10.0
Noise power, dBW ..... -205.1
Threshold signal/noise, dB 20
Threshold carrier power, dBW ..... -185.1
Performance margin, dB 11.8

Data Detection Performance
Data power/total power, dB ..... -0.3
Data reception and detection losses, dB ..... -0.5
Received data power, dBW ..... -158.7
Noise bandwidth, dB (Effective noise bandwidth for matched
   filter detection of 115.2 kbits/s data) 50.6
Noise power, dBW ..... -164.5
Threshold SNR, dB (0.005 bit error rate) 2.3
Threshold data power, dBW ..... -162.2
Performance margin, dB 3.5

Bibliography

Anderson, J. D. [1973] Lectures on Physical and Technical Problems Posed by Precision Radio Tracking; Experimental Gravitation, Academic Press Inc., NY., NY., 163-199.

Couvillon, L.A., et al, [September 1970] Communicating with Outer-Planet Spacecraft, Astronautics and Aeronautics, Vol. 8, No. 9, 62-68.

Curkendall, D.W. and Stephensen, R. R. [May, 1970] Earthbased Tracking and Orbit Determination - Backbone of the Planetary Navigation System, Astronautics and Aeronautics, Vol. 8, No. 5, 30-36.

Davies, M. E. and Murray, B.C. [1971]. The View From Space. Columbia University Press, New York.

Edelson, R.E. [July, 1972] Telecommunications Systems Design Techniques Handbook Technical Memorandum 33-571, Jet Propulsion Laboratory.

Forney, G.D. Jr. [June, 1970] Coding and Its Application in Space Communications; IEEE Spectrum, 47-58.

Hennes, J.P. and Fulmer, C.V. [March, 1972] Identifying Relevant Scientific Goals in Planetary Exploration, Journal of Spacecraft and Rockets, Vol. 9, No. 3, 205-213.

Lindsey, W.C. and Simon, M.K. [1973] Telecommunication Systems Engineering, Prentice Hall Inc., Englewood Cliffs, New Jersey.

Mac Doran, P.F. [1970] A First Principles Deviation of the Differential Range Versus Integrated Doppler (DRVID) Charged-Particle Calibration Method. Space Programs Summary 37-62, Vol. II The Deep Space Network, pp 28-34, Jet Propulsion Laboratory, March 31, 1970.

Melbourne, W. G. [1976] Navigation Between the Planets. Scientific American, Vol. 234, No. 6, 58-74.

Michael, W.H. Jr. et al, [February, 1972] Radio Science Experiments, the Viking Mars Orbiter and Lander, Icarus, Vol. 16, No. 1, 57-73, Academic Press, NY., NY.

NASA [1976] A Forecast of Space Technology 1980-2000, Scientific and Technical Information Office, National Aeronautics and Space Administration, Washington, D.C. 20546.

Reid, M.S., Clauss, R.C., Bathker, D.A. and Stelzreid, C.T. [Sept. 1973] Low-Noise Microwave Receiving Systems in a Worldwide Network of Large Antennas, Proceedings of IEEE, Vol. 61, No. 9, 11. 1330-1335.

Rogers, A.E.E., "Very Long Baseline Interferometry With Large Effective Bandwidth for Phase-Delay Measurements," Radio Sci., Vol. 5, No. 10, pp. 1239-1248, October 1970.

Ruze, J. [1966] Antenna Tolerance Theory - A Review Proc. IEEE, Vol. 54, 4, 633-640.

Swenson, G.W., and Mathur, N.C., "The Interferometer in Radio Astronomy," Proc. IEEE, Vol. 56, p. 2114, 1968.

Viterbi, A.J. [1966] Principles of Coherent Communications, McGraw Hill, New York.

Key Words

Deep space research
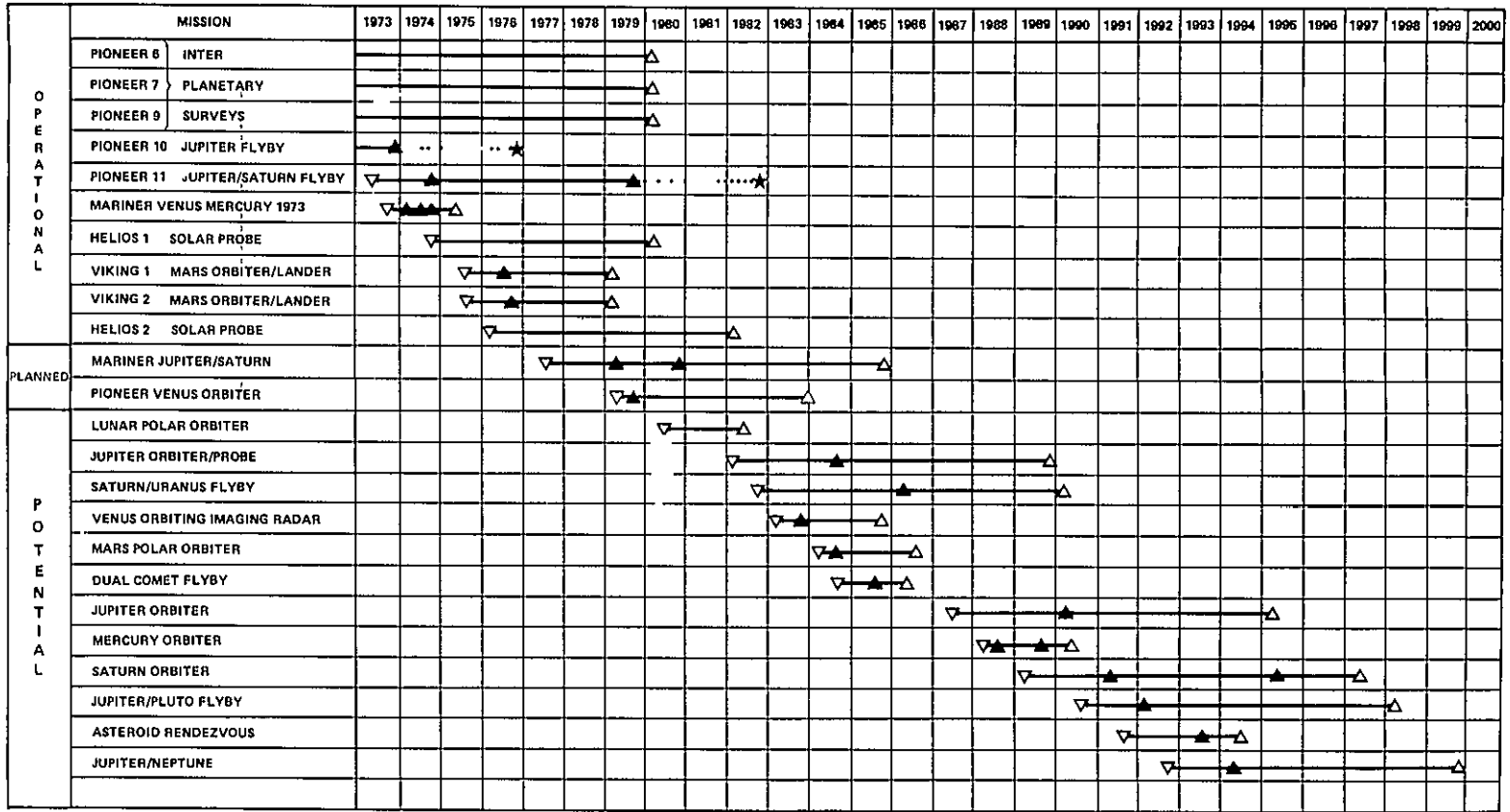
Telecommunications

Telemetering

Telecommand

Tracking

Equipment

Requirements

Characteristics

Missions

Radio science

	MISSION	1973	1974	1975	1976	1977	1978	1979	1980	1981	1982	1983	1984	1985	1986	1987	1988	1989	1990	1991	1992	1993	1994	1995	1996	1997	1998	1999	2000
O P E R A T I O N A L	PIONEER 6 — INTER							△																					
	PIONEER 7 — PLANETARY							△																					
	PIONEER 9 — SURVEYS							△																					
	PIONEER 10 — JUPITER FLYBY	▲		✶																									
	PIONEER 11 — JUPITER/SATURN FLYBY	▽	▲					▲			✶																		
	MARINER VENUS MERCURY 1973	▽▲▲▲△																											
	HELIOS 1 — SOLAR PROBE		▽					△																					
	VIKING 1 — MARS ORBITER/LANDER			▽	▲			△																					
	VIKING 2 — MARS ORBITER/LANDER			▽	▲			△																					
	HELIOS 2 — SOLAR PROBE				▽				△																				
PLANNED	MARINER JUPITER/SATURN					▽		▲		▲			△																
	PIONEER VENUS ORBITER							▽▲				△																	
P O T E N T I A L	LUNAR POLAR ORBITER								▽	△																			
	JUPITER ORBITER/PROBE								▽			▲			△														
	SATURN/URANUS FLYBY								▽				▲		△														
	VENUS ORBITING IMAGING RADAR									▽▲		△																	
	MARS POLAR ORBITER										▽▲		△																
	DUAL COMET FLYBY										▽	▲	△																
	JUPITER ORBITER															▽		▲			△								
	MERCURY ORBITER																▽▲	▲	△										
	SATURN ORBITER																	▽		▲			▲		△				
	JUPITER/PLUTO FLYBY																		▽	▲					△				
	ASTEROID RENDEZVOUS																			▽		▲	△						
	JUPITER/NEPTUNE																				▽		▲						△

FIGURE 1

Duration of U S deep space missions

▽ = Launch Date
▲ = Arrival Date
△ = End of Data Date
✶ = End of Mission Not Known

-17-

-18-
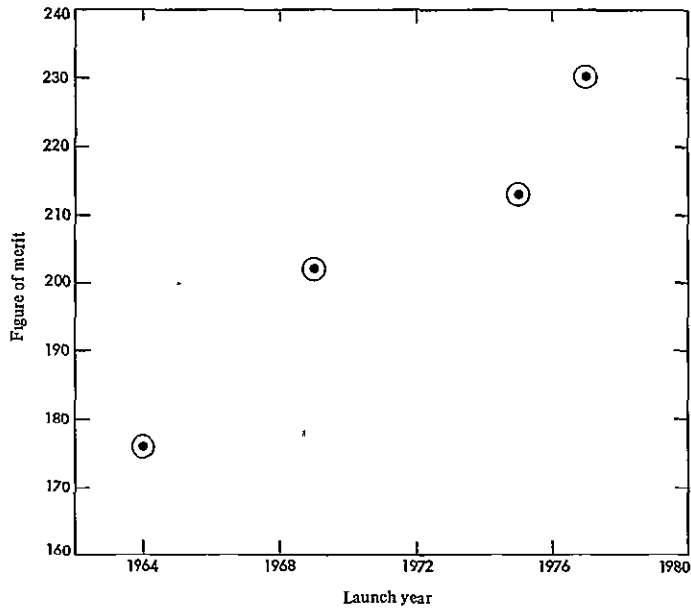

FIGURE 2

Telemetering figure of merit vs launch year

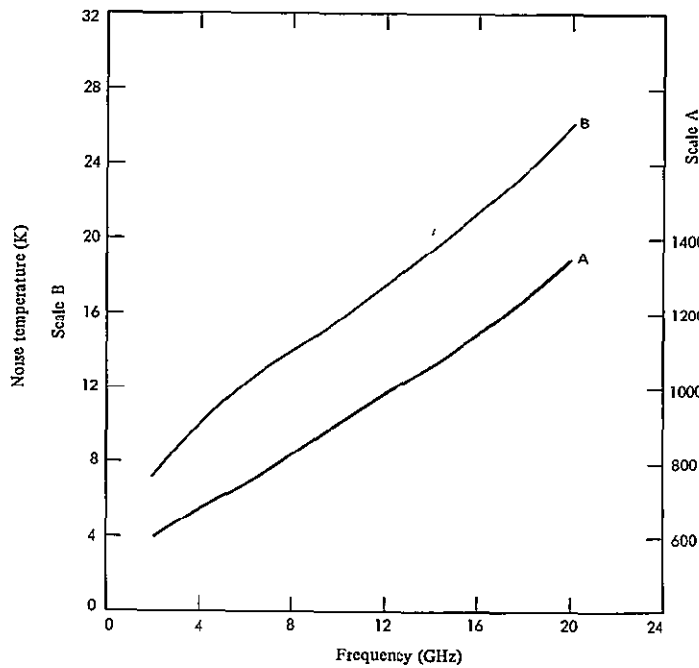figure of merit = $10 \log_{10}$ (data rate x distance^2)

FIGURE 3

*Noise temperature of receiving equipment
including antenna losses*
A space station   B earth station
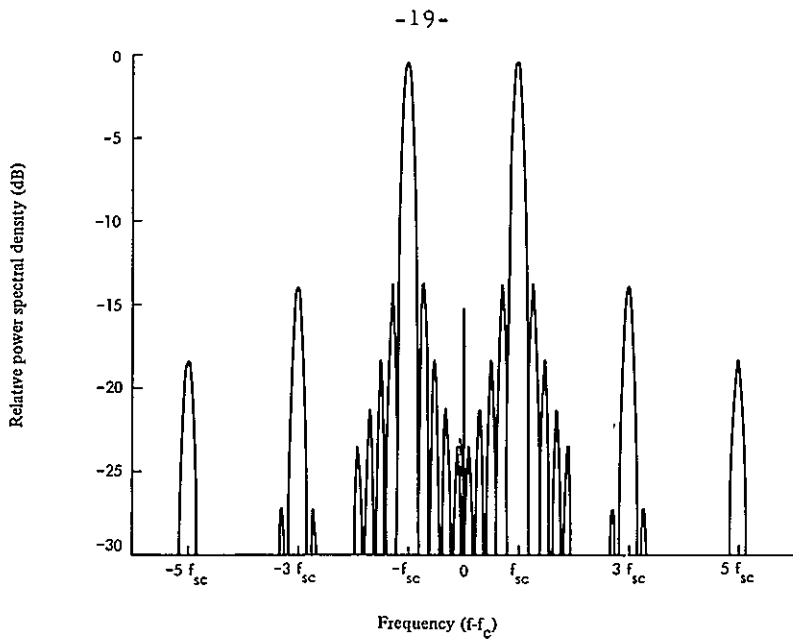
FIGURE 4

Telemetering power density spectrum (Space to-Earth)

f Frequency
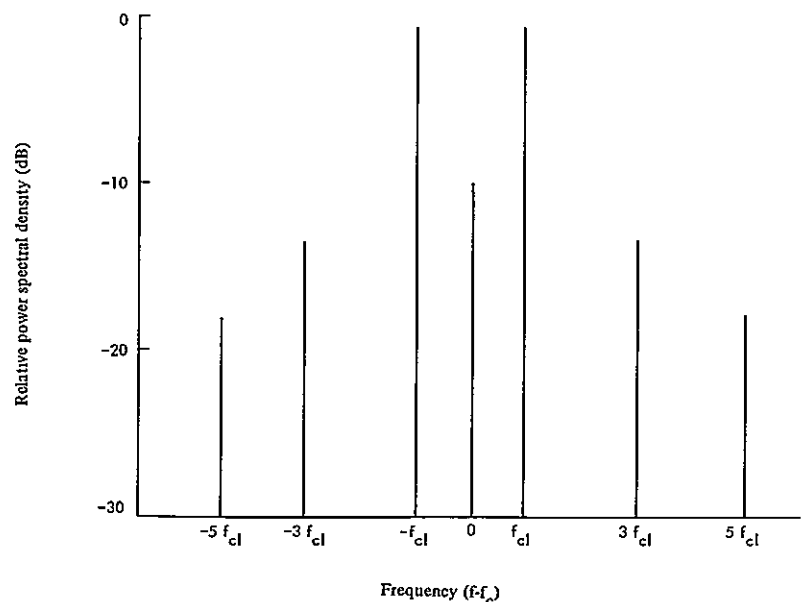f_c Carrier frequency
f_{sc} Subcarrier frequency

FIGURE 5

Ranging Power density spectrum (Earth to-Space)

f Frequency
f_c Carrier frequency
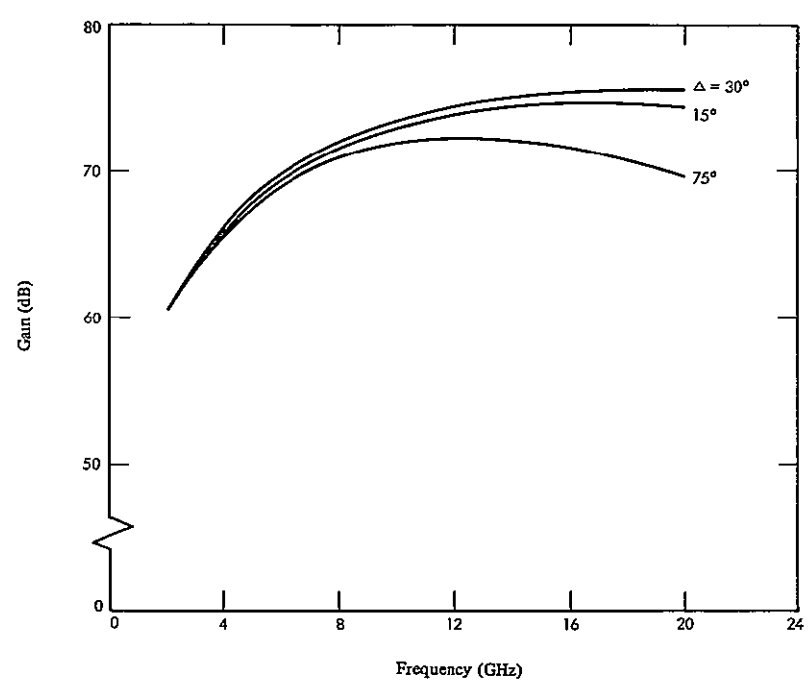f_{cl} Ranging clock frequency

-20-

FIGURE 6

Gain of 64m earth station antenna

Δ = elevation angle of earth station antenna

N78-24183

Dual Coupler Configuration at DSS 14 for the Voyager Era

T. Y Otoshi, K B. Wallace, and R B Lyon

Radio Frequency and Microwave Subsystems Section

This article describes the dual coupler configuration which was recently installed at DSS 14 for station delay calibrations during the Voyager era The Z-correction values determined for this new and previous configurations are presented.

I. Introduction

During the antenna down time at DSS 14 (April-June 1977), a new S-band WR430 waveguide coupler was installed near the input to the S-Band Polarization Diversity (SPD) feed as shown in Fig 1 This waveguide coupler, referred to as the "dual coupler," samples the uplink S-band signal and injects the translated downlink S-band signal on opposite walls of the WR430 waveguide coupler at basically the same point in the system The dual coupler is used with the Block 4 translator for purposes of station delay calibrations Each coupling arm of the dual coupler is a compact loop coupler assembly (actual length less than 5 cm) and has a coupling value of 54 dB and 25 dB minimum directivity The dual coupler is water-cooled and able to pass 400 kW of CW power without arcing [1]

There are several advantages to this new configuration One main advantage is that the sampling-injection points are both close to the feed horn (see Fig 1), so the same S-band Z-corrections (Ref 1) apply whether you are using the SPD maser, Mod III maser, or the maser bypass mode This reduces calibration measurements and bookkeeping problems by a factor of three The second main advantage is that the diplexer and MTF filter delays no longer have to be precalibrated as was done in Ref 2. Accuracy is improved because measure-

ment errors of the diplexer and filter delays are eliminated It is no longer necessary to assume that these component delays are frequency insensitive or stable with time, or that they are the same at all stations The third advantage is that for this new dual coupler location near the feed horn, there are almost no WR430 waveguide delays that need to be calculated This configuration currently appears to be the best compromise between having most of the desirable features of a dish-mounted zero delay device (ZDD) such as on 26-m antennas, and yet not having the undesirable features such as 64-m antenna multipath errors

As discussed in Ref 1, Z-corrections are necessary for correcting the measured ground station delays and referring them to the DSS reference location This information is needed for determining the true range to the spacecraft The new Z-corrections for this new configuration were determined from the same basic equation derived in Ref 1 for the Block 4 Translator Method This equation is

$$Z = \tau_{XLTR} - \sum_{i=3}^{6} \tau_i \qquad (1)$$

where τ_{XLTR} is the delay of the translator path between the uplink sampling point and the downlink injection point The

---

[1] The dual coupler is discussed elsewhere in this volume by K Wallace

term τ_3 is the microwave delay from the uplink sampling point to the transmit horn phase center, and τ_4 is the microwave delay from the receive horn phase center to the downlink injection point The terms τ_5 and τ_6 are, respectively, the uplink and downlink airpath delays from the horn phase centers to the DSS reference location via the convoluted Cassegrain antenna optics paths. These terms are defined more clearly and precisely in Ref 1 The purpose of this article is to document the Z-correction determination method, the measured translator path delay values, and theoretical constants which will be useful for future reference and comparison purposes

II. Translator Path Delay Measurement

As may be seen in Eq. (1), one of the terms needed to determine the Z-correction is the translator path delay τ_{XLTR}. This term includes the delays of the Level Set Attenuator Assembly, Block 4 Translator Assembly, Test Signal Control Assembly, and interconnecting cables Because of the complexity of this path, this delay is measured rather than calculated The translator path for the dual coupler configuration is basically the same as before (Ref 3) except for the new locations of the sampling-injection points, which are now ports on the dual coupler near the feed horn (See Fig 1) Due to new interconnecting cables that were installed for this new configuration, the translator path delay needed recalibration The measurement procedure for its calibration is identical to that described previously (Ref 3) with the exception that the sampling-injection points are different.

As described in Ref 3, a portable zero delay device and its cables are substituted for the Block 4 translator path, and the range delay D_{ZDD} is measured Then the ZDD cables are inserted in series with the Block 4 translator path, and the range delay is again measured and denoted as D'_{XLTR} The measured translator delay is calculated from

$$(\tau_{XLTR})_m = D'_{XLTR} - D_{ZDD} + \tau_{ZDD} \qquad (2)$$

where τ_{ZDD} is the delay of the portable ZDD without its external cables This value of τ_{ZDD} is known and had been precisely precalibrated in the laboratory Equation (2) results in a measured value of the translator path between coaxial connection points to which the ZDD cables can be conveniently connected However, the actual translator path must be defined internal to the waveguide system to points common to the "range on spacecraft path" Therefore small corrections need to be applied to measured values for the additional lengths of coax to waveguide paths involved The true translator path delay is determined from the expression

$$\tau_{XLTR} = (\tau_{XLTR})_m + \tau_{WG,up} + \tau_{WG,down} \qquad (3)$$

The term $\tau_{WG,up}$ is a small correction term needed to go from the actual measurement uplink sampling point to the same point to where τ_3 is defined The term $\tau_{WG,down}$ is a small correction term needed to go from the actual measurement downlink sampling point to the same point where τ_4 is defined.

Because the sampling-injection points are now located at the same plane for the dual coupler, the terms τ_3, τ_4, and τ_{XLTR} have a convenient common reference plane. This reference plane is the WR430 flange on the "dual coupler" assembly, which is connected to port K of the WR430 waveguide switch SW3 shown in Figs 2 and 3 For the X-band downlink path, τ_4 and τ_{XLTR} are defined up to the midpoint of the X-band waveguide coupler installed directly in front of the X-band receive only (XRO) maser. For X-band the last coaxial connection point is the input to the XRO noise box, and the correction term $\tau_{WG,down}$ is the additional delay of the waveguide run through the XRO noise box assembly to the midpoint of the X-band waveguide coupler

The translator delays measured at DSS 14 during July-August 1977 are shown in Table 1 There were more scatter and cyclic variations (±3 ns peak) in the measured translator path delays than were observed in the past. It is not clear whether this was due to a measurement problem (leakage in the ZDD cables or bad connectors) or due to an actual system leakage problem Averaging the data at each channel over several test periods showed that the delay of the translator was essentially the same for Channels 9, 14, 18, and 22 Therefore an overall average was taken of the data to provide a best nominal value for the Voyager and Viking missions

The corrected translator path delay values as well as values of $\tau_{WG,up}$ and $\tau_{WG,down}$ are tabulated in Table 2 For comparison purposes, the τ_{XLTR} values of the previous DSS 14 translator path delays are also shown

III. Determinations of Theoretical Delays

As may be seen in Eq (1), the Z-correction requires not only knowledge of τ_{XLTR} but also of $\tau_3, \tau_4, \tau_5,$ and τ_6 In contrast to determination of τ_{XLTR}, which is a measured value, the τ_3 . , τ_6 are theoretical delays[2] calculated from physical dimensions and theoretical group velocities These calculated delays are assumed to be constant with time and constant over the bandwidths of interest

---

[2] In the previous configurations at DSS 14, some of the component delays of τ_3 and τ_4 had to be determined through measurements (Ref 2)

The values of the individual component delays of τ_3 and τ_4 are shown tabulated in Figs 2 and 3 for S-band. Some of these component delay values have been recalculated using computer programs and are slightly different from those reported previously in internal JPL reports However, with the exception of the feed horn delays, the differences are small The major changes in τ_3 and τ_4 for S-band are due to the new locations of the sampling-injection points

The values of τ_5 and τ_6, which are theoretical airpath delays, did not change for the S-band uplink and downlink airpaths For the X-band system, installation of new components in the XRO feed assembly has caused changes in the downlink values of τ_4 and τ_6 for X-band These changes have been pointed out by Buchanan (Ref 4), and individual component delays of τ_4 were recomputed and tabulated as shown in Table 3

IV. Z-Corrections

The final Z-corrections for the new dual coupler configurations are computed and shown in Table 4 For comparison purposes, the old values are also shown It can be seen that the

major differences in the old and new Z-corrections are in the τ_3 and τ_4 values due to the new locations of the sampling-injection points As shown in Table 4, the new Z-corrections for DSS 14 are currently

$$Z_s = [-38\ 83 \pm 0\ 99\ (1\sigma)]\ \text{ns}$$

$$Z_x = [-48.67 \pm 0\ 94\ (1\sigma)]\ \text{ns}$$

The 1σ errors shown for the Z-corrections are estimates based on translator delay measurement standard deviations, tolerances on the delay of the portable ZDD used as the calibration standard, and also tolerances on the theoretical τ_3, , τ_6 delay values These individual error sources and estimated error contributions are shown in Table 5. The lists of error sources do not include waveform distortion. This is presently a source of error that has not been investigated by this author, and the effects on calibration accuracy are not presently known. The methods described by Komarek (Ref. 5), however, have been applied to correct and minimize possible waveform distortion errors.

Acknowledgements

References

1 Komarek, T, and Otoshi, T., "Terminology of Ranging Measurements and DSS Calibrations," in the *Deep Space Network Progress Report 42-36*, pp 35-40, Jet Propulsion Laboratory, Pasadena, Ca , Dec 15, 1976

2 Lay, R , "Phase and Group Delay of S-Band Megawatt Cassegrain Diplexer and S-Band Megawatt Filter," in the *Deep Space Network Progress Report 42-37*, pp 198-203, Feb 15, 1977

3. Otoshi, T Y., Batelaan, P D., Wallace, K B , and Ibanez, F , "Calibration of Block 4 Translator Path Delays at DSS 14 and CTA 21," in the *Deep Space Network Progress Report 42-37*, pp 188-197, Feb 15, 1977.

4 Buchanan, H , private communication.

5. Komarek, T , private communication.

Table 1. Measured translator path delays via dual coupler configuration

	(S,S) translator path				
Channel	Using new portable ZDD			Using crystal mixer ZDD	Average at each channel, ns
	Jul 17, 1977, ns	Aug 8, 1977, ns	Aug 9, 1977, ns	Aug 9, 1977, ns	
9	203.4	212.8	$\begin{bmatrix} 210.1 \\ 203.6 \end{bmatrix}$	203.5	206.68 ± 1.99 (1σ)
14	208.2	209.0	208.2	205.0	207.60 ± 1.77 (1σ)
18	202.0	209.1	205.9	$\begin{bmatrix} 211.7 \\ 210.7 \end{bmatrix}$	207.88 ± 1.77 (1σ)
22	207.6	206.4	202.3	211.3	206.90 ± 1.85 (1σ)
Avg.	205.3	209.3	206.0	208.4	

Overall average of $\left(\tau_{XLTR,S}\right)_m = [207.3 \pm 0.80\ (1\sigma)]$ ns

	(S,X) translator path			
Channel	Using new portable ZDD			Average at each channel, ns
	Jul 17, 1977, ns	Aug 8, 1977, ns	Aug 9, 1977, ns	
9	172.7	168.6	168.0	169 77 ± 1 47 (1σ)
14	169.6	168.4	172.2	170.07 ± 1 12 (1σ)
18	171.2	167.5	$\begin{bmatrix} 169.0 \\ 167.0 \end{bmatrix}$	168 68 ± 1 89 (1σ)
22	162.2	167.9	164.5	164.87 ± 1.66 (1σ)
Avg.	168.9	168.1	168.1	

Overall average of $\left(\tau_{XLTR,X}\right)_m = [168.4 \pm 0\ 80\ (1\sigma)]$ ns

Table 2. Comparisons of old and new translator path delays at DSS 14

Config [a]	$(\tau_{XLTR})_m$, ns	$\tau_{WG,up}$, ns	$\tau_{WG,down}$, ns	τ_{XLTR}, ns
(S,S) translator path				
Old config Viking era Ch 17	187 78	0 0	2 46	190 24
New config Voyager era Ch 9 → 22	207 3 (from Table 1)	0 42	0.41	208 13
(S,X) translator path				
Old config Viking era Ch 17	177 04	0 0	6 01	183 05
New config Voyager era Ch 9 → 22	168 4 (from Table 1)	0 42	6 01	174 83

[a]Old configuration data applicable from Dec 17, 1975 to April 1977
New configuration data applicable from June 1977 to present

Table 3. Group delay of XRO cone feed assembly with RCP/LCP select feature

Feed part	Length, cm (in)	λ_{co}, cm (in)	ns/cm (in)	τ_g, ns [a]
Horn	*	*		2 07
#1 rotary joint	10 160 (4 000)	5 933 (2 336)	0.04169 (0 1059)	0 4236
#2 rotary joint	10 160 (4 000)	5 933 (2 336)	0 04169 (0 1059)	0 4236
Polarizer	10 452 (4 115)	5 761 (avg) (2 268)	0 04244 (0 1078)	0 4436
Cosine taper	12 700 (5 000)	6 142 (2 418)	0 04094 (0 1040)	0 5200
W G switch	8 484 (3.340)	6 350 (2 500)	0 04028 (0 1023)	0 3417
W G elbow	13.970 (5 500)	6 350 (2 500)	0 04028 (0 1023)	0 5627
Adaptor	1 097 (0 432)	6 015 (2 368)	0 04138 (0 1051)	0 0454
New W G spacer	6 020 (2 370)	5 933 (2 336)	0 04169 (0 1059)	0 2510
WR112 to mid-point of coupler	6 033 (2 375)	5 700 (2 244)	0 04272 (0 1085)	0 2577

Total delay = 5 3393

[a]Calculated at 8420 MHz Data obtained from internal JPL report by H Buchanan

Table 4. Comparisons of old and new theoretical constants and Z-corrections for DSS 14

(S,S) translations

Configuration	$\tau_{XLTR,S}$, ns	Waveguide[a]		Airpath		$\sum_{3}^{6} \tau_i$, ns	Z_S, ns
		τ_3, ns	$\tau_{4,S}$, ns	τ_5, ns	$\tau_{6,S}$, ns		
Old config Viking era Ch 17	190.24 (from Table 2)	62 32	45 88	102.56	102 56	313 32	−123 08
New config Voyager era Ch 9 → 22	208.13 (from Table 2)	22 18	19.66	102 56	102 56	246 96	−38 83
Difference	−17 89	40 14	26 22	0 00	0.00	66.36	−84.25

(S,X) translations

Configuration	$\tau_{XLTR,X}$, ns	Waveguide[b]		Airpath		$\sum_{3}^{6} \tau_i$, ns	Z_X, ns
		τ_3, ns	$\tau_{4,X}$, ns	τ_5, ns	$\tau_{6,X}$, ns		
Old config Viking era Ch 17	183 05 (from Table 2)	62 32	6 08	102 56	93 62	264 58	−81 53
New config. Voyager era Ch 9 → 22	174.83 (from Table 2)	22 18	5 34	102 56	93 42[c]	223 50	−48.67
Difference	8 22	40 14	0.74	0 00	0.20	41.08	−32 86

[a]New values of τ_3 and $\tau_{4,S}$ calculated in Figs 2 and 3.

[b]New value of $\tau_{4,X}$ given in Table 3

[c]New value of $\tau_{6,X}$ shortened by 0 2 ns per H Buchanan (Ref 4).

Table 5. Estimated error contributions for Z-corrections for dual coupler configuration

Parameter	S-band (1σ) tolerances, ns	X-band (1σ) tolerances, ns
$\tau_3 + \tau_4$ values	±0.5	±0 4
τ_{ZDD}	±0 2	±0 2
$\tau_5 + \tau_6$	±0 2	±0 2
$\tau_{WG,up} + \tau_{WG,down}$	±0.1	±0 1
Measurement scatter on τ_{XLTR}	±0.80 (see Table 1)	±0 80 (see Table 1)

Total error = $\sqrt{[\Sigma \sigma^2]}$

= 0.99 ns for S-band Z-correction

= 0 94 ns for X-band Z-correction
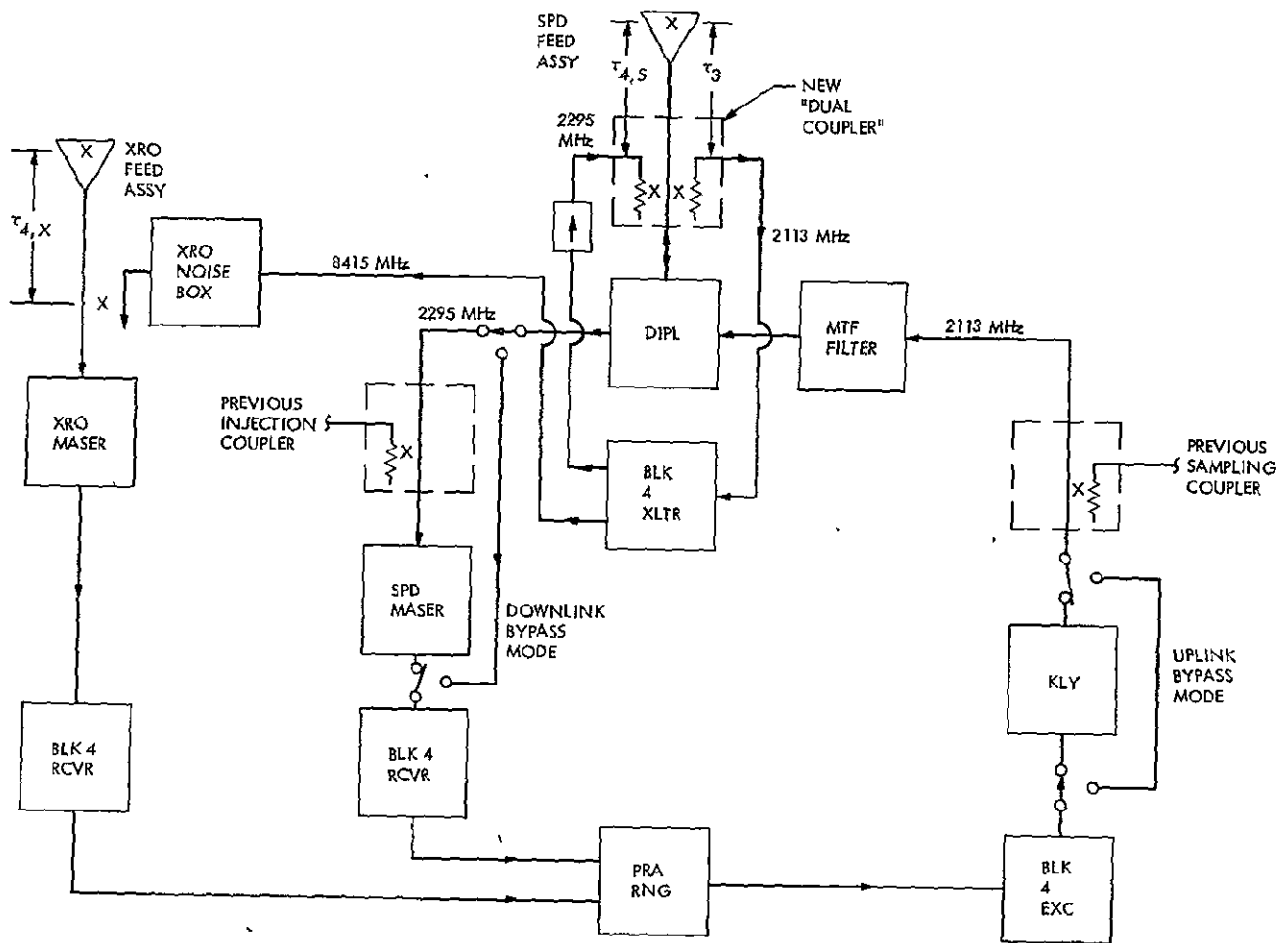
Fig. 1. Simplified block diagram of new dual coupler DSS 14 range calibration configuration
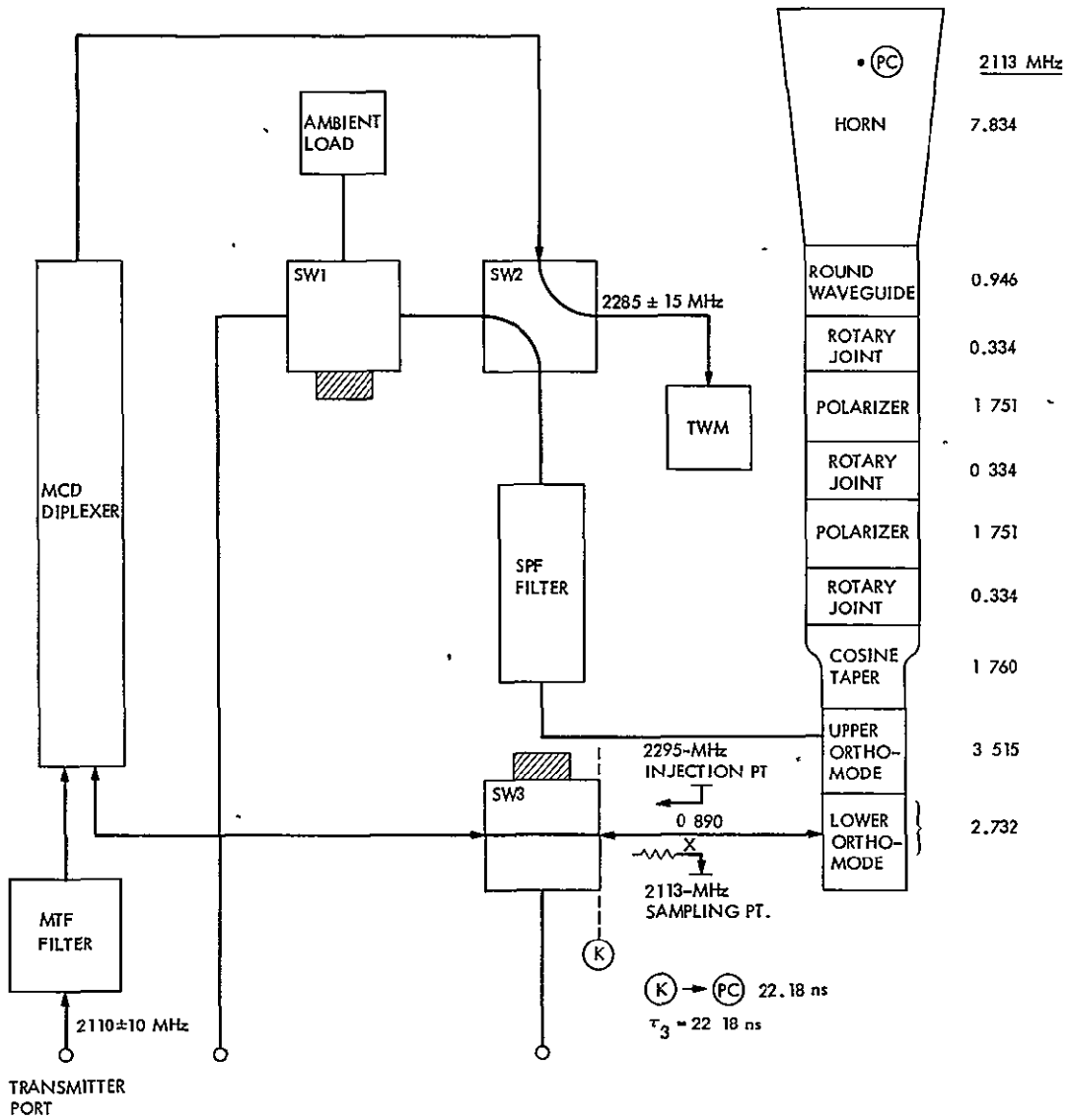
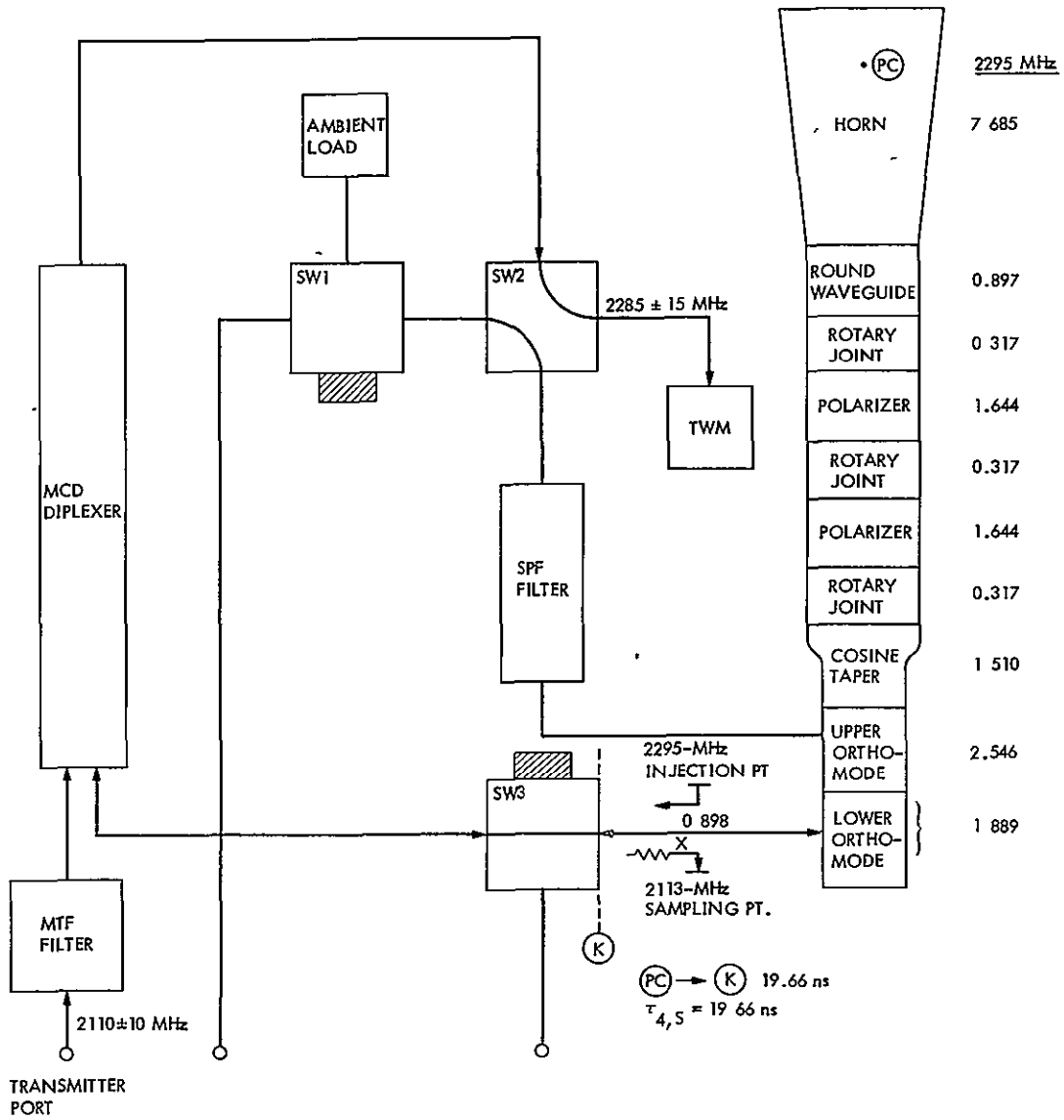Fig 2 Block diagram of SPD feed horn assembly and values of component delays for τ_3 at S-band

Fig. 3. Block diagram of SPD feed horn assembly and values of component delays for τ_4 at S-band

A High-Power Dual-Directional Coupler

K B Wallace and T Y. Otoshi

Radio Frequency and Microwave Subsystems Section

A dual-directional loop coupler in WR 430 waveguide has been installed at DSS 14 as part of the system to measure station range delay. This installation was necessary to provide special test translator signal injection ports for the Voyager near-earth calibration sequence, which required that the SPD maser be bypassed to prevent saturation of the receivers The design of the dual coupler and testing of this device at high power is discussed.

I. Introduction

During the Voyager near-Earth calibration sequence, the received power levels at the traveling wave maser (TWM) inputs are high enough to saturate the station receivers, and the high-power uplink can saturate the spacecraft receiver A solution to this problem is to bypass the klystron, i.e., use the exciter only, and to bypass both the S-band TWM and the X-band TWM All equipment to accomplish this, including the coupler under discussion, was installed at DSS 14 during the recent update period for Voyager The X-band bypass is achieved by turning off one of the two K-band pumps, which reduces the TWM gain by approximately 45 dB The S-band TWM is bypassed by means of waveguide switches

In this configuration, means must be provided to inject a sufficient test translator signal level for range delay precals. This is accomplished at X-band by removing attenuation in the test translator signal path to the TWM For S-band, a dual-directional WR-430 waveguide coupler is used This article describes the coupler and the test results

II. Description and Testing

Figure 1 shows the S-band polarization diversity (SPD) cone waveguide configuration and the location of the coupler. Figure 2 is a block diagram of the system prior to installation of the bypass equipment. As is evident from Figs. 1 and 2, there is no simple waveguide section near the feed horn that could be replaced by the new coupler. It was decided that the matching section (Fig. 3) could be replaced with a new matching section incorporating two identical compact loop couplers of 54 dB each A coupling value of 54 dB was specified for the sampling port because the previous sampling port was this value (Fig 2), which provides an appropriate signal level The test translator injection port coupling value was also made 54 dB because, at 400 kW, the power coupled out is at a tolerable receiver system input level (approximately 1 6 W for 54 dB as compared to 40 W for 40 dB coupling value)

Various coupler designs were considered A dual cross guide coupler could be made to fit the available space, but is

difficult or impossible to water-cool at high power levels: Other coupler designs such as broadwall and sidewall couplers are too large physically. A loop coupler was considered the most promising type for this purpose, because of its compactness and good electrical characteristics. Previous experience with this design (SLU cone-1973) indicated that sufficient directivity, bandwidth, and stability were possible.

A single coupler test model was designed and fabricated by Maury Microwave Corp (MMC) (Figs 4-7) The photographs show the loop coupler module and its installation in the waveguide section This unit was checked electrically by MMC before delivery (see test report, Appendix A) The coupler was then tested at the Microwave Test Facility at Goldstone to verify operation at 400 kW. Test results (Appendix B) show deterioration of the test coupler due to resistive termination burnout at high power. It was not designed to withstand 40 W. The initial coupling value was 40 dB, but later changed to 54 dB The test results for the 40-dB coupling value, however, did prove that the waveguide main line suffered no degradation due to arcing or overheating. There had been some doubt that the device would pass the high power test, because the coupling loops appear to present appreciable discontinuities in the waveguide walls (Fig 6)

The final design dual coupler was fitted with two 54-dB modules (Fig 8 and Appendix C) and tested at 400 kW The test of this unit was more difficult than that of the test coupler since the dual coupler assembly included the normal matching posts needed to tune out reflections of the feed horn orthomode transducer structure An external tuning device was used to improve the VSWR of the dual coupler assembly in the test system The test report is given in Appendix D

This unit was installed in the SPD cone at DSS 14 and has since been used as part of the range delay calibration system Figure 9 is a simplified block diagram of the Block 4 test translator method utilizing the dual coupler. The 2113-MHz signal is derived from the transmitted power (usually 10 to 20 kW) through port 1 of the dual coupler The 2295-MHz signal from the test translator is injected into the receiving system through port 2. Two coaxial isolators were added to the 2295-MHz translator path to prevent 2113-MHz signal from entering this line and reflecting back to cause a multipath effect.

This configuration has advantages other than its use in the TWM bypass mode. Injection of the test translator signal is at a point as near the feed horn as possible, allowing direct range delay measurement of all parts of the system below the feed horn at this one point. In the old configuration (Fig 2 and Ref. 1), some of the component delays below the feed horn had to be calculated or precalibrated before installation into the system. The range delay for each TWM system was measured separately at its respective input port. Reference 2 describes in more detail the advantages of this configuration for station delay calibration.

III. Conclusion

During the Voyager 1 near-Earth ranging sequence, DOY 254-256, 1977, this system was successfully used as planned to calibrate the station delay. Successful operation of the described calibrating system indicates that the installation of the dual coupler should be made permanent, not only at DSS 14 but at other stations as well.

Acknowledgment

References

1. Otoshi, T Y, et al, "Calibration of Block 4 Translator Path Delays at DSS 14 and CTA 21," *DSN Progress Report 42-37*, p. 188, Jet Propulsion Laboratory, Pasadena, Calif

2 Otoshi, T Y, Wallace, K. B., and Lyon, R. B., "Dual Coupler Configuration at DSS 14 for the Voyager Era," *DSN Progress Report 42-42* (this issue)
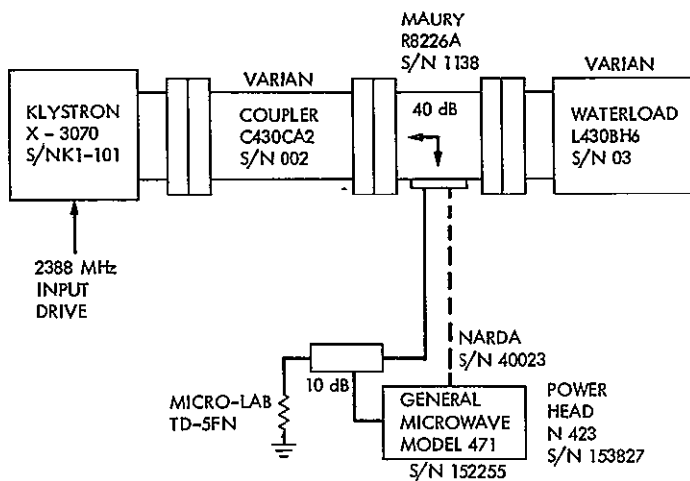
.Appendix A

Maury Microwave Corporation Test Report on 40-dB Test Model Loop Coupler Assembly

Frequency, MHz	Coupling	VSWR, primary	VSWR, sec	Directivity
2 245	39.5	1 01	1 11	20.0
2.285	39.5	1 01	1.11	20 4
2.325	39.4	1 01	1 10	20 8

Appendix B

Test Report on 40-dB Loop Coupler Assembly High Power Test (From M. Gregg JPL Internal Report)

The following test setup was made to test the Maury microwave coupler model R 8226A, S/N 1138, for operations at 400 kW. The following data was taken as the power was increased in steps to obtain the 400-kW operation

Time	Pwr out, kW	T WL °C	WL flow, gpm	Temp coupler	Pwr meter, dB
Test set 1, pwr meter direct to test coupler					
7 30	10 2	0 381	100	Cool	11 5
7 45	20 3	0 77	100	Cool	14.3
8 00	20.3	0 77	100	Cool	13 7
8 00	50.8	1 926	100	Cool	17 8
8 15	50 6	1 92	100	Warm	17 1
8 15	100 1	3.80	100	Warm	23 1
8 30	100 1	3.80	100	43°C	22 7
8 30	200 1	7.58	100		32.0
8 45	200 1	7.58	100	54°C	38 2

Test set 2 installed 10-dB coupler and load					
8:46	200 6	7 60	100		27.6
8·50	100 1	3 80	100		24 6
9.30	200 6	7 60	100	54°C	27.6
9 30	301	11 40	100		29.5
9 35	301	11 40	100	60°C	29 5
9 45	301	11 40	100	66°C	29 5
10 00	401	15 2	100	71°C	30 0
10 30	401	15.2	100	77°C	29 9
11 00	401	15 2	100	77°C	29.9
11:30	401	15.2	100	77°C	29.9
System turned off					
12 40	401	15 2	100		30 0
12 45	401	15 2	100		20 9
12 46	401				34 2
12 48	401		·		31 2
13 18	401	15 2	100		31 1

It can be noted in the data that at 200 kW the coupler output changed from 32 0 dB to 38 2 dB when the 10-dB coupler and load was installed in the output and the reference taken at 200 kW. The system power was then reduced to 100 kW and reference taken as noted in the data With the system off for over an hour the temperature of the coupler was allowed to return to room temperature

The system was then brought to 400 kW directly, without any warmup time The coupler output went from 32.0 to 20 9 dB in the space of 5 min and then raised to an output of 34 2 dB within the next 3 min It settled to an output of 31 1 dB after 30 min

The cycle was again repeated and the radical changes seen at the early time were not noted. The coupler had a steady output of 31.1 ± 0 1 dB at 401 kW The Narda coupler calibrated at 2388 Mhz = 9.9 dB.

Appendix C

Maury Microwave Corporation
Test Report on 54-dB Dual
Coupler Assembly

	1 Port					2 Port			
Frequency,	Coupling	VSWR	Directivity	Main line VSWR	Frequency,	Coupling	VSWR	Directivity	Main line VSWR
2093	53 8				2093	54 3			
2113	53 9	1 10	20 6	1.30	2113	54 4	1 12	20.6	
2133	59 0				2133	54 4			
2275	53 5				2275	53.8			
2295	53.1	1 09	23.9	1 34	2295	53.5	1 15	25 0	
2315	53.2				2315	53.6			

Appendix D

Test Report on 54-dB Dual Loop Coupler Assembly High Power Test (From M. Gregg JPL Internal Report)

The following test setup was made to test the Maury microwave coupler model R 8226C, S/N 1160, for operations at 400 kW. The following data was taken as the power was increased in steps to obtain the 400-kW operation The VSWR of tuner and coupler = 1.09, flow waveguide = 2 gpm
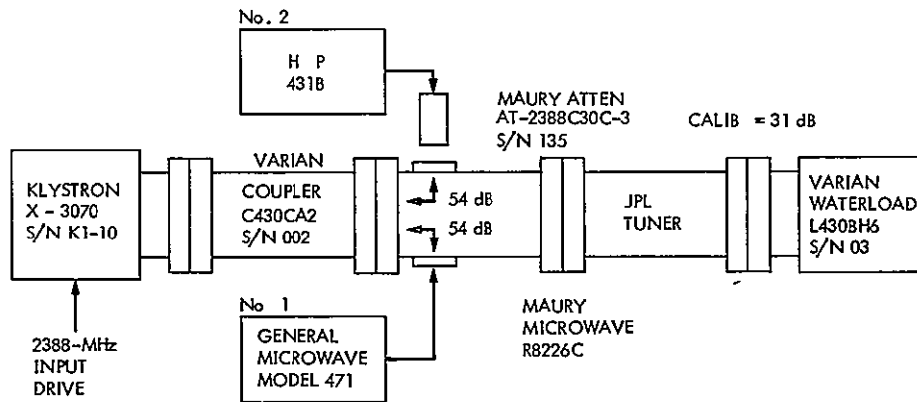
Time	Pwr out, kW	Refl pwr, kW	Sys H_2O Temp, °C	ΔT °C	WL flow, GPM	Coupler temp	No 1 pwr mtr, dB	No 2 pwr mtr, dB
8 45	50	0 15	28 9	1 9	98	Cool	22 8	22 8
9 00	50	0 14	35 6	1 9	98	Cool	22 6	22 2
9 00	100	0 26	31 6	3 85	98	Luke warm	26 0*	26 2
9 15	100	0 275	29 6	3 86	98	Luke warm	26 0	26 3
9 15	150	0 38	29 5	5 8	98	Warm	27 8	28 2
9 30	150	0 39	30 4	5 8	98	Warm	27.7	28 2
9 30	200	0 49	30 5	7 75	98	Warm	29 1	29 5
9 45	200	0 50	32 0	7.75	98	Warm	29.1	29 6
9 45	250	0 59	32 2	9 68	98	Warm	30.2	30 7
10 00	250	0 62	33.7	9.68	98	Warmer	30 2	30 7
10 00	300	0 72	33.9	11.6	98	Warmer	30 9	31 1
10 15	300	0 74	35.0	11 6	98	Warmer	30 9	31 1
10 15	350	0.87	35 3	13 55	98	Warmer	31 6	31.8
10:30	350	0 90	36 7	13 55	98	43°C	31 6	31.8
10 30	395	1 03	37 2	15 3	98	43°C	32 1	32 3
10.40	400	1.1	38 1	15 46	98	49°C	32 2	32 4
11 00	400	1 16	38 9	15 46	98	49°C	32 1	32 4
11 15	400	1.17	38 8	15 46	98	49°C	32 1	32 4
11 30	400	1.17	39 2	15 46	98	49°C	32 1	32 4
11 45	400	1 19	39 8	15 46	98	49°C	32 1	32 4

The RF and beam were turned off, with water on system, which allowed the system to stabilize to normal temperature of 28.5°C. The system was then brought directly to 400 kW and the following data was then taken

| 12 50 | 400 | 0 8 | 34 9 | 15 5 | 98 | Warm | 32 5 | 32 3 |
| 01 20 | 400 | 1 1 | 39 5 | 15 5 | 98 | — | 32 1 | 32 3 |

At no time during the test were any arcings or kickoffs experienced, the only thing noted was some jitter in the reflected power monitor.
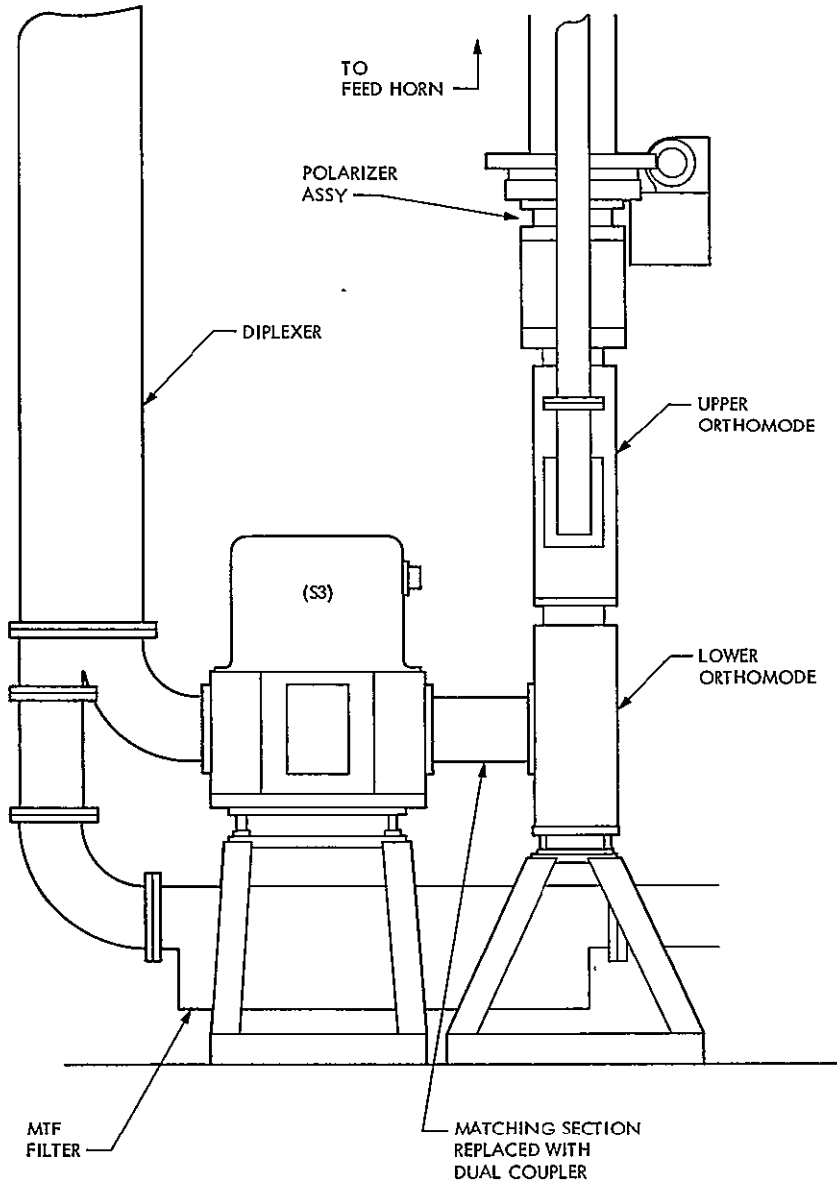
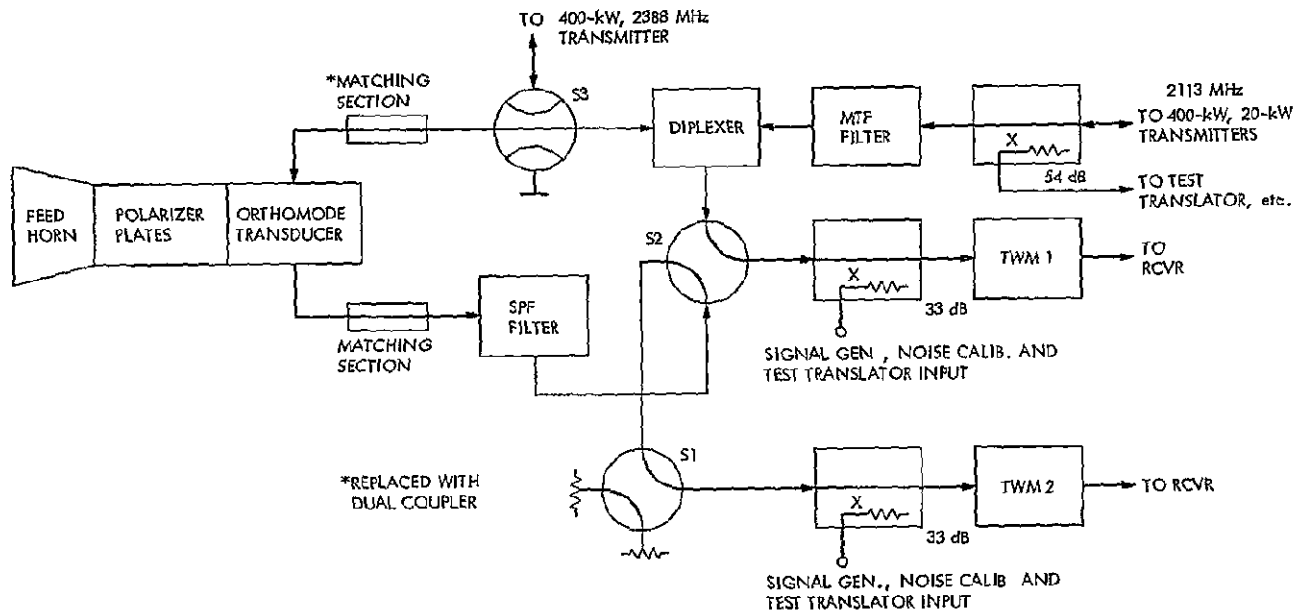**Fig. 1. Dual coupler location in SPD cone waveguide system**
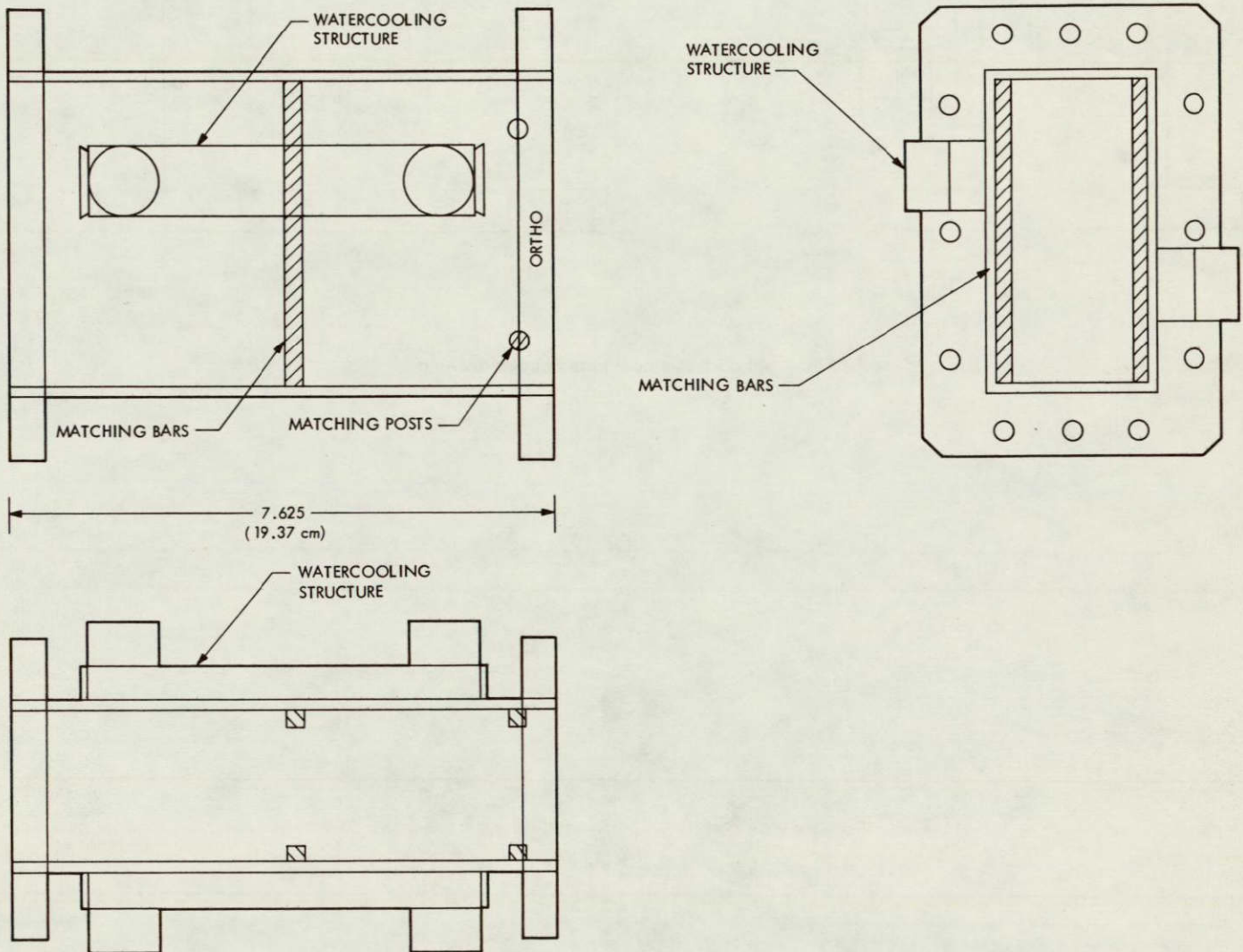
Fig. 2. Simplified block diagram of S-band microwave system at DSS 14

Fig. 3. Waveguide matching section for lower orthomode transducer
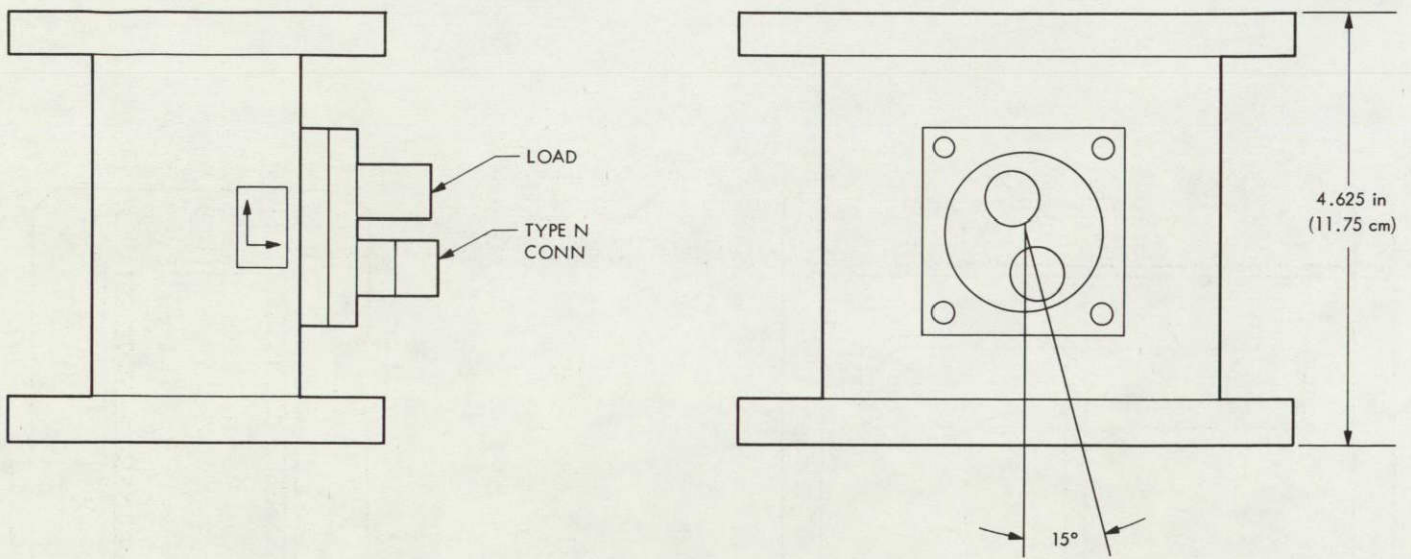
Fig. 4. 40-dB test model loop coupler drawing

LOAD

TYPE N CONN
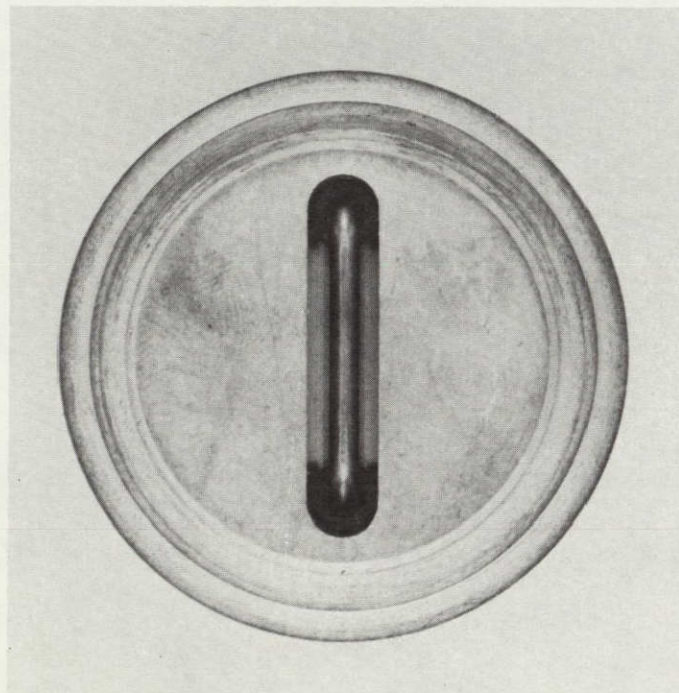
4.625 in (11.75 cm)

15°

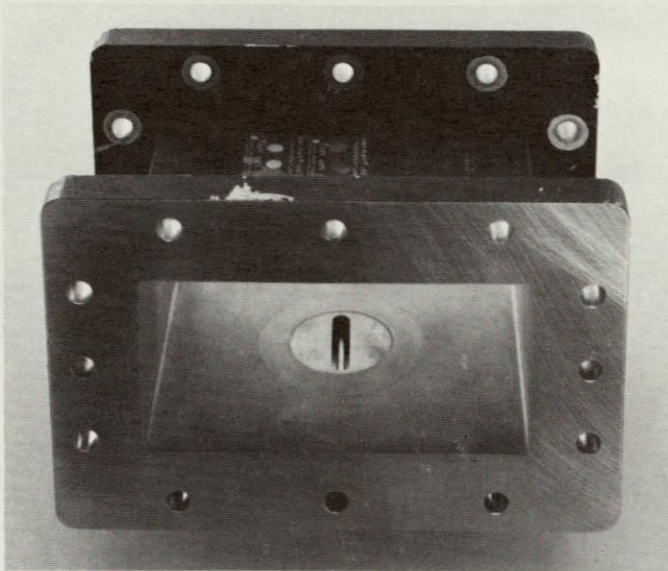Fig. 5. 40-dB loop coupler module

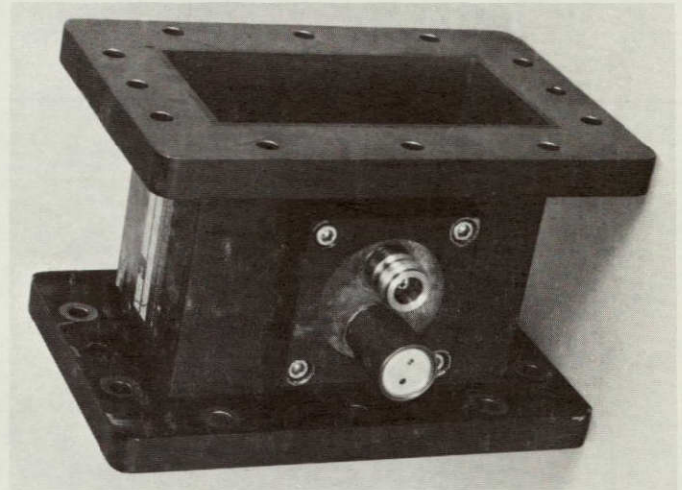Fig. 6. 40-dB loop coupler module inserted into WR 430 section (internal view)

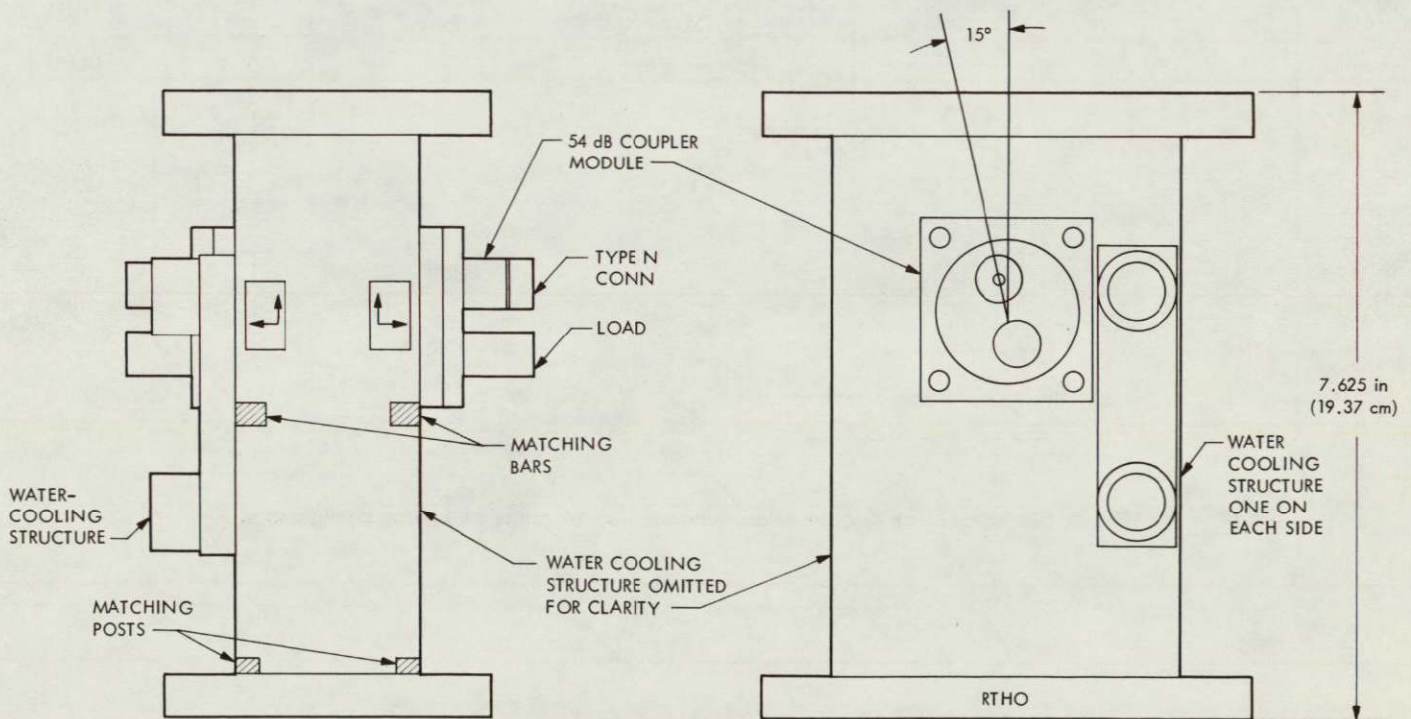Fig. 7. 40-dB loop coupler module inserted into WR 430 section (external view)

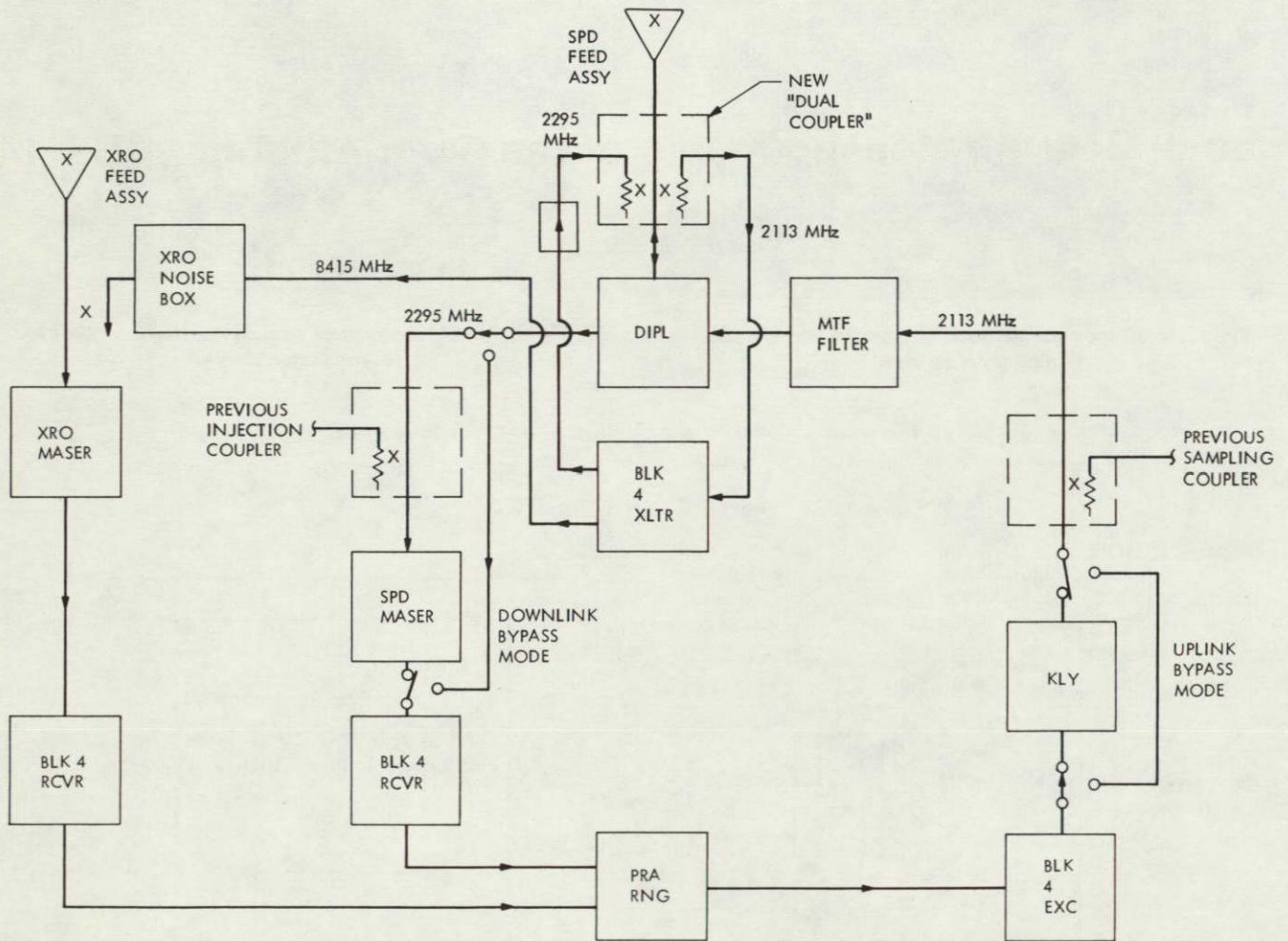Fig. 8. 54-dB dual loop directional coupler assembly (with waveguide matching section and water cooling plumbing)

Fig. 9. Simplified block diagram of dual coupler DSS 14 range calibrating configuration

N78-24185

Radial Bearing Measurements of the 64-m Antenna, DSS 14

G. Gale

DSN Engineering Section

This article describes the inspection fixtures and methods used to determine the extent of the azimuth radial bearing deformation at the 64-m DSS 14. An annular separation has developed between the circular steel runner and the grout, suggesting either failure of the grout or, as the case appears to be, stretching of the circular steel runner due to the formation of rust on the runner at the grout interface.

I. Introduction

At DSS 14 the azimuth radial bearing is a steel runner 9.144 m (30 ft) in diameter, mounted on the central concrete pedestal of the antenna and supported by grout between the steel runner and the rough concrete of the pedestal. Three truck assemblies, each with two large rollers which support the alidade base triangle at 120 degrees, are preloaded radially inward onto the steel runner and pedestal with a force of 1.47×10^6 newtons (330,000 lb) to eliminate motions of the antenna under maximum wind loads.

An annular separation has developed between the circular steel runner and the grout, suggesting either failure of the grout or, as the case appears to be, stretching of the circular steel runner due to the formation of rust on the runner at the grout interface.

II. Special Tooling

A set of inspection fixtures has been designed to study the changes in the radial bearing and to be used in case a major maintenance replacement of runner becomes necessary. A theodolite and a trammel bar assembly, located at the center of the antenna (Fig. 1), was used to establish a set of 24 equally spaced reference or bench marks located in a circle near the circular steel runner (Figs. 2 and 3). A second fixture (Fig. 4), which uses the bench marks for location, has been designed to measure the radial runout of the circular steel runner.

A review of tolerances and other operating considerations which affect the repeatability of measurements taken with the radial bearing inspection fixtures indicates the radial precision of the bench marks is ±0.127 mm (±0.005 in.) and that the repeatability of the measurements made with the base assembly and carriage, including the bench mark tolerance, is ±0.381 mm (±0.015 in.).

When used, the inspection fixture, which spans 30-deg, is moved in 15-deg increments around the antenna. Measurement points are indicated on top of the rail at 1/2-deg intervals. Several of the measurements made at each end of the fixture are repeated each time a set is made. This allows a check for repeatability of part of the data taken each time the inspection fixture is aligned with the bench marks.

A series of measurements was made over a 100-deg area (the antenna was at rest and 100 deg is about the maximum

that can be made between radial bearing trucks). The limited amount of time available prevented a complete 360-deg survey. Every precaution was made to assure the best possible repeatability during these measurements. A review of the data showed that the maximum difference between any of the repeated points was 0.203 mm (0.008 in.) and the mean of all of the repeated data was 0.076 mm (0.003 in.).

The inspection tools revealed that the circular steel runner had stretched more around the bottom edge than at the top, causing the radial bearing running surface to be conical instead of cylindrical. A verticality measurement tool was designed to measure the angular deviation from a vertical cylindrical surface (Fig. 5).

III. Observations

These data also indicated that there was a bulge midway between the radial bearing truck assemblies of approximately 0.9 to 1 mm (0.035 to 0.040 in.). Measurements made previously with the antenna parked at a different azimuth position indicated similar bulges but at a different azimuth location. To partially explain these bulges, consider a concrete ring 9.14 m (30 ft) OD, with a cross section 0.914 m (36 in.) thick and 2.03 m (80 in.) high (the dimensions of the portion of the pedestal which supports the radial bearing), with three inward radial loads of 1.47 to 1.78 newtons (330 to 400 kips) applied at 120-deg intervals. The outer surface at the point of application will distort inward.

The deflection inward may be estimated by the following formula:

$$\text{Deflection } \delta = \frac{WR^3}{2EI} \times \left[\frac{1}{(\sin \theta)} \right.$$

$$\times \left(\frac{\theta}{2} - \frac{\sin \theta \cos \theta}{2} \right) - \left. \frac{1}{\theta} \right]$$

where

$$\theta = \frac{120^\circ}{2} = 60^\circ = 1.047 \text{ radians}$$

$$R = 4.445 \text{ m (175 in.) (OD of concrete)}$$

$$I = \frac{2.032 \, (0.9144)^3}{12} = 0.12946 \text{ m}^4$$

$$E = 4.48 \times 10^{10} \text{ N/m}^2 \ (6.5 \times 10^6) \text{ (concrete)}$$

$$W = 1.779 \times 10^6 \text{ N/m}^2 \ (400,000 \text{ lb) (preload at present)}$$

$$\delta = \frac{1.7793 \times 10^6 \times (4.445)^3}{2 \times 4.48 \times 10^{10} \times 0.12946} \left[\frac{1}{(0.866)^2} \right.$$

$$\times \left(\frac{1.047}{2} - \frac{0.866 \times 0.5}{2} \right) - \left. \frac{1}{1.047} \right]$$

$$= 0.4257 \text{ mm (0.017 in.) inward deflection}$$

As the concrete ring is distorted inward, it will also be distorted outward midway between the truck assemblies. The approximation for this can be calculated by

$$\delta = \frac{WR^3}{4EI} \left[\frac{2}{\theta} - \frac{1}{\sin \theta} - \frac{\theta - \cos \theta}{(\sin \theta)^2} \right]$$

$$\delta = \frac{1.7793 \times 10^6 \times (4.445)^3}{4 \times 4.48 \times 10^{10} \times 0.12946}$$

$$\left[\frac{2}{1.047} - \frac{1}{0.866} - \frac{1.047 \times 0.5}{(0.866)^2} \right]$$

$$= 3.82 \times 10^{-4} \text{ m or } 0.381 \text{ mm (0.015 in.)}$$

The total deformation of the pedestal by the radial bearing preload is then approximately 0.4257 + 0.381 = 0.8067 mm (0.032 in.).

When the inspection tool was used, an amount approximately this great was observed between measurements made near the truck assemblies and the measurements made midway between the trucks.

The steel ring offers little opposition to the preload forces and will deflect inward or outward the same amount as the concrete. The ring complies in this manner because of the circumferential tension caused by the stretching of the ring due to rust. The radial force applied by stretching the steel runner can be estimated by the formula

$$P = \frac{\epsilon E \times 2t}{D}$$

For an average radial change in the runner at the center of approximately 0.050, the radial force is

$$\epsilon = \frac{2\pi \times 0.050}{2\pi \times 180} = 2.78 \times 10^4$$

and

$$P = \frac{2.78 \times 10^4 \times 20.677 \times 10^6 \times 2 \times 0.1016}{9.144}$$

$$= 1.28 \times 10^2 \text{ N}$$

which is negligible compared to the 1.78×10^6 newton preload.

The hoop stress is only $2.78 \times 10^{-4} \times 20 \times 10^{10} = 5.56 \times 10^7$ N/m^2 (8340 psi), well within the elastic limit of the steel.

IV. Conclusion

The result of these investigations indicates:

(1) The bench marks must be located with no preload on the radial bearing trucks, because the top of the pedestal will be distorted radially in the area of the bench marks when the preload is on.

(2) All measurements using the radial bearing inspection fixture must be made with the preload removed.

(3) The repeatability of the measurements made by the inspection tool with reasonable care should be adequate to relocate a replacement radial bearing runner if it becomes necessary.

(4) The repeatability of the inspection' tool could be improved by locating it directly from the center theodolite mount using two equal rods to position it at each end, thereby eliminating several of the larger tolerance-contributing joints. This, however, would considerably increase the time needed to make a full set of observations.

(5) Should it be necessary to make measurements while the preload is on the radial bearing trucks, these measurements should be made radially between the theodolite mount in the center of the pedestal and a vertical bar, bearing on the center of the wearstrip, located between the wheels at one of the truck assemblies. Such a set of data would require rotation of the antenna in 15-deg increments and be good at the 15-deg points only.
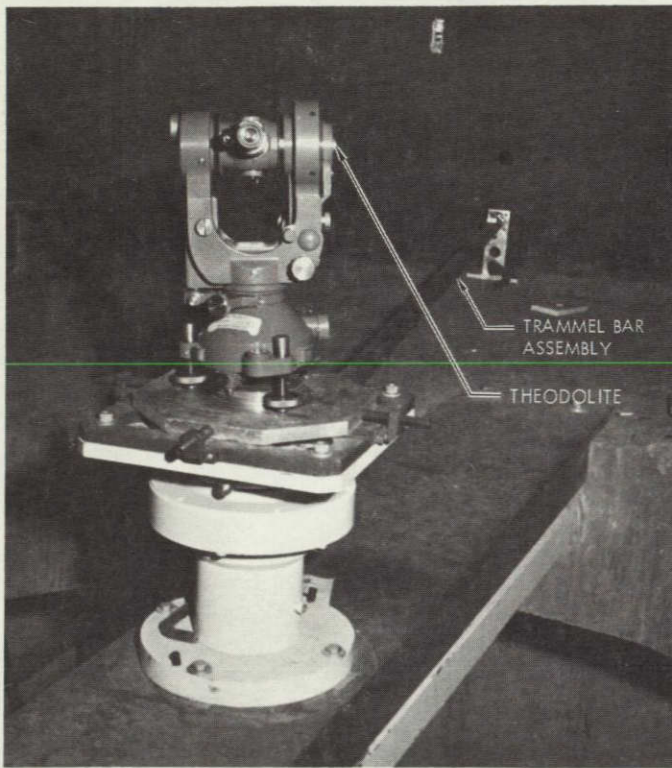
Fig. 1. Central theodolite and mount
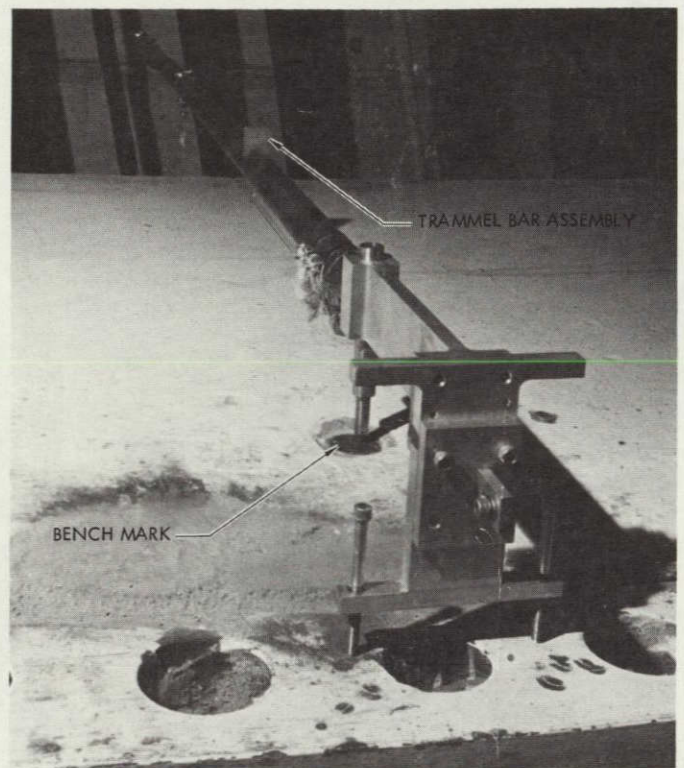
Fig. 2. Bench mark and trammel bar assembly
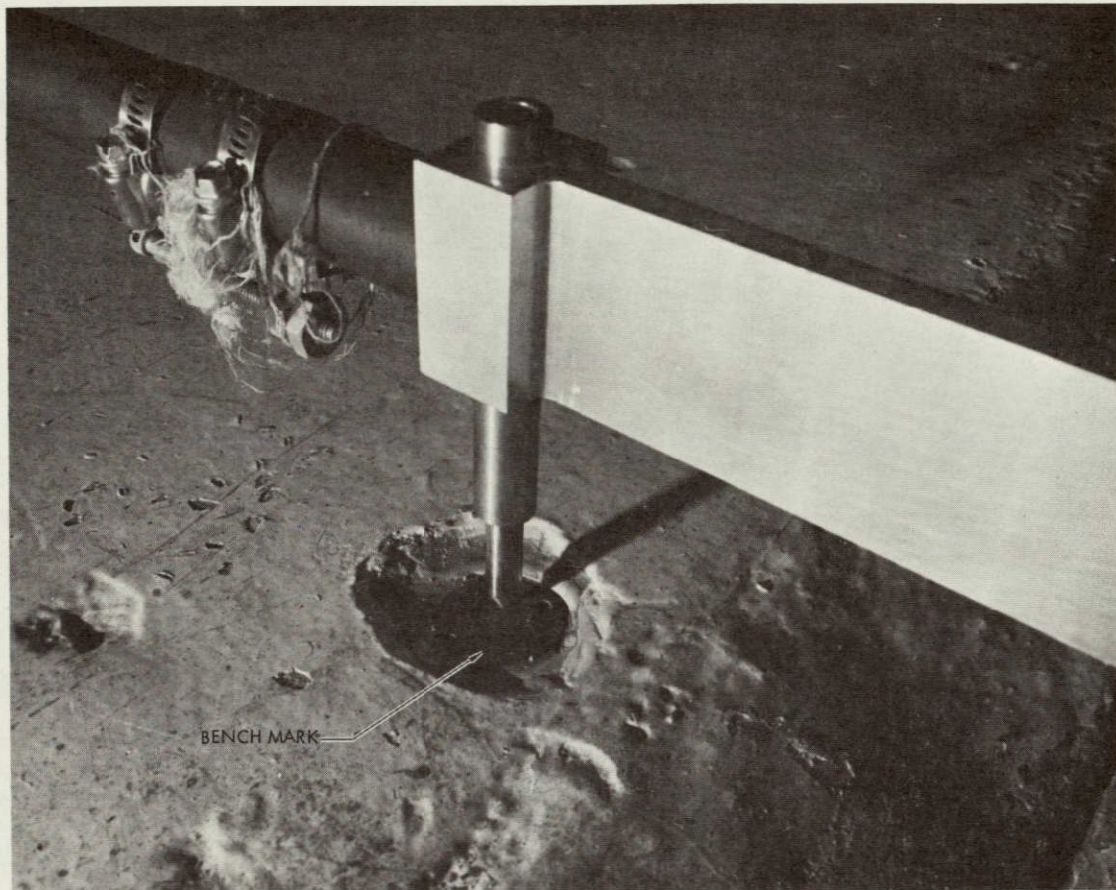
Fig. 3. Bench mark location

BENCH MARK

OPTICAL SIGHT TUBE
OVER BENCH MARK

SPIRIT LEVEL

DIAL INDICATOR USED
TO MEASURE RADIUS OF
RADIAL BEARING RUNNER

OPTICAL SIGHT
TUBE OVER BENCH
MARK

STEEL RUNNER
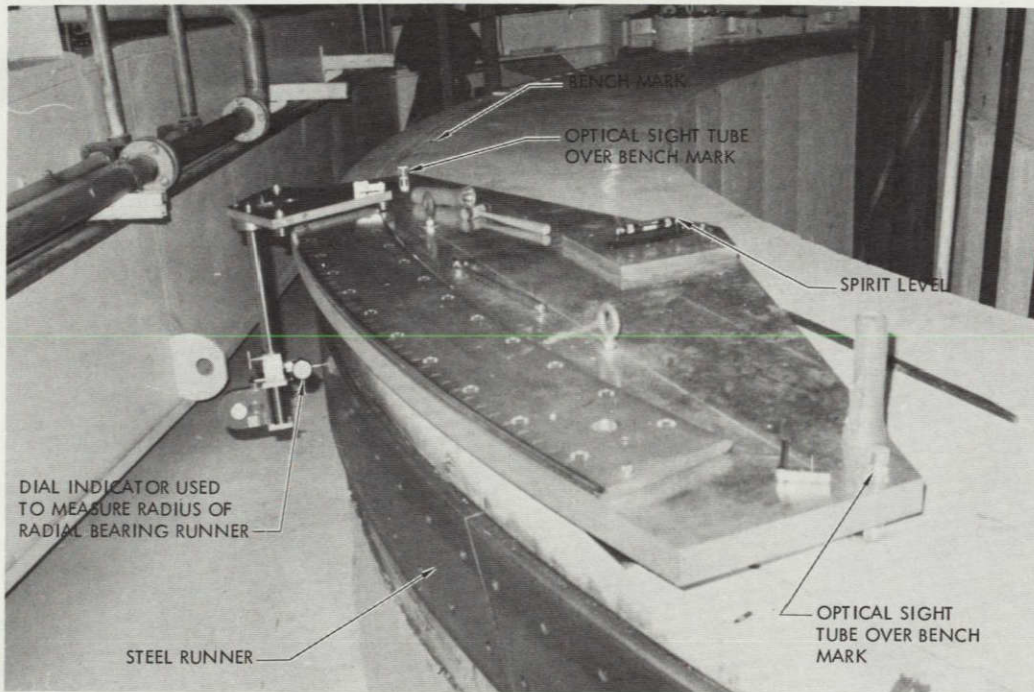
Fig. 4. Radial bearing measurement tool

Fig. 5. Verticality measurement tool

N78-24186

Cost Evaluation of a DSN High Level Real-Time Language

M. McKenzie

TDA Planning

The hypothesis that the implementation of a DSN High Level Real-Time Language will reduce real-time software expenditures is explored. The High Level Real-Time Language is found to be both affordable and cost-effective.

I. Introduction

The Deep Space Network (DSN) spends approximately $3 million a year on real-time software. It has been hypothesized that the implementation of a DSN High Level Real-Time Language (HLRTL) would reduce this expenditure substantially by increasing programmer efficiency and program maintainability. To explore this hypothesis, the HLRTL costs and DSN real-time software expenditures were evaluated; a Cost/ Savings model was applied to the expenditures. The results confirmed the hypothesis — over ten years the DSN will save from $6 million to $16 million above costs with the implementation of a High Level Real-Time Language.
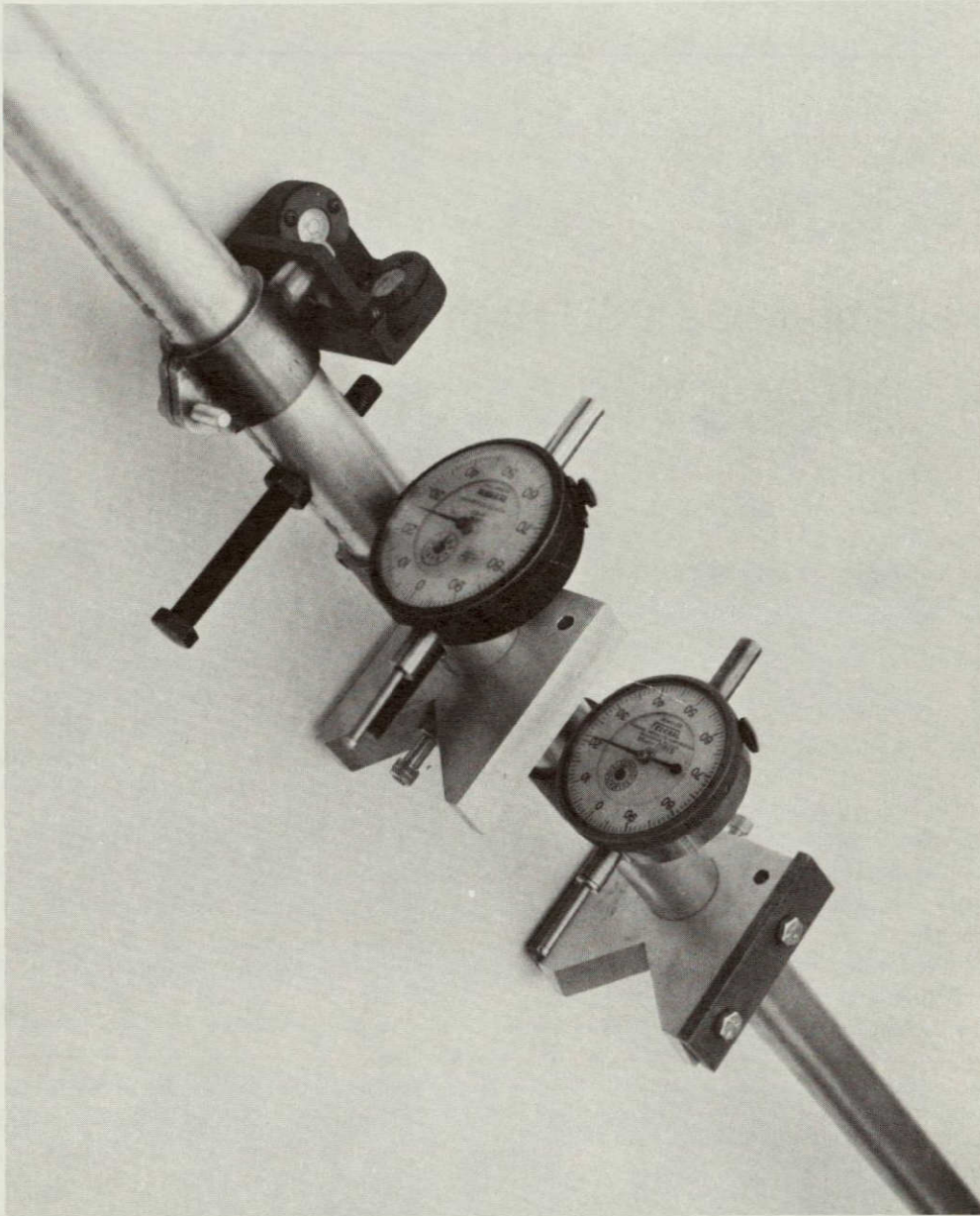
II. Cost

To calculate the cost of the HLRTL, the following assumptions were made:

(1) There will be a single HLRTL machine-independent design, with all necessary manuals.

(2) The HLRTL machine-independent design will be implemented on five machines. The implementations will occur during years 1, 2, 3, 6, and 9, each requiring a one-year period.

(3) The first implementation will affect 50% of DSN Real-time Software. With the second implementation, 80% will be affected; with the third, 100%. The remaining implementations are replacements of machines on which the HLRTL has already been implemented.

(4) The time period of the HLRTL, the life-cycle assumed by this study, is ten years. This was found to be more applicable than the usual implementation-plus-ten-year-maintenance cycle, due to the implementation of the HLRTL on different machines at different times.

(5) The HLRTL will be of sufficiently high quality to ensure no increase in hardware resource requirements. Although high level languages generate programs with less than optimal computer efficiency, with an optimizing compiler the machine code generated can still be at least as efficient as that produced by a low level language (for most programmers).

With these assumptions, and component costs as listed in Appendix A-1, the projected life-cycle cost of the DSN High Level Real-Time Language is $2620K in constant dollars (Appendix A-2).

III. Affordability

From an economic viewpoint, the DSN can afford the HLRTL if its implementation will save at least enough money to cover its costs It will be shown that the DSN High Level Real-Time Language is highly affordable, the breakeven point probably occurring within 3 years or less of its implementation.

IV. Expenditures on Real-Time Software

Based on a search through the 77-1 Work Authorization Document (WAD) and the Format A job description of each DSN work unit, it was estimated that the DSN will spend $14,880K on real-time software over the period 1977-1982 (Appendix B-1) An independent estimate validated this approach (Appendix B-2)

The DSN ten-year real-time software cost is assumed to be twice this five-year expenditure This is a low estimate, if anything, since Fiscal Year 77 is at the end of the large Mark III Data System implementation and thus does not include major funding of the previous two years. Hence, the ten-year DSN real-time software expenditures are conservatively estimated at $29,760K (constant dollars). With reference to assumption 3, implementation of the HLRTL will affect $27,677K of the estimated expenditures

V. Real-Time Software Cost-Savings Model

As seen in the Cost-Savings Model, the effect of a High Level Real-Time Language on DSN real-time software production will vary across size and phase of projects For instance, the larger the project, the more likely that a HLRTL will save effort in the testing phase. So using industrial and DSN data, the applicable DSN ten-year real-time software expenditures are first distributed by size and phase (Appendix C-1).

Within each phase of a project, one expects an increase in cost-effectiveness with the High Level Real-Time Language Specifically, the HLRTL will allow savings in each phase as shown in Table 1

The increase in efficiency, by phase and size, is difficult to ascertain However, estimates were derived from data found in

the software industry and literature (Appendix C-2). The distributed real-time software costs were multiplied by these efficiency factors (measures of increased efficiency under the HLRTL system). The result of the multiplication is the cost per element when using a High Level Real-Time Language Summing these elemental costs gives the total real-time software cost when using the HLRTL

VI. Savings

DSN savings are equal to the ten-year DSN real-time software costs using a low level language minus those using the HLRTL. The savings were calculated assuming the efficiency data derived from software industry and literature The DSN real-time software savings stream, for ten years, was also calculated using this assumption (Appendix D-1). By comparing these yearly savings to the HLRTL cost stream, it was calculated that the HLRTL is affordable and would save $14,196K over costs (constant dollars) The breakeven point, at the beginning of year three, is shown in Appendix D-2

The efficiency factors are derived from industrial and literature data representing a variety of projects, languages, methodologies, and years, so they cannot be taken as absolute predictors of DSN software costs using a High Level Real-Time Language. In recent work for NASA and the U S. Air Force, E. N Dodson of General Research Corporation reports indications that real-time "assembly language programs are approximately two to five times more expensive to develop *per object instruction*," and two to five times more expensive to maintain, than real-time high level programs. Therefore, to check sensitivity of the model, savings were recalculated assuming this range for the efficiency factors (Appendix C-2). The HLRTL is still affordable and saves from $5,921K to $16,013K over costs (in constant dollars).

VII. Conclusion

The DSN High Level Real-Time Language is clearly affordable — savings cover costs Furthermore, additional savings can be expected to run from $6 million to $16 million over a ten-year period In fact, in view of the reinforcement produced by the software standard practices employed by the DSN, it is probable that savings will be on the high side of this range near the $14 million value. The proposed High Level Real-Time Language is affordable and cost-effective

Table 1. Source of savings by software phase

Phase	HLRTL Attribute	Result
Design	Emphasis on top-down design Fits well with modular development.	Fewer design errors More efficient designing
Coding	Flexible language designed for the programmer.	Fewer coding errors Faster coding
Testing	High readability of code Allows modular testing Allows top-down testing.	Fewer errors Easier correction of errors Higher management visibility
Transfer to Ops	Lends itself to clear documentation	More efficient testing More efficient transfer to Ops.
Sustaining	Enhanced readability of code Documentation is tied to code	Fewer errors Errors easier to correct. More efficient sustaining.

REAL-TIME SOFTWARE COST, USING THE HLRTL

$\sum$ OVER ALL ELEMENTS

REAL-TIME SOFTWARE COST, PER ELEMENT, USING THE HLRTL

10-YEAR EXPENDITURES
BY PHASE AND SIZE

APPLICABLE 10-YEAR DSN REAL-TIME SOFTWARE EXPENDITURES	×	SIZE AND PHASE DIS-TRIBUTION FACTORS

× | EFFICIENCY FACTORS = (EFFORT REQUIRED WITH THE HLRTL)/(EFFORT REQUIRED NOW) FOR EACH SOFTWARE SIZE AND PHASE |
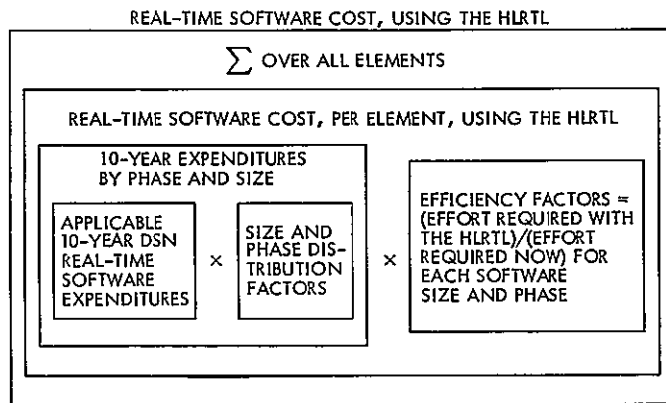
Fig. 1. Cost-savings model

Appendix A-1

HLRTL Life-Cycle Component Costs

Implementation Costs[a]	
One-time machine-independent design (5 MY at $60K/MY)	$ 300K
User Manuals (4 contractor MY at $30K/MY)	$ 120K
Five HLRTL implementations (4 5 MY each at $60K/MY)	$1350K
Sustaining Costs[b]	
Machine-independent design and manuals ($30K/year for 9 years)	$ 270K
HLRTL on five machines ($20K/year per machine)	$ 580K

[a]Derived from information supplied by TDA Engineering using a Work Authorization Document baseline (4/77) and the JPL System for Resource Management (12/76)

[b]This is a high estimate, if anything, based on the sustaining costs of the DSN High Level Non-Real Time MBASIC[tm] Language

Appendix A-2

HLRTL Cost Stream

Year	1	2	3	4	5	6	7	8	9	10
Implementation ($K)										
Machine-independent design	300									
Five implementations	270	270	270			270			270	
User manuals	120									
Sustaining ($K)										
• Machine-independent design and manuals	-	30	30	30	30	30	30	30	30	30
HLRTL — Machine 1		20	20	20	20	20	20	20	20	20
HLRTL — Machine 2			20	20	20	20	20	20	20	20
HLRTL — Machine 3				20	20	20	20	20	20	20
HLRTL — Machine 4							20	20	20	20
HLRTL — Machine 5										20
Yearly Totals	690	320	340	90	90	360	110	110	380	130

Total for 10 years $2620K (constant dollars)

Appendix B-1

DSN Real-Time Software Expenditures (in $K) Derived From The 77-1 Work Authorization Document and Format A's

Work Unit 311-03	1977 Impl[a]	1977 Sus[b]	1978 Impl	1978 Sus	1979 Impl	1979 Sus	1980 Impl	1980 Sus	1981 Impl	1981 Sus
13-24-01	110	110	117	117	122	122	128	128	133	133
13-24-02	90	90	77	77	82	82	87	87	92	92
14-12-01		81		154		164		172		181
14-12-02		161		131		139		146		155
14-12-92		34		32		32		33		33
14-20-02	58	58	67	67	71	71	75	75	80	80
23-10-03	44		47				23		24	
41-01-01	127		98							
41-01-04			27		52		82		35	
41-01-16					28		21			
41-05-10					16					
41-01-09			12		52		55		29	
42-49-07	6									
42-53-04	153		59							
42-53-05	72		24							
42-54-06	115		43							
42-54-22			60		85		15			
42-60-01	151		97							
42-60-02	106		15							
42-60-03	13		17							
42-60-11	214		248							
42-60-16	23		24							
42-60-18	23									
42-61-13	58									
43-10-04	192		222		234		248		262	
43-10-06	66									
43-20-01	60		67		74		80		80	
43-20-04	57		41		42		45		49	
44-12-01		41		62		96		144		119
44-12-04		82		90		83		51		88
44-12-05		60		80		80		89		94
44-12-06		81		48		50		56		62
44-12-07		78		86		51		54		58
44-21-02	62		24		26		27		29	
44-21-03	68		104		108		60		64	
44-23-01	104		76		82		88		94	
44-30-01	350		346		364		429		476	
311-06										
20-00-72		93		97		150		234		296
30-00-62	36		44		57					
40-00-59	87		65		57					
40-00-60	96		66							
Subtotals	2541	969	2087	1041	1552	1120	1463	1269	1447	1391
Yearly totals	$3510K		$3128K		$2672K		$2732K		$2838K	

Category totals.	Implementation costs	$9090K (61%)
	Sustaining costs	$5790K (39%)
	5-year costs	$14880K (constant dollars)

[a]Implementation Cost
[b]Sustaining Cost

Appendix B-2

Accuracy Evaluation

To check the accuracy of the estimate shown in Appendix B-1, a second method was used to estimate FY77 expenditures on real-time software It was hypothesized that the DSN Data Systems Section comprises half of DSN real-time software budget This section invested $1 8 million in real-time software in FY77 Thus, the two methods show DSN FY77 real-time software expenditures as.

| WAD estimate | $3510K |
| Independent Estimate | $3600K |

This high degree of agreement only means that the two independent estimates derived similar results Yet the second estimate does lend credence to the five-year estimate of Appendix B-1

Appendix C-1

Cost Distribution of the DSN Ten-Year Real-Time Software Expenditures[a]

Distribution Element	Distribution Factor, %	Source of Factor
Ten-year costs	100	
Implementation phase	60	1
Large software projects	76	1
Design phase	55	2
Code phase	11	2
Test phase	22	2
Transfer to Ops phase	12	2
Small software projects	24	1
Design phase	55	2
Code phase	11	2
Test phase	22	2
Transfer to Ops phase	12	2
Sustaining phase	40	1
Large software projects	76	1
Small software projects	24	1

[a]It is assumed that over ten years, the distribution of the DSN real-time expenditures will approach that of a software project

Sources

1 *Work Authorization Document,* 77-1, Deep Space Network, and corresponding Format A's

2 Edmund B. Daly, "Management of Software Development;" *IEEE Transactions on Software Engineering,* May 1977, p 232, and Thomas J Devenny, "An Exploratory Study of Software Cost Estimating at the Electronic Systems Division," NASA Report #N77-18791, Air Force Institute of Technology, p 29

Appendix C-2

Efficiency Factors Measured in (Effort Required with the HLRTL)/(Effort Required Now) as Derived from Software Literature and Industry Data

Element	Efficiency Factor	Maximum Value	Minimum Value	Source of Factor
Ten-year costs				
Implementation phase				
Large software projects				
Design phase	0 31	1.00	0.30	1
Code phase	0 20	0 30	0 20	2
Test phase	0 39	0 50	0 20	3
Transfer to Ops phase	0 39	0 50	0 20	4
Small software projects				
Design phase	0 46	1 00	0 45	5
Code phase	0 25	0 45	0.25	6
Test phase	0 54	0 50	0 20	7
Transfer to Ops phase	0 54	0 50	0 20	8
Sustaining Phase				
Large Software Projects	0.27	0 50	0 20	9
Small Software Projects	0 23	0.50	0 20	10

Sources

1 B C Nichols, "SAFEGUARD Data-Processing System Structured Programming and Program Production Librarians," in L A Howard et al (eds), *The Bell System Technical Journal Special Supplement,* American Telephone and Telegraph Company, U.S A , 1975, p S215

and

F. Terry Baker, "Structured Programming in a Production Programming Environment," *IEEE Transactions on Software Engineering,* Vol SE-1, No. 2, June 1975, p 251

The increase in efficiency for the design phase is due to the use of structured programming techniques, more easily applied in a high level language environment These techniques are already included in the DSN software methodology, however, so the maximum value of the efficiency factor was chosen as 1 0, corresponding to no increase in efficiency

2 B C Nichols, *loc cit*

and

F Terry Baker, *loc cit*

These sources determined the maximum value of the efficiency factor To determine the actual and minimum value, it is assumed that a source statement can be coded as quickly in assembly language as a high level language, but that one high level statement is equivalent to five assembly statements These

assumptions were strongly supported at the Goddard Space Flight Center Software Conference, September 19, 1977

3 B C Nichols, *loc cit*

and

Montgomery Phister, Jr, *Data Processing Technology and Economics,* Santa Monica Publishing Co , Santa Monica, California, 1974, p 217

and

E N Dodson, *Resource Analysis for Data-Processing Software,* General Research Corporation RM-2117, Santa Barbara, California, August 1977, p 19

4 B C Nichols, *loc cit*

and

Montgomery Phister, Jr , *loc cit*

and

E N Dodson, *loc cit*

5 B C Nichols, *loc cit*

Again, the maximum value was assumed to be 1 0

6 B C Nichols, *loc cit*

The minimum and actual values were again chosen with reference to the Goddard Space Flight Center Software Conference information However, since small programs tend to be

less complicated than larger ones, it was assumed here that one high level statement is equivalent to four assembly language statements

7. B. C. Nichols, *loc cit*

and

Montgomery Phister, Jr , *loc cit*

and

E N. Dodson, *loc cit*

8 B C Nichols, *loc cit*

and

Montgomery Phister, Jr., *loc. cit*

and

E N. Dodson, *loc cit*

9 E N Dodson, pp 17 and 19.

10 E N Dodson, pp 17 and 19.

Appendix D-1

Cost and Savings Streams (in $K) Assuming the Efficiency Factors Listed in Appendix C-2

Year	1	2	3	4	5	6	7	8	9	10
HLRTL cost stream	690	320	340	90	90	360	110	110	380	130
Savings, assuming the efficiency factors listed in Appendix C-2	0	1013	1621	2026	2026	2026	2026	2026	2026	2026
Affordability stream = HLRTL cost − savings (in constant dollars)	-690	+693	+1281	+1936	+1936	+1666	+1916	+1916	+1646	+1896

Ten-year Totals · HLRTL $ 2620K   (constant dollars)
Savings $16816K   (constant dollars)
Affordability $14196K   (constant dollars)

Appendix D-2

Cumulative Savings (Above Costs)